



HAL
open science

Impact of the debris cover on High Mountain Asia glacier mass balances : a multi-scale approach

Fanny Brun

► **To cite this version:**

Fanny Brun. Impact of the debris cover on High Mountain Asia glacier mass balances : a multi-scale approach. Glaciology. Université Grenoble Alpes, 2018. English. NNT : 2018GREAU024 . tel-01927944

HAL Id: tel-01927944

<https://theses.hal.science/tel-01927944>

Submitted on 20 Nov 2018

HAL is a multi-disciplinary open access archive for the deposit and dissemination of scientific research documents, whether they are published or not. The documents may come from teaching and research institutions in France or abroad, or from public or private research centers.

L'archive ouverte pluridisciplinaire **HAL**, est destinée au dépôt et à la diffusion de documents scientifiques de niveau recherche, publiés ou non, émanant des établissements d'enseignement et de recherche français ou étrangers, des laboratoires publics ou privés.

THÈSE

Pour obtenir le grade de

DOCTEUR DE LA COMMUNAUTE UNIVERSITE GRENOBLE ALPES

Spécialité : **Science de la Terre et de l'Environnement**

Arrêté ministériel : 25 mai 2016

Présentée par

Fanny BRUN

Thèse dirigée par **Patrick WAGNON**
Et codirigée par **Etienne BERTHIER**

préparée au sein de l'**Institut des Géosciences de
l'Environnement**
dans l'Ecole Doctorale **Terre, Univers, Environnement**

Influence de la couverture détritique sur le bilan de masse des glaciers des Hautes Montagnes d'Asie : une approche multi-échelle

Thèse soutenue publiquement le **10 septembre 2018**,
devant le jury composé de :

Mme Delphine SIX

Physicienne, Observatoire des Sciences de l'Univers, IGE, Grenoble,
France, Présidente du jury

Mme Lindsey NICHOLSON

Chercheuse, Innsbruck University, Innsbruck, Autriche, Rapportrice

M Matthias HUSS

Maître assistant, ETHZ, Zurich, Suisse, Rapporteur

Mme Ann ROWAN

Chercheuse, Sheffield University, Sheffield, Royaume Uni, Examinatrice

M Laurent LONGUEVERGNE

Directeur de recherche CNRS, Géosciences Rennes, Rennes, France,
Examineur

M Patrick WAGNON

Directeur de recherche IRD, IGE, Grenoble, France, Directeur

M Etienne BERTHIER

Directeur de recherche CNRS, LEGOS, Toulouse, France, Co-directeur



The most important thing about expedition food is that there is some.
Eric Shipton

Abstract

High Mountain Asia (HMA) hosts the largest glacierized area outside the polar regions. Approximately 15 % of the $\sim 100\,000\text{ km}^2$ of HMA glaciers is covered by a debris layer of various thickness. The influence of this debris on the HMA glacier response to climate change remains debated. In principle, the presence of a thick layer of debris reduces the melt of the ice beneath it, due to the insulating effect. However, other processes such as ablation of bare ice cliff faces, subaqueous melt of supraglacial ponds and internal ablation due to englacial hydrology could substantially contribute to enhance the debris-covered glacier mass losses. The aim of this PhD work is to assess the impact of the debris on glacier mass balance in HMA. Up to now, the influence of the debris cover has been assessed through glacier front position changes or on a restricted sample of glaciers, and no large scale study of the influence of the debris cover on the glacier-wide mass balance is available.

As a starting point, we derived glacier mass changes for the period 2000-2016 for the entire HMA, with an unprecedented resolution, using time series of digital elevation models (DEMs) derived from Advanced Spaceborne Thermal Emission and Reflection Radiometer (ASTER) optical satellite imagery. We calculated a total mass loss of $-16.3 \pm 3.5\text{ Gt yr}^{-1}$ ($-0.18 \pm 0.04\text{ m w.e. yr}^{-1}$) with contrasted rates of regionally-averaged mass changes ranging from $-0.62 \pm 0.23\text{ m w.e. yr}^{-1}$ for the eastern Nyainqentanglha to $+0.14 \pm 0.08\text{ m w.e. yr}^{-1}$ for the western Kunlun Shan.

At the scale of HMA, the pattern of glacier mass changes is not related to the presence of debris, but is linked with the climatology. Consequently, we studied the influence of the debris-cover on mass balance within climatically homogeneous regions. Based on the mass balances of individual glaciers larger than 2 km^2 (more than 6 500 glaciers, which represent 54 % of the total glacierized area), we found that debris-covered glaciers have significantly more negative mass balances for four regions out of twelve, a significantly less negative mass balance for one region and non-significantly different mass balances for the remaining seven regions. The debris-cover is generally a less significant predictor of the mass balance than the slope of the glacier tongue or the glacier mean elevation. The influence of the debris is not completely clear and complicated to untangle from the effect of the other morphological parameters, because heavily debris-covered tongues are situated at lower elevations than debris-free tongues, where ablation is higher.

However, such a statistical analysis of the influence of the debris-cover on the glacier-wide mass balance variability is not very informative in terms of glaciological processes. In order to better constrain the contribution of the different ablation processes on debris-covered tongues, work at a finer scale is required. For the debris-covered tongue of Changri Nup Glacier, Everest region, Nepal, we quantified the contribution of ice cliffs to the ablation budget. Using a combination of very high resolution DEMs derived from Pléiades images and an unmanned aerial vehicle, we found that ice cliffs contributed to $\sim 23 \pm 5\%$ of the total net ablation of the tongue, over two contrasted years, although they occupy only 7 to 8 % of its area. Ice cliffs are large contributors to the ablation of a debris-covered tongue, but they cannot alone explain the so-called debris cover anomaly, i.e. the fact that debris free and debris covered tongues have similar thinning rates. This anomaly is probably due to smaller emergence velocity over debris-covered tongues than over debris-free tongues, resulting in similar thinning rates, despite less negative surface mass balance rates. We advocate for more measurements of ice thickness of debris-covered tongues in order to better understand their dynamics.

Keywords: High Mountain Asia, glaciers, debris-covered glaciers, remote sensing, ice cliff

Résumé

Les Hautes Montagnes d'Asie (HMA) abritent la plus grande superficie de glaciers en dehors des régions polaires. Environ 15 % des $\sim 100\,000\text{ km}^2$ de glaciers des HMA sont couverts de débris d'épaisseur variable. L'influence de cette couverture détritique sur la réponse des glaciers au changement climatique reste méconnue. Au-delà d'une épaisseur critique (quelques cm), les débris protègent les glaciers de la fonte par effet isolant. Mais ces glaciers présentent des structures qui pourraient sensiblement accentuer leur fonte : en surface ce sont les falaises où la glace est à nue et les lacs supra-glaciaires, alors qu'au cœur des glaciers c'est leur réseau hydrologique intra-glaciaire complexe. L'objectif de cette thèse est d'évaluer l'influence de la couverture détritique sur le bilan de masse des glaciers des HMA. Jusqu'à présent, cette influence a été évaluée à partir de changements de longueurs ou sur des échantillons de glaciers restreints, et aucune étude n'a quantifié l'influence de la couverture détritique sur le bilan de masse des glaciers à grande échelle.

Nous avons d'abord traité plus de 50 000 couples stéréoscopiques du capteur ASTER (Advanced Spaceborne Thermal Emission and Reflection Radiometer) pour dériver des modèles numériques de terrain (MNTs) sur la quasi-totalité des glaciers des HMA. Nous avons mesuré ainsi le bilan de masse régional entre 2000 et 2016 avec une résolution jamais atteinte auparavant. La perte totale est de $16.3 \pm 3.5\text{ Gt a}^{-1}$ soit un bilan de masse moyen de $-0.18 \pm 0.04\text{ m éq. eau a}^{-1}$, très variable spatialement, avec une perte de masse record pour le Nyainqentanglha ($-0.62 \pm 0.23\text{ m éq. eau a}^{-1}$) et un léger gain pour le Kunlun ($+0.14 \pm 0.08\text{ m éq. eau a}^{-1}$).

Cette variabilité spatiale des bilans de masse reflète au premier ordre la variabilité des climats, différents d'un bout à l'autre des HMA. Pour s'en affranchir, nous avons découpé cette région en 12 sous-régions supposées homogènes climatiquement, où nous avons étudié l'influence de la couverture détritique sur le bilan de masse des glaciers de plus de 2 km^2 ($>6\,500$ glaciers soit 54 % de la surface englacée totale). Statistiquement, la couverture de débris n'est pas un bon prédicteur du bilan de masse. Dans quatre sous-régions, les glaciers couverts ont des bilans de masse plus négatifs que les glaciers blancs, c'est l'opposé dans le Tien Shan alors que pour les sept sous-régions restantes, les bilans ne sont pas différents statistiquement entre glaciers blancs et couverts. Souvent, la couverture détritique a une influence plus faible que la pente de la langue ou l'altitude moyenne du glacier, car les langues couvertes de débris descendent plus bas en altitude, là où l'ablation est la plus forte.

Ce type d'étude statistique est intéressant pour se forger une intuition, mais reste peu informatif en termes de compréhension des processus glaciologiques. Pour mieux contraindre les contributions des processus responsables de la fonte, nous avons travaillé en parallèle à une échelle plus fine en nous intéressant au glacier du Changri Nup (2.7 km^2) situé non loin de l'Everest au Népal. À partir de MNTs haute résolution dérivés d'images des satellites Pléiades ou acquises avec un drone, nous avons montré que les falaises de glace, bien qu'elles n'occupent que 7 à 8 % de la surface de la langue de ce glacier, ont contribué à $\sim 23 \pm 5\%$ de l'ablation nette totale au cours de deux années contrastées. Ces falaises sont donc des zones d'ablation préférentielle mais couvrent des surfaces trop faibles pour compenser la réduction d'ablation induite par la couverture détritique environnante. Si l'on observe des taux d'amincissement similaires sur les langues couvertes ou non de débris, c'est que la vitesse d'émergence est plus faible sur les langues couvertes ce qui compense un bilan de masse de surface moins négatif que sur les glaciers blancs. Il est néanmoins nécessaire de mieux comprendre la dynamique des langues couvertes de débris.

Mots clés : Hautes Montagnes d'Asie, glaciers, glaciers couverts de débris, télédétection,

falaises de glace

Merci

Après trois ans d'aventures, d'enthousiasme et de belles rencontres, il est temps de finir cette thèse. Ces trois années m'ont convaincue que la science ne se construit pas dans un coin de cerveau, mais grâce à des interactions et échanges, je prends ici l'occasion de remercier tous ceux et celles qui ont contribué à cette thèse.

Merci aux membres du jury, Lindsey Nicholson, Matthias Huss, Ann Rowan, Delphine Six et Laurent Longuevergne d'avoir accepté d'évaluer mon travail et d'avoir fait le déplacement pour la soutenance.

Pour ce travail, j'ai eu la chance de collaborer avec de nombreuses équipes internationales et rencontrer des chercheurs et chercheuses à l'enthousiasme débordant. Merci à Andreas Kääb, Désirée Treichler, Walter Immerzeel, Philip Kraaijenbrink, Jakob Steiner, Evan Miles, Francesca Pellicciotti, Pascal Buri, Dibas Shrestha, Joe Shea, Anna Sinisalo et Farooq Azam. Un merci tout particulier à Amaury Dehecq et Simon Gascoin pour des discussions par mail toujours passionnées et pleines d'humour.

Pierre Ribstein et Phillip Deline ont été particulièrement disponibles et investis dans mon comité de thèse, un grand merci à vous pour ce travail de l'ombre.

Les missions de terrain dans les Alpes et au Népal ont été des aventures humaines exceptionnelles, j'ai eu la chance d'y côtoyer Vincent Jomelli, Olivier Sanchez, Aurélie Gourdon, Sonam Sherpa, Arbindra Khadka, Emmy Stigter et Max Litt.

Toutes ces aventures ne seraient possibles sans l'intervention des gestionnaires, un grand merci donc à Odette Nave, Carole Bienvenu, Valérie Lanari, Amélie Vazquez, Mélissa Dibilio, Manon Garreau, Bérénice Boeuf, François Mercier, Carméline Meli et Eric Chollet.

Un grand merci aux membres de l'équipe CYME pour le traditionnel café du matin et pour plein de discussions scientifiques ou autres : Yves, Antoine, Olivier L., Martin, et bien sûr Christian et Delph, qui m'ont tout appris sur la vitesse d'émergence et les mesures de terrain !

Merci à tous les doctorants et doctorantes qui sont toujours là pour les moments difficiles, les conseils techniques et pour boire des coups. Merci aux "anciens" : Olivier P., Etienne V., Ilann, Marion R. et Hélène A., Cyril, Julien Br., Elsa, Véro, Chloé, Ambroise, Arsène, Alexis, Camille J. et tous les autres. Merci aussi aux "nouveaux et actuels" : Julien Be., Cédric, Jinhwa, Joseph, Louise, Kévin, Maria, Julie, Jordi, Lucas, Jay, Marion, Jonathan, Philémon, Ugo, Magdalena, Céline, David et tous ceux et celles que j'oublie.

J'ai le plaisir de collaborer de façon proche avec Ali, Louise, Romain H., Camille R. et Lucas, merci à vous pour tout ce que vous m'avez appris. Inès, j'ai adoré travailler avec toi et de profiter de ton énergie rayonnante, j'espère que cela va continuer longtemps.

Etienne et Patrick vous avez été des directeurs de thèse exceptionnels, tant sur le plan scientifique que sur le plan humain. Toujours à l'écoute, patients et bienveillants, vous m'avez donné toutes les cartes pour m'épanouir au cours de ces trois années. La mission de terrain de novembre 2016 restera un superbe souvenir, merci à tous les deux.

Merci à tous ceux et celles qui ont fait le déplacement pour ma soutenance, merci les copains/copines de l'ENS et de prépa (Marthe, Stef, JB, Louise, Pierre, Etienne, Lucile, Pauline, Mathilde, Claire, Rémi, Tom, Clara, Raph), merci à ceux venus de loin (Alex, Coline, Jean, Françoise, Joel et Céline) et merci aux grimpeurs et grimpeuses Grenoble pour tous les weekends, soirées et sorties de ces dernières années.

Un immense merci à la famille, et en particulier à mes tontons, tatas et cousines qui étaient là pour m'écouter causer, à mes grand parents, qui ont toujours été là pour leur petite fille. Merci à mes parents, pour tout ce que vous m'avez apporté et pour m'avoir soutenue et encouragée dans mes choix. Merci à mon grand frerot de m'avoir montré la voie de la science, mais aussi et surtout de plein d'autres choses dans la vie.

Enfin, merci à Ilan pour tout, et surtout pour le reste.

Contents

1	Introduction	xiii
2	High Mountain Asia climate and glaciers	1
2.1	High Mountain Asia geography and climate	3
2.1.1	High Mountain Asia geography	3
2.1.2	High Mountain Asia climate	4
2.2	High Mountain Asia glaciers	7
2.2.1	Glacier inventories	7
2.2.2	Glacier distribution and climate	8
2.2.3	Seasonal cycle and glacier contribution to stream flow	9
2.2.4	Debris-covered glaciers	13
2.3	Heterogeneous glacier changes over the last 50 years in High Mountain Asia	14
2.3.1	A brief introduction to glacier change measurements	14
2.3.2	End of the twentieth century mass change (1970s-2000)	16
2.3.3	Beginning of the twenty-first century mass change (2000-present) . .	18
2.3.4	The 'debris-cover anomaly': no reduced thinning rates are observed for debris-covered tongues, compared to debris-free tongues	25
2.4	Processes unraveled by local studies to understand the influence of the debris cover on glacier mass balance	26
2.4.1	Influence of the debris thickness and moisture content	27
2.4.2	Ice cliffs	31
2.4.3	Supraglacial and englacial hydrology	32
2.4.4	Towards a closure of the mass and energy budget of debris-covered tongues?	34
	Summary and objectives of this PhD work	35
3	A spatially resolved estimate of High Mountain Asia glacier mass balances from 2000 to 2016	37
3.1	A short introduction	39
3.2	Abstract	40
3.3	Introduction	41
3.4	Methods	42
3.4.1	Generation and adjustment of ASTER DEMs	42
3.4.2	Extracting the rate of elevation change	43
3.4.3	From elevation changes to glacier mass-balance	43
3.4.4	Uncertainty assessment	43
3.5	Results and discussion	44

3.5.1	Glacier surface elevation changes	44
3.5.2	Altitudinal distribution of thickness changes	46
3.5.3	Spatial variability of individual glacier mass balances	48
3.5.4	Comparison with other regional mass balance estimates	49
3.5.5	HMA glacier contribution to SLR and hydrology	50
3.6	Conclusion	51
3.7	Supplementary information	52
3.7.1	Supplementary text	52
3.7.2	Supplementary tables	56
3.7.3	Supplementary figures	60
3.8	Going one step further	72
3.8.1	Towards an evaluation of the magnitude of the SRTM-C band penetration for the entire HMA?	72
3.8.2	Glacier contribution to streamflow: balance versus imbalance contributions	75
3.8.3	Spatially resolved geodetic observations, new data to calibrate and/or validate global glacier models	76
4	Non ubiquitous influence of debris cover and proglacial lakes on the variability of the High Mountain Asia glacier mass balances	79
4.1	A short introduction	81
4.2	Abstract	82
4.3	Introduction	83
4.4	Data and methods	84
4.4.1	Glacier-wide mass balance and morphological data	84
4.4.2	Debris-covered glaciers and debris-free glaciers	87
4.4.3	Lake-terminating and land-terminating glaciers	87
4.4.4	Multivariate linear model	87
4.5	Results	88
4.5.1	Contrasted glacier morphologies in the different regions	88
4.5.2	Morphological variables and glacier-wide mass balance	88
4.5.3	No systematic difference between debris-covered and debris-free glaciers in terms of glacier-wide mass balance	89
4.5.4	Influence of proglacial lakes on glacier-wide mass balance	91
4.6	Discussion	91
4.6.1	Complex influence of the morphological variables and debris-cover on the glacier-wide mass balance	91
4.6.2	Specificities of debris-covered glaciers	93
4.6.3	Proglacial lake influence on glacier mass balance	93
4.6.4	Limitations of our analysis	93
4.7	Conclusion	94
4.8	Supplementary methods	94
4.9	Going one step further	96
5	Ice cliff contribution to the tongue-wide ablation of Changri Nup Glacier, Nepal, Central Himalaya	99
5.1	A short introduction	101
5.2	Abstract	101
5.3	Introduction	102
5.4	Study area	104

5.5	Data	104
5.5.1	Terrestrial photogrammetry	104
5.5.2	UAV photogrammetry	105
5.5.3	Pléiades tri-stereo photogrammetry	106
5.5.4	Update of existing datasets	109
5.6	Methods	110
5.6.1	Emergence velocity	110
5.6.2	Ice cliff backwasting calculation	112
5.6.3	Sources of uncertainty on the ice cliff backwasting	114
5.7	Results	117
5.7.1	Comparison of TIN based and DEM based estimates	117
5.7.2	Sensitivity to the emergence velocity	121
5.7.3	Importance of the glacier flow corrections	121
5.7.4	Total contribution of ice cliffs to the glacier tongue net ablation for the period November 2015–November 2016	123
5.7.5	Total contribution of ice cliffs to the glacier tongue net ablation for the period November 2016–November 2017	123
5.8	Discussion	124
5.8.1	Cliff evolution and comparison of two years of acquisition	124
5.8.2	Influence of emergence velocity and glacier flow correction on f_C and f_C^*	125
5.8.3	Ice cliff ablation and the debris-cover anomaly	126
5.8.4	Applicability to other glaciers	128
5.9	Conclusions	129
5.10	Going one step further	131
6	Conclusions and outlook	133
6.1	Summary of the results	135
6.2	Outlook for future research	137
6.2.1	About debris-covered glaciers	137
6.2.2	About HMA climatology	138
6.2.3	About methodological developments	139
	Additional Publication	141
	Bibliography	178

Introduction

Why are we concerned about glaciers?

"Changes in the longer-lived components of the cryosphere (e.g., glaciers) are the result of an integrated response to climate, and the cryosphere is often referred to as a 'natural thermometer'. But as our understanding of the complexity of this response has grown, it is increasingly clear that elements of the cryosphere should rather be considered as a 'natural climate-meter', responsive not only to temperature but also to other climate variables (e.g., precipitation). However, it remains the case that the conspicuous and widespread nature of changes in the cryosphere (in particular, sea ice, glaciers and ice sheets) means these changes are frequently used emblems of the impact of changing climate." This citation, quoted from the fifth Intergovernmental Panel on Climate Change (IPCC) assessment report (Vaughan *et al.*, 2013), highlights the gap between the striking observations of massive retreat of glaciers and the in-depth understanding of the causes of these changes.

As a first step, good observations of glacier mass changes are needed to make a reliable diagnostic of the past and recent glacier mass changes. The glacier contribution to the current sea level rise (SLR) for the beginning of the twenty-first century was only recently comprehensively assessed (Gardner *et al.*, 2013), and the future evolution of glaciers and ice sheets is the main source of uncertainty in the SLR projections (Church *et al.*, 2013). For the beginning of the twenty-first century, and more precisely for the 2003-2009 period, glaciers contributed to 30 % of the observed SLR (Gardner *et al.*, 2013). Then, the second step is to develop models of glacier evolution, which can help to understand the processes responsible for glacier changes, and for example attribute the share of anthropic forcings (Marzeion *et al.*, 2014). They can predict the future evolution of glaciers under different climate scenarios (Marzeion *et al.*, 2012; Radić *et al.*, 2014; Huss and Hock, 2015; Marzeion *et al.*, 2018). Third, the glacier evolution models can be further used as inputs for hydrological models to assess the impacts of glacier changes on water resources for populations living downstream at a local scale (Huss *et al.*, 2017; Huss and Hock, 2018; Milner *et al.*, 2017).

However, the lack of good observational data disrupts the implementation of glacier models, this is the case for High Mountain Asia (HMA) glaciers (Bolch *et al.*, 2012; Azam *et al.*, 2018).

Why in High Mountain Asia?

The lack of glacier measurements, despite extensive glacier coverage, is all the more problematic, as HMA glaciers sustain the river discharge during the dry months for some densely populated basins (*Kaser et al.*, 2010; *Immerzeel et al.*, 2010; *Schaner et al.*, 2012; *Huss et al.*, 2017), and therefore, realistic projections of HMA glacier changes are crucially needed. Satellite based techniques can partially alleviate the lack of field studies, but they are limited to pluri-annual averages (*Kääb et al.*, 2012; *Gardelle et al.*, 2013).

Under a similar CO₂ emission scenario (Representative Concentration Pathway (RCP) 4.5), different glacier models predict a mass loss of 49 to 55 % of the current glacier mass for the entire HMA by 2100 (*Marzeion et al.*, 2012; *Radić et al.*, 2014; *Huss and Hock*, 2015; *Kraaijenbrink et al.*, 2017). The good agreement among these models for the end of the century is surprising, because they are calibrated with different strategies, and they strongly differ for the early twenty-first century mass changes. For instance, *Marzeion et al.* (2012) model prediction for 2000-2016 is more than twice as negative as *Gardner et al.* (2013) observation (for the period 2003-2009) on which *Huss and Hock* (2015) model is calibrated. This example rises important questions about the models calibration and about the relevance of the processes modeled.

The large tongues of HMA glaciers are often covered by a thick layer of debris (*Scherler et al.*, 2011a), which effect was included in only one of the above mentioned models (*Kraaijenbrink et al.*, 2017).

Why a focus on debris?

At the scale of HMA, the model prediction of *Kraaijenbrink et al.* (2017) does not significantly differ from the other models, despite an explicit modeling of the debris effect on ice ablation. However, at the scale of the local Dudh Koshi catchment, two studies found irreconcilable results for the future of glaciers by 2100 (*Rowan et al.*, 2015; *Shea et al.*, 2015). Different choices in glacier modeling led to the prediction of glacier mass reduction of 8-10 % in one case (*Rowan et al.*, 2015) and 84-95 % in the other case (*Shea et al.*, 2015). The two studies are not directly comparable, because they investigated different areas and used different climate change inputs, but the main source of discrepancy is the modeling of the debris effect on ablation and the modeling of debris transport in one case (*Rowan et al.*, 2015).

Glaciological knowledge is based mostly on debris free glaciers, but the extent of the debris cover is expected to increase in a context of global warming, with a widespread slowdown of glacier tongues (*Heid and Kääb*, 2012), which favors debris emergence (*Kirkbride and Deline*, 2013; *Anderson and Anderson*, 2016; *Rowan et al.*, 2015; *Wirbel et al.*, 2018). The recent increase in debris cover extent has been documented, for example, in the Alps (e.g., *Deline*, 2005; *Gardent et al.*, 2014), in Garhwal (e.g., *Bhambri et al.*, 2011) and in the Everest region (e.g., *Thakuri et al.*, 2014).

Consequently, within the course of the coming years, we might partially change our vision of glacier tongues, and debris. It was before considered as anecdotal feature, but has become very common. The potential influence of debris on the glacier evolution is still unclear, and it is therefore needed to better understand the relationship between debris and glacier mass balance. Within this long-term prospects, the aim of this PhD work is to assess the

recent evolution of HMA glaciers and to quantify the influence of debris on the glacier mass balance. This work is based on a multi-scale approach where large scale observations help to build a statistical intuition and/or validate models behavior, while, in parallel, fine scale approaches are developed to study processes, even if they are localized and their conclusions are not easy to extrapolate.

A short note to the reader

This manuscript organization follows a general direction from large scales to small scales. It starts with a review of the current state of the art knowledge about HMA climate and glaciers (chapter 2), at the end of which the detailed research questions addressed in this manuscript can be found. The main body consists in three chapters, each of which is based on an article (one published, one accepted and one in review). The articles are introduced by a short note and for some of them I present further development and research directions. A conclusion summarizes this work and provides future research directions (chapter 6). An article published in 2016 and based on a work I did for my master's thesis is appended at the end of the manuscript, as it was an important basis for the chapter 5.

This structure implies some repetitions among the different chapters and a couple of inconsistencies, such as the use of m w.e. a^{-1} or m w.e. yr^{-1} for the mass balance units, which are imposed by the different journal styles (both in compliance with *Cogley et al.*, 2011).

High Mountain Asia climate and glaciers

Contents

2.1 High Mountain Asia geography and climate	3
2.1.1 High Mountain Asia geography	3
2.1.2 High Mountain Asia climate	4
2.2 High Mountain Asia glaciers	7
2.2.1 Glacier inventories	7
2.2.2 Glacier distribution and climate	8
2.2.3 Seasonal cycle and glacier contribution to stream flow	9
2.2.4 Debris-covered glaciers	13
2.3 Heterogeneous glacier changes over the last 50 years in High Mountain Asia	14
2.3.1 A brief introduction to glacier change measurements	14
2.3.2 End of the twentieth century mass change (1970s-2000)	16
2.3.3 Beginning of the twenty-first century mass change (2000-present)	18
2.3.4 The 'debris-cover anomaly': no reduced thinning rates are observed for debris-covered tongues, compared to debris-free tongues	25
2.4 Processes unraveled by local studies to understand the influence of the debris cover on glacier mass balance	26
2.4.1 Influence of the debris thickness and moisture content	27
2.4.2 Ice cliffs	31
2.4.3 Supraglacial and englacial hydrology	32
2.4.4 Towards a closure of the mass and energy budget of debris-covered tongues?	34
Summary and objectives of this PhD work	35

2.1 High Mountain Asia geography and climate

2.1.1 High Mountain Asia geography

High Mountain Asia (HMA) refers to the Tibetan Plateau (TP) and surrounding mountain ranges. HMA spreads over 2 000 km in the north-south direction, from the north of the Tien Shan to the foothills of the Himalaya (figure 2.1). From west to east, high mountain ranges are almost continuous over 3 000 km from the Hindu Kush to the Eastern Nyainqentanglha, east of which some smaller mountain ranges can still be found in the Hengduan Shan (figure 2.1). The average elevation of the Tibetan Plateau is about 4 200 m a.s.l. and all the fourteen eight thousanders summits are located in the Karakoram and Himalaya ranges.

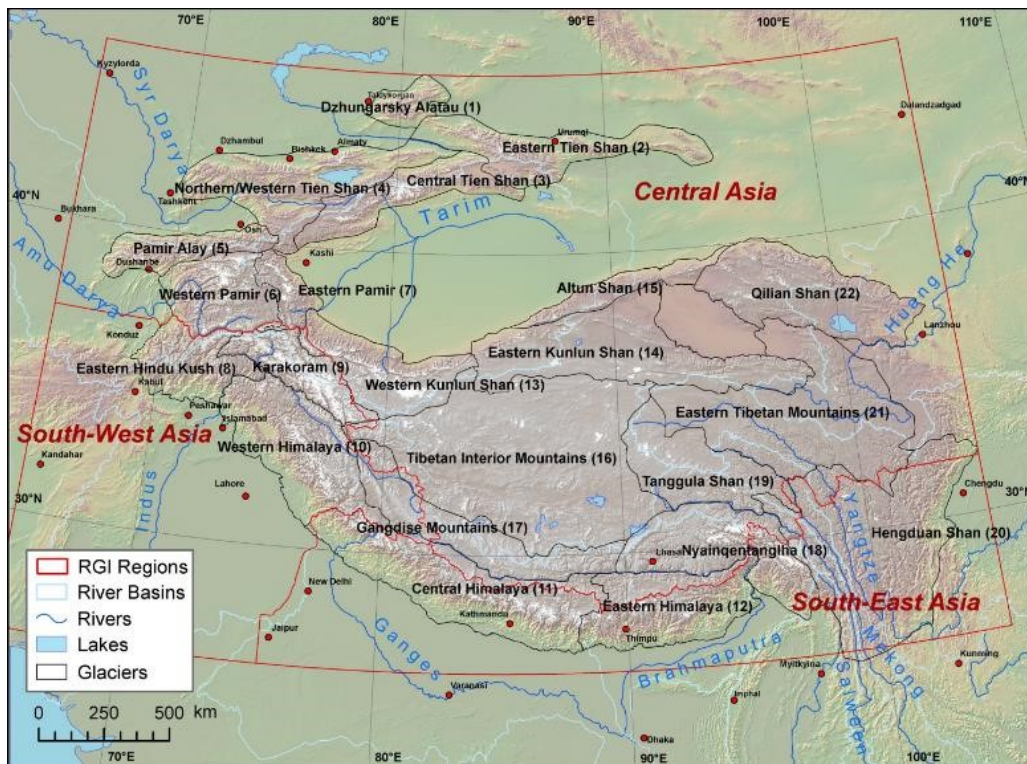


Figure 2.1: Map of HMA regions from the HIMAP assessment report (Bolch et al., 2018).

Some of the world largest rivers originate from HMA. The Indus, Ganges and Brahmaputra rivers have their sources in the Garwhal (Western Himalaya) and they provide water to over a billion of people (Immerzeel et al., 2010). The Yangtze, Mekong and Salween rivers originate from the eastern side of HMA. The famous Syr Darya and Amu Darya rivers feed the Aral Sea and the Tarim River vanishes into the Taklamakan desert; all of them have their sources in the north-western HMA (Pamir, Tien Shan and Western Kunlun Shan).

At the moment, there is no consensus about the naming of the different regions of HMA. First many borders are not accepted by all the parties, for instance the Kashmir region is still disputed between Pakistan and India, but also large parts of border between India and China are disputed in the Arunachal Pradesh region, as well as portions of the border between Bhutan and China. Second, the names of the regions and summits have often a complex history, which results in multiple names for a given geographical unit. An emblematic example could be the Everest summit, which was named in 1865 after the name of the previous Surveyor General of India (Waugh, 1857). This was done despite an already

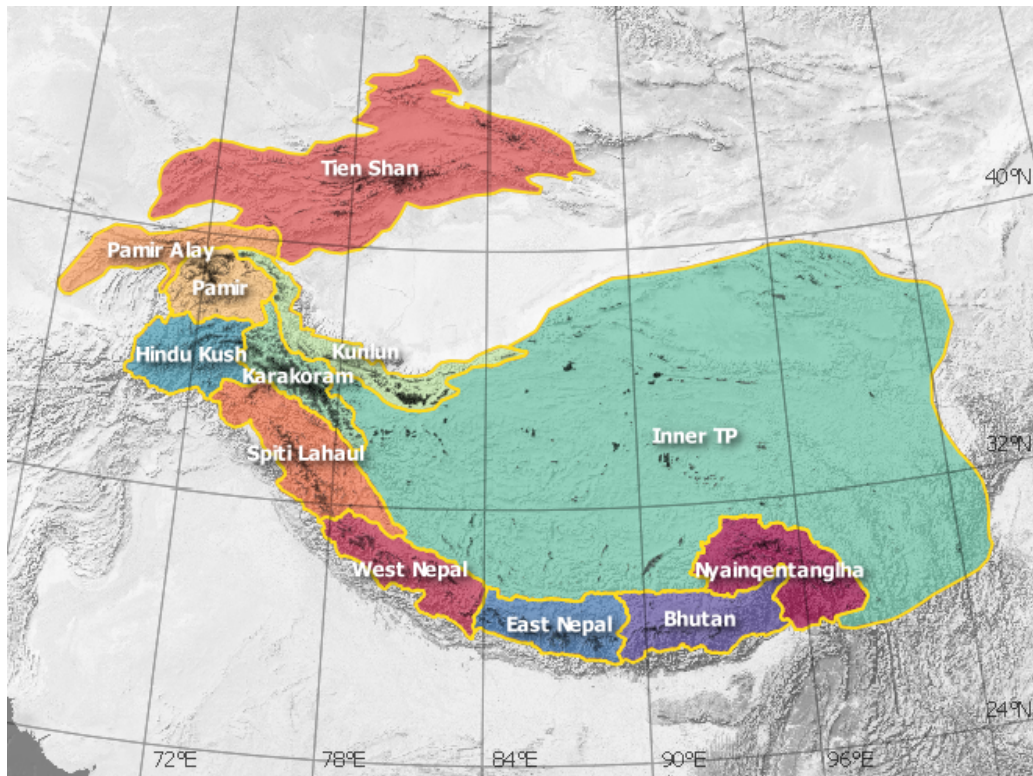


Figure 2.2: Alternative definition of regions and names (used by Kääh *et al.* (2015), Brun *et al.* (2017) and through the manuscript).

existing name in the Tibetan culture: Qomolangma (or Chomolungma, meaning the Earth goddess). As this summit is also in Nepal, it has a Nepali name (different from the Sherpa name, which is similar to the Tibetan one): Sagar-Matha. In a tense political context, the names are never neutral and there is currently no consensus in the scientific community on geographical units of HMA. Third, the local names are written or told in Sanskrit, Chinese or other languages and therefore their romanised spellings are subject to interpretation and for a given name, different spellings exist (e.g., Tianshan and Tien Shan). In this manuscript I use a mix of names as they are reported in the literature, names defined in Kääh *et al.* (2015) and later extended in Brun *et al.* (2017) (figure 2.2) and names from the Hindu Kush Himalayan Monitoring and Assessment Programme (HIMAP) report (Bolch *et al.*, 2018, figure 2.1).

2.1.2 High Mountain Asia climate

Due to a lack of high altitude long term meteorological measurements, large parts of the current knowledge about HMA climate come from satellite observations and atmospheric modeling. The southern part of HMA is relatively well covered by the Tropical Rainfall Measurement Mission (TRMM), which produces temporally sparse precipitation estimates on a 5×5 km grid (Bookhagen and Burbank, 2006). Due to non-continuous measurements in time, part of the rain events are missed and the data need to be calibrated against rain gauges (Bookhagen and Burbank, 2006). TRMM does not perform very well in capturing the solid precipitation, which introduces biases (Yin *et al.*, 2008; Ménégos *et al.*, 2013). The most commonly used climate product is ERA-Interim, which consists in meteorological variable fields at 0.75×0.75 degree resolution produced by a re-analysis (Dee *et al.*, 2011). Unfortunately, in HMA because of the strong orographic gradients and the lack of observations,

these data sometimes have a relatively low quality, in particular for the precipitation, and other products are more commonly used instead. For instance, the observation based Asian Precipitation-Highly Resolved Observational Data Integration Towards Evaluation of Water Resources (APHRODITE) precipitation dataset (Yatagai *et al.*, 2012) was shown to perform better than ERA-Interim (Andermann *et al.*, 2011; Malsy *et al.*, 2015). Alternatively, the use of the Weather Research and Forecasting (WRF, Skamarock and Klemp, 2008) model on a refined grid and forced at the domain boundaries by ERA-Interim resulted in improved estimates for the precipitation and temperature (Maussion *et al.*, 2014).

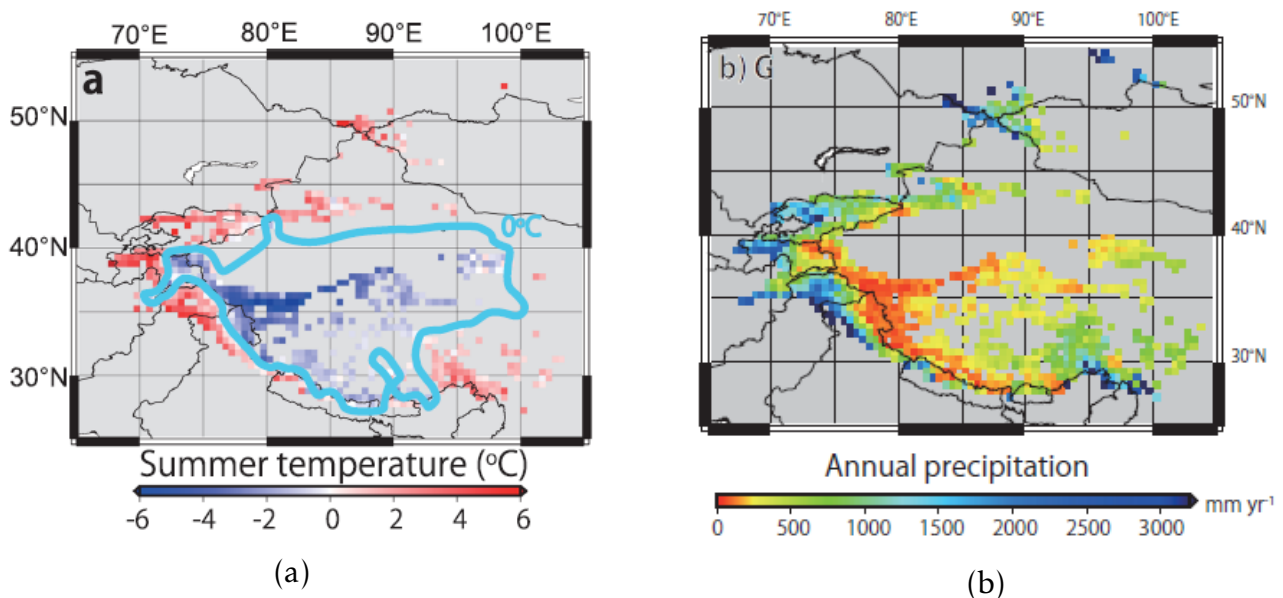


Figure 2.3: HMA climatology. (a) summer average temperature, based on the ERA-Interim data. The blue line shows the 0° isotherm. The grid cells that contain glaciers are the only ones represented. Figure from Sakai and Fujita (2017). (b) APHRODITE annual precipitation corrected for the orographic effect. Figure from Sakai *et al.* (2015).

The large spatial extent of HMA and its extreme topography result in very heterogeneous climate settings in the different sub-regions. The temperature distribution is primarily driven by the elevation and therefore some parts of HMA (for instance the inner TP) have low temperatures all year round and even in summer (figure 2.3). The moisture is brought from the Arabian Sea and potentially even the Mediterranean region by the Westerlies and from the Bay of Bengal by the Indian Summer monsoon (e.g., Bookhagen and Burbank, 2010; Burbank *et al.*, 2012, figure 2.4).

The Indian Summer monsoon (referred hereafter as the monsoon), is often portrayed as a large-scale sea breeze (Qian and Lee, 2000). In winter, the land/ocean temperature contrast favors land to sea breeze, leading to dry atmospheric conditions from Central Himalaya to eastern Nyainquentanglha. In summer, the winds are reversed because the land temperature is higher than the sea surface temperature. This brings ocean moisture over the Indian sub-continent, leading to intense rainfalls from May to September, in particular in the windward side of the Himalayas, but also to some extent in the Spiti Lahaul and Tien Shan (Maussion *et al.*, 2014). The monsoon phenomenon is much more complex than this simple breeze effect, and it interferes with the synoptic circulation (e.g., Zhang *et al.*, 2004).

The recent evolution of the monsoon is still debated. In particular, it is not sure whether it has weakened or strengthened since the beginning of the twenty-first century, since different monitoring networks capture different trends (e.g., Jin and Wang, 2017). The influence of

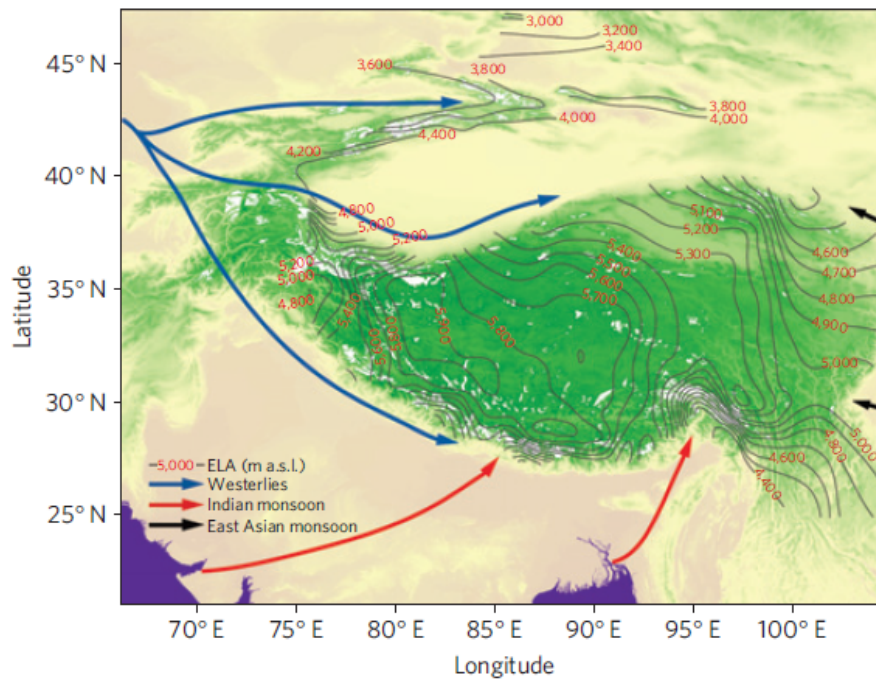


Figure 2.4: Principal sources of moisture in HMA. The East Asian monsoon has a limited influence compared to the other sources for most of HMA and is therefore not further discussed in this manuscript. Figure from Yao *et al.* (2012).

the monsoon on glaciers remains poorly known. There are evidences of its influence on the glaciers located in the southern flank of the Himalayas (e.g., Salerno *et al.*, 2015; Sherpa *et al.*, 2017; Azam *et al.*, 2014a, see section 2.2.3), but also on glaciers located in the Tibetan Plateau (Mölg *et al.*, 2012).

The westerlies are a high altitude jet, which is produced by a geopotential height gradient (e.g., Maussion *et al.*, 2014). They bring moisture to the western part of HMA from the Arabian sea. They dominate in winter and therefore bring mostly snow. The moisture content of the air masses decreases as they travel eastwards, and consequently the winter months are dry in the Central Himalaya and inner TP (Bookhagen and Burbank, 2010; Burbank *et al.*, 2012; Wagnon *et al.*, 2013). In summer, the westerlies are weaker than in winter, and the maximum of the jet intensity is shifted northward around 40°N, versus 25-30°N in winter (Maussion *et al.*, 2014). Consequently, the Pamir, Karakoram and Hindu Kush receive most of their precipitation in winter, whereas the Himalayas, Nyainquentanglha and Tien Shan receive most of their precipitation during summer.

The vision depicted here is very simplistic, and the interplay of these two climatic systems is more complex, with influence of the monsoon in far reaches, for example in the inner TP or Spiti Lahaul (Mölg *et al.*, 2012; Azam *et al.*, 2014a), and influence of the westerlies during summer as well (Mölg *et al.*, 2013, 2017). The spatio-temporal distribution of temperature and precipitation determines the spatial pattern of the equilibrium line altitude (ELA, Sakai *et al.*, 2015; Yao *et al.*, 2012, box 2.1 and figure 2.4) and therefore the possibility for glaciers to exist at certain locations and not at others.

2.2 High Mountain Asia glaciers

2.2.1 Glacier inventories

The challenge of knowing where the glaciers are seems a bit odd for Europeans who are used to accurate topographic maps, on which the glaciers are carefully delineated. However, the production of high quality glacier inventories require both high quality topographic data and expert knowledge, as it is sometimes not easy to distinguish between glaciers and snow patches. In HMA, some historical maps were produced by explorers in the twentieth century, but their quality is not good enough to use them for glacier mapping (e.g., *Bolch et al.*, 2012). Some reliable historical sources are the Survey of India maps which were produced in the 1960s (e.g., *Azam et al.*, 2018).

Since the 1980s, in order to produce standardized glacier outlines, glaciers have generally been mapped from optical satellite images, and more specifically from visible (VIS) and shortwave infrared (SWIR) data. The semi-automatic methods are based on the contrast between the low reflectance of snow and ice in SWIR and high reflectance in VIS (*Paul et al.*, 2015). The glacier outlines are usually first determined based on semi-automatic methods, which include band ratios and are then manually edited based on published recommendation guidelines issued by the Global Land Ice Measurements from Space (GLIMS) initiative (e.g., *Racoviteanu et al.*, 2009). As a baseline, it can be kept in mind that the differences between the different mapping applied to a given satellite scene usually lead to $\pm 5\%$ uncertainty in glacier area (*Paul et al.*, 2013). Nevertheless, this uncertainty is higher when mapping debris-covered tongue outlines, due to the lack of contrast between the glacier tongue and the surrounding moraines (*Paul et al.*, 2013). A very efficient method to map such tongues is to use synthetic aperture radar (SAR) loss of coherence on these slow moving tongues (e.g., *Frey et al.*, 2012; *Robson et al.*, 2015), but this method has not yet been applied over extended area.

In HMA, multiple glacier inventories exist. To my knowledge, no multi-temporal inventory is available for the entire HMA and most inventories rely on Landsat images acquired from 1980 to present (even if some Landsat images were acquired in earlier missions, their quality is usually too low for accurate glacier mapping). In order to produce a global consistent glacier inventory, the best inventories available for each region are compiled together in the Randolph Glacier Inventory (RGI, *Pfeffer et al.*, 2014); its current version is 6.0. In the RGI 6.0, most outlines originate from two sources: the GAMDAM Glacier Inventory (GGI, *Nuimura et al.*, 2015) and the second Chinese Glacier Inventory (CGI, *Guo et al.*, 2015). These inventories have a very consistent methodology and they now tend to replace the International Center for Integrated Mountain Development (ICIMOD) inventory for the Pamir-Karakoram-Himalaya (PKH, *Bajracharya and Shrestha*, 2011). For the Karakoram region, the RGI includes outlines produced by Technische Universität Dresden, in the framework of the Glaciers Climate Change Initiative (*Mölg et al.*, 2018).

Differences up to 20 %, which is much larger than the 5 % of *Paul et al.* (2013), have been reported between the different glacier inventories of HMA (*Nuimura et al.*, 2015; *Azam et al.*, 2018). These differences have multiple origins, including the different dates of acquisitions of the images, but the two main sources of difference are the presence of snow on some images which can lead to an overestimation of the glacier area and methodological differences in the delineation of the upper limit of glaciers (*Nuimura et al.*, 2015). The presence of snow on Landsat images acquired in the 1980s led to an overestimation of the glacier area in ICIMOD inventory, which in turn led to an exaggerated rate of glacier retreat when these out-

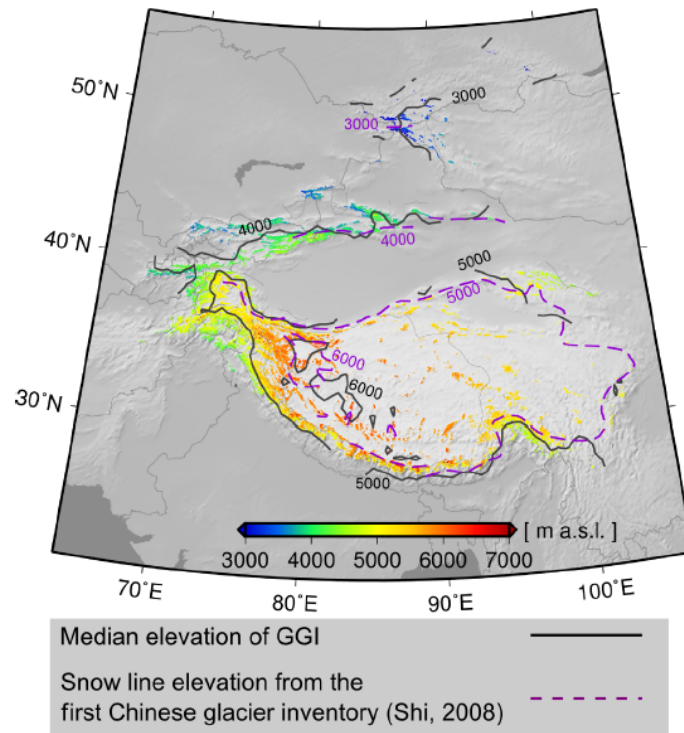


Figure 2.5: Distribution of HMA glaciers from GGI colored as a function of their median elevation. Figure from *Nuimura et al.* (2015).

lines were compared with glacier outlines derived from more recent images in Bhutan (*Bajracharya et al.*, 2014). In terms of methodological differences, some inventories include the steep slopes above the bergschrund, as they contribute to the glacier accumulation through snow avalanches, and other do not include them because there is no ice flowing along these slopes (*Nuimura et al.*, 2015). The differences between inventories and their influence on the calculation of geodetic mass balance are further discussed in section 3.7.

2.2.2 Glacier distribution and climate

Glacier inventories covering the entire HMA give insight in the glacier spatial distribution, which is linked with the topography and climate (figure 2.5). For instance, for glaciers located in the western part of HMA (Hindu Kush, Karakoram), an east-west altitudinal gradient of glacier median elevation is observed, which corresponds to glaciers being in a drier climate in the interior and therefore with less accumulation, which prevents them from flowing down to low elevations. Similarly, glaciers flow to lower elevations on the southern flank of the Central Himalaya than in the northern flank, due to both the stronger influence of the monsoon on the windward side, but also the higher elevation of the topography on the northern side

Box 2.1: ELA

The glacier equilibrium line altitude (ELA), is the altitude at which the glacier surface mass balance is equal to 0. It is defined on an annual basis and can be approximated by the maximum annual transient snow-line elevation (e.g., *Rabatel et al.*, 2005). The ELA corresponding to a glacier-wide mass balance equal to 0 is named the ELA_0 .

(figure 2.5).

It is possible to go further and use glaciers as indicators of the local climate conditions, or even as pluviometers (*Immerzeel et al., 2012a, 2015; Sakai et al., 2015*). Indeed, the glacier median elevation can be used as a first order proxy of the glacier ELA₀ (box 2.1), where ablation and accumulation balance each other. To back up this assumption, figure 2.5 shows the similarity between the median elevation of glaciers and the snowline derived from another study.

Assuming glacier ablation at the elevation of the ELA from degree-day modeling (see box 2.3), it is possible to calculate how much snow must fall at this elevation to balance the ablation (e.g., *Braithwaite et al., 2006*). This method was applied at the scale of HMA to correct the APHRODITE precipitation product (*Sakai et al., 2015*), and for the Upper Indus basin, where the high altitude precipitation was found to be 2 to 10 times higher than previously thought (*Immerzeel et al., 2015*).

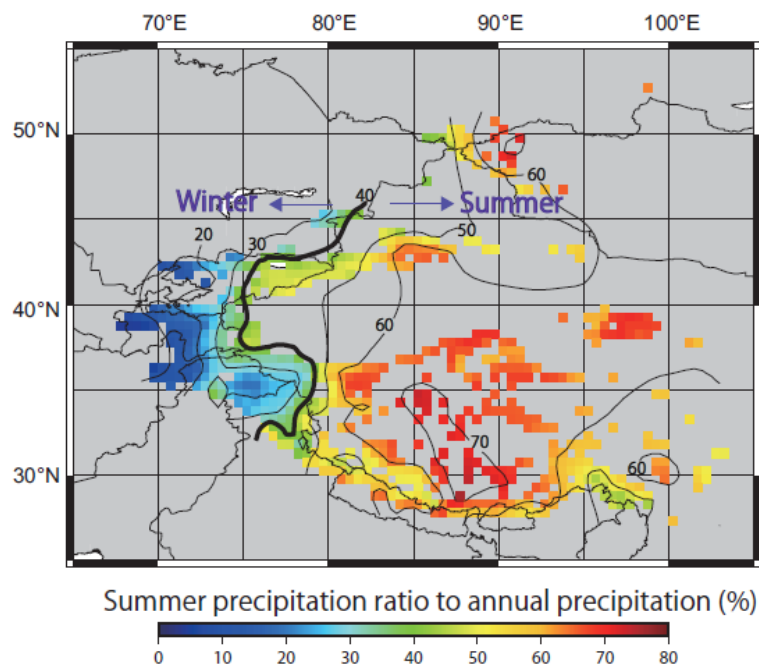


Figure 2.6: Spatial distribution of summer precipitation ratio to annual precipitation from APHRODITE data. The black thick line indicates the contour of the 40 % summer precipitation ratio. Figure from *Sakai et al. (2015)*.

2.2.3 Seasonal cycle and glacier contribution to stream flow

The location of a glacier reflects the total amount of precipitation it receives, and also its seasonality. The glaciers located in the westernmost part of HMA receive their precipitation in winter, which is the cold season (*Maussion et al., 2014; Sakai et al., 2015, figure 2.6*). Therefore they are winter accumulation type glaciers. The glaciers located in the easternmost part of HMA receive their precipitation during summer, they are therefore spring or summer accumulation type glaciers. These different influences can be observed in the glacier seasonal thickness changes, with large seasonal fluctuations in the western HMA and small fluctuations in the Central Himalaya (*Wang et al., 2017*). The same observation holds for the albedo cycle, which was found to be pronounced for Chhota Shigri Glacier in Spiti Lahaul (which is

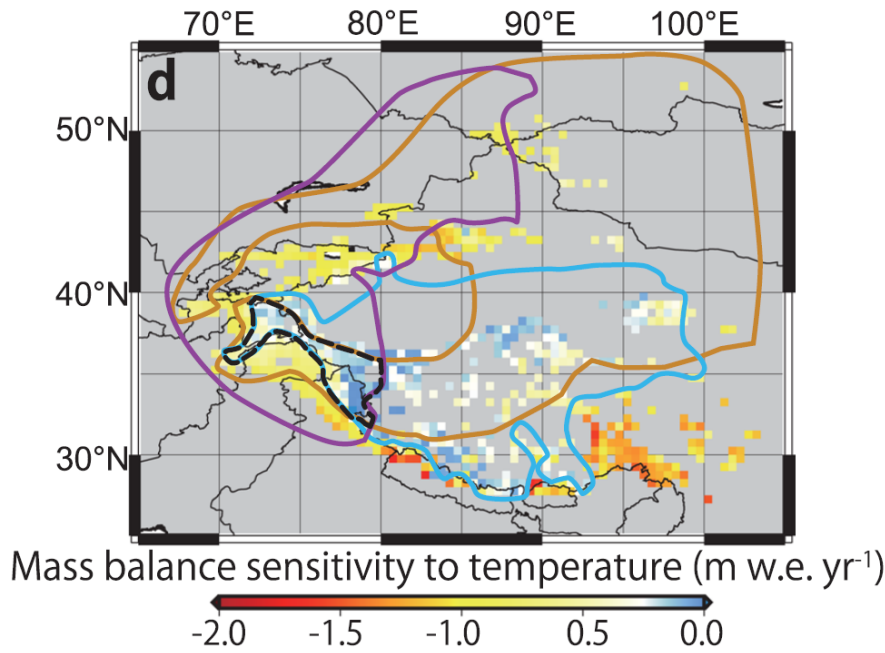


Figure 2.7: Spatial distribution of the mass balance sensitivity to a 1°C temperature change. The light blue line encircles the area where the summer temperature is below 0°C, the brown line encircles the area where the annual temperature range is larger than 20°C and the purple line encircles the area where the summer precipitation represent less than 50 % of the annual precipitation. The dashed line encircles the area where these three conditions are satisfied. Figure from Sakai and Fujita (2017).

in the transition zone between the westerlies and the monsoon influences) and not marked for Mera Glacier in the Everest region (where the monsoon influence dominates), with a range of albedo values from 0.4 to 0.8 and from 0.6 to 0.8, respectively (Brun *et al.*, 2015).

Box 2.2: mass balance sensitivity

The glacier mass balance sensitivity (MBS) to temperature is defined as the amount of change in the mass balance ($\Delta\dot{M}$) induced by a 1°C change in the temperature (ΔT):

$$\text{MBS} = \frac{\Delta\dot{M}}{\Delta T} \quad (2.1)$$

It is generally assessed by tuning a mass balance model, and then perturbing it. Maritime glaciers with a high mass turnover have a higher MBS than continental ones (Oerlemans and Reichert, 2000). The same quantity can be defined for precipitation. In this case a $\pm 10\%$ change is assumed.

Even more interestingly, a recent study suggested that the glacier mass changes were driven at first order by the glacier mass balance sensitivity to temperature (box 2.2 and Sakai and Fujita, 2017). This means that the heterogeneity in the climate change is probably not the main driver of the heterogeneous recent glacier changes (section 2.3). Sakai and Fujita (2017) also linked this mass balance sensitivity to the climate seasonality and showed that glaciers with a low summer temperature, a large temperature range and a low summer precipitation ratio were the least sensitive to an increase in the mean temperature. These glaciers with a low mass balance sensitivity are located in the western Kunlun Shan, Eastern Pamir, Eastern Karakoram and parts of the inner TP (figure 2.7).

The seasonal fluctuations of glaciers are also of importance for hydrology. There is currently no consensus about the definition of the glacier contribution to downstream hy-

drology (Lambrecht *et al.*, 2011; Schaner *et al.*, 2012; Radić and Hock, 2014; Weiler *et al.*, 2018). Some definitions are based on the annual or pluri-annual glacier changes (i.e. the glacier-wide annual mass balance). This definition is favored by glaciologists, because it is directly linked to glaciological measurements (see section 2.3.1). Nevertheless, this definition is not very useful for hydrologists because the glaciers actually influence the downstream discharge on a seasonal scale (e.g., Huss, 2011; Radić and Hock, 2014, figure 2.8). When the glaciers are located in a climatic region where the accumulation and ablation seasons are distinct, the glaciers play a role in sustaining the river flows during the dry season, this is called the seasonally delayed runoff (e.g., Kaser *et al.*, 2010). The runoff originating from the glacier outlet is generated by multiple processes, such as ice melt, snow melt on glacier, but also rain on glacier, and these different processes are expected to respond differently in a changing climate. Recent work suggested to homogenize these definitions, and in particular to make the difference between processed-based, surface-based and particle tracking-based definitions (e.g., Weiler *et al.*, 2018; Mimeau *et al.*, 2018). This is rather appealing, except that these definitions are model oriented (and probably model dependent) and are complex to apply to field and space measurements. Alternatively, the glacier contribution to stream-flow can be calculated as the difference between two model runs, with and without glacier (e.g., Akhtar *et al.*, 2008). This approach is interesting because it is easy to implement in models, but again it is useful only in modeling studies.

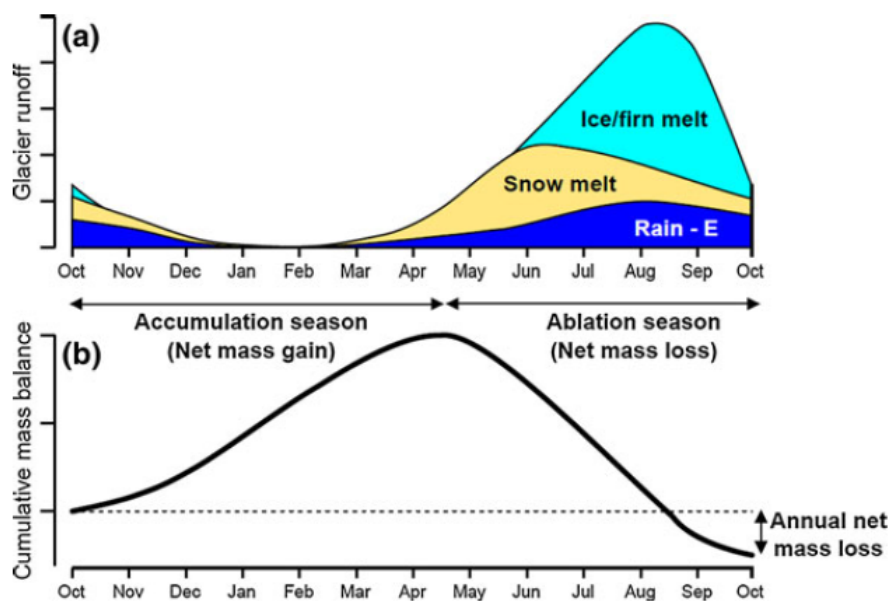


Figure 2.8: a- Schematic seasonal variation of total glacier runoff and its components, E is evaporation. b- cumulative glacier mass balance in specific units (m w.e. a^{-1}) showing a year with negative annual balance. Figure from Radić and Hock (2014).

This being said, the challenge of unravelling the glacio-hydrology of HMA as a whole or of selected catchments has already been tackled by some studies. Immerzeel *et al.* (2010) focused on the southern part of HMA (Indus, Ganges, Brahmaputra, Yellow and Yangtze rivers) and showed that glaciers and snow play an important role in the upper Indus and Brahmaputra basins, due to the seasonally delayed runoff. These first estimates were probably too large and were later revised (Lutz *et al.*, 2014). By using a first order mass conservation approach ("what comes in must go out"), Kaser *et al.* (2010) estimated the annual glacier ablation as the integral of the precipitation on the glacier surface and redistributed the ablation at monthly scale using a degree-day scaling approach. They found a lower contribution to the Indus than Immerzeel *et al.* (2010), but stressed the importance of the

glacier runoff for the Aral Sea basin, where the climate is dry, the seasonality is pronounced and where many people live in the upper reaches of the catchment (Kaser *et al.*, 2010). *Andermann et al.* (2012) found a contribution of snow and ice melt of $\sim 10\%$ of the annual river discharge of the mountainous Nepalese catchments and stressed the role of groundwater in delaying the discharge. It is noteworthy that these studies were published when we knew little about the HMA glacier mass changes (see section 2.3) and assumed no perennial changes in the glacial storage and therefore examined only the seasonal or "balance" glacier contribution (Pritchard, 2017)¹. It would be interesting in the future to incorporate the decennial glacier mass changes in such studies (section 3.8.2), as it was done in *Gardelle et al.* (2013), who found 10 year average "imbalance" contribution of the same order of magnitude as the seasonal delay for the Indus, and two to three times larger for the Ganges and Brahmaputra.

In order to separate the different terms of the hydrologic budget, numerous studies were conducted on small catchments, associated with intensive meteorological sensor deployment and mass balance field measurements. The Langtang catchment (e.g., *Immerzeel et al.*, 2012b; *Ragettli et al.*, 2015), the Dudh Koshi catchment (e.g., *Racoviteanu et al.*, 2013; *Nepal et al.*, 2014; *Savéan et al.*, 2015; *Soncini et al.*, 2016; *Mimeau et al.*, 2018), the Tsho Rolpa Glacial Lake–Trambau Glacier catchment (e.g., *Fujita and Sakai*, 2014) and sub-catchments of the Tarim Basin (e.g., *Duethmann et al.*, 2015) have been investigated over the last years. These studies relies on glacio-hydrological modeling, with different level of complexities and found various snow and glacier melt contribution to streamflow. Regardless the choice of the model and despite the installation of tipping bucket or rain gauges, all these studies faced the challenge of the uncertain precipitation amount and spatio-temporal distribution, which is probably the main source of uncertainty in such studies (e.g., *Pellicciotti et al.*, 2012; *Immerzeel et al.*, 2014b; *Savéan et al.*, 2015; *Eeckman et al.*, 2017). Another limitation is the challenge to model the glacier surface energy balance (e.g., *Fujita and Sakai*, 2014; *Mimeau et al.*, 2018, box 2.4) or to parametrize the glacier surface melt (e.g., *Immerzeel et al.*, 2012b; *Ragettli et al.*, 2015), and to reconcile the glacier budget with field observations (*Mimeau et al.*, 2018).

Box 2.3: degree-day modeling

Degree-day (or temperature index) modeling is based on an empirical relationship between snow/ice ablation and the sum of the positive mean daily temperatures. These models are calibrated with field data and are very efficient to retrieve the ablation for the glaciers on which the model is calibrated. Nevertheless, these models are not physically based, and therefore their spatial and temporal extrapolation is challenging (*Réveillet et al.*, 2017).

Concerning the future of the glacier melt water availability in HMA two effects have to be considered for glaciers in a warming climate. First, the glacier surface melt increases, due to an increase in the surface energy intake and leading to an increase in glacier runoff. Second, the glacier area shrinks, leading to a reduction in the contributing surface and therefore a reduction in glacier runoff. As a consequence, all the other runoff components assumed unchanged, the total runoff increases until a maximum (the "peak water") and then decreases to return to its initial value (e.g., *Huss and Hock*, 2018). In the Baltoro and Langtang watersheds, the peak water has not been reached yet and is expected in the middle in the twenty-first century (*Immerzeel et al.*, 2013; *Ragettli et al.*, 2016a). This was also verified for

¹*Pritchard* (2017) was retracted in 2018, based on a mistake in the glacier "imbalance" contribution to streamflow. Nevertheless, this mistake does not affect some parts of the paper, and therefore I decided to cite this article for some of the concepts developed in it.

all the Himalaya and Karakoram catchments (*Lutz et al.*, 2014) and also for the entire HMA (*Huss and Hock*, 2018). These changes will be associated with a shift towards more melt at the beginning of the melt season (*Lutz et al.*, 2016; *Huss and Hock*, 2018). Nevertheless, it should be kept in mind that the main sources of uncertainties of these studies are the future changes in precipitation (*Lutz et al.*, 2016).

2.2.4 Debris-covered glaciers

Part of the glacier runoff originates from their lower parts, where the melt is the highest. In HMA, the lower parts of glaciers are often covered by a thick debris mantle (*Scherler et al.*, 2011a; *Benn et al.*, 2012; *Kraaijenbrink et al.*, 2017). In HMA, ~ 15 % of the glacierized area is covered by debris (chapter 4). On top of this, the debris cover increases in a context of retreating glaciers (*Bhambri et al.*, 2011; *Gardent et al.*, 2014; *Thakuri et al.*, 2014), and is stable in regions where the glaciers do not retreat (*Herreid et al.*, 2015), meaning that it is important to understand the influence of the debris on glacier evolution, as debris is expected to extend in the coming years. The debris-covered glaciers form in a context of high relief and deeply incised valleys, where the steep unglacierized slopes above the glaciers can supply the debris (*Scherler et al.*, 2011b). Debris is transported englacially and emerges in the ablation area of the glacier (*Small et al.*, 1979; *Kirkbride and Deline*, 2013; *Rowan et al.*, 2015; *Wirbel et al.*, 2018).

There is currently no accepted definition of debris-covered or debris-free glaciers, as there is a continuum of various debris coverage and few glaciers have no debris cover at all. Nevertheless, there is a general agreement for large debris-covered glaciers, such as Khumbu or Ngozumpa glaciers (Everest region, Nepal). In general, the debris-covered glaciers have long and gently sloped tongues (*Scherler et al.*, 2011b; *Salerno et al.*, 2017). They are characterized by slow flowing tongues (*Quincey et al.*, 2009; *Scherler et al.*, 2011a) and spatially variable rates of surface elevation changes (e.g., *Thompson et al.*, 2016; *Ragettli et al.*, 2016b; *King et al.*, 2017; *Huang et al.*, 2018). They have stable front positions and, in the context of a climate imbalance, they respond through surface lowering and limited front retreat, contrary to the clean-ice glaciers (*Scherler et al.*, 2011a; *Rowan*, 2017; *Salerno et al.*, 2017).

The debris has a strong influence on the surface energy balance of the glacier, and therefore on the amount of energy available for the melt at the ice-debris interface (*Nicholson and Benn*, 2006). This is a phenomenon which has been known for a long time: when ice is buried beneath a debris layer thick enough, it melts less than the near-by clean ice (*Østrem*, 1959). The debris thickness for which the ice ablation is reduced compared to debris-free ice is called the critical debris thickness (*Lejeune et al.*, 2013). The differential ablation leads to the apparition and persistence of remarkable features such as glacier tables and dirt cones (e.g., *Swithinbank*, 1950; *Drewry*, 1972). Nevertheless, there is a large gap between the naive observation of differential ablation and the actual quantification of the energy fluxes through a debris layer, which is still a very active field of research (section 2.4.1).

The surface of debris-covered glaciers is highly heterogeneous (*Benn et al.*, 2012; *Casey et al.*, 2012) and the debris thickness is variable and extremely challenging to measure over large areas (section 2.4.1). Little is known about the spatio-temporal variability of the debris properties, such as its thermal conductivity, its moisture content or its grain size and porosity distributions (*Benn et al.*, 2012). To further complicate the story, striking features, namely ice cliffs and supraglacial ponds, are widely observed and persist at the surface of debris-covered glaciers (*Benn et al.*, 2012). They play an important role as entry points for the energy in the system, as it was suggested by pioneering studies in the 2000's (e.g., *Sakai*

et al., 1998, 2000, 2002). The influence of these features are detailed in sections 2.4.2 and 2.4.3. The last major unknown about the debris-covered energy budget is the role of internal ablation through the development of englacial hydrology networks (e.g., *Benn et al.*, 2017).

In order to understand the influence of the debris cover on the glacier mass balance, I first reviewed the glacier mass balance changes at the scale of HMA over the last 50 years.

2.3 Heterogeneous glacier changes over the last 50 years in High Mountain Asia

2.3.1 A brief introduction to glacier change measurements

Historically, glacier length fluctuations were the first observations of glacier evolution (*Lliboutry*, 1965). In the Alps, some of the glacier area or snout position change observations go back in time as far as the nineteenth century, based on historical maps, paintings or photographs (*Nussbaumer et al.*, 2007). In HMA, they extend back to the 1960's (*Leclercq et al.*, 2014; *Cogley*, 2016). Unfortunately, glacier geometry fluctuations are indirect responses of glaciers to a changing climate because they result from a combination of immediate climate influence (the mass balance) and ice dynamics as the flow is dependent of the glacier itself (geometry, slope, area...; *Cuffey and Paterson*, 2010).

A more direct link between glacier change and climate is the glacier mass balance. Glacier mass balance is the integral of all the mass fluxes through the glacier boundary. The total mass (M) of a land terminating glacier changes at a rate \dot{M} (expressed in kg a^{-1} or in $\text{m}^3 \text{ w.e. a}^{-1}$) as (*Cuffey and Paterson*, 2010):

$$\dot{M} = \int_A [\dot{b}_s + \dot{b}_e + \dot{b}_b] dA \quad (2.2)$$

where A (m^2) is the glacier map view area, \dot{b}_s , \dot{b}_e and \dot{b}_b are the surface, englacial and basal mass balances, expressed in $\text{kg m}^{-2} \text{ a}^{-1}$ or in m w.e. a^{-1} . For most glaciers, the dominant term of the integral is the surface mass balance, and therefore the glacier-wide mass balance is often approximated by the surface mass balance:

$$\dot{M} \simeq \int_A \dot{b}_s dA \quad (2.3)$$

Two important methods are used to measure \dot{M} :

The glaciological method consists in a direct measurement of \dot{b}_s , either at an annual or a sub-annual frequency, if possible. In the accumulation zone (figure 2.9), the mass balance is measured with snow pit measurements (including density measurements) at the end of the accumulation season and with stakes inserted in the snow pits in the ablation season. In the ablation zone, the mass balance is measured by snow probing at the end of the accumulation season and by stake inserted in the ice for the ablation season. \dot{M} is thus the area weighted average of point measurements extrapolated over the entire glacier, this extrapolation adds some uncertainty (e.g., *Thibert et al.*, 2008). This is a very basic overview and the method can be refined, in particular by including

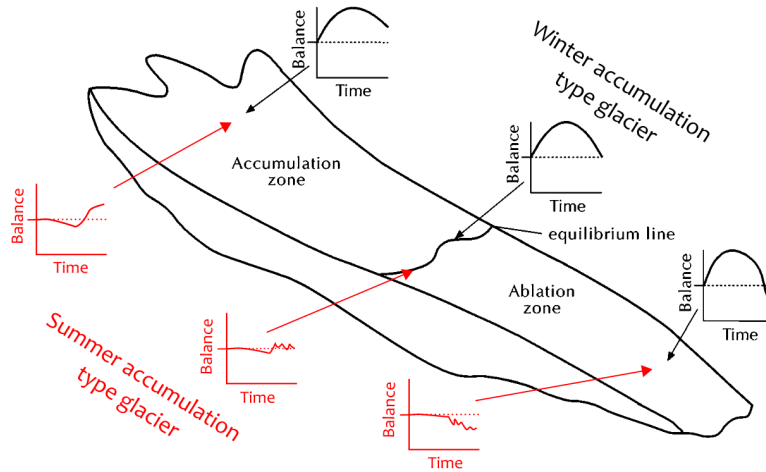


Figure 2.9: Idealized glacier separated in its accumulation zone (where $\dot{b}_s > 0$ on the annual scale) and its ablation zone (where $\dot{b}_s < 0$ on the annual scale). The black (resp. red) small plots show the evolution of \dot{b}_s at the annual scale for winter (resp. summer) accumulation type glaciers. Figure modified from *Cuffey and Paterson (2010)*.

frequent surveys through the ablation season (e.g., *Six and Vincent, 2014; Réveillet, 2016; Zekollari and Huybrechts, 2018*).

For summer accumulation type glaciers (for instance in the central Himalaya), the monsoon corresponds to both the accumulation and the ablation season (*Fujita and Nuimura, 2011*). Therefore, \dot{b}_s does not follow the idealized seasonal cycle depicted for winter accumulation type glaciers in figure 2.9. It has consequences in terms of field monitoring: the strong westerlies wind blowing in winter re-mobilize part of the snow in the higher part of the glacier and the absence of a season during which ablation only occurs creates a very complicated internal layering of the snow (e.g., *Wagnon et al., 2013; Sherpa et al., 2017*). As a consequence, there is a need to mark the reference snow surface measured by spreading colored powder on the snow surface (*Wagnon et al., 2013*).

The geodetic method aims at measuring the total glacier volume change through repeat surveys of its surface topography. The survey of a fraction (e.g., a centerline or the glacier tongue only) of the glacier surface can introduce large bias in the total glacier volume change estimate (e.g., *Berthier et al., 2010*). Consequently, the method of differencing two digital elevation models (DEMs) obtained either from airborne photogrammetry or from satellite topographic missions, which can both ensure a relatively complete coverage of the glacier surface under some conditions (e.g., enough contrast in the accumulation area and no clouds), is now favored. In this case, the total glacier volume change (ΔV in m^3) is expressed as:

$$\Delta V = r^2 \sum_{k=1}^K \Delta h_k \quad (2.4)$$

where r (in m) is the pixel size (on a regularly spaced grid), K is the number of pixel on the glacier area and Δh_k (in m) is the individual glacier pixel elevation change (*Zemp et al., 2013*). Geodetic measurements are usually performed for time spans larger than 5 or 10 years in order to minimize the associated uncertainties. The rate of volume change (\dot{V}) is then converted to a rate of mass change using a volume to mass

conversion factor, referred to as the density assumption (*Huss, 2013*):

$$\dot{M} = f_{\Delta V} \dot{V} \quad (2.5)$$

Under some hypothesis, it has been shown that the volume to mass conversion factor ($f_{\Delta V}$) can be approximated by a constant value of $f_{\Delta V} = 850 \pm 60 \text{ kg m}^{-3}$ (*Huss, 2013*).

It is noteworthy that these two methods measure different quantities, as the geodetic method integrates \dot{b}_b and \dot{b}_e as well. Sometimes these two terms are non negligible contributors to the glacier-wide mass balance (e.g., *Alexander et al., 2011; Oerlemans, 2013; Andreassen et al., 2016*), and can lead to discrepancies between the geodetic and the glaciological mass balances. Glacier-wide mass balances measured with the glaciological method can be biased and need to be calibrated with geodetic measurements (e.g., *Thibert et al., 2008; Zemp et al., 2013*).

Glacier mass changes are sparsely sampled world-wide (*Zemp et al., 2015; WGMS, 2017*). This is particularly true for the HMA, partially explaining the IPCC controversy about the predicted rapid disappearance of these glaciers (*Cogley et al., 2010*). Nevertheless, over the last ten years, an incredible amount of knowledge was gained about the mass and volume changes of the HMA glaciers from ~ 1970 to present (*Bolch et al., 2012; Azam et al., 2018*).

2.3.2 End of the twentieth century mass change (1970s-2000)

From field surveys and reconstructions

Very few HMA glaciers were continuously monitored with the glaciological method at the end of the twentieth century for many reasons. First, few countries had long term national glacier monitoring programs, with the notable exception of China that has continuously conducted the survey of Urumqi Glacier No. 1 since 1978, Kazakhstan that has continuously monitored the Tsentralniy Tuyuksuyskiy Glacier since 1956 and the Soviet Union which monitored about 17 glaciers, including Abramov Glacier, with some of the time series covering about 20 years, from ~ 1970 to ~ 1990 (*WGMS, 2017; Hoelzle et al., 2017*). The collapse of the Soviet Union in 1991 interrupted the measurements (*Hoelzle et al., 2017*). Only two glaciers in HMA are reference glaciers (Urumqi Glacier No. 1 and Tsentralniy Tuyuksuyskiy Glacier) of the World Glacier Monitoring Service (WGMS), as these are the only two uninterrupted series of annual mass balance longer than 30 years (*WGMS, 2017*). Second, most glaciers located in the Himalayas,

Box 2.4: energy balance models

The energy balance models (e.g., *Reid and Brock, 2010*) express the conservation of energy at the atmosphere/glacier boundary and are used to calculate the energy available for melt M , when the surface temperature is equal to 0, as

$$M = S + L + H + LE + P + G \quad (2.6)$$

where S is the net solar energy radiation, L is the net longwave radiation, H is the sensible heat transfer, LE is the latent heat transfer, P is the heat transfer due to precipitation and G is the conductive heat flux below the surface. The energy balance model is the basis of a physical modeling of the different fluxes, this is very advantageous for ubiquitous models, but it implies that the model is very sensitive to the input data.

Western Nyianqentanghla, Western Kunlun Shan or Pamir are at high elevation and on remote locations, making field work hard to conduct there. Third, some of the glaciers are very large (larger than 100 km²) and it is not possible to calculate their mass balance with the glaciological method, even if sparse glaciological measurements are performed (e.g., on Baltoro Glacier, *Mayer et al.*, 2006).

As a consequence, a large part of our knowledge about the twentieth century HMA glacier changes comes from reconstruction of time series of glacier mass balance. Different reconstruction strategies have been applied. For instance, *Azam et al.* (2014b) used a simple degree-day model (box 2.3) to reconstruct the annual glacier-wide mass balance of Chhota Shigri Glacier (Western Himalaya, India) from 1969 to present, using meteorological data from a meteorological station located ~ 50 km away from the glacier. Interestingly, Chhota Shigri glacier-wide mass balance was close to equilibrium between 1986 and 2000. Geodetic studies assessed the representativeness of Chhota Shigri Glacier, and showed that its mass balance was close to the region average (*Vincent et al.*, 2013; *Mukherjee et al.*, 2018). A more sophisticated model was implemented on Abramov Glacier (Pamir Alay, Kyrgyzstan) to fill in the measurement gap of the late nineties and two-thousands (*Barandun et al.*, 2015). Based mostly on the historical measurements and marginally on the reconstruction, they found sustained mass loss for this glacier at a rate of -0.44 ± 0.10 m w.e. a⁻¹ for the period 1968-2014 (*Barandun et al.*, 2015). For the entire Tien Shan, *Farinotti et al.* (2015) reconstructed 50 years of persistent glacier mass loss of -0.36 ± 0.15 m w.e. a⁻¹ with a glaciological model calibrated on the recent period.

From remote sensing surveys

Box 2.5: SRTM penetration

The Shuttle Radar Topography Mission (SRTM) DEM was acquired in February 2000. The acquisition was made in the C-band frequency, which is known to penetrate into ice and snow up to about 10 m (*Rignot et al.*, 2001). Even after correction, the penetration depth is likely underestimated (e.g., *Gardelle et al.*, 2012a; *Dehecq et al.*, 2016). Consequently glacier thickness changes estimates which use SRTM as a start date are probably too positive and those which use SRTM as an end date are probably too negative.

The geodetic method is the only way to obtain direct observations of glacier mass changes back in time, for areas where glaciers were not monitored in the field. Most of the published studies relied on the Shuttle Radar Topography Mission (STRM) DEM for the reference topography of 2000, despite the penetration bias (box 2.5). Most of the earlier DEMs used for differentiation were extracted from spy satellite acquisitions (Corona and Hexagon missions), which started in 1959 but peaked in the 1970s. Since the pioneering study of *Bolch et al.* (2008), many glaciological studies made use of these data to assess region-wide mass balances for selected regions (table 2.1 and figure 2.10). With the notable exception of *Maurer et al.* (2016), most of these

studies manually processed the images, preventing the method from a wide application. These studies found the most negative mass balances in the Ak-Shirak (Tien Shan) region, with a mass balance of -0.51 ± 0.36 m w.e. a⁻¹ (*Pieczonka and Bolch*, 2015). The most positive mass balance was observed in the eastern part of the West Kunlun Shan, with a mass balance of $+0.05 \pm 0.14$ m w.e. a⁻¹ (*Zhou et al.*, 2018). Even if they are far from exhaustive, these studies showed a relatively homogeneous pattern of glacier mass changes (figure

2.10). The Karakoram, Spiti Lahaul, Muztagh Ata and Western Kunlun Shan regions were close to equilibrium (*Mukherjee et al., 2018; Bolch et al., 2017; Zhou et al., 2018; Zhang et al., 2016; Holzer et al., 2015; Zhou et al., 2017*). The central Himalaya was in slight imbalance (*Robson et al., 2018; Zhou et al., 2018; Bolch et al., 2011; Lamsal et al., 2017; Maurer et al., 2016*), and the Tien Shan in marked imbalance, in particular its western part (*Pieczonka and Bolch, 2015*). One should keep in mind that most of these studies used the SRTM DEM as end date and therefore the mass balance values are likely too negative (box 2.5).

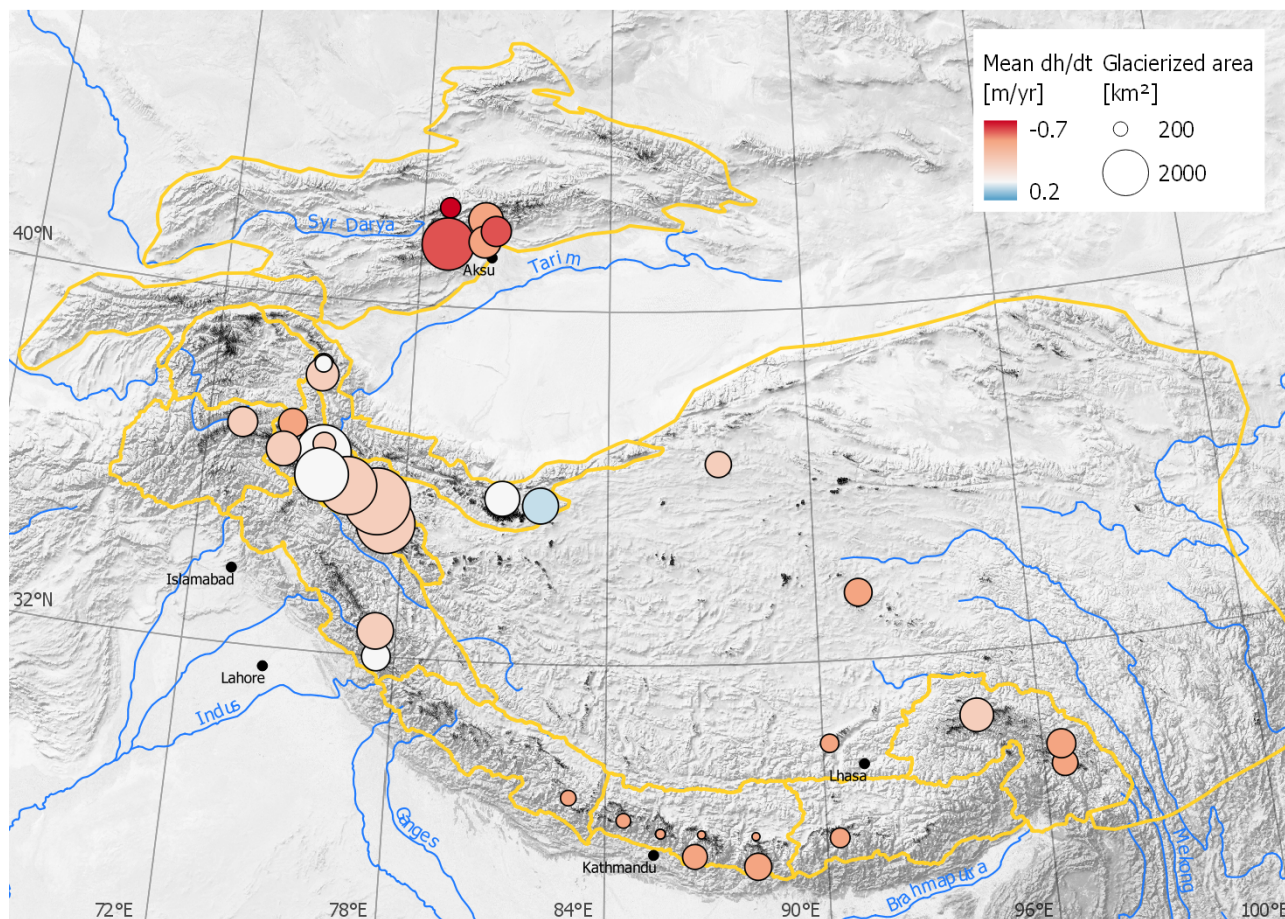


Figure 2.10: Summary of the geodetic mass balance studies for the period 1970's-2000. For the precise dates and references, please refer to table 2.1. For the sake of consistency and comparison with the chapter 3, the mass balance values have been converted to mean rate of elevation changes using a volume to mass conversion factor of 850 kg m^{-3} (*Huss, 2013*).

Some studies investigated individual glacier or regional changes based on historical maps (*Lambrecht et al., 2014; Wu et al., 2018*) or on historical surveys of the glacier topography (*Vincent et al., 2013*).

2.3.3 Beginning of the twenty-first century mass change (2000-present)

ICESat and GRACE

Two satellite missions launched in 2002 and 2003, Gravity Recovery and Climate Experiment (GRACE) and Ice, Cloud, and land Elevation Satellite (ICESat), tremendously increased the state of knowledge about the evolution of glacier masses worldwide, but in particular in HMA (*Gardner et al., 2013*).

Table 2.1: Summary of the published estimates of HMA geodetic mass balances based on the Corona and Hexagon missions. The *Wu et al. (2018)* study is based on a topographical map for the earlier DEM and not a Corona or Hexagon DEM. Most of the studies used SRTM as the latter DEM. *Pieczonka et al. (2013)* also did an additional 1976-2009 estimate not including the SRTM DEM (not shown on figure 2.10).

Source	Region	Area (km ²)	BM (m w.e. a ⁻¹)	Start date	End date
<i>Bolch et al. (2011)</i>	Everest	62	-0.32 ± 0.08	1970	2007
<i>Pieczonka et al. (2013)</i>	Aksu-Tarim	846	-0.40 ± 0.23	1976	1999
<i>Pieczonka et al. (2013)</i>	Aksu-Tarim	839	-0.22 ± 0.19	1976	2009
<i>Holzer et al. (2015)</i>	Muztag Ata	273	-0.04 ± 0.42	1971/76	1999
<i>Maurer et al. (2016)</i>	Bhutan	365	-0.17 ± 0.05	1974	2006
<i>Pellicciotti et al. (2015)</i>	Langtang	95	-0.32 ± 0.18	1974	2000
<i>Pieczonka and Bolch (2015)</i>	Ak-Shirak	383	-0.51 ± 0.36	1973	1999
<i>Pieczonka and Bolch (2015)</i>	Aksu/Sary-Djaz Catch.	2556	-0.35 ± 0.34	1973	1999
<i>Pieczonka and Bolch (2015)</i>	Inylchek area	1117	-0.20 ± 0.44	1973	1999
<i>Pieczonka and Bolch (2015)</i>	Tomur area	953	-0.33 ± 0.30	1973	1999
<i>Pieczonka and Bolch (2015)</i>	Inylchek area	1117	-0.20 ± 0.44	1973	1999
<i>Ragetti et al. (2016b)</i>	Langtang	87	-0.24 ± 0.08	1974	2006
<i>Zhang et al. (2016)</i>	Muztag Ata	376	-0.15 ± 0.18	1971/76	1999
<i>Zhang et al. (2016)</i>	Kongur Tagh	1002	-0.16 ± 0.18	1971/76	1999
<i>Bolch et al. (2017)</i>	Hunza Catchment	2868	-0.01 ± 0.09	1973	2000
<i>Lamsal et al. (2017)</i>	Kanchenjunga	60	-0.18 ± 0.17	1975	2010
<i>Zhou et al. (2017)</i>	E Karakoram E	3236	-0.07 ± 0.05	1974	2000
<i>Zhou et al. (2017)</i>	E Karakoram W	4184	-0.13 ± 0.08	1980	2000
<i>Zhou et al. (2017)</i>	C Karakoram E	3179	-0.16 ± 0.07	1979	2000
<i>Zhou et al. (2017)</i>	C Karakoram WN	478	-0.14 ± 0.05	1973	2000
<i>Zhou et al. (2017)</i>	C Karakoram WS	2708	-0.03 ± 0.05	1973	2000
<i>Zhou et al. (2017)</i>	W Karakoram N	771	-0.17 ± 0.06	1973	2000
<i>Zhou et al. (2017)</i>	W Karakoram S	1124	-0.08 ± 0.05	1973	2000
<i>Robson et al. (2018)</i>	Manaslu	200	-0.31 ± 0.12	1970	2000
<i>Mukherjee et al. (2018)</i>	Lahaul Spiti	1250	-0.07 ± 0.10	1971	1999
<i>Wu et al. (2018)</i>	Kangri Karpo	788	-0.24 ± 0.16	1980	1999
<i>Zhou et al. (2018)</i>	Parlung Zangbo	615	-0.19 ± 0.14	mid 70's	2000
<i>Zhou et al. (2018)</i>	Yigong Zangbo	1055	-0.11 ± 0.14	mid 70's	2000
<i>Zhou et al. (2018)</i>	Western Nyain	316.8	-0.25 ± 0.15	mid 70's	2000
<i>Zhou et al. (2018)</i>	Sikim	689	-0.30 ± 0.12	mid 70's	2000
<i>Zhou et al. (2018)</i>	Central Nepal	578	-0.28 ± 0.11	mid 70's	2000
<i>Zhou et al. (2018)</i>	Western Nepal	228	-0.23 ± 0.18	mid 70's	2000
<i>Zhou et al. (2018)</i>	Spiti Lahaul	776	-0.04 ± 0.10	mid 70's	2000
<i>Zhou et al. (2018)</i>	Hindu Raj	841	-0.11 ± 0.13	mid 70's	2000
<i>Zhou et al. (2018)</i>	W Kunlun W	1147	-0.02 ± 0.14	mid 70's	2000
<i>Zhou et al. (2018)</i>	W Kunlun E	1209	0.05 ± 0.14	mid 70's	2000
<i>Zhou et al. (2018)</i>	Ulugh Muztagh	642	-0.06 ± 0.12	mid 70's	2000
<i>Zhou et al. (2018)</i>	Geladandong	720	-0.22 ± 0.12	mid 70's	2000

ICESat is a laser altimeter, which operated from 2003 to 2009. As the ICESat tracks are sparse (and the distance between adjacent tracks increases when the latitude decreases) and not exactly repeated from one campaign to another, the extraction of the signal of glacier volume change is challenging over glaciers (e.g., *Moholdt et al.*, 2010). Moreover, the precision of individual measurements decreases when the slope increases (e.g., *Kääb et al.*, 2012). Overall, using ICESat over mountainous areas is challenging and this is why the first estimate of glacier mass change in HMA using this sensor was published ten years after the launch of the satellite. The most common approach consists in calculating the so-called dh temporal trend for a given region. In this case the dh are individual elevation differences between ICESat elevation and the elevation of a reference DEM (usually the SRTM) at the same location. This method ensures a consistent topographic reference, but is strongly affected by the quality of the reference DEM (*Treichler and Kääb*, 2016). Another limitation of this method is the fact that it works only on sufficiently large regions homogeneously sampled from year to year campaigns (supplementary information of *Kääb et al.*, 2012).

ICESat studies revealed a heterogeneous pattern of glacier thickness changes at the scale of HMA (e.g., *Gardner et al.*, 2013; *Kääb et al.*, 2012; *Neckel et al.*, 2014; *Kääb et al.*, 2015). The most negative mass losses were found in the Eastern Nyainqentanglha Shan (figure 2.11), whereas the Western Kunlun Shan and some regions of the North-West Tibet interior had positive mass balances (*Neckel et al.*, 2014; *Kääb et al.*, 2015). The total mass changes for HMA was estimated at -24 Gt a^{-1} (*Kääb et al.*, 2015, without the Tien Shan) and at $-29.0 \pm 13.4 \text{ Gt a}^{-1}$ (*Gardner et al.*, 2013, table S5).

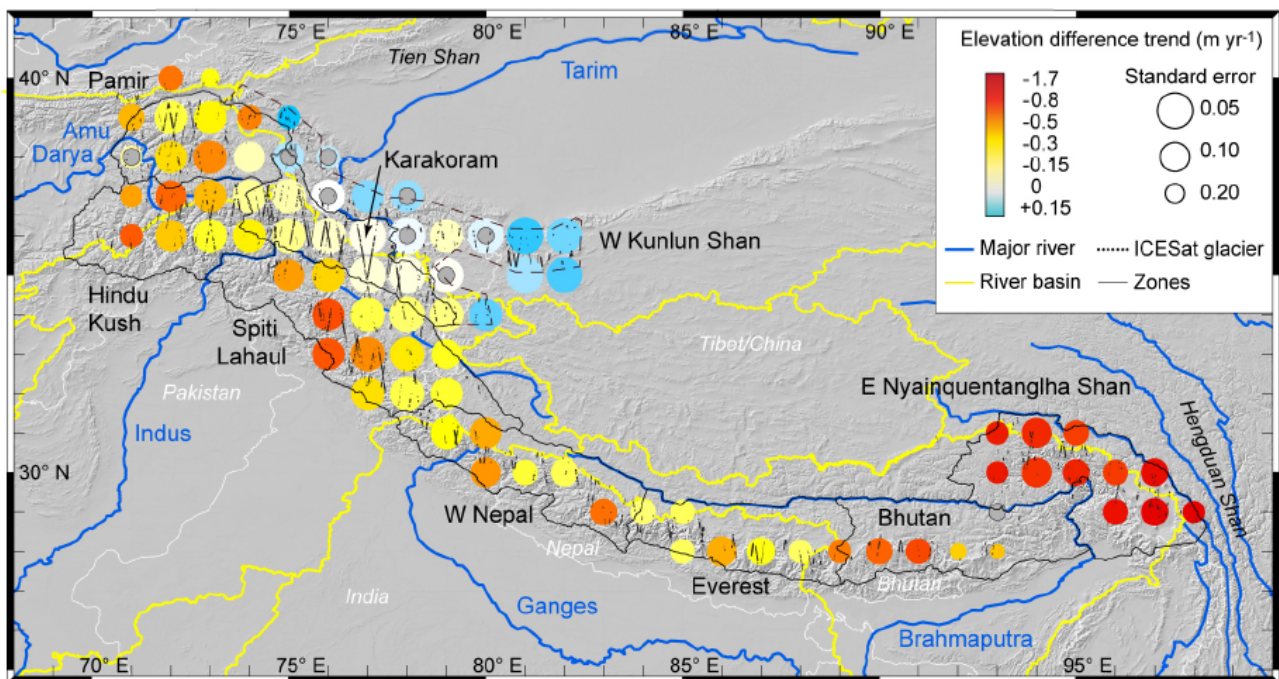


Figure 2.11: Map of ICESat derived rates of glacier elevation changes aggregated on a $1^\circ \times 1^\circ$ grid. Figure from *Kääb et al.* (2015).

GRACE mission consists in two twin satellites, which fly on the same orbit and constantly monitor the distance between themselves, allowing to retrieve for the spatial variations of Earth surface gravity fields at a monthly temporal resolution (e.g., *Tapley et al.*, 2004). Different processing centers provide monthly values of the Earth gravity field decomposed in spherical harmonics. These sets of Stokes coefficients are called "GRACE solutions". When trying to retrieve glacier mass changes on a limited region from GRACE data two main dif-

difficulties arise: the signal of gravity change at a given location is influenced by the large spatial scale and therefore there is a need to re-focus GRACE solutions, and the changes in the gravity field do not result from glacier mass changes only, but also from changes in the surface and sub-surface hydrology (*Ramillien et al.*, 2008; *Longuevergne et al.*, 2013). The tectonic uplift, the erosion and the glacial isostatic adjustment should also be taken into account and are poorly constrained in HMA (*Yi and Sun*, 2014).

To my knowledge, eight main studies tackled the challenge of monitoring the HMA glacier mass changes from GRACE. Two of them were based only on GRACE data for the period 2003-2009, 2003-2010 and 2003-2012 (*Matsuo and Heki*, 2010; *Jacob et al.*, 2012; *Yi and Sun*, 2014, respectively). *Jacob et al.* (2012) found a moderate glacier mass changes in HMA, at a rate of $-4 \pm 20 \text{ Gt a}^{-1}$. This is in strong contradiction with an earlier study, which found rates of mass changes of $-47 \pm 12 \text{ Gt a}^{-1}$ (*Matsuo and Heki*, 2010). The discrepancies between the two studies may be due to different values attributed to the India ground water storage depletion (*Jacob et al.*, 2012). *Yi and Sun* (2014) found again a different estimate of $-35 \pm 5.8 \text{ Gt a}^{-1}$, which they reconcile by arguing that *Jacob et al.* (2012) included some positive mass changes which originated from non-glacierized areas. An unexplained $+30 \text{ Gt a}^{-1}$ signal is observed on the TP (*Yi and Sun*, 2014). Recent work suggests that this could originate from an increase in the lake volumes due to a recent increase (starting around 1995) in the precipitation over the TP (e.g., *Zhang et al.*, 2017; *Yang et al.*, 2018). *Schrama et al.* (2014) calculated global glacier and ice sheet mass changes from GRACE data only, and they provide an estimate for HMA for the period 2003-2013 of $-16.5 \pm 3.8 \text{ Gt a}^{-1}$. Using a combination of ICESat and GRACE data, *Gardner et al.* (2013) found a glacier mass change of $-26 \pm 12 \text{ Gt a}^{-1}$ ($-23 \pm 12 \text{ Gt a}^{-1}$, using GRACE data only). The large spread in the estimates shows the challenge to extract glacier change signal from GRACE data at large scale, where the glacial isostatic adjustment and the other components of the hydrological cycle are not known.

Two last studies dealt with more local mass changes and focused only on the Tien Shan (*Farinotti et al.*, 2015; *Yi et al.*, 2016). Using an ensemble of GRACE solutions, mascons attribution and Land Surface Models, *Farinotti et al.* (2015) produced an estimate of Tien Shan glacier mass changes, which was in good agreement with ICESat based estimates (for the overlapping period) and with glacier mass balance modeling. However, the positive glacier mass changes after 2009 and the high 5-year variability observed in the GRACE data was later attributed to a signal leakage from the near-by Pamir and Pamir Alay region (*Yi et al.*, 2016).

As a conclusion, ICESat and GRACE revolutionized the knowledge of glacier changes at a global scale, but more specifically over HMA, where very few field measurements are available (*Bolch et al.*, 2012; *Azam et al.*, 2018). Despite its very short lifetime, ICESat was preferred to GRACE in HMA to evaluate the glacier contribution to changes in the land water storage (*Reager et al.*, 2016). This is due to the challenges associated with GRACE processing and the poor constraints on the other sources of Earth gravity changes. Probably, the main future use of GRACE in glacierized areas will be the assessment of changes in the components of terrestrial water storage other than glaciers, as it is usually now easier to constrain the glacier decennial changes from other sources than from GRACE (e.g., *Bamber et al.*, 2018).

From field surveys

An alternative method consists in compiling all the glaciological measurements based on field surveys and on geodetic surveys to produce region-wide averages (Cogley, 2009). This approach is not limited to large regions. It is possible to monitor individual glaciers and to resolve fine spatial patterns with an annual temporal resolution, which is totally impossible with GRACE and ICESat. The main drawback of this method is that for insufficiently monitored regions, such as HMA, the extrapolation of local measurements to the entire region can lead to strongly biased estimates, such as the $-86 \pm 26 \text{ Gt a}^{-1}$ estimate of Cogley (2009) reported in Gardner *et al.* (2013).

Glaciological estimates of the glacier-wide mass balance are produced for relatively small glaciers and at high temporal resolution (Zemp *et al.*, 2015). Continuous measurements are sparse for HMA for the post 2000 period and there is a lack of long-term monitoring programs (WGMS, 2017). For the Karakoram-Himalaya, a maximum of eight glaciers were monitored around 2010 (Azam *et al.*, 2018), but these series are very short and the longest continuous one is the Chhota Shighri Glacier series, which started in October 2002 (Azam *et al.*, 2016). It is noteworthy that there is only one glaciological survey in Karakoram, and it was limited to the ablation area of Baltoro Glacier (Mayer *et al.*, 2006). In Central Asia, the re-establishment of long-term monitoring programs will greatly improve the situation within the coming years (Hoelzle *et al.*, 2017). Recent studies, which relied on field data, combined with glacier modeling and remote sensing surveys shed light on the regional relationship between glacier and climate (e.g., Barandun *et al.*, 2018). It is likely that this kind of approach will become more and more popular.

The field surveys in HMA were the first ones to reveal the heterogeneous glacier changes (Yao *et al.*, 2012) and they are vital to understand the climate-glacier relationship (Azam *et al.*, 2014a; Sherpa *et al.*, 2017). Long-term field measurements are needed as well, even if they cannot be used to directly assess regional glacier mass changes and glacier contribution to sea level rise (Gardner *et al.*, 2013; Azam *et al.*, 2018).

From geodetic surveys

The geodetic surveys revealed a more contrasting pattern of glacier mass balance in the post-2000 than in the pre-2000 period, probably partially because more studies cover the post-2000 period (figures 2.10 and 2.12). They are mostly based on two types of DEM differences: the optical method, when an optical DEM (e.g., WorldView, SPOT, CartoSat) is differentiated with the SRTM and the radar method, when a X-band radar DEM (e.g., TanDEM-X, TerraSAR-X) is differentiated with the SRTM (table 2.2). The most negative mass budgets are found in the Eastern Nyainqentanglha and in the Spiti Lahaul, where they can be as negative as $-0.71 \pm 0.48 \text{ m w.e. a}^{-1}$ (Neckel *et al.*, 2017). A signal of moderate mass loss, or even positive mass balance is observed in some parts of the Karakoram (Gardelle *et al.*, 2012b; Lin *et al.*, 2017). This was referred to as the "Karakoram anomaly" (box 2.6). A similar signal was also observed in the Western Kunlun Shan (Lin *et al.*, 2017), in the Eastern Pamir / Muztag Ata region (Lin *et al.*, 2017) and is disputed for the central Pamir where a clear positive signal was observed with SPOT5-SRTM DEM difference (Gardelle *et al.*, 2013), but not with TanDEM-X-SRTM DEM difference (Lin *et al.*, 2017).

It is noteworthy that the optical estimates are often less negative (or more positive) than the radar estimates (figure 2.12). They are not always directly comparable because the extent

Table 2.2: Summary of the published estimates of HMA geodetic mass balances for the post 2000 period. Except for the study of *Ragetli et al. (2016b)*, all these estimates use the SRTM as the earlier DEM. The latter DEM is either an optical DEM (e.g., derived from SPOT5 or WorldView satellite images) or an X-band radar DEM (e.g., derived from TanDEM-X or TerraSAR-X satellite acquisitions).

Source	Region	Area (km ²)	BM (m w.e. a ⁻¹)	Start date	End date	Method
<i>Gardelle et al. (2013)</i>	E Nyainquentanglha	1390	-0.33 ± 0.14	1999	2011	optical
<i>Gardelle et al. (2013)</i>	Bhutan	1367	-0.22 ± 0.13	1999	2010	optical
<i>Gardelle et al. (2013)</i>	Everest	1432	-0.26 ± 0.14	1999	2010	optical
<i>Gardelle et al. (2013)</i>	West Nepal	890	-0.32 ± 0.14	1999	2010	optical
<i>Gardelle et al. (2013)</i>	Spiti Lahaul	2080	-0.45 ± 0.14	1999	2011	optical
<i>Gardelle et al. (2013)</i>	Hindu Kush	798	-0.12 ± 0.16	1999	2008	optical
<i>Gardelle et al. (2013)</i>	Karakoram E	5327	0.11 ± 0.14	1999	2010	optical
<i>Gardelle et al. (2013)</i>	Karakoram W	5707	0.09 ± 0.18	1999	2008	optical
<i>Gardelle et al. (2013)</i>	Pamir	3185	0.14 ± 0.14	1999	2011	optical
<i>Pieczonka et al. (2013)</i>	Aksu-Tarim	840	-0.22 ± 0.19	1999	2009	optical
<i>Ragetli et al. (2016b)</i>	Langtang	87	-0.38 ± 0.17	2006	2015	optical
<i>King et al. (2017)</i>	Everest	1708	-0.52 ± 0.14	2000	2015	optical
<i>Robson et al. (2018)</i>	Manaslu	500	-0.25 ± 0.05	2000	2013	optical
<i>Neckel et al. (2013)</i>	Purogangri Ice Cap	408	-0.41 ± 0.20	2000	2011/12	radar
<i>Rankl and Braun (2016)</i>	Central Karakoram	1107	-0.09 ± 0.12	2000	2012	radar
<i>Vijay and Braun (2016)</i>	Spiti Lahaul	1712	-0.58 ± 0.37	2000	2012/13	radar
<i>Li and Lin (2017)</i>	W Nyainquentanglha	576	-0.24 ± 0.13	2000	2013/14	radar
<i>Li et al. (2017)</i>	Central Tien Shan	7240	-0.20 ± 0.19	2000	2012	radar
<i>Lin et al. (2017)</i>	W Pamir	2836	-0.12 ± 0.06	2000	2014	radar
<i>Lin et al. (2017)</i>	E Pamir	1001	0.12 ± 0.07	2000	2014	radar
<i>Lin et al. (2017)</i>	Hindu Kush	569	-0.14 ± 0.09	2000	2014	radar
<i>Lin et al. (2017)</i>	W Kunlun	2980	0.13 ± 0.06	2000	2014	radar
<i>Lin et al. (2017)</i>	E Karakoram	7395	-0.02 ± 0.06	2000	2014	radar
<i>Lin et al. (2017)</i>	W Karakoram	7739	-0.10 ± 0.06	2000	2014	radar
<i>Neckel et al. (2017)</i>	E Nyainquentanglha	177	-0.71 ± 0.48	2000	2014	radar
<i>Li et al. (2018)</i>	Everest	1708	-0.38 ± 0.04	2000	2012	radar
<i>Vijay and Braun (2018)</i>	Jammu Kashmir E	2261	-0.16 ± 0.19	2000	2012	radar
<i>Vijay and Braun (2018)</i>	Jammu Kashmir W	1570	-0.43 ± 0.24	2000	2012	radar
<i>Wu et al. (2018)</i>	Kangri Karpo	788	-0.71 ± 0.10	2000	2014	radar

and the date of the second DEM acquisition can differ. For instance, in the Eastern Nyainqentanglha the area studied by *Gardelle et al.* (2013), and named Hengduan Shan in their study, does not overlap with the regions of *Neckel et al.* (2017) and *Wu et al.* (2018). But in central Pamir, Everest region, Spiti Lahaul and Karakoram the comparison is more relevant.

Box 2.6: Karakoram anomaly

The "Karakoram anomaly" refers to the anomalous behavior of Karakoram glaciers, which showed advancing termini since the mid 1990s, while glaciers were retreating worldwide (*Hewitt, 2005*). It was later shown quantitatively that the glaciers were in balance conditions since the 1970's (*Zhou et al., 2017; Bolch et al., 2017; Gardelle et al., 2012b*). The climate drivers of the anomaly are not clear and could be synoptic circulation anomalies (*Kapnick et al., 2014; Forsythe et al., 2017*) or local effects, such increase in the moisture content due to irrigation development (*de Kok et al., 2018*).

The difference between the estimates can be up to $\sim 0.2 \text{ m w.e. a}^{-1}$ between the studies, with some spatial variability. The main differences between these studies could originate from the radar signal penetration correction (box 2.5). The geodetic estimates rely on the SRTM-C band DEM because it has a global coverage. This DEM is corrected from penetration at this frequency using the SRTM-X band DEM, which was acquired simultaneously, but along narrower swath and therefore with a sparse coverage. The X-band (9.65 GHz) signal penetrates less than the C-band (5.3 GHz) signal into snow and ice (e.g., *Rignot et al., 2001; Dall et al., 2001*). Assuming a negligible penetration of the X-band signal, *Gardelle et al.* (2012a) proposed to correct the SRTM-C band DEM based on the difference with SRTM-X band DEM, when available. As

the X-band signal penetrates as well, the correction is probably a lower bound of the C-band penetration estimate (*Dehecq et al., 2016*). Recent work suggested a mean SRTM C-band penetration depth of 8 and $9 \pm 3 \text{ m}$ for the Swiss Alps and the Mont-Blanc glaciers, respectively (*Fischer et al., 2015; Berthier et al., 2016*), whereas the X-band correction led to an estimate of about 3 m of penetration over roughly the same area (*Berthier et al., 2016*). Consequently, the X-band correction is more relevant for the radar geodetic estimates (especially if the second DEM is acquired under similar snow conditions) than the optical estimates, the best option being to rely only on optical DEMs. There is a real need, but in the end little hope, to obtain precise estimate of this penetration bias because it is highly spatially variable as it is related to the electro-magnetic properties of the snowpack of February 2000, for which there is no direct observation in HMA and which are extremely difficult to model correctly.

The heterogeneity of the methods used, together with the SRTM penetration and the inconsistencies between the end dates of the surveys shows the need for consistent, temporally extended and spatially resolved estimate of HMA glacier volume changes for the beginning of the twenty-first century. We produced such an estimate using time series of DEMs derived from Advanced Spaceborne Thermal Emission and Reflection Radiometer (ASTER) images. This work is presented with more details in chapter 3 of this manuscript.

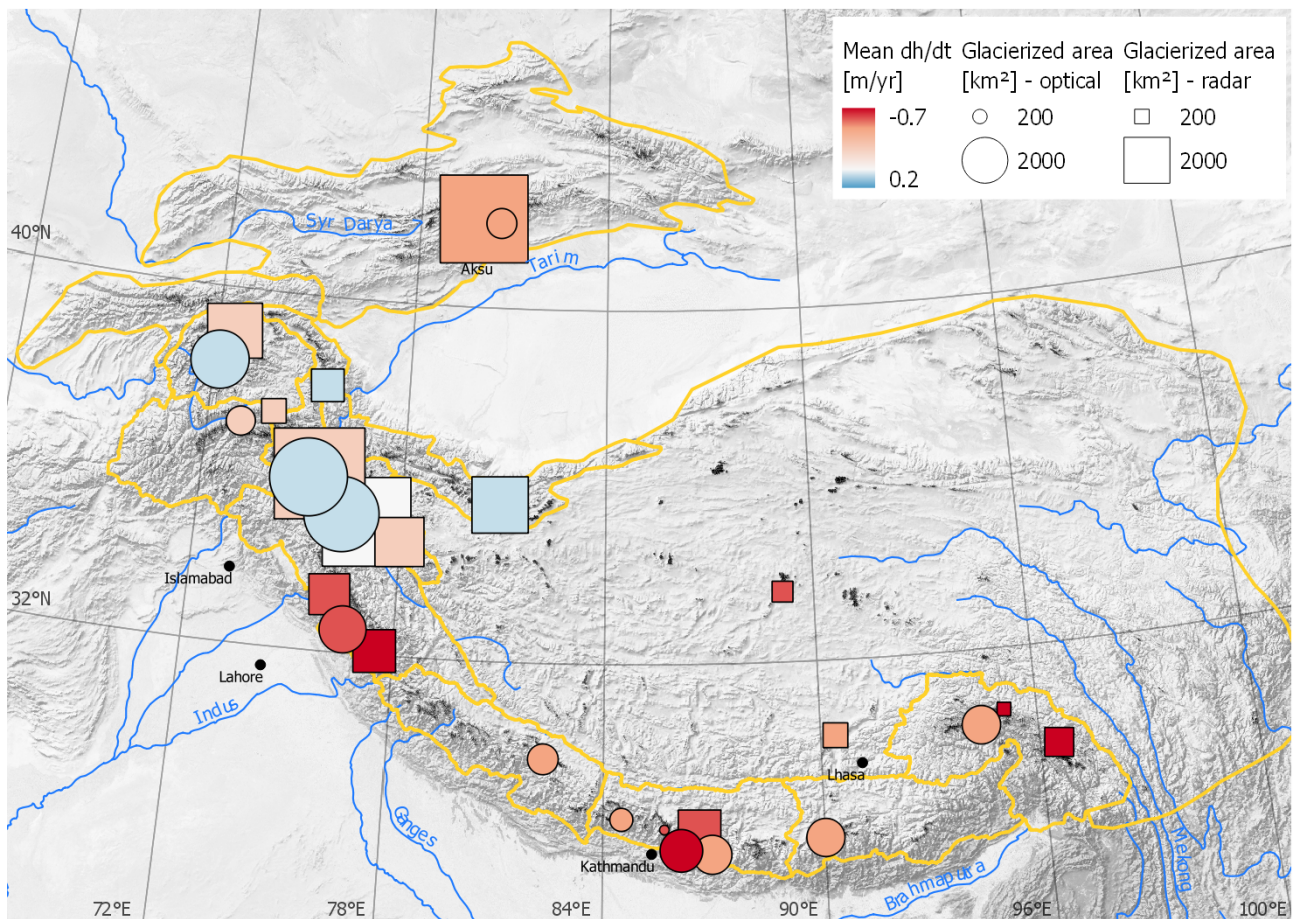


Figure 2.12: Summary of the geodetic mass balance studies for the post 2000 period. For the precise dates and references, please refer to table 2.2. For the sake of consistency and comparison with the chapter 3, the mass balance values have been converted to mean rate of elevation changes using a volume to mass conversion factor of 850 kg m^{-3} (Huss, 2013). The circles represent the studies that used an optical DEM for the latter DEM and the squares the studies that used a radar DEM for the latter DEM. With the exception of *Ragetli et al. (2016b)*, all these studies relied on the SRTM for their first DEM.

2.3.4 The 'debris-cover anomaly': no reduced thinning rates are observed for debris-covered tongues, compared to debris-free tongues

When the first large scale studies of glacier thickness changes became available, it was very tempting to compare the rate of mass changes between debris-covered and debris-free ice. The first attempt can be tracked back to two studies: *Gardelle et al. (2012a)* and *Kääb et al. (2012)*. Both were aware of the shortcoming of comparing rates of thickness changes, which are the results of surface mass balance and ice dynamics. In order to avoid the influence of the ice dynamics on the rate of thickness changes, *Kääb et al. (2012)* examined pairs of ICESat footprints on debris-covered and debris-free ice that were closer than 1 km to each other. On average, they did not find a reduced thinning rate for debris-covered ice (*Kääb et al., 2012*). *Gardelle et al. (2012a)* found similar thinning rates for debris-free and debris-covered tongues of Karakoram glaciers. A similar observation was made in the Everest region (*Nuimura et al., 2012*). This observation was then extended to multiple regions of HMA, where various patterns of thinning were observed, with again no reduced thinning beneath the debris (*Gardelle et al., 2013*). To my knowledge, this was later named the "debris-cover anomaly" for the first time in *Pellicciotti et al. (2015)*, where they could not re-

ally conclude on the similarity or dissimilarity of the thinning rates because of insufficient hypsometric overlap of the debris-covered and debris-free tongues in the Langtang catchment. The observation of no reduced thinning rates for the debris-covered tongues was then widely repeated: for Siachen Glacier (*Agarwal et al.*, 2017), in the Kangri Karpo Mountains (*Wu et al.*, 2018), for Kanchenjunga Glacier (*Lamsal et al.*, 2017) or in Muztag Ata-Kongur Tagh (*Zhang et al.*, 2016).

This observation was in apparent contradiction with the *Østrem* (1959)'s curve, which predicts that the ablation rate of ice beneath a thick debris layer is approximately 25 % of the clean-ice ablation under similar conditions, if the debris thickness exceeds ~ 20 cm (figure 2.13). The immediate consequence of this observation, and apparent contradiction, was a tremendous increase in the interest in the ablation processes of debris-covered glaciers. Nevertheless, this contradiction is only apparent as thinning rates are not directly comparable to surface mass balance rates, because at any location the glacier thickness change is the sum of the emergence/submergence velocity and the mass balance (*Cuffey and Paterson*, 2010; *Vincent et al.*, 2016; *Banerjee*, 2017).

The above mentioned large scale studies revealed a very heterogeneous pattern of glacier mass loss at the scale of HMA. To explain this heterogeneous pattern, the heterogeneous climate, and therefore the different glacier mass balances sensitivities (*Sakai and Fujita*, 2017), as well as the heterogeneity of the climate change, have necessarily a very strong influence on the recent glacier mass changes. Nevertheless, these influences are expected to be modulated by the geometry of each individual glacier. In chapter 4, we explore the statistical relationships between the individual glacier mass balances and their morphological variables, and in particular their debris cover. When looking at smaller spatial scales (i.e. around a hundred or a thousand of square kilometers), the factors governing the spatial variability of glacier mass balances are mostly unresolved, and there is a real need to better understand the local climate (not developed in this dissertation) and the processes which influence the glacier energy and mass balances, and in particular the processes related to the presence of a debris cover. These processes are investigated at a more local scale, generally by the use of a combination of field observations and modeling.

2.4 Processes unraveled by local studies to understand the influence of the debris cover on glacier mass balance

Few large scale studies exist about debris-covered glaciers (*Scherler et al.*, 2011a,b; *Kraaijenbrink et al.*, 2017). Instead the research groups focused on small-scale measurements to quantify the different processes responsible for the energy and mass balances of debris-covered glaciers. Most of the research was conducted on Miage Glacier in the Alps (e.g., *Brock et al.*, 2010; *Reid and Brock*, 2010), in the Langtang catchment and more precisely on Lirung Glacier (e.g., *Sakai et al.*, 1998; *Immerzeel et al.*, 2014a), in the Everest region on Khumbu Glacier (e.g., *Nakawo et al.*, 1985; *Sakai et al.*, 2002; *Watson et al.*, 2017a) and on Ngozumpa Glacier (e.g., *Benn et al.*, 2017) and in China on Koxar Glacier (e.g., *Han et al.*, 2006).

2.4.1 Influence of the debris thickness and moisture content

Ice melt beneath a debris layer

Based on field experiments on ice-cored moraines, *Østrem* (1959) stressed the concept of enhanced ice ablation for ice covered by a very thin debris layer (lower than few centimeters) and reduced ice ablation for ice covered by a thick debris layer. The critical debris thickness was later defined as the debris thickness for which the ice ablation is reduced compared to debris-free ice (*Lejeune et al.*, 2013). This early work set the basis that debris thickness was the main control on the ablation, and numerous studies tried to better constrain the *Østrem* (1959)'s curve by three main approaches: field measurements, experiments and energy balance modeling.

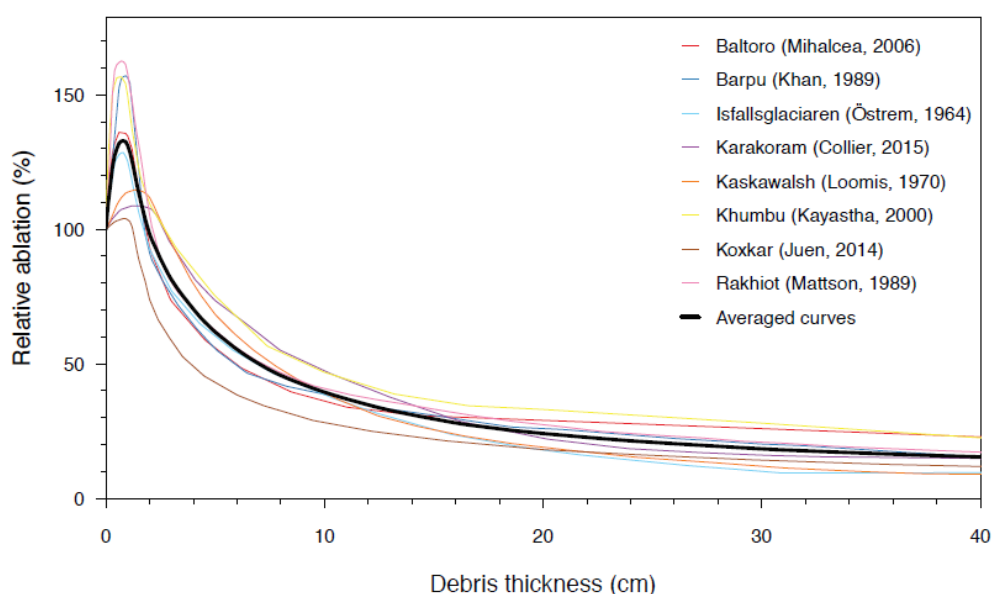


Figure 2.13: Summary of the different estimates of the relative ablation beneath a debris layer as a function of the debris thickness (*Østrem* (1959)'s curve). Figure from *Kraaijenbrink et al.* (2017).

The field measurements consisted generally on stake readings at various locations. The stakes are difficult to drill into debris-covered ice because one needs to remove the debris layer before drilling into the ice. Consequently, most measurements were performed for debris thickness lower than 30 cm. Debris is replaced when the stake is inserted into ice. The stake emergence is then measured at various time scales: from a couple of weeks to years. At first glance most of the studies are in good agreement and they all find a decreasing ablation for an increasing debris thickness (e.g., *Nakawo and Young*, 1981; *Kayastha et al.*, 2000; *Mihalcea et al.*, 2006; *Han et al.*, 2006; *Hagg et al.*, 2008). Unfortunately, it is not possible to compare these studies with each other because the measurements were performed at different elevations, for different meteorological conditions and for different debris properties.

The experiments, which consist usually in spreading sand on a snow or ice surface, allow for a better control of the environment and therefore a better reproducibility. *Fujii* (1977) measured the ablation of snow covered by sand during one day near Rikha Samba Glacier (Hidden Valley, Nepal) and found that the ablation followed nicely the *Østrem* (1959)'s curve. Interestingly, *Reznichenko et al.* (2010) demonstrated the strong influence of the diurnal cycle, as the ice covered by debris had a similar ablation as the debris-free ice under steady

illumination, after the equilibrium was reached. An experimental setup was used to validate the representation of debris in a physically-based model of snowpack (Lejeune *et al.*, 2013).

Classically in the field of glaciology, two main approaches have been implemented to understand/predict the melt of ice beneath debris: degree-day modeling (box 2.3) versus surface energy balance modeling (box 2.4).

Degree-day models have been implemented for the sake of distributed or semi-distributed melt modeling (Azam *et al.*, 2014b; Juen *et al.*, 2014) or to reconcile observation of ablation performed at various elevations (Mihalcea *et al.*, 2006). The implementation of an "enhanced temperature-index" model (e.g., Pellicciotti *et al.*, 2005) was performed to model the melt of Miage Glacier (Carenzo *et al.*, 2016). These models are efficient to predict the melt from limited input data if they have been calibrated properly. Nevertheless, they are not informative about the processes at stake and therefore are not transferable to other sites.

For the sake of reproducibility and transferability to different sites, energy balance models were developed. The debris layer is generally discretized into N sub-layers (N being equal to 1 for the simplest models) at the interface of which the energy fluxes are resolved (figure 2.14). The general formulation for the surface energy models is given by equation (2.6) in box 2.4. The largest unknowns are the following: transient heat transfers, debris moisture content, debris conductivity, porosity and debris surface roughness.

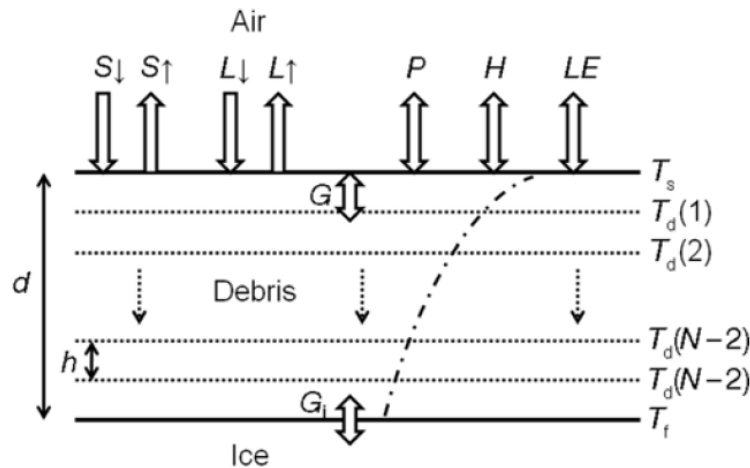


Figure 2.14: Schematic representation showing heat fluxes at the top and bottom of a debris layer of thickness d . The debris temperature is calculated for N layers of thickness h , with boundary conditions defined by the surface temperature, T_s , and the temperature of the debris/ice interface, which is assumed to stay at $T_f = 0$ °C. The dash-dot curve is an example temperature profile, where temperature increases towards the right. Figure from Reid and Brock (2010).

Steady-state models versus transient modeling The first models (e.g., Nakawo and Young, 1982; Han *et al.*, 2006) made the simplistic assumption of a linear temperature gradient through the debris, assuming a balance of fluxes at the debris surface and at the debris/ice interface. This assumption was based on the observations of linear temperature profile in the debris layer, but was challenged by Conway and Rasmusen (2000) and Nicholson and Benn (2006), who showed that the debris thermal regime was influenced by the daily cycle. As a consequence, Nicholson and Benn (2006) also assumed a linear gradient of temperature in the debris layer but ran the model at a daily time step only (and not over night and day separately). To run the model at a higher temporal

resolution (hourly), one needs to explicitly resolve the heat transfer through the different debris layer (*Reid and Brock, 2010; Lejeune et al., 2013*) or to introduce a "debris heat storage" flux (*Brock et al., 2010*).

Moisture content of the debris *Nicholson and Benn (2006)* hinted the role of moisture within the debris layer with the use of two end-member cases (fully dry and fully wet debris), for which they changed the thermal conductivity of the debris. The effective thermal conductivity of the debris varied by about 30 % between winter and summer for Ngozumpa Glacier, meaning that the moisture content and phase changes within the debris have a strong influence on their thermal properties (*Nicholson and Benn, 2012*). By developing a reservoir-based model, *Collier et al. (2014)* showed that the moisture exchange and phase transitions within the debris layer could influence the sub-debris ice melt. But the total effect of these processes can either be more or less ablation over the course of one season (*Collier et al., 2014*).

The role of the turbulent fluxes Modeling of a ice melt beneath a porous dry layer of debris stressed the role of turbulent fluxes (*Evatt et al., 2015*). The turbulent fluxes are modeled in energy balance models using the bulk method, and therefore are highly sensitive to the roughness lengths, and in particular to the aerodynamic roughness length ($z_{0,m}$). Consequently, recent studies evaluated $z_{0,m}$ for debris-covered glaciers based on geometric methods (*Rounce et al., 2015; Miles et al., 2017a; Quincey et al., 2017*). They found values for $z_{0,m}$ between 0.02 and 0.05 m (which is higher than most values from the literature for snow and clean ice). These values were estimated from geometric considerations and analysis of very high resolution DEMs, and should be evaluated against aerodynamic values of z_0 calculated from the eddy covariance method, which require sophisticated sensors that are challenging to deploy on HMA glaciers.

The physically-based models perform well on the cases where they are constrained by observations of the physical properties of debris, which are spatially variable and usually unknown (*Nicholson and Benn, 2012*). There are still unanswered questions about the ice melt beneath thick debris (i.e. higher than 50 cm), which represent a large share of the debris in HMA, but one of the major challenges at the moment is how to distribute the melt models at the scale of a glacier or a region, which can be reduced to the problem of measuring distributed debris thickness and properties.

The challenge of measuring debris thickness

An empirical link between debris thickness and debris surface temperature was established and used as the basis of remote sensing based estimates of debris thickness (*Mihalcea et al., 2008a*). The debris surface temperature can be monitored at a 90 m resolution from ASTER or Landsat thermal bands. The point measurements can thus be extrapolated at the scale of a glacier, based on the satellite thermal images (*Mihalcea et al., 2008a,b*). Nevertheless, two weaknesses can be pointed out in this method. First, the empirical relationship between the debris thickness and the surface temperature is not well constrained and second, the 90 m pixels of ASTER cannot capture the fine scale spatial variability of the debris distribution. If there is not much to do against the second limitation (except maybe for a limited spatial extent; e.g., *Kraaijenbrink et al., 2018*), attempts were made to improve the empirical relationship between the debris surface temperature and debris thickness based on the *Reid and Brock (2010)*'s debris thermal model (*Foster et al., 2012*). Despite the improvement in simulating relatively thick debris (i.e. > 50 cm), the model was still highly dependent on

the input meteorological data and their spatial extrapolation (*Foster et al.*, 2012).

This general method of linking the satellite measured debris temperature to debris thickness was applied to other glaciers in HMA (*Zhang et al.*, 2011; *Juen et al.*, 2014; *Rounce and McKinney*, 2014; *Schauwecker et al.*, 2015; *Gibson et al.*, 2017). The results of the thickness inversion are generally very sensitive to the choice of the model used for the inversion (e.g., *Juen et al.*, 2014), which has a strong impact on the modeled sub-debris ablation (*Juen et al.*, 2014). It is also noteworthy that the debris thickness obtained by these methods are often not realistic (e.g., *Rounce and McKinney*, 2014; *Schauwecker et al.*, 2015), because they predict debris thicknesses that are too small compared to more direct measurements on similar debris-covered tongues (e.g., *McCarthy et al.*, 2017; *Nicholson and Mertes*, 2017).

A recent study (*Rounce et al.*, 2018), derived the debris thickness for most large debris-covered tongues of Everest region glaciers based on the inversion of the *Østrem* (1959)'s curve (similarly to *Ragetti et al.*, 2015). The sub-debris melt was estimated from DEM differencing and ice emergence approximation based on the surface velocity and the ice thickness (*Huss and Farinotti*, 2012). The method is very appealing, but it relies heavily on the ice thickness estimated by (*Huss and Farinotti*, 2012), which can be inaccurate for individual glaciers (*Farinotti et al.*, 2017). This study would be greatly strengthened with the use of field measured ice thickness from ground penetrating radar (GPR) for example (*Gades et al.*, 2000). They also relied on the spatial distribution of local meteorological measurements, which is difficult to achieve in this region (e.g., *Eeckman et al.*, 2017).

Huang et al. (2017) estimated the debris thickness of Koxkar Glacier using the Phased Array L-band Synthetic Aperture Radar (PALSAR, 1270 MHz) on-board of the Advanced Land Observing Satellite (ALOS). They found a good relationship between their 556 field measured debris-thicknesses and the volume scattering of the radar signal, measured from satellite, for debris thicknesses lower than ~ 50 cm, but the method did not work for thick debris.

The above mentioned studies tried to derive the debris thickness at relatively large scales and for low resolution. There is currently a tendency to produce high quality, resolved, field-based debris thickness estimates. GPR surveys were conducted on Koxkar Glacier (*Wu and Liu*, 2012), Lirung Glacier (*McCarthy et al.*, 2017) and Ngozumpa Glacier (*Nicholson and Mertes*, 2017). They demonstrated that GPR was suitable for debris thickness mapping. By combining GPR measurements and direct observations of the debris thickness at the cliff edges, *Nicholson and Mertes* (2017) showed that the debris thickness was very variable within a short distance, probably due to debris redistribution controlled by slope stability and gravitational mass transport (*Moore*, 2018; *Nicholson et al.*, 2018). These studies provide very useful data to better understand the debris spatial distribution. Nevertheless, they are restricted to limited areas because they require extensive field work.

As the lower parts of the debris-covered tongues of the HMA glaciers are often covered by a debris layer that can be thicker than one meter (*Nicholson and Mertes*, 2017), very reduced ablation is expected. Consequently, any other ablation process happening on these tongues has the potential to contribute disproportionately to the total ablation budget, even if it happens only on a limited area.

2.4.2 Ice cliffs

Ice cliffs are striking features of debris-covered tongues (figure 2.15). They are characterized by a bare ice face with an angle higher than the repose angle of debris (usually steeper than 30/35 degrees). The ice faces can be clean or covered by dust or a very thin debris layer. They are sometimes over-hanging, especially when they are associated with a pond at their foot (e.g., *Kraaijenbrink et al.*, 2016b; *Watson et al.*, 2017a, figure 2.15). In the Himalayas, they are mostly north-facing (e.g., *Sakai et al.*, 2002; *Buri and Pellicciotti*, 2018) and occupy a relatively small fraction of the glacier map view area (*Herreid and Pellicciotti*, 2018).



Figure 2.15: Picture of an ice cliff and associated supraglacial pond taken on Changri Nup Glacier in November 2016. The cliff height is approximately 15 m.

Some pioneering studies by a Japanese team in the early 2000s suggested that ice cliffs could contribute disproportionately to the ablation of debris-covered tongues, despite their reduced spatial extent (*Sakai et al.*, 1998). This is due to the fact that bare and sometimes dirty ice, with a low albedo, is exposed at low elevation in a very hot environment, because the surrounding debris surface temperature can be high. Observations during the pre-monsoon and post-monsoon reported cliff melt rates ranging from 0.1 to 12 cm day⁻¹ on Lirung Glacier (*Sakai et al.*, 1998; *Steiner et al.*, 2015) and between 5.9 to 8.1 cm day⁻¹ on Miage Glacier during summer (*Reid and Brock*, 2014).

The first tentative energy balance model was developed for ice cliffs on Lirung and Khumbu glaciers to try to explain the predominance of north-facing cliffs (*Sakai et al.*, 2002). It was further refined by *Han et al.* (2010), *Reid and Brock* (2014) and *Steiner et al.* (2015). The main difficulty of the point scale energy balance modeling at the cliff surface is the influence of the cliff aspect and the influence of the surrounding topography on the incoming longwave and shortwave radiation. The model was then gridded to represent the variability of slopes and aspects within a given cliff (*Buri et al.*, 2016a) and additional processes, such as the energy exchange with a lake were ultimately added (*Buri et al.*, 2016b). The various versions of the models were usually validated against stake inserted in the cliff face (e.g., *Reid and Brock*, 2014; *Steiner et al.*, 2015; *Buri et al.*, 2016a). Unfortunately the stakes could only be

surveyed for a short period (a couple of weeks) and during the pre- or post-monsoon seasons (or summer in the Alps), due to logistic constraints and due to rocks falling along the cliff face and breaking the stakes. The geometric quantification of the cliff melt over more than one season validated the good performance of the models over longer time span (*Brun et al.*, 2016; *Watson et al.*, 2017a).

The problem of the dominant aspect of the north facing cliffs was recently solved by modeling flattening of south-facing cliffs as a result of their vertical gradient of incoming solar radiation and sky view factor (*Buri and Pellicciotti*, 2018).

High resolution topographic data, such as unmanned aerial vehicles (UAV) or stereo satellite DEMs have the potential to extend spatially and temporally the stake observations and the outputs of the models. Many studies reported high thinning rates associated with the presence of ice cliffs (*Immerzeel et al.*, 2014a; *Thompson et al.*, 2016) and even a positive correlation between the thinning rate and the cliff density for a given elevation band (*Ragetti et al.*, 2016b; *Watson et al.*, 2017b; *Huang et al.*, 2018). Even if these results stress the potential importance of ice cliff contribution to the total glacier tongue mass balance, they lack precise quantification, which is possible only when accounting for the ice flux (e.g., *Berthier and Vincent*, 2012; *Vincent et al.*, 2016).

2.4.3 Supraglacial and englacial hydrology

Supraglacial lakes and ponds, where the water has a positive temperature, are also very common features of debris-covered glaciers (figure 2.15) and they have been recognized as efficient entry points for the energy within the glacier system (*Sakai et al.*, 2000). To my knowledge it is very complicated to measure directly the total melt rate of a supraglacial lake (*Röhl*, 2006) and it has never been done in the HMA. Therefore it is crucially needed to model sub-aqueous ablation and to validate such a model against independent observations, such as the water temperature stratification. There are two main mechanisms for the sub-aqueous melt of a supraglacial lake: the wind-driven currents and the free convection, which both produce thermo-erosion (*Xin et al.*, 2012). The different terms of the mass and energy budgets of a supraglacial lakes are summarized on figure 2.16 (*Miles et al.*, 2016). Sub-aqueous melt rates of Himalayan supraglacial ponds were found between 1 and 65 cm day⁻¹ (summarized in *Miles et al.*, 2016). The large spread can be explained by the variety of ponds considered in the different studies, but it also highlights the high uncertainty associated with the pond energy balance modeling.

The supraglacial lakes play the role of entry points for the energy into the glacier system, but the study of their dynamics reveals that they are also connected with a fast evolving supraglacial and englacial drainage system. Supraglacial lakes are known to be highly dynamic features, which can expand and drain quickly. For instance, *Benn et al.* (2001) documented the rapid growth of a supraglacial lake on Ngozumpa Glacier, as its size tripled and its level raised of 8.8 m within one year, and then almost completely drained the following year. The supraglacial lake annual and seasonal dynamics were investigated with satellite images (*Watson et al.*, 2016; *Miles et al.*, 2017b) and field surveys (*Watson et al.*, 2018). Using high resolution imagery available in Google Earth for the period 2002-2015, *Watson et al.* (2016) were able to map 9340 ponds on the debris-covered tongues of the Everest region. They observed an increase in the pond area for six of the nine glacier-tongue they surveyed. The temporally sparse sampling revealed a large temporal variability, in terms of pond total area, which makes the finding of a pond area increase more uncertain (*Watson et al.*, 2016). These findings were also supported by the analysis of 172 Landsat scenes in the Langtang

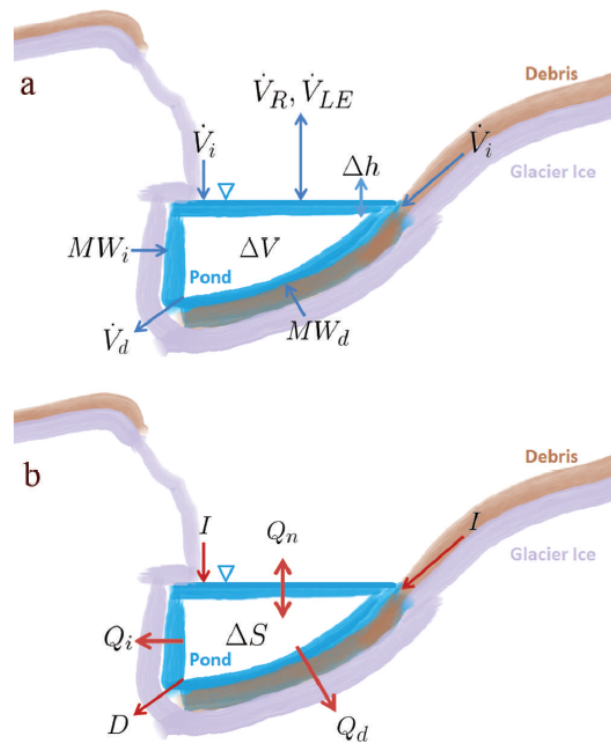


Figure 2.16: Conceptual (a) mass and (b) energy exchanges for the pond control volume. For (a): ΔV (m^3) is the pond volume change, Δh (m) is the pond surface elevation change, \dot{V}_i ($\text{m}^3 \text{ s}^{-1}$) is the ice melt or catchment runoff, \dot{V}_d ($\text{m}^3 \text{ s}^{-1}$) is the discharge, \dot{V}_R ($\text{m}^3 \text{ s}^{-1}$) is the rainfall and \dot{V}_{LE} ($\text{m}^3 \text{ s}^{-1}$) are the latent fluxes. For (b): ΔS (J) is the change in stored energy, Q_n (W m^{-2}) is the net surface flux from the atmosphere, Q_i (W m^{-2}) is the energy exchange at subaqueous bare-ice surface, Q_d (W m^{-2}) is the energy exchange through subaqueous debris, I (W) is the energy advected into the pond by runoff inputs and D (W) is the energy removed from the pond by discharge. Figure from Miles *et al.* (2016).

catchment, which revealed a marked seasonal cycle as ponds grow in the pre-monsoon and monsoon and then drain or freeze in winter (Miles *et al.*, 2017b). The field surveys are limited to a small number of ponds. Some ponds have a mean positive temperature during winter and their potential drainage would lead to substantial ablation (Watson *et al.*, 2018). Recently it was shown that the supraglacial ponds were an important transient reservoir for water that could regulate the glacier runoff (Irvine-Fynn *et al.*, 2017).

Multiple evidences showed the importance and role of englacial conduits for debris-covered tongue drainage systems (Benn *et al.*, 2017). First, englacial conduits have been explored with speleological techniques on the major debris-covered glaciers of the Everest region (Gulley and Benn, 2007; Gulley *et al.*, 2009; Benn *et al.*, 2017). Their morphology and the network of galleries can be interpreted within a cut-and-closure mechanism framework (Gulley *et al.*, 2009). This mechanism consists in the progressive burial of supraglacial channels which incise the ice faster than the surrounding surface melts. Then the upper part of the channel walls collapse, creating the channel roof (Gulley *et al.*, 2009). Second, the supraglacial lakes are reservoir of water that can store relatively warm water. Watson *et al.* (2018) measured a mean temperature of 4°C for some ponds even in winter. This warm water has a strong ablation potential, which can be released by ice melt through englacial circulation through previously abandoned or newly formed conduits (Miles *et al.*, 2017c). Third, englacial conduit ablation could be responsible for some of the surface lowering pat-

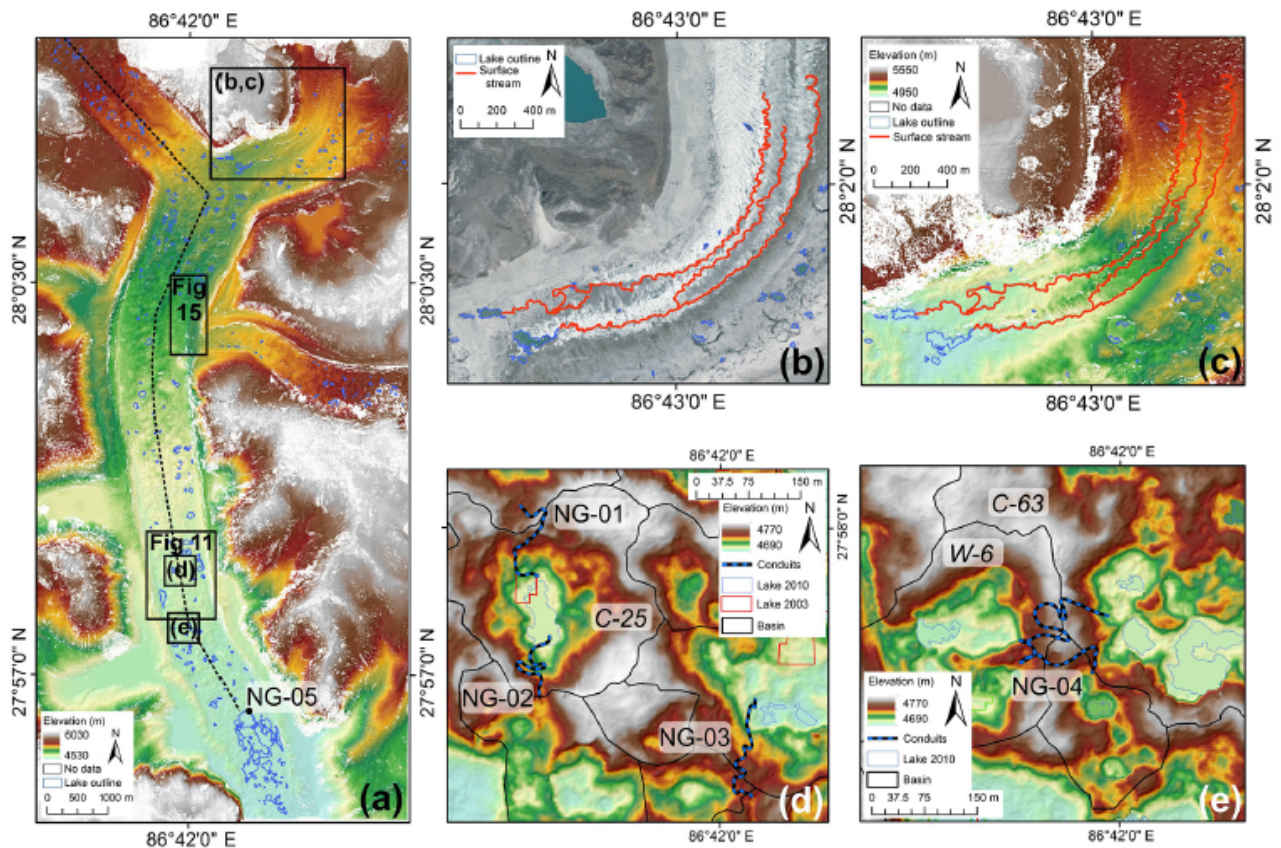


Figure 2.17: Examples of surface topography, supraglacial meltwater channels, and englacial conduit locations on Ngozumpa Glacier: (a) DEM of the lower ablation zone of the glacier, based on GeoEye-1 stereo imagery from June 2010, showing location of enlarged panels and englacial conduit NG-05; (b) supraglacial channels shown on the 2010 imagery; (c) the same area shown on the 2010 DEM; (d) hummocky debris-covered ice, showing the boundaries of closed surface basins and locations of englacial conduits NG-01 to NG-03 (considerable basin expansion occurred in the four ablation seasons between the conduit surveys (December 2005) and the date of the DEM (June 2010)); and (e) hummocky debris-covered ice and location of englacial conduit NG-04 (surveyed November 2009, 7 months before the date of the DEM). Figure from *Benn et al.* (2017).

terns observed from high resolution DEM differencing (*Immerzeel et al.*, 2014a; *Thompson et al.*, 2016).

A comprehensive overview of the drainage system of Ngozumpa Glacier was recently published (*Benn et al.*, 2017). The take-home message of their study is that the drainage system evolves from mostly supraglacial channels to a combination of supraglacial channels and englacial conduits as the elevation decreases (figure 2.17). The level of Spillway Lake, which is the proglacial lake at the terminus of Ngozumpa Glacier, controls the base level of the drainage system and therefore its level fluctuations and recent expansion have a strong influence on the entire drainage system (*Thompson et al.*, 2016; *Benn et al.*, 2017, figure 2.17).

2.4.4 Towards a closure of the mass and energy budget of debris-covered tongues?

The closure of the mass and energy budget of a debris-covered tongue has two major applications: a realistic prediction of the discharge at the glacier tongue outlet and the partition

of the contribution of each process to the total glacier energy/mass balance.

Few studies incorporated the enhanced ablation due to ice-cliffs and supraglacial lakes into debris-covered glacier mass balance modeling and none of them incorporated englacial ablation. Most studies are based on satellite based debris-thickness measurements, which are then incorporated in an energy balance model (Fyffe *et al.*, 2014; Juen *et al.*, 2014; Rounce *et al.*, 2015; Shaw *et al.*, 2016) or into a degree-day model (Fujita and Sakai, 2014; Carenzo *et al.*, 2016). Alternatively, some studies modeled the glacier ablation as if it were debris-free and applied a global reduction factor for the debris-covered parts (Rowan *et al.*, 2015; Shea *et al.*, 2015; Mimeau *et al.*, 2018). The inclusion of ice-cliffs and supraglacial lakes is challenging because the parametrizations of the melt originating from these features are not very robust (Juen *et al.*, 2014). Moreover, they evolve quickly and dynamic modeling is probably needed to represent them on the seasonal to pluri-annual time scale (Buri *et al.*, 2016b). The validation of the melt models is challenging because the discharge at the glacier outlet can be dominated by other processes (e.g., snow melt from the off glacier catchment areas, Fyffe *et al.*, 2014), or delayed by transient storage (Irvine-Fynn *et al.*, 2017; Mimeau *et al.*, 2018).

The quantification of each process at the scale of a debris-covered tongue would be a clear step forward, and a combination of modeling and observation is probably required to achieve this. From field measured ice thickness and remotely sensed or field measured surface elevation change, it is possible to quantify the total mass balance of a debris-covered tongue (Vincent *et al.*, 2016). This method provides a tongue-wide value for the ablation, which needs to be distributed among the different processes. In chapter 5, and based on previous methodological developments (Brun *et al.*, 2016), we quantify the total contribution of ice cliffs to the ablation of Changri Nup Glacier tongue. Then the melt beneath debris could be modeled based on fine scale debris thickness mapping, which is currently very challenging. Consequently, the supraglacial and englacial hydrology contribution to ablation could be expressed as the residual of all these terms. This would still be far from closing the mass budget of a debris-covered tongue, as one of the term would be estimated as the residual of the overall budget and another one would be calculated from a distributed melt model, but would be a reference case for testing different sub-debris, cliff and supraglacial melt models.

Summary and objectives of this PhD work

Despite recent spectacular improvement in the knowledge about HMA glaciers, the influence of the debris cover on the glacier mass balance is not clearly understood. With this work I want to address three research questions:

Question 1 What are the recent changes of glaciers at the scale of HMA? Can we produce homogeneous glacier elevation change data with a resolution high enough to capture individual glacier mass balances?

Question 2 What is the influence of the debris cover on the glacier-wide mass balance? Is it possible to quantify this influence? Are the debris-covered and debris-free glaciers different in terms of glacier-wide mass balances?

Question 3 Which terms of the ablation budget of a debris-covered tongue are quantifiable from remote sensing and field observations?

I worked at different spatial and, to a lesser extent, temporal scales to try to address these different questions:

At the scale of the entire HMA ($\sim 100\,000\text{ km}^2$ of glaciers). One does not expect to observe a clear influence of the debris on the regional glacier mass balance, which is mainly driven by climate. However, given the limitations of the estimates that were available when I started this PhD in September 2015, there was a real need to produce a new spatially resolved estimate of the HMA glacier mass balances for the beginning of the twenty-first century. This work is presented in **chapter 3**.

At the scale of HMA regions (2 200 to 18 000 km^2 of glaciers). It is the relevant scale to detect the influence of debris on glacier-wide mass balances, assuming these regions to be climatically homogeneous. In **chapter 4**, I analyze the 16 year individual glacier mass balances in relationship with their morphological parameters and in particular their debris cover.

At the scale of a small debris-covered tongue (1.5 km^2). Working on a single glacier enables extensive deployment of sensors, together with specific very high resolution satellite acquisitions. This is the basis to quantify/constrain some of the sources of ablation. In **chapter 5**, I present the quantification of the cliff contribution to the tongue-wide ablation of Changri Nup Glacier (Everest region, Nepal) for two consecutive years.

A spatially resolved estimate of High Mountain Asia glacier mass balances from 2000 to 2016

Contents

3.1	A short introduction	39
3.2	Abstract	40
3.3	Introduction	41
3.4	Methods	42
3.4.1	Generation and adjustment of ASTER DEMs	42
3.4.2	Extracting the rate of elevation change	43
3.4.3	From elevation changes to glacier mass-balance	43
3.4.4	Uncertainty assessment	43
3.5	Results and discussion	44
3.5.1	Glacier surface elevation changes	44
3.5.2	Altitudinal distribution of thickness changes	46
3.5.3	Spatial variability of individual glacier mass balances	48
3.5.4	Comparison with other regional mass balance estimates	49
3.5.5	HMA glacier contribution to SLR and hydrology	50
3.6	Conclusion	51
3.7	Supplementary information	52
3.7.1	Supplementary text	52
3.7.2	Supplementary tables	56
3.7.3	Supplementary figures	60
3.8	Going one step further	72
3.8.1	Towards an evaluation of the magnitude of the SRTM-C band penetration for the entire HMA?	72
3.8.2	Glacier contribution to streamflow: balance versus imbalance contributions	75

3.8.3	Spatially resolved geodetic observations, new data to calibrate and/or validate global glacier models	76
-------	--	----

This chapter is written after:

Brun, F., E. Berthier, P. Wagnon, A. Kääb, and D. Treichler (2017), A spatially resolved estimate of High Mountain Asia glacier mass balances from 2000 to 2016, *Nature Geoscience*, 10, 668–673

3.1 A short introduction

The first objective of my PhD work was to assess the large scale influence of the debris on the glacier-wide mass balance of individual glaciers. Unfortunately, at the time when I started (September 2015) neither individual glacier mass balances nor a consistent map of the debris-cover extend for HMA were available. The geodetic studies all together covered less than half of the glacierized area of the HMA (Figure 3.1), with large gaps of monitoring for the Western Kunlun Shan, the Eastern Pamir, the Tien Shan, the Hindu Kush and the eastern Nyainqentanglha. Only one study had explored the variability of individual glacier mass balances in the Everest region (*King et al.*, 2017).

Moreover, these estimates were mostly based on the difference between an optical or radar DEM acquired from 2010 to 2016 and the SRTM (February 2000). This means that they were both temporally and methodologically inconsistent and probably biased towards positive values of mass changes due to the SRTM penetration (box 2.5). Consequently, there was a real need of a spatially resolved estimate of glacier mass changes for HMA, using a consistent methodology. We used the GAMDAM glacier inventory (*Nuimura et al.*, 2015), as it is more consistent than the RGI at the scale of HMA.

The last motivation for producing such an estimate was the need for long term (or at least longer than the ICESat 6-year period) glacier mass changes estimates, for the assessment of glacier contribution both to sea level rise and terrestrial water storage. ICESat and GRACE data can be used for such purposes, but ICESat operated only from 2003 to 2008/2009 and the interpretation of GRACE data is complicated in HMA. This was stressed by a recent study, where the authors tried to close the water budget for the period 2003-2015; they temporally extrapolated ICESat trends for glacier changes in HMA, as they had no better estimate available (*Reager et al.*, 2016). Our new estimate is now regarded as a benchmark estimate favored over the GRACE-based estimates (*Bamber et al.*, 2018). The individual glacier mass balances for more than 6 500 glaciers will be included in the next WGMS database release in September 2018.

The validation of our ASTER-based mass balances relied partly on unpublished geodetic estimates based on SPOT5-Pléiades DEM differences for three locations (Spiti Lahaul, Pamir Alay, Garhwal). These geodetic estimates, not affected by radar penetration, were produced by Etienne Berthier and one of them covers Abramov Glacier. It was later used to calibrate/-validate a mass balance model constrained with repeated snow line observations (*Barandun et al.*, 2018). The re-analysis of the Spiti Lahaul dataset revealed that Chhota Shigri Glacier mass balance was probably estimated negatively in a previous publication (*Azam et al.*, 2016). The present article was the opportunity to rectify this. These data are described in the supplementary of the article (section 3.7).

This work gave me the opportunity to collaborate with Andreas Kääb and Désirée Treichler (University of Oslo) and to visit their research group twice. Together with them, we reanalyzed some of the previous ICESat based estimates. We tested various hypothesis to explain

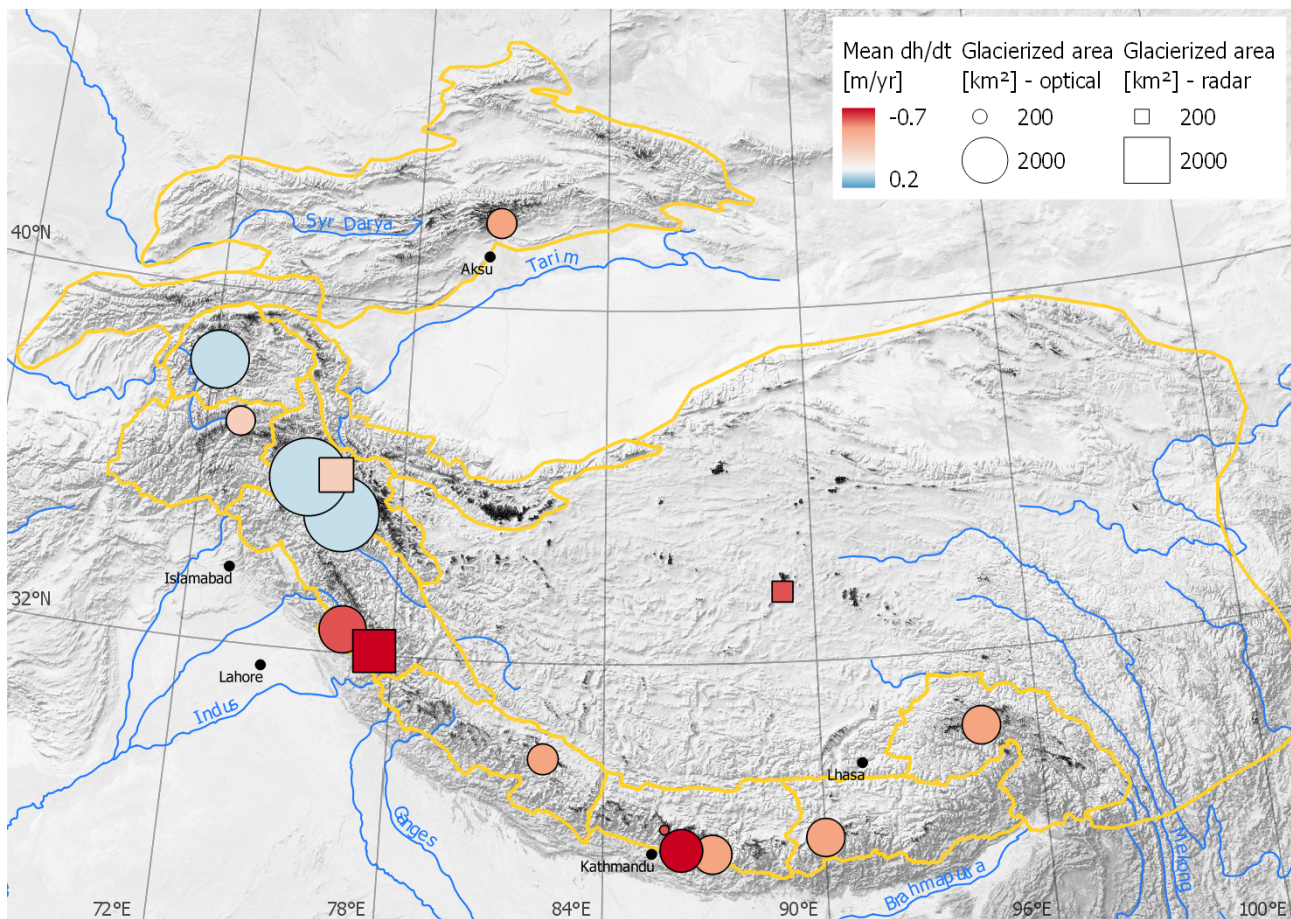


Figure 3.1: Geodetic (radar and optical) estimates of HMA glacier mass changes for the beginning of the twenty-first century available in spring 2017 (at the time of the submission of *Brun et al.*, 2017). See figure 2.12 for a comparison of the currently available estimates and the recent "surge" of geodetic mass balance studies in HMA.

the differences between ICESat and ASTER estimates. In particular, we showed that ICESat spatial sampling, despite its sparsity was adequate to monitor glacier mass balances. However, ICESat estimates are very sensitive to the temporal sampling, due to the short lifetime of the satellite. The complete analysis is presented in the supplementary information of the article (section 3.7).

I presented this work at the Alpine Glaciology Meeting 2017 (Zürich) and at the European Geoscience Union meetings of 2017 and 2018 (Vienna).

3.2 Abstract

High Mountain Asia hosts the largest glacier concentration outside the polar regions. These glaciers are important contributors to streamflow in one of the most populated areas of the world. Past studies have used methods that can only provide regionally-averaged glacier mass balances to assess the High Mountain Asia glacier contribution to rivers and sea level rise. Here we compute the mass balance for about 92 % of the glacierized area of High Mountain Asia using time series of digital elevation models derived from satellite stereo-imagery. We calculate an average region-wide mass balance of $-16.3 \pm 3.5 \text{ Gt yr}^{-1}$ ($-0.18 \pm 0.04 \text{ m w.e. a}^{-1}$) between 2000 and 2016, which is less negative than most previous esti-

mates. Region-wide mass balances vary from $-4.0 \pm 1.5 \text{ Gt yr}^{-1}$ ($-0.62 \pm 0.23 \text{ m w.e. a}^{-1}$) in Nyainqentanglha to $+1.4 \pm 0.8 \text{ Gt yr}^{-1}$ ($+0.14 \pm 0.08 \text{ m w.e. a}^{-1}$) in Kunlun, with large intra-regional variability of individual glacier mass balances (standard deviation within a region $0.20 \text{ m w.e. a}^{-1}$). Specifically, our results shed light on the Nyainqentanglha and Pamir glacier mass changes, for which contradictory estimates exist in the literature. They provide crucial information for the calibration of the models used for projections of future glacier response to climatic changes, models that presently do not capture the pattern, magnitude and intra-regional variability of glacier changes in High Mountain Asia.

3.3 Introduction

The recent global estimates of glacier contribution to sea level rise (SLR) stressed the need to better constrain High Mountain Asia (HMA) glacier mass change (Jacob *et al.*, 2012; Gardner *et al.*, 2013). Two main strategies have been used to estimate the glacier mass loss for the ca. $100,000 \text{ km}^2$ of glaciers covering the Tibetan Plateau (TP) and its surrounding mountain ranges including Himalaya, Karakoram, Pamir, and Tien Shan (Figure 3.2).

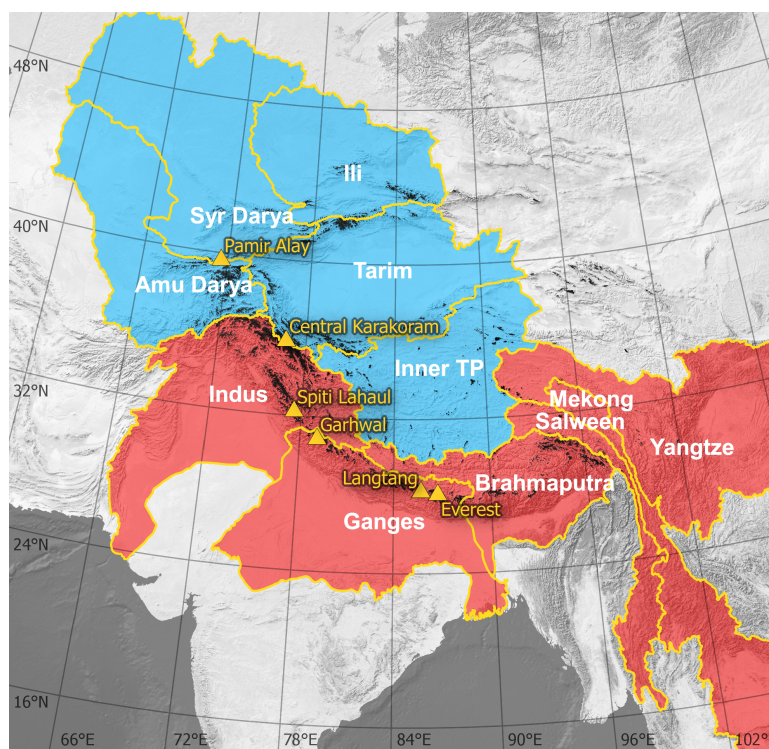


Figure 3.2: High Mountain Asia major drainage basins. The endorheic basins are in blue and the exorheic basins are in red. The yellow triangles show the validation sites (named after the region or a summit) where we evaluated the glacier mass balance obtained with the ASTER method (see Supplementary Information and Figs 3.8–3.11). The glaciers from the GAMDAM glacier inventory (Nuimura *et al.*, 2015) are shown in black.

(i) The first strategy consists in compiling all local observations of glacier mass changes, either from field measurements (glaciological method) or from local remote sensing analysis (geodetic method using digital elevation model (DEM) differencing), and extrapolating them to the rest of the mountain ranges. In HMA, this strategy suffers from the scarcity of local measurements in space and time (Bolch *et al.*, 2012) and the consequent need to extrapolate to vast unsampled areas. This is problematic, given that the pattern of glacier

mass change in HMA is now known to be strongly heterogeneous (Kääb *et al.*, 2015). For example, only two discontinuous in-situ mass balance measurements (Muztagh Ata and Abramov glaciers) are available for subsets of the 2000-2015 period in the western part of HMA, hosting more than 40,000 km² of glaciers (GMBAL database, (Cogley, 2009)). Geodetic DEM differencing provided mass balance estimates for areas smaller than a few thousand square kilometers only (Gardelle *et al.*, 2013; Pieczonka *et al.*, 2013; Holzer *et al.*, 2015; Pieczonka and Bolch, 2015; Ragettli *et al.*, 2016b; Vijay and Braun, 2016; Rankl and Braun, 2016; Bhattacharya *et al.*, 2016) and for varying periods. Earlier studies have demonstrated that these sub-regional measurements are not representative of the larger region (Gardner *et al.*, 2013). This is all-the-more problematic as such local measurements are needed to calibrate future projections of glacier evolution (Huss and Hock, 2015; Marzeion *et al.*, 2017). (ii) The second strategy consists in using large-scale satellite measurements, such as variations in the earth gravity field (GRACE mission (Jacob *et al.*, 2012)) or laser altimetry (ICESat (Kääb *et al.*, 2012)). The difficulty of applying GRACE data at the scale of HMA is mainly due to the strong influence of terrestrial water storage on the GRACE signals – not least in the large endorheic basins (Figure 3.2), but also of underground water depletion, for instance from India, or monsoon intensity change (Jacob *et al.*, 2012; Chanard *et al.*, 2014; Yi and Sun, 2014; Reager *et al.*, 2016). The ICESat laser altimeter, on the other hand, operated only from 2003 to 2009, and had a sparse spatial sampling leading to potential large bias (Treichler and Kääb, 2016). In this study, we bridge the gap between these two strategies and compute the mass balance of 92 % of the glacierized area in HMA. Our results have high spatial resolution and extend the temporal coverage of previous studies. This provides new insights about the mass balance of controversial regions such as Pamir or Nyainqentanglha where previous studies disagree. Our study stresses the inability of existing region-wide glacier mass balance models to capture the pattern of glacier mass changes and provides highly resolved data useful to tune or validate these models. Another advantage is that our new spatially-detailed estimates can be directly evaluated or compared to numerous published local geodetic studies, which is not feasible with GRACE and ICESat estimates. This systematic evaluation increases the confidence in our revised estimates.

3.4 Methods

3.4.1 Generation and adjustment of ASTER DEMs

ASTER DEMs were derived from AST_L1A data (freely available to download at <http://reverb.echo.nasa.gov>) using the open-source Ames Stereo Pipeline (ASP) (Shean *et al.*, 2016). The correlation kernel size was set to 7 pixels and we used the void filled version of SRTM (SRTMGL1 V003) as a seed for the generation of the ASTER DEMs. No ground control point was used. The DEMs were corrected for planimetric and altimetric shifts (Nuth and Kääb, 2011) using SRTM as a reference. Then the across track, along track and curvature bias were corrected by fitting fifth order polynomials to the elevation difference on stable ground (Berthier *et al.*, 2016), after excluding glaciers and water bodies. For that purpose, we used the GAMDAM glacier inventory (Nuimura *et al.*, 2015) together with water bodies from the Global Lakes and Wetlands Database (Lehner and Döll, 2004).

3.4.2 Extracting the rate of elevation change

For each 30-m DEM pixel, we first excluded all the elevation values from the time series that have an absolute difference larger than 150 m from the non-void filled SRTM or from the temporal median of all ASTER elevation values. As a first guess, we fitted a linear trend to the time series of SRTM and ASTER elevation values and subsequently excluded the data points that lay outside the 99 % confidence interval of this initial linear regression. We then fitted a final linear trend to ASTER elevation time series only. Further details are available in *Berthier et al. (2016)*. An example of the distribution of the rate of elevation change on stable terrain as a function of elevation, curvature, slope and aspect is shown on Figure S13.

3.4.3 From elevation changes to glacier mass-balance

We averaged the 30-m gridded elevation change rates on four distinctive spatial units: (i) individual glaciers, (ii) $1^\circ \times 1^\circ$ tiles, (iii) geographic regions and (iv) main river basins. For a given spatial unit, the elevation change rate on glaciers was calculated for each 100 m elevation band as the mean of all pixels belonging to this band. This means that for $1^\circ \times 1^\circ$ tiles, geographic regions and main river basins (ii-iv), the glacierized area was considered as one virtual contiguous ice body. For each elevation band, the pixels were filtered to the level of three normalized median absolute deviations (NMAD; *Höhle and Höhle, 2009*) with respect to the median of the elevation band. Pixels exceeding this threshold were considered not valid (table 3.5, figure 3.6). The total rate of volume change was calculated as the sum of the mean rate of elevation change multiplied by the area for each elevation band. If no data were available for an elevation band (e.g., for the uppermost reaches), a zero elevation change rate was assigned. This never happened when calculating the region-wide averages, but could happen for individual glacier mass balances. The rate of volume change was converted to rate of mass change assuming a volume to mass conversion factor of $850 \pm 60 \text{ kg m}^{-3}$ (*Huss, 2013*).

3.4.4 Uncertainty assessment

The total uncertainty of a given mass balance estimate ($\sigma_{(\Delta M, tot)}$) can be calculated as the quadratic sum of a random ($\sigma_{(\Delta M, rdn)}$) and a systematic ($\sigma_{(\Delta M, sys)}$) error (*Nuth and Kääb, 2011*):

$$\sigma_{(\Delta M, tot)} = \sqrt{\sigma_{(\Delta M, rdn)}^2 + \sigma_{(\Delta M, sys)}^2} \quad (3.1)$$

Uncertainty assessment – random error

The random error on mass balance has three main sources, which are assumed to be independent: the uncertainty on the rate of elevation change ($\sigma_{\Delta z}$), the uncertainty on glacierized area (σ_A) and the uncertainty on volume to mass conversion ($\sigma_{f_{\Delta V}}$). The uncertainty on the rate of elevation change follows *Fischer et al. (2015)* and *Rolstad et al. (2009)*¹

$$\sigma_{\Delta z} = \begin{cases} \sigma_{\Delta h} \sqrt{\frac{A_{cor}}{5A}} & ; A \geq A_{cor} \\ \sigma_{\Delta h} & ; A < A_{cor} \end{cases} \quad (3.2)$$

¹The equation 3.2 is erroneously written in the article as the signs greater than (\geq) and lower than ($<$) are inverted. This will be corrected on the online version of the article soon.

where $\sigma_{\Delta h}$ is the standard deviation of the rate of elevation change on stable ground, A is the glacier area and $A_{cor} = \pi L^2$, with L being the decorrelation length, taken here as 500 m.

Assuming independence between the uncertainty on area and the uncertainty on the rate of elevation change, the total uncertainty on the rate of volume change ($\sigma_{\Delta V}$) is:

$$\sigma_{\Delta V} = \sqrt{(\sigma_{\Delta z}(p + 5(1-p))A)^2 + (\sigma_A \Delta z)^2} \quad (3.3)$$

where Δz is the mean rate of elevation change for the glacierized area and $\sigma_A = 10/100A$ (Kääb *et al.*, 2012) and p is the proportion of surveyed area. In the equation above, we conservatively assume a factor of 5 in the elevation change uncertainty in non-surveyed areas (Berthier *et al.*, 2014).

Assuming independence between the uncertainty on the rate of volume change and the volume to mass conversion factor, the random uncertainty on geodetic mass balance is:

$$\sigma_{(\Delta M,rdn)} = \sqrt{(\sigma_{\Delta V} f_{\Delta V})^2 + (\sigma_{f_{\Delta V}} \Delta V)^2} \quad (3.4)$$

where $f_{\Delta V} = 850 \text{ kg m}^{-3}$ is a volume to mass conversion factor (Huss, 2013), $\sigma_{f_{\Delta V}} = 60 \text{ kg m}^{-3}$ is the uncertainty on the volume to mass conversion factor (Huss, 2013) and ΔV is the volume change.

Uncertainty assessment – systematic error

The systematic error is almost never evaluated in the literature (Nuth and Kääb, 2011). To assess this error, we studied the absolute value of the triangulation residual, noted r , between two sub-periods:

$$r = |\Delta M_{2000-2016} - \frac{1}{2}(\Delta M_{2000-2008} + \Delta M_{2008-2016})| \quad (3.5)$$

where $\Delta M_{xxxx-yyyy}$ is the annual mass balance (expressed in m w.e. a^{-1}) for the period between the year $xxxx$ and $yyyy$. We found that these residuals depended mostly on the mean number on DEMs used to calculate $\Delta M_{2000-2016}$. We found that residuals calculated with less than 8 DEMs were higher than those calculated with more than 8 DEMs. Therefore, we assigned the value of the 67th percentile of each of these populations to the systematic error. This gives $\sigma_{(\Delta M,sys)}$ equals to 0.07 m w.e. a^{-1} for mass balances calculated with more than 8 DEMs and 0.19 m w.e. a^{-1} for mass balances calculated with less than 8 DEMs. The total uncertainty on HMA glacier mass change was calculated as the quadratic sum of the uncertainties in Gt yr^{-1} for each region or basin. This results in a relative uncertainty of 21 %, which was transferred to the area weighted mean obtained in m w.e. a^{-1} .

3.5 Results and discussion

3.5.1 Glacier surface elevation changes

We apply a fully automated method to compute DEMs from the vast amount of freely available ASTER optical satellite stereo pairs. We use these DEMs to assess glacier volume changes over the entire HMA for the period 2000-2016. We fit a linear regression

Table 3.1: region-wide mass balance from ASTER time series compared to ICESat estimates. The glacierized areas are calculated from the GAMDAM glacier inventory (*Nuimura et al., 2015*). For the column “ASTER MB [2000 – 2016] with ICESat sampling” ASTER-derived trends have been sampled at ICESat footprint locations (Supplementary Information), these numbers should be considered as indicative and are not provided with an uncertainty. ICESat data are taken from *Kääb et al. (2015)* except for Kunlun, Inner TP, Tien Shan and Pamir Alay, which were extended for this study using the same method.

Region	Glacier area km ²	ASTER MB [2000 – 2016] m w.e. a ⁻¹	ASTER MB [2000 – 2016] with ICESat spatial sampling m w.e. a ⁻¹	ICESat MB [2003 – 2008] m w.e. a ⁻¹
Bhutan	2,291	-0.42 ± 0.20	-0.30	-0.76 ± 0.20
East Nepal	4,776	-0.33 ± 0.20	-0.33	-0.31 ± 0.14
Hindu Kush	5,147	-0.12 ± 0.07	-0.14	-0.42 ± 0.18
Inner TP	13,102	-0.14 ± 0.07	-0.12	-0.06 ± 0.06
Karakoram	17,734	-0.03 ± 0.07	-0.06	-0.09 ± 0.12
Kunlun	9,912	0.14 ± 0.08	0.17	0.18 ± 0.14
Nyainqentanglha	6,378	-0.62 ± 0.23	-0.51	-1.14 ± 0.58
Pamir Alay	1,915	-0.04 ± 0.07	+0.00	-0.59 ± 0.27
Pamir	7,167	-0.08 ± 0.07	-0.05	-0.41 ± 0.24
Spiti-Lahaul	7,960	-0.37 ± 0.09	-0.33	-0.42 ± 0.26
Tien Shan	10,802	-0.28 ± 0.20	-0.20	-0.37 ± 0.31
West Nepal	4,806	-0.34 ± 0.09	-0.27	-0.37 ± 0.15
Total	91,990	-0.18 ± 0.04	-0.15	-0.34 ± 0.06

through time series of co-registered ASTER DEMs to estimate the rate of elevation change for each 30-m pixel (*Berthier et al., 2016*) and Methods section). Inspired from previous studies (*Nuimura et al., 2015; Willis et al., 2012; Wang and Kääb, 2015*), this methodology was further developed and validated on the Mont-Blanc area in the European Alps (*Berthier et al., 2016*). Contrary to earlier studies, we did not rely on DEMs available online (the so-called 14DMO product) but directly calculated more than 50,000 DEMs from L1A ASTER images using the Ames Stereo Pipeline (*Shean et al., 2016*). One strength of this method is that it relies exclusively on satellite optical data. Thus, it is not affected by signal penetration, which is a major source of uncertainty in DEMs derived from radar sensors (e.g., from Shuttle Radar Topography Mission; SRTM), for which the signal penetrates to a mostly unknown depth of up to many meters into snow and ice (*Kääb et al., 2012; Fischer et al., 2015; Berthier et al., 2016*). We integrate these elevation changes and use a mass to volume conversion factor of $850 \pm 60 \text{ kg m}^{-3}$ (*Huss (2013)* and Supplementary Information). Our glacier mask for DEM co-registration and for integrating the glacier elevation change is derived from the GAMDAM inventory (*Nuimura et al., 2015*), as this is the only homogenous inventory covering the entire HMA. As a sensitivity test, we compare our GAMDAM-based estimates with those obtained using the ICIMOD inventory (*Bajracharya and Shrestha, 2011*), the ESA CCI inventory (*Glaciers_cci consortium, 2015*) and the Randolph Glacier Inventory (*Pfeffer et al., 2014*) (Supplementary Information).

Over our study region, the method is evaluated using published estimates for individual glaciers or groups of several glaciers. Our volume change estimates are compared with Chhota Shigri glaciological mass balance during 2002-2014 (*Azam et al., 2016*, the only

series available in HMA validated against geodetic mass balance and covering almost the same time frame as our study) and independent geodetic estimates over 6 selected areas (Supplementary Information and Figures 3.2, 3.8, 3.9). For 60 individual glaciers larger than 2 km², we obtain a mean difference between the published values and our estimates of -0.07 m w.e. a⁻¹ and a standard deviation of the residual of 0.17 m w.e. a⁻¹.

For visualization, we provide mass changes averaged over a 1°×1° grid (Figure 3.3a) and aggregated them over the regions of *Kääb et al.* (2015) for the sake of comparison (Figure 3.3b). Our total HMA glacier mass change is -16.3 ± 3.5 Gt yr⁻¹ (-0.18 ± 0.04 m w.e. a⁻¹) between March 2000 and November 2016. This mass change is calculated on more than 92 % of the glacierized area of HMA (total area of 91,990 km² in the GAMDAM inventory (*Nuimura et al.*, 2015)). The remaining 8 % correspond to the 1°×1° degree tiles with less than 150 km² glacier area each. The latter were not processed and their glacier change signal was substituted by the regional averages. Our results confirm that the mass balance anomaly, first observed over the Karakoram and named the “Karakoram anomaly” (*Gardelle et al.*, 2012b), is in fact also extending to the Kunlun and West Pamir regions (Figure 3.3). The most positive mass change of 0.26 ± 0.07 m w.e. a⁻¹ is observed in the Kunlun (hypso-metric average of the tile spanning between 35°N, 36°N, 82°E and 83°E). The glacier mass balance anomaly appears thus to be centered over Western Kunlun. According to our results, Pamir and Karakoram are both regions of transition from positive to negative mass balance (*Kääb et al.*, 2015). The most negative changes are found for the eastern HMA in Nyainqentanglha with -0.62 ± 0.23 m w.e. a⁻¹ (even as negative as -0.80 ± 0.25 m w.e. a⁻¹ in for the hypso-metric average of the tile spanning between 29°N, 30°N, 97°E and 98°E). The mass balance pattern is homogeneous in Tien Shan, with mass losses averaging at -0.28 ± 0.20 m w.e. a⁻¹ for the entire region. Moderate mass losses are observed along the Himalayan range with values ranging from -0.42 ± 0.20 m w.e. a⁻¹ in Bhutan to -0.33 ± 0.20 m w.e. a⁻¹ in the East Nepal region.

3.5.2 Altitudinal distribution of thickness changes

In addition to these regional averages, we compute the altitudinal distribution of surface elevation change within each region (Figure 3.4 and Figure 3.7). These curves highlight the potential of our method to understand the elevation behavior of glaciers over large regions, even in elevation zones that are otherwise hardly measured using optical satellite stereo due to the lack of image contrast on snow. Overall, we observe decreasing thinning rates with elevation, which is a commonly observed pattern (*Gardelle et al.*, 2013; *Ragettli et al.*, 2016b). Exceptions are the glaciers in Bhutan, which exhibit a reduced thinning at their terminus, potentially due to the thick debris-cover, and those in Kunlun, which show a rather constant thickening rate for all elevations. In Nyainqentanglha and Spiti Lahaul, significant thinning rates are observed even at high elevations. This finding stresses the importance of taking into account the changes occurring in the accumulation area of glaciers when computing geodetic mass balance estimates from optical stereo methods. The altitudinal distribution of elevation changes is the result of the combined effects of glacier dynamics and surface mass balance (*Huss and Farinotti*, 2012). In Nyainqentanglha and Spiti Lahaul, two regions with highly negative mass balances (Figure 3.3) and where field observations are also available (*Yao et al.*, 2012), the thinning observed even at highest elevations reveals that the glaciers are losing large parts of their accumulation areas, with equilibrium line altitudes approaching the uppermost glacier elevations. A similar behavior is observed for Alpine glaciers (*Fischer et al.*, 2015), which are also in an advanced state of decline. In contrast, the thickening of high elevations in Kunlun could be a direct mass-balance signal, combined

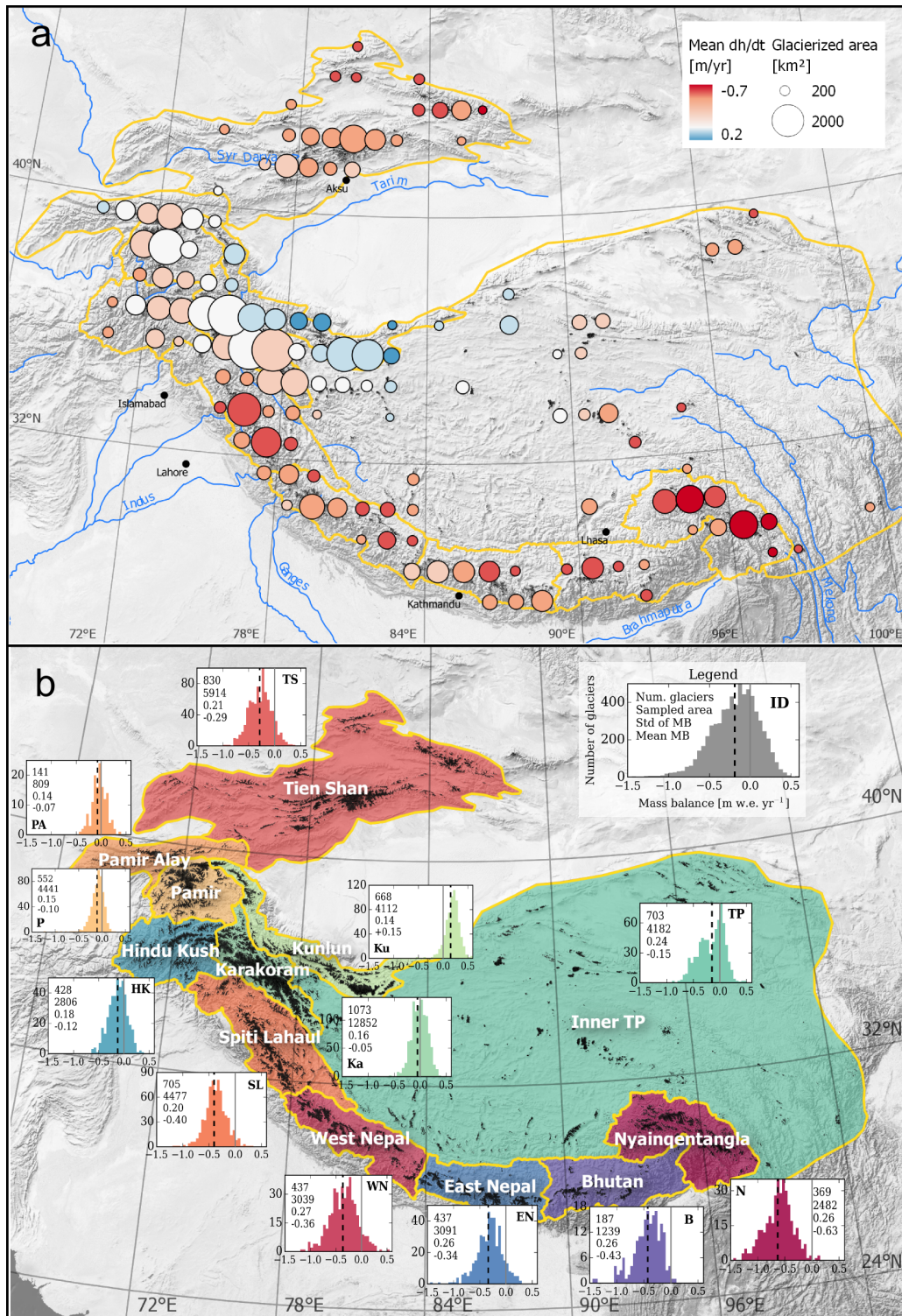


Figure 3.3: Glacier elevation changes and mass balance for High Mountain Asia (2000–2016). a, Map of glacier mean elevation change on a $1^\circ \times 1^\circ$ grid. b, For each region in Kääb *et al.* (2015), the distribution of glacier-wide mass balance for every individual glacier (> 2 km²) is represented in histograms of the number of glaciers (y axis) as a function of MB (x axis in m w.e. a⁻¹). The black dashed line represents the area-weighted mean. The numbers denote the total number of individual glaciers (first), the corresponding total area (in km², second), the standard deviation of their mass balances (in m w.e. a⁻¹, third) and the area-weighted average mass balance (in m w.e. a⁻¹, fourth). Initials of the respective regions are repeated in bold.

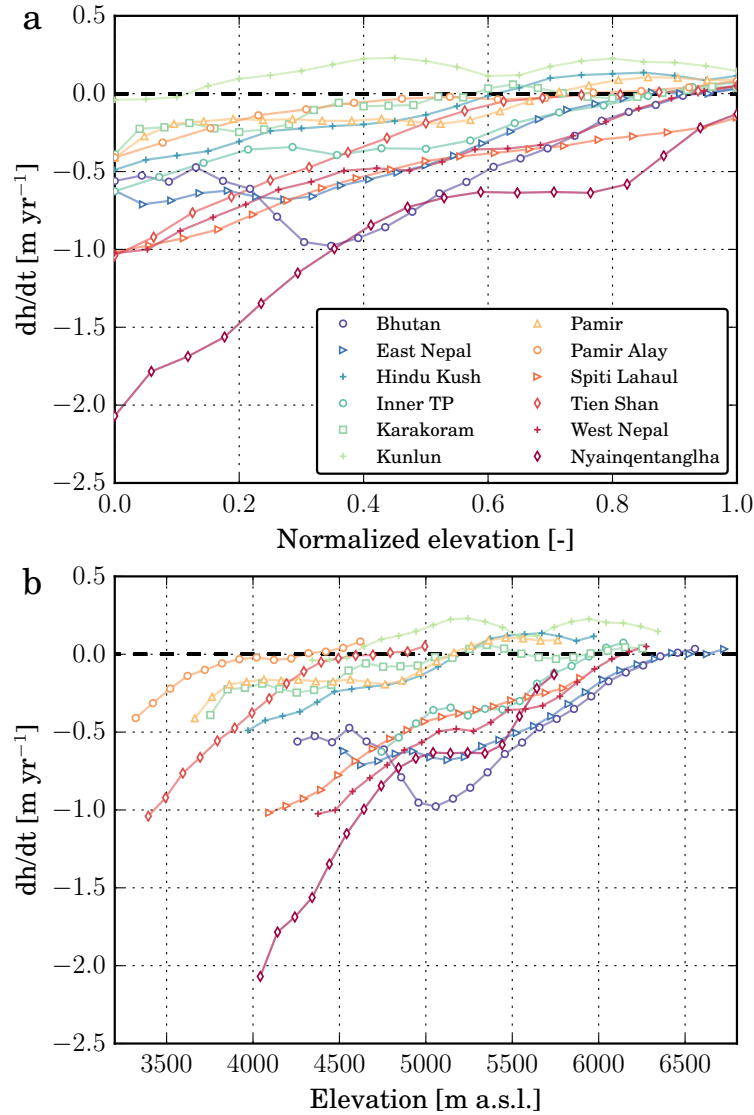


Figure 3.4: Altitudinal distribution of glacier elevation change. a, Rate of elevation change for the period 2000–2016 as a function of normalized elevation, which is defined as $(z - z_{2.5}) / (z_{97.5} - z_{2.5})$, where z is the elevation and $z_{2.5}$ and $z_{97.5}$ are the elevation of the 2.5 and 97.5 percentile of area, respectively. b, Rate of elevation change for the period 2000–2016 as a function of elevation (in m a.s.l.).

with a dynamic signal due to a delay of the glaciers to reach their balance velocities. The altitudinal dependency of thickness change is thus a valuable validation for glaciological models (Cogley, 2009).

3.5.3 Spatial variability of individual glacier mass balances

To calculate the mass balance of individual glaciers, we restricted our analysis to the 6350 glaciers larger than 2 km^2 and with more than 70 % of valid data (i.e. pixel values within a conservative range of possible elevation changes, see method section). They represent $49,450 \text{ km}^2$ (about 54 % of the glacierized area of HMA). The glacier-wide mass balances for the period 2000–2016 are variable from glacier to glacier for regions with negative mass balance (Figure 3.3b), with a standard deviation of $\sim 0.25 \text{ m w.e. a}^{-1}$. In contrast, balanced regions have a low variability of $\sim 0.15 \text{ m w.e. a}^{-1}$. The very large Inner TP region is an

aggregation of climatically heterogeneous sub-regions, which results in a bi-modal distribution of glacier mass balance, and a high dispersion. This is also the case to a lower extent for West Nepal and Tien Shan. Maybe counter-intuitively, regions with a large number of surge-type glaciers such as Pamir, Pamir Alay and Karakoram (*Sevestre and Benn, 2015*) show a lower variability of ~ 0.15 m w.e. a^{-1} , perhaps related to the fact that these surge-clusters are mostly in regions with stable or slightly increasing glacier mass. The differences between regions in terms of individual glacier-wide mass balance variability should be taken into account when performing regional calibration of mass balance models (*Huss and Hock, 2015*).

The intra-regional variability is well illustrated for three neighboring sub-regions (Everest, Langtang and Kanchenjunga) defined in Figure 3.12. Their sub-region-wide glacier mass balances are very similar (ranging from -0.35 to -0.42 m w.e. a^{-1}), with strong similarities of their altitudinal pattern of elevation change (Figure 3.13d). By contrast, mass balances of individual glaciers larger than 2 km² differ considerably from these averages (Figure 3.13e), with standard deviations of 0.21 , 0.23 and 0.28 m w.e. a^{-1} respectively for Everest, Kanchenjunga and Langtang. Our remote sensing analysis is in line with field measurements that showed also a strong mass balance variability for glaciers smaller than 2 km² in the Everest region (*Sherpa et al., 2017*). The most negative glacier-wide mass balance for each region (around -2 m w.e. a^{-1} , -1.5 m w.e. a^{-1} and -1 m w.e. a^{-1} for Langtang, Everest and Kanchenjunga, respectively) correspond to glaciers terminating in proglacial lakes (*King et al., 2017*). Our new mass balance dataset can thus be used to assess the representativeness of single-glacier measurements and to complement them.

3.5.4 Comparison with other regional mass balance estimates

From previous studies, it is well established that the contrasted climatic setting of HMA (*Maussion et al., 2014*) leads to a heterogeneous response of glaciers (*Kääb et al., 2012; Gardelle et al., 2013; Gardner et al., 2013*). The spatial pattern of glacier thickening and thinning from the present study over the period 2000-2016 is consistent with the pattern during 2003-2008 (*Kääb et al., 2015*), underlying its temporal persistence. For seven regions out of twelve (Tien Shan, Karakoram, Kunlun, Spiti Lahaul, East Nepal, West Nepal and Inner TP), there is a good agreement between our glacier mass change and published values (Table 3.6).

The remaining five regions (each covering $1,900$ to $7,000$ km² of glaciers) are controversial (i.e. Pamir Alay, Pamir, Hindu Kush, Bhutan and Nyainqentanglha), as contradictory estimates of glacier mass changes have been published for the first decade of the 21st century (Table 3.6). In particular, the Pamir region was reported to have a significantly negative rate of elevation change in *Kääb et al. (2015)* (-0.48 ± 0.14 m yr^{-1} for 2003-2008, in the following section, elevation change results are given in m yr^{-1} to avoid uncertainty due to the volume to mass conversion), whereas it was less negative in *Gardner et al. (2013)* (-0.13 ± 0.22 m yr^{-1} for 2003-2008) and even positive in *Gardelle et al. (2013)* ($+0.16 \pm 0.15$ m yr^{-1} for 1999-2011). Similarly, the Nyainqentanglha region was reported to have a very negative rate of elevation change in *Kääb et al. (2015)* (-1.34 ± 0.29 m yr^{-1} for 2003-2008), whereas it was less negative in *Gardner et al. (2013)* (between -0.30 and -0.40 m yr^{-1} for 2003-2008) and in *Gardner et al. (2013)* (-0.39 ± 0.16 m yr^{-1} for 1999-2010). For these two regions, we find respectively -0.05 ± 0.08 m yr^{-1} (Pamir) and -0.72 ± 0.27 m yr^{-1} (Nyainqentanglha) between 2000 and 2016. We verify that the sparse sampling of ICESat is not the reason for these differences (Table 3.1, Supplementary Information and Table 3.3). Further, there is

no consistent shift in ASTER mass balances between the sub-periods 2000-2008 and 2008-2016 that could explain the disagreement (Supplementary Information and Table 3.4). In contrast, we find that the inter-annual variability of the observed surface elevation is much higher for these five controversial regions than the others (Figure 3.14). Consequently, for such regions of large inter-annual variability, removing one year of acquisition from the trend fitting might impact the resulting ICESat-derived trend more than for other regions with low inter-annual variability (Figure 3.15c). This likely explains the contradictory results in the literature and stresses the need for caution when extrapolating in time ICESat trends of elevation change or other short-term glacier elevation of mass balance changes. The total difference between the HMA mass change estimate derived from ASTER and ICESat is 11.2 Gt yr^{-1} , in which 9.0 Gt yr^{-1} originates from the controversial regions (Figure 3.14a, b and Table 3.1).

To complete the comparison with other mass balance estimates, we compare our results with *Gardner et al.* (2013), based on Randolph Glacier Inventory (*Pfeffer et al.*, 2014) glacier mask and regions (Table 3.8).

3.5.5 HMA glacier contribution to SLR and hydrology

We provide spatially resolved estimates for the potential contribution of HMA glaciers to SLR and changes in the downstream hydrology (Table 2), aggregated by major river basins. We find a total sea level contribution of $16.3 \pm 3.5 \text{ Gt yr}^{-1}$ ($14.6 \pm 3.1 \text{ Gt yr}^{-1}$ when including only the exorheic basins), corresponding to $0.046 \pm 0.009 \text{ mm yr}^{-1}$ SLE ($0.041 \pm 0.009 \text{ mm yr}^{-1}$ SLE when including only the exorheic basins). This estimate is in marked disagreement with the total estimate of $46 \pm 15 \text{ Gt yr}^{-1}$ from *Cogley* (2009) and *Marzeion et al.* (2015) commonly used in the sea level budget studies (*Chambers et al.*, 2017). The model contribution estimates of *Cogley* (2009) and *Marzeion et al.* (2015) for the period 2000-2013 are nearly four times larger than our estimate for Central Asia (22 Gt yr^{-1} for the model versus 6 Gt yr^{-1} for this study) and over twice as large for South Asia East and South Asia West (14 Gt yr^{-1} for the model vs. 6 Gt yr^{-1} for this study and 9 Gt yr^{-1} for the model vs 4 Gt yr^{-1} for this study for the two regions respectively; Randolph Glacier Inventory regions (*Pfeffer et al.*, 2014) Table 3.4). These discrepancies can be explained by the lack of direct measurements to constrain both the interpolation method of *Cogley* (2009) and the model tuning and/or the high temporal smoothness of atmospheric models of *Marzeion et al.* (2015). In particular, these estimates attribute mass losses to Karakoram and Kunlun, two regions with a large glacierized area where we find only little mass loss or even mass gain (Figure 3.16). The importance of glacier runoff to total river discharge refers to multiple concepts and definitions, especially when looking at seasonality of glacier runoff (*Radić and Hock*, 2014). As we provide averages of annual mass balance, we can only calculate the annual “excess discharge”, which constitutes the additional water due to a reduction in the water stored by glaciers (*Lambrecht and Mayer*, 2009; *Radić and Hock*, 2014). According to this definition, glacierized catchments with a positive or balanced glacier mass balance have an excess discharge of zero (this is the case for Tarim basin only, Table 3.2). The largest contributions originate from Indus and Brahmaputra basins, each accounting for roughly a third of HMA’s total excess discharge. The Indus basin contributes largely because of its large glacierized area and Brahmaputra mostly because of the strongly negative mass balance (Table 3.2).

Table 3.2: mass balance of the main river basins originating in HMA for 2000-2016. Following *Lambrecht and Mayer (2009)* and *Radić and Hock (2014)* the excess discharge is 0 for glaciers with balanced or positive mass budget (which is the case only for the Tarim basin). We added an extra significant digit for the Mekong basin, because the values were too small to be adequately represented otherwise. Excluding endorheic basins, the total contribution is $-14.6 \pm 3.1 \text{ Gt yr}^{-1}$ or $0.041 \pm 0.009 \text{ mm yr}^{-1}$ SLE. The endorheic basins are noted with an asterisk.

Basin name	Glacierized area [km ²]	Mass budget [Gt yr ⁻¹]	Annual excess discharge [m ³ s ⁻¹]
Amu Darya*	10,784	-1.0 ± 0.8	-31 ± 24
Brahmaputra	9,513	-5.1 ± 2.1	-163 ± 66
Ganges	8,314	-2.7 ± 0.7	-84 ± 24
Ily*	4,316	-1.6 ± 0.9	-49 ± 27
Indus	24,698	-4.0 ± 2.0	-125 ± 63
Inner TP*	7,285	-0.4 ± 0.5	-12 ± 16
Mekong	221	-0.09 ± 0.04	-3 ± 2
Salween	1,195	-0.8 ± 0.3	-24 ± 9
Syr Darya*	2,336	-0.3 ± 0.2	-10 ± 5
Tarim*	18,409	0.4 ± 1.3	0 ± 41
Yangtze	1,422	-0.5 ± 0.3	-14 ± 9

3.6 Conclusion

In this study we provide new and spatially resolved estimates of glacier mass change over the entire HMA for the period 2000-2016 and, additionally, for individual glaciers larger than 2 km², which represent ~54 % of the glacierized area. On a regional basis, these estimates are in line with ICESat laser altimetry studies, indicating that the contrasted pattern of glacier mass change has been persistent during nearly two decades, except for five regions where the inter-annual variability in glacier mass balance is high. For the latter regions, the 5-year ICESat trends are strongly influenced by individual years (especially 2003 and 2008) due to the short sampling interval. Our new estimate of HMA glacier contribution to SLR for 2000-2016 ($0.041 \pm 0.009 \text{ mm yr}^{-1}$ SLE, when excluding endorheic basins) is slightly smaller than the values of *Kääb et al. (2015)* ($0.06 \pm 0.01 \text{ mm yr}^{-1}$ SLE) and *Gardner et al. (2013)* ($0.07 \pm 0.03 \text{ mm yr}^{-1}$ SLE), but much smaller than the model-based estimate of *Cogley (2009)* and *Marzeion et al. (2015)* ($0.13 \pm 0.05 \text{ mm yr}^{-1}$ SLE), although the latter are widely used in the literature (*Church et al., 2013; Chambers et al., 2017*). Nevertheless, the increasing number of mass balance observations that are available to calibrate mass balance models will lead to an improvement of these models and will thus help to reconcile observed and modelled estimates.

3.7 Supplementary information

3.7.1 Supplementary text

ASTER mass balance spatial coverage

The ASTER DEMs were generated and processed based on $1^\circ \times 1^\circ$ tiles. Large parts of HMA are sparsely glacierized and the processing of one tile is computationally expensive (typically 4 days on a 6 core computing cluster), therefore we had to find a compromise between the needs in calculation resources and the area covered. For instance, there are many small glacierized catchments in the inner TP, which would have a very poor ratio in terms of computing time versus area of ice monitored. To optimize computing time, we calculated the cumulative distribution of glacierized area for all tiles (Figure 3.5), and computed the mass balance of the 130 most glacierized tiles, in order to estimate the volume change of more than 92 % of the glacierized area of HMA (Figure 3.5 and Table 3.5). We further added two extra tiles in Nyainqentanglha and inner TP with little glacier area but of specific interest. For the period 2000-2016, for each region, more than 75 % of the sample area was retrieved (Table 3.5), with a decrease in the proportion of the sampling area with elevation, due to the greater occurrence of snow and consequently a lower visual contrast necessary for stereo parallax matching and thus elevation retrieval (Figure 3.6). For a given tile/region/glacier, the volume change (and derived mass change) is calculated as the hypsometric average of elevation change. As a consequence for any regular grid, glaciers are sometimes split in between multiple tiles. For instance, in the endmember case of the large ($\sim 936 \text{ km}^2$) Siachen Glacier in the eastern Karakoram, the accumulation area of the glacier is on one tile and the ablation area in another tile. Therefore, the gridded estimates are primarily intended to visualize the general pattern of elevation change – as the mass continuity condition is not fulfilled for parts of a glacier, where a change in surface elevation can be the consequence of either ice dynamics or a mass balance signal. For our regional estimates, glaciers are not split. The estimates are thus similar to glacier-wide mass balance as the ice dynamics effects cancel out. Note that the restriction to glaciers $> 2 \text{ km}^2$ is only valid for our mass balance estimates for individual glaciers, in order to ensure sufficient sampling of each hypsometric band within the small area of a single glacier. For the tile-/region-based estimates, glaciers smaller than 2 km^2 also contribute to the tile-/region-averaged mass balance.

Evaluation of individual glacier mass balance estimates

We limited the comparison to glaciers larger than 2 km^2 because glaciers smaller than this size have, in most cases, an uncertainty higher than $\pm 0.35 \text{ m w.e. a}^{-1}$ (see uncertainty assessment in the Method Section, all uncertainties are given at the 1 sigma confidence level). For validation of our ASTER-based results, we use elevation change maps derived from SPOT5 (2003 in the Abramov Glacier area, 2005 for the Gangotri and Chhota Shigri regions) and Pléiades (2015 for the Abramov area and 2014 for the Gangotri and Chhota Shigri regions) DEMs (Figure 3.8 and 3.9). The methodology followed to compute the SPOT5 and Pléiades DEMs, to adjust them horizontally and vertically on the stable terrain, and to estimate the glacier-wide MB has been described in detail in ref. 1 for similar datasets acquired over the Mont Blanc area, European Alps. The uncertainties were estimated over Mont Blanc glaciers using repeated field GPS measurements¹. Elevation changes from SPOT5/Pléiades DEM differencing were found to be accurate within $\pm 1.3 \text{ m}$ and this error level was conservatively multiplied by a factor of 5 for regions where at least one of the DEMs had data

gaps¹. We converted volume change to glacier-wide MB using a conversion factor of $850 \pm 60 \text{ kg m}^{-3}$ (Huss, 2013). The only glaciological mass balance series published in HMA that is long enough to be comparable to our data is the Chhota Shigri series³. For the 2005–2014 period, the glaciological annual mass balance was $-0.41 \pm 0.40 \text{ m w.e. a}^{-1}$ and the geodetic mass balance was initially estimated at $-0.40 \pm 0.28 \text{ m w.e. a}^{-1}$ (Azam *et al.*, 2016). The SPOT5/Pléiades map of elevation change used to calculate the geodetic mass balance in Azam *et al.* (2016) exhibits a suspicious increase of thinning for elevations above 5000 m a.s.l. (black dashed line in Figure 3.9b), which biased the glacier-wide mass balance towards too negative values. The geodetic mass balance was thus recomputed using a new Pléiades stereo-pair acquired 26 September 2014, nearly at the exact same time of year as the SPOT5 stereo pair (20 and 21 September 2005). Thus no seasonal correction was applied. The curvature correction⁴ had been neglected in Azam *et al.* (2016) and is now applied. The revised SPOT5-Pléiades elevation changes are in much better agreement with the ASTER results (red crosses in Figure 3.9b). The new glacier wide mass balance of Chhota Shigri Glacier using SPOT5-Pléiades is $-0.23 \pm 0.28 \text{ m w.e. a}^{-1}$ versus $-0.27 \pm 0.13 \text{ m w.e. a}^{-1}$ for ASTER.

Sensitivity to the choice of the glacier inventory

We calculate the mean rates of elevation change based on the ICIMOD glacier inventory⁵ and the CCI glacier inventory for Karakoram⁶ to test the sensitivity of our results to the inventory type and quality. The ICIMOD glacier inventory covers about 30,000 km² of ice in total. In the Karakoram, it results in 6.1 % less glacier area than the GAMDAM glacier inventory for the same region. The glacier volume change calculated on the ICIMOD glacier inventory is 8.8 % smaller than the volume change calculated based on the GAMDAM glacier inventory. The CCI glacier inventory for Karakoram covers about 22,000 km². This is 15.4 % larger than GAMDAM for the same region. The glacier volume change calculated based on the CCI glacier inventory is 7.1 % smaller than the volume change calculated based on the GAMDAM glacier inventory. The differences between the inventories are mainly due to varying acquisition dates of the underlying satellite imagery and different, but valid choices for glacier delineations⁷. This suggests that the uncertainty in volume change is not completely independent from the glacier area and definition of a glacier, as often assumed in the literature. However, the influence of the area considered on the volume change calculation is not straightforward to assess as it depends on the sensitivity of the mean rate of elevation change to the area change and on the sign of the mean rate of elevation change. As we do not have means to understand this complex response, we use an uncertainty of 10 % on area, which is larger than the widely-used value of 5 % from Paul *et al.* (2013), and we still assume that the uncertainties on the mean rate of elevation change and the uncertainty on area are independent. To our knowledge, no multi-temporal glacier inventory is available for entire HMA. Therefore, we assumed a constant glacierized area, and that variations in area are covered by our 10 % area uncertainty. Additionally, we provide estimates of glacier mass changes for the regions and glacier mask defined in Randolph Glacier Inventory (Pfeffer *et al.*, 2014) (Table 3.7).

Detailed comparison with ICESat estimates

For most regions, we found a good agreement between ICESat and ASTER mass change estimates (Table 3.6 and 3.7). However, significant differences exist for five controversial regions, i.e. Bhutan, Hindu Kush, Nyainqentanglha, Pamir Alay and Pamir. To understand

these differences, we test three hypotheses: H1- ICESat scarce spatial sampling introduces bias; H2- the glacier mass balance changed between the early 2000s and recent years; H3- some regions have higher inter-annual variability of mass balance, to which the short ICESat acquisition period of five years only and the annually varying sample distribution might be sensitive to.

- To test H1, i.e. the representativeness of ICESat sampling, we extracted the ASTER elevation trends at the footprint locations only. The ASTER points were extracted in a circle of 70 m radius around the ICESat footprint center. This 70 m radius of the circle (twice as large as the 35 m radius of the ICESat footprint) was chosen as a compromise to average over enough ASTER DEM points so that the noise level is acceptable, and to average not over too many pixels to avoid contamination from pixels belonging to different area (e.g., from off-glacier terrain). As a consequence, the mean rate of elevation change for 16 to 21 ASTER pixels was assigned to each individual ICESat footprint on a glacier. From this collection of rates of elevation changes, we calculated the region-wide glacier mass balance by two means: 1- by calculating the mean elevation changes for each 100 m elevation band (area weighted or hypsometric average); 2- by calculating the dh for each point (dh is defined as the retrieved value of elevation extracted from an averaged ASTER trend at the date of ICESat acquisition, minus the SRTM elevation) and then fitting a robust trend of elevation change (completely analogous to *Kääb et al. (2015)*). Results obtained with both methods are shown in Table 3.3. It is not straightforward to estimate uncertainties for these retrieved values because ASTER elevations are much noisier than ICESat elevations at a given location. The resulting numbers are in very good agreement with the estimates calculated from the whole ASTER dataset (Table 3.3 and Table 3.1). This confirms that the spatial sampling of ICESat is adequate to represent the entire regions, at least for the entire ASTER period (2000-2016).
- To test H2, i.e. temporal shift in mass balances, we calculate the mass balance for the sub-periods 2000-2008 and 2008-2016 from ASTER DEMs. For these shorter sub-periods, the final number of available and retained DEMs is lower, and therefore uncertainties on these estimates are higher (see Method section). We observe no consistent shift in mass balances between the two periods (Table 3.4) that would help explaining the difference to the ICESat-based results. Unfortunately, estimates based on the 2003-2008 ASTER data only are too noisy, forcing us to limit this test to the 2000-2008 period that does not directly compare to the ICESat period.
- To test H3, spatio-temporal variability in mass balances, we explored the distribution of de-trended ICESat dh (ICESat-SRTM; Figure S10). For the non-controversial regions, the absolute value of the annual median of the de-trended dh is always below 1 m (the only exception is East Nepal in 2008), whereas it is often over 1 m and sometimes larger than 2 m for the controversial regions (Figure S10). In principle, high deviation of the median dh of one ICESat campaign indicates especially positive/negative glacier mass balance for that particular year, but the deviation could also be caused by bias in the ICESat or SRTM elevation data, a different hypsometry sampling biased towards tongues (typically stronger thinning) or accumulation areas (rather stable surface elevations), or snow fall right before ICESat's surface elevation sampling (*Treichler and Kääb, 2016*). Bias is more likely for regions/campaigns with few ICESat samples. The controversial regions have rather lower ICESat samples (<5,000 footprints; Table 3.3) spread over regions of similar size as the non-controversial regions. The regions may consist of different topo-climatic sub-regions that react differently to climate change. However, Figure 3.3b shows that a high (small) intra-regional dis-

person in glacier-wide mass balances alone does not suffice as an indicator for (non-) controversial regions. To further test the potential influence of the inter-annual variability of glacier mass balance for the period 2003-2008, we calculated robust fits of elevation trends for the ICESat data in different configurations. First, we calculated the fit through the entire dataset for each region. Second, we removed one year of acquisition and fitted the trend to the remaining data. This was repeated for all six individual years from 2003 to 2008. The results are presented in Figure 3.15c, where each dot represents a fit with one year removed and the thick diamonds the fit which includes all six ICESat years. In this bootstrap test, all five controversial regions showed very high sensitivity to the removal of one year of data, contrary to the other regions (Figure 3.15c). They are especially highly sensitive to the removal of the first (2003) and last (2008) year of acquisition. In particular for Pamir, the year 2008 appears to be very dry (*Yi and Sun, 2014; Pohl et al., 2017*). Also for Abramov Glacier in Pamir Alay, *Barandun et al. (2015)* found particularly negative values for 2008 in their reconstructed mass balance series. A particularly negative mass balance in 2008 could explain the negative trend in ICESat for these regions, where ASTER data suggest nearly balanced conditions.

We conclude that the sparse ICESat sampling used to derive region-wide mass balances in HMA from 2003 to 2008 is spatially representative, but when addressing longer-term processes (the data are often used for sea level rise estimates), it should be kept in mind that the mass balance calculated from ICESat trends are only valid within the short (5-year) monitoring period. They cannot be extrapolated to longer periods, in particular for these five regions.

3.7.2 Supplementary tables

Table 3.3: Rate of glacier elevation change from ASTER trends [2000-2016] resampled with ICESat sampling.

Region	Mean rate of elevation change [m yr ⁻¹], from hypsometric average	Robust linear trend of elevation [m yr ⁻¹], from point cloud fit	Number of ICESat samples
Bhutan	-0.36	-0.29	1849
East Nepal	-0.39	-0.36	3990
Hindu Kush	-0.16	-0.24	3442
Inner TP	-0.14	-0.12	11467
Karakoram	-0.07	-0.03	14396
Kunlun	+0.20	+0.21	9543
Nyainqentanglha	-0.60	-0.58	3423
Pamir Alay	0.00	-0.07	920
Pamir	-0.06	-0.03	4260
Spiti-Lahaul	-0.39	-0.39	7579
Tien Shan	-0.23	-0.26	9619
West Nepal	-0.31	-0.30	4330

Table 3.4: Region-wide mass balance for ASTER sub-periods.

	ASTER MB [2000 – 2008] [m w.e. a ⁻¹]	ASTER MB [2008 – 2016] [m w.e. a ⁻¹]
Bhutan	-0.31 ± 0.20	-0.50 ± 0.23
East Nepal	-0.32 ± 0.20	-0.22 ± 0.20
Hindu Kush	-0.14 ± 0.19	-0.05 ± 0.19
Inner TP	-0.01 ± 0.19	-0.24 ± 0.20
Karakoram	-0.06 ± 0.19	0.05 ± 0.19
Kunlun	0.24 ± 0.20	0.05 ± 0.19
Nyainqentanglha	-0.32 ± 0.22	-0.55 ± 0.26
Pamir Alay	-0.07 ± 0.19	-0.03 ± 0.19
Pamir	-0.04 ± 0.19	0.05 ± 0.20
Spiti-Lahaul	-0.49 ± 0.22	-0.11 ± 0.19
Tien Shan	-0.24 ± 0.20	-0.11 ± 0.20
West Nepal	-0.44 ± 0.21	-0.18 ± 0.20
Total	-0.15 ± 0.03	-0.11 ± 0.02

Table 3.5: Summary of the sampled area and percentage of valid data for each sub period.

Region	Total glacierized area [km ²]	Sampled area [km ²]	Percentage of sampled area	Percentage of valid data within the sampled area (2000-2016)	Percentage of valid data within the sampled area (2000-2008)	Percentage of valid data within the sampled area (2008-2016)
Bhutan	2291	1957	85.4	88	76.9	62.2
East Nepal	4776	4708	98.6	89.9	78.6	67.1
Hindu Kush	5147	5008	97.3	89.3	80.5	68
Inner TP	13102	9104	69.5	81.5	61.1	66.1
Karakoram	17734	17734	100.0	81.9	62.2	69.6
Kunlun	9912	9582	96.7	77.5	64.5	59.5
Nyainqentanglha	6378	6052	94.9	75	38.4	51.9
Pamir Alay	7167	7015	97.9	85.4	75.9	73.2
Pamir	1915	1665	86.9	89.1	78.8	54.2
Spiti-Lahaul	7960	7633	95.9	90.7	75.6	72.5
Tien Shan	10802	9832	91.0	87.9	80.8	44.6
West Nepal	4806	4787	99.6	89.4	75.2	61.6
Total	91990	85077	92.5	84.1	68.3	63.2

Table 3.6: Previously published region-wide mass balance estimates for HMA. For ICESat and GRACE based studies we do not provide the areas covered, as they do not correspond directly to the sampled areas.

Region	MB [m w.e. a ⁻¹]	MB [Gt a ⁻¹]		Area [km ²]	Study
Bhutan	-0.42 ± 0.20	-1.0 ± 0.5	2000-2016	2300	This study
	-0.76 ± 0.20	-	2003-2008	-	<i>Kääb et al. (2015)</i>
	-0.22 ± 0.13	-	1999-2010	1380	<i>Gardelle et al. (2013)</i>
East Nepal	-0.33 ± 0.20	-1.6 ± 1.0	2000-2016	4780	This study
	-0.31 ± 0.14	-	2003-2008	-	<i>Kääb et al. (2015)</i>
	-0.26 ± 0.13	-	1999-2011	1460	<i>Gardelle et al. (2013)</i>
	-0.79 ± 0.52	-	2002-2007	50	<i>Bolch et al. (2011)</i>
	-0.40 ± 0.25	-	2000-2008	200	<i>Nuimura et al. (2012)</i>
	-0.52 ± 0.22	-	2000-2016	N/A	<i>King et al. (2017)</i>
Hindu Kush	-0.12 ± 0.07	-0.6 ± 0.4	2000-2016	5150	This study
	-0.42 ± 0.18	-	2003-2008	-	<i>Kääb et al. (2015)</i>
	-0.12 ± 0.16	-	1999-2008	800	<i>Gardelle et al. (2013)</i>
Inner TP	-0.14 ± 0.07	-1.8 ± 0.9	2000-2016	13100	This study
	-0.06 ± 0.06	-	2003-2008	-	This study
	0.02 ± 0.30	-	2003-2008	7240	<i>Neckel et al. (2014)</i>
Karakoram	-0.03 ± 0.07	-0.5 ± 1.2	2000-2016	17700	This study
	-0.09 ± 0.12	-	2003-2008	-	<i>Kääb et al. (2015)</i>
	0.11 ± 0.22	-	1999-2008/2010	10750	<i>Gardelle et al. (2013)</i>
	-0.08 ± 0.12	-	2000-2012	1110	<i>Rankl and Braun (2016)</i>
Kunlun	0.14 ± 0.08	1.4 ± 0.8	2000-2016	9910	This study
	0.18 ± 0.14	-	2003-2008	-	This study
Nyainqentanglha	-0.62 ± 0.23	-4.0 ± 1.5	2000-2016	6380	This study
	-1.14 ± 0.58	-	2003-2008	-	<i>Kääb et al. (2015)</i>
	-0.83 ± 0.57	-	2000-2014	280	<i>Neckel et al. (2017)</i>
Pamir Alay	-0.04 ± 0.07	-0.1 ± 0.1	2000-2016	1910	This study
	-0.59 ± 0.27	-	2003-2008	-	This study
Pamir	-0.08 ± 0.07	-0.6 ± 0.5	2000-2016	7170	This study
	-0.41 ± 0.24	-	2003-2008	-	<i>Kääb et al. (2015)</i>
	0.14 ± 0.13	-	1999-2011	3180	<i>Gardelle et al. (2013)</i>
Spiti Lahaul	-0.37 ± 0.09	-2.9 ± 0.7	2000-2016	7960	This study
	-0.42 ± 0.26	-	2003-2008	-	<i>Kääb et al. (2015)</i>
	-0.45 ± 0.13	-	1999-2011	2110	<i>Gardelle et al. (2013)</i>
	-0.55 ± 0.37	-	2000-2012	1710	<i>Vijay and Braun (2016)</i>
Tien Shan	-0.28 ± 0.30	-3.0 ± 2.2	2000-2016	10800	This study
	-0.37 ± 0.31	-	2003-2008	-	This study
	-0.23 ± 0.19	-	2000-2009	3000	<i>Pieczonka et al. (2013)</i>
	-	-5.4 ± 2.8	2003-2009	13190	<i>(Farinotti et al., 2015)</i>
	-	-3.4 ± 0.8	2003-2009	11400	<i>(Yi et al., 2016)</i>
	-	-4.0 ± 0.7	2003-2014	11400	<i>(Yi et al., 2016)</i>
West Nepal	-0.34 ± 0.09	-1.6 ± 0.4	2000-2016	4810	This study
	-0.37 ± 0.15	-	2003-2008	-	<i>Kääb et al. (2015)</i>
	-0.32 ± 0.13	-	1999-2011	910	<i>Gardelle et al. (2013)</i>

Table 3.7: Region-wide mass balances from ASTER (2000-2016) calculated on RGI inventory and RGI regions (*Pfeffer et al., 2014*).

RGI regions	Region ID	MB ASTER 2000-2016 [m w.e. a ⁻¹]	MB ASTER 2000-2016 [Gt a ⁻¹]
Hissar Alay	13_01	-0.04 ± 0.07	-0.1 ± 0.1
Pamir	13_02	-0.06 ± 0.07	-0.6 ± 0.7
W Tien Shan	13_03	-0.20 ± 0.08	-1.9 ± 0.7
E Tien Shan	13_04	-0.40 ± 0.20	-1.1 ± 0.5
W Kun Lun	13_05	0.16 ± 0.08	1.3 ± 0.6
E Kun Lun	13_06	-0.01 ± 0.07	0.0 ± 0.2
Qilian Shan	13_07	-0.29 ± 0.08	-0.5 ± 0.1
Inner Tibet	13_08	-0.19 ± 0.08	-1.5 ± 0.5
S and E Tibet	13_09	-0.55 ± 0.23	-2.2 ± 0.8
Hindu Kush	14_01	-0.13 ± 0.07	-0.4 ± 0.2
Karakoram	14_02	-0.03 ± 0.07	-0.6 ± 1.7
W Himalaya	14_03	-0.38 ± 0.09	-3.0 ± 0.7
C Himalaya	15_01	-0.28 ± 0.08	-1.5 ± 0.5
E Himalaya	15_02	-0.38 ± 0.20	-1.9 ± 0.9
Hengduan Shan	15_03	-0.56 ± 0.23	-2.5 ± 1.0

Table 3.8: Comparison of region-wide mass balances values obtained by *Gardner et al. (2013)* for 2003-2009 and with ASTER for 2000-2016.

Region ID	MB from <i>Gardner et al. (2013)</i> (2003-2009) [m w.e. a ⁻¹]	MB from ASTER (2000-2016) [m w.e. a ⁻¹]
Pamir Hissar Alay	-0.12 ± 0.24	-0.06 ± 0.07
Tien Shan	-0.52 ± 0.24	-0.25 ± 0.11
W Kun Lun	+0.16 ± 0.18	+0.16 ± 0.08
E Kun Lun and Inner TP	-0.01 ± 0.15	-0.14 ± 0.08
Qilian Shan	-0.29 ± 0.33	-0.29 ± 0.08
S and E Tibet	-0.27 ± 0.16	-0.55 ± 0.23
Karakoram and Hindu Kush	-0.10 ± 0.18	-0.04 ± 0.07
W Himalaya	-0.48 ± 0.17	-0.38 ± 0.09
C Himalaya	-0.40 ± 0.23	-0.28 ± 0.08
E Himalaya	-0.80 ± 0.22	-0.38 ± 0.20
Hengduan Shan	-0.36 ± 0.43	-0.56 ± 0.23

3.7.3 Supplementary figures

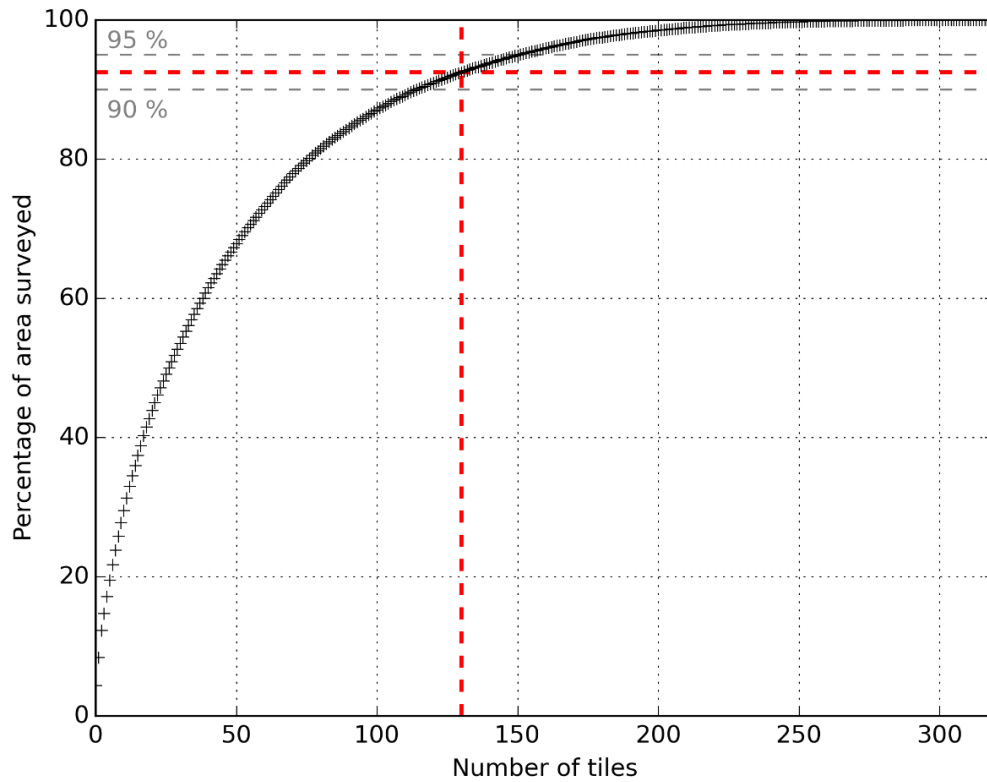


Figure 3.5: Cumulative distribution of glacierized area as a function of the number of tiles considered (sorted in descending order). For the 130 most glacierized tiles, we reach a total percentage of 92 % (red dashed lines).

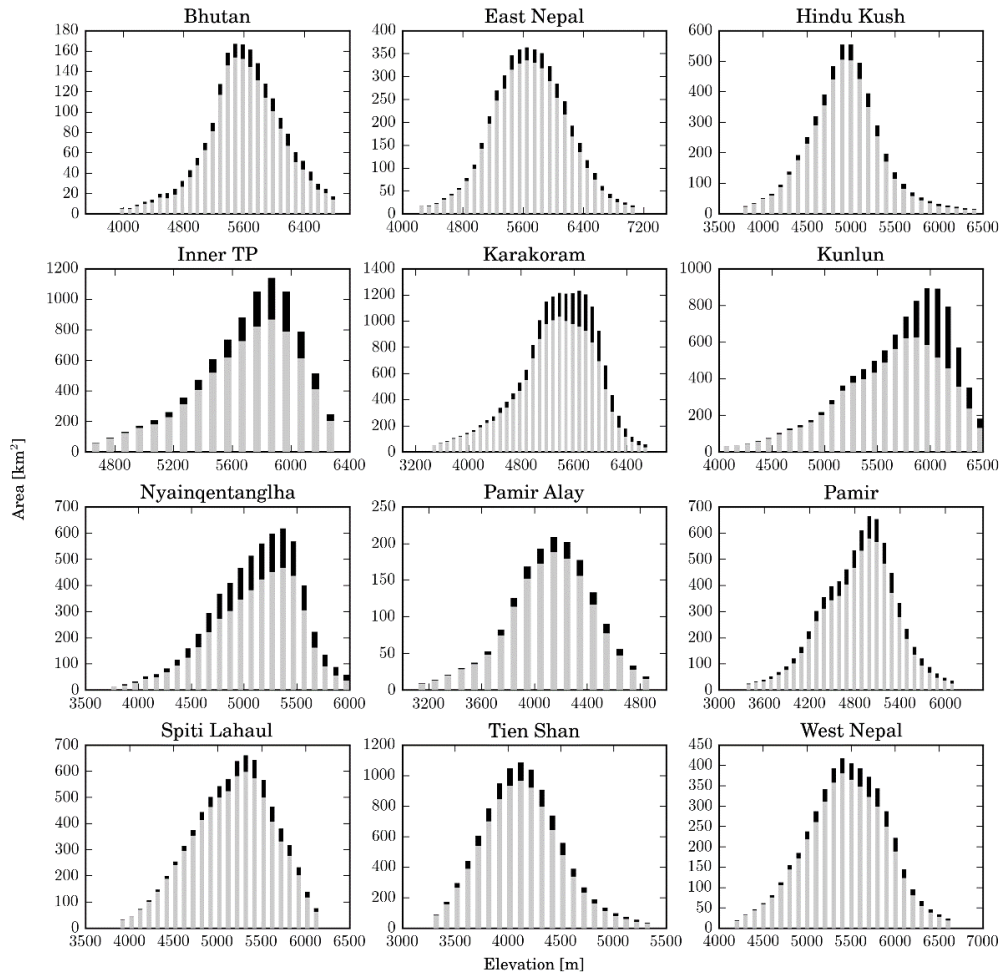


Figure 3.6: Hypsometry of the 12 surveyed regions. The black bars represent the total area and the grey superimposed bars the area for which data considered as valid were obtained from ASTER DEMs for the period 2000-2016.

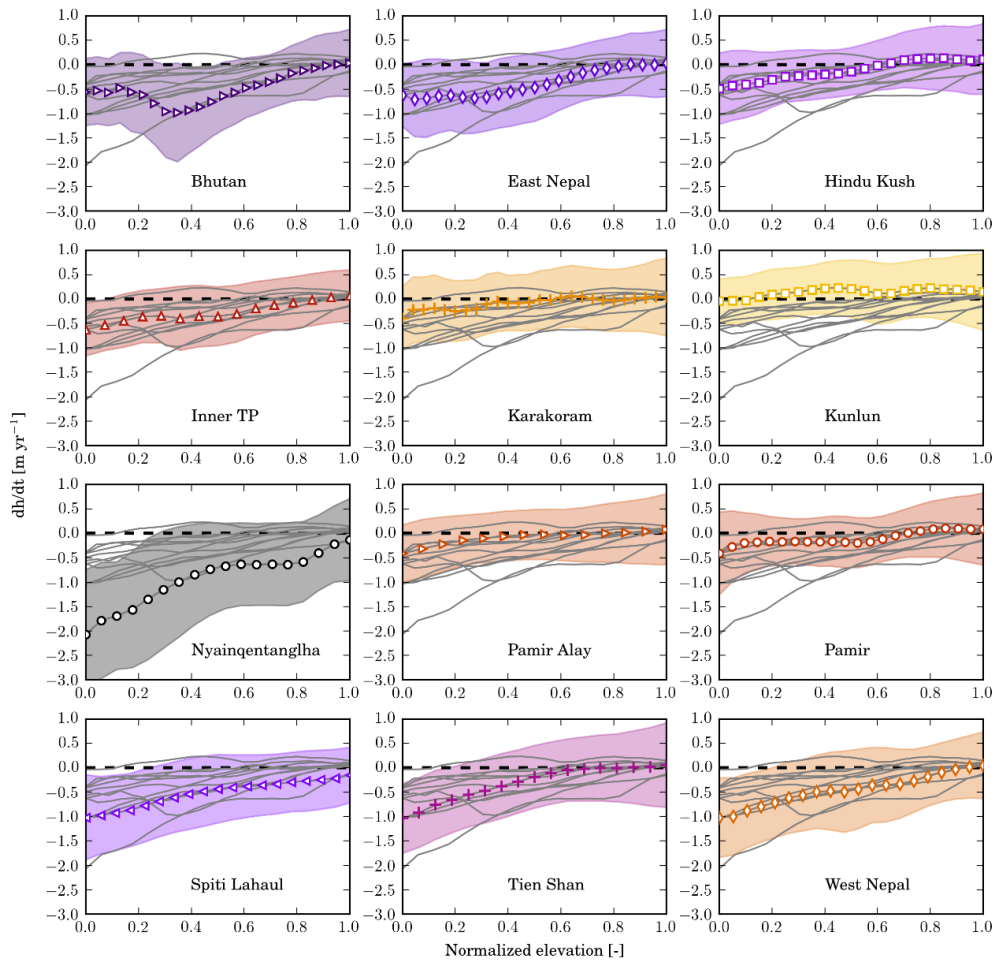


Figure 3.7: Rate of elevation change as a function of normalized elevation. For each panel, the shaded area represents the mean of rate of elevation change ± 1 NMAD. The grey curves represent the other regions, for comparison.

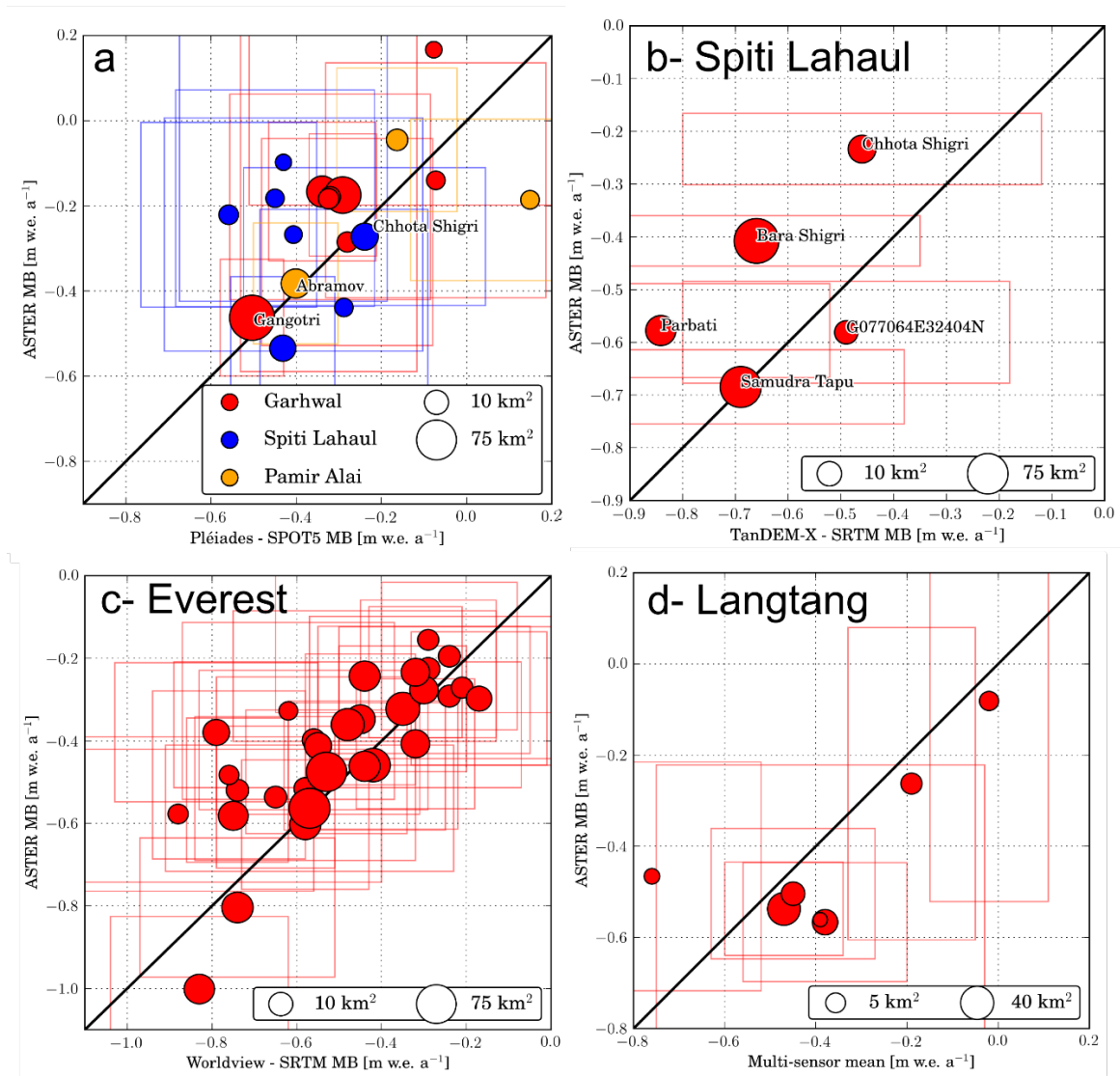


Figure 3.8: Glacier-wide estimates from ASTER method versus estimates for the same glaciers using multiple Pléiades - SPOT5 DEM differences (a), TanDEM-X – SRTM differences (b- the mass balance estimates and uncertainties come from *Vijay and Braun (2016)*), Worldview – SRTM differences (c- the mass balance estimates and uncertainties come from *King et al. (2017)*), multiple sensor elevation difference (d- the mass balance estimates and uncertainties come from *Ragetti et al. (2016b)*). The thick line is the 1:1 line. The rectangles represent the error bars associated with the two methods. The location of these validation sites are shown by yellow triangles in Figure 3.2.

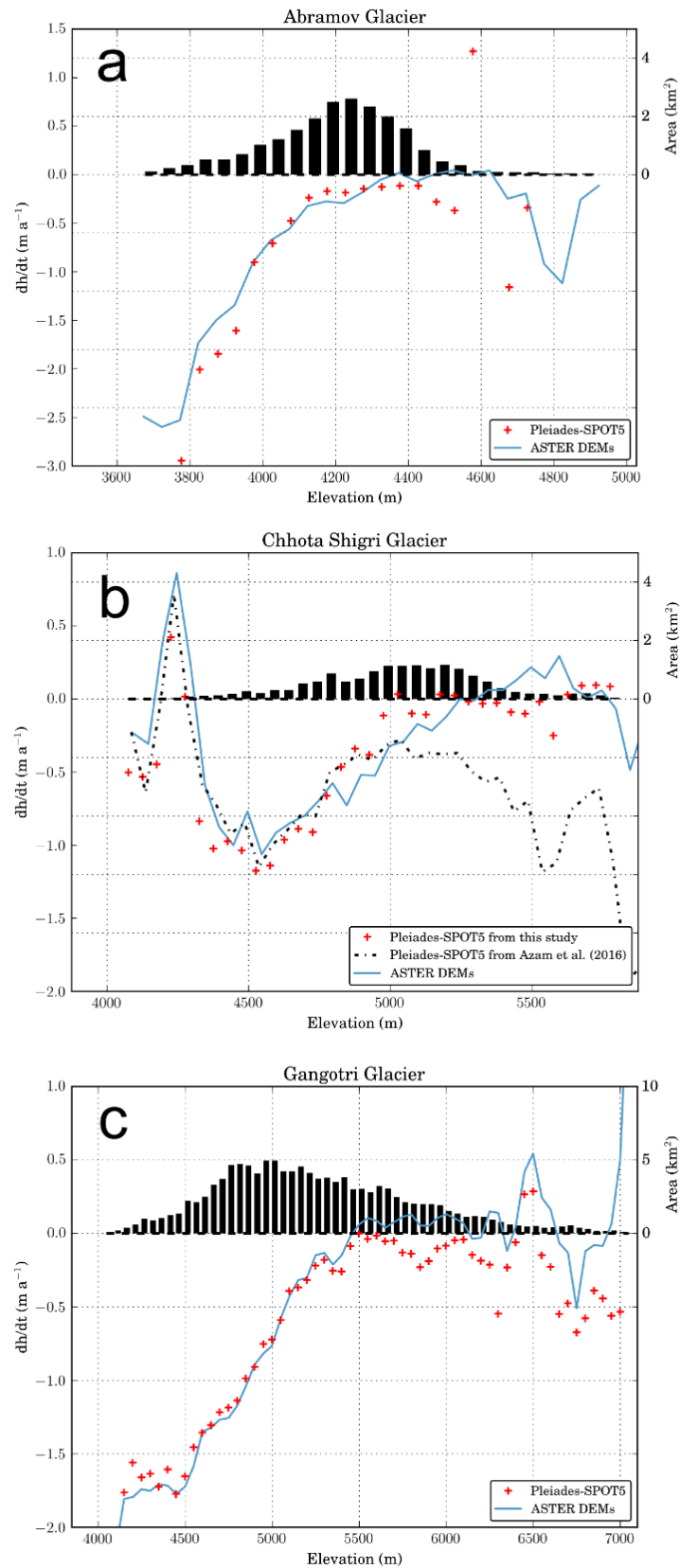


Figure 3.9: Rate of elevation change for a- Abramov Glacier (Pamir Alay) derived from a Pléiades - SPOT 5 difference (images acquired in Aug. 2003 and Sept. 2015), b- Chhota Shigri Glacier (Spiti Lahaul) derived from a Pléiades - SPOT 5 difference (images acquired in Sept. 2005 and Sept. 2014), c- Gangotri Glacier (Garhwal) derived from a Pléiades - SPOT 5 difference (images acquired in Nov. 2004 and Aug. 2014) and from ASTER DEMs for the same periods.

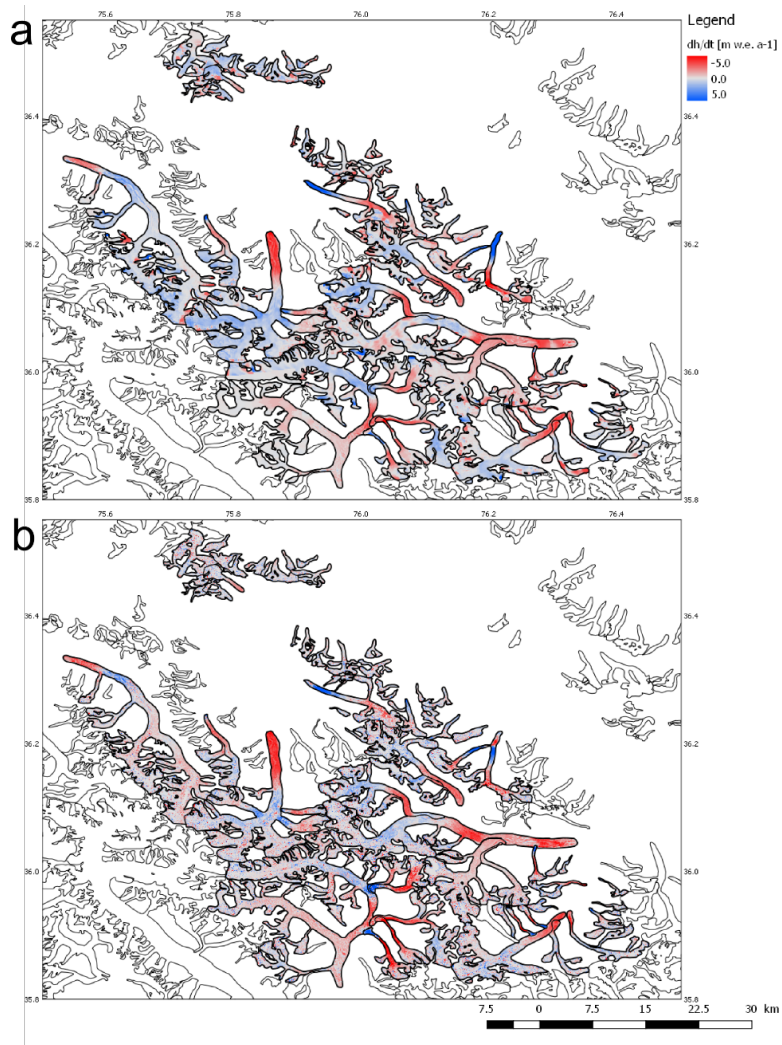


Figure 3.10: Map of elevation change [m yr⁻¹] for the period 2000-2012 over central Karakoram from Rankl and Braun (2016) (a) and from this study (b).

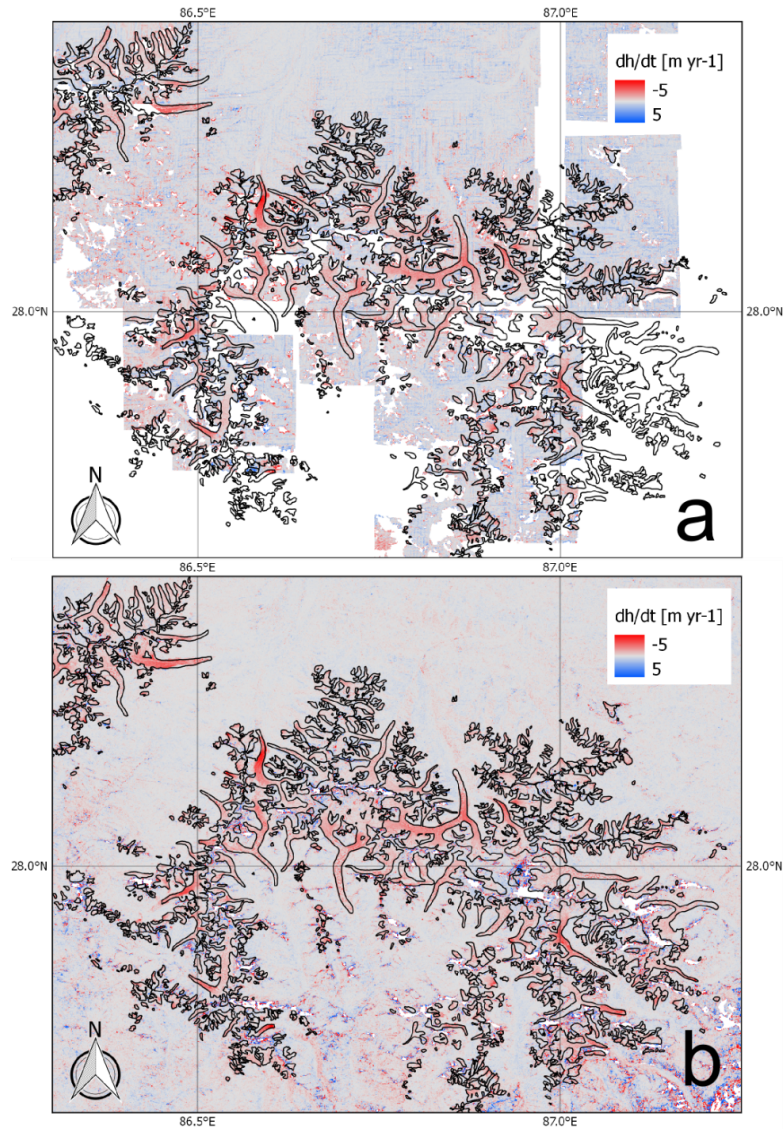


Figure 3.11: Map of elevation change [$m a^{-1}$] for the period 2000-2016 over a subset of Everest region from *King et al.* (2017) (a) and from this study (b).

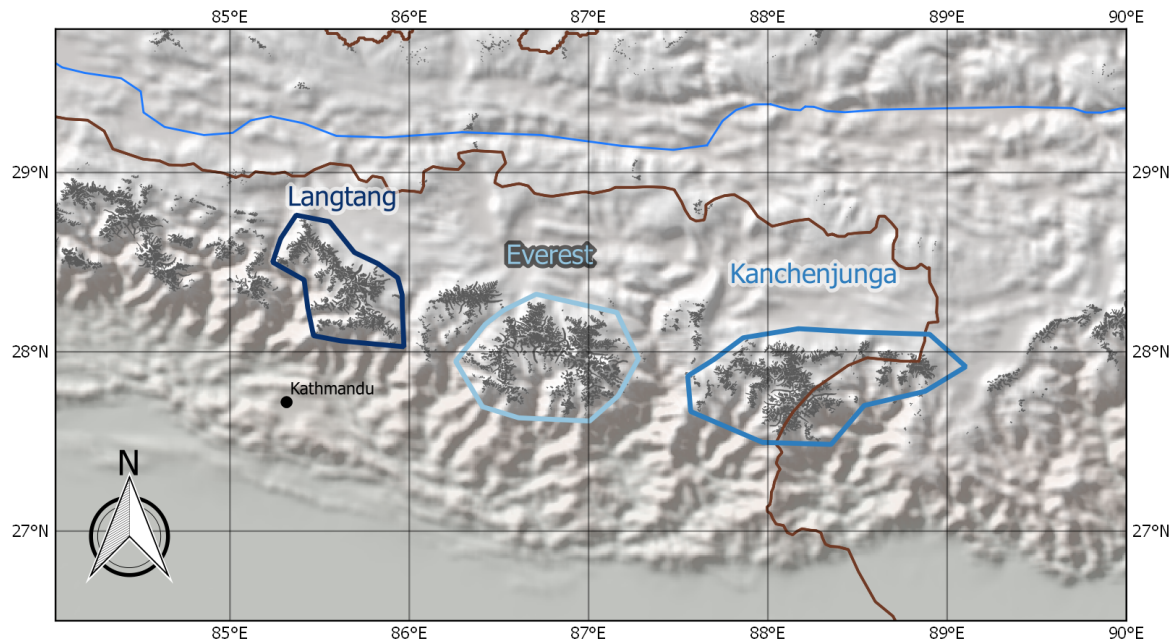


Figure 3.12: Location of the three sub-regional studies discussed in the section “Spatial variability of individual glacier mass balances”.

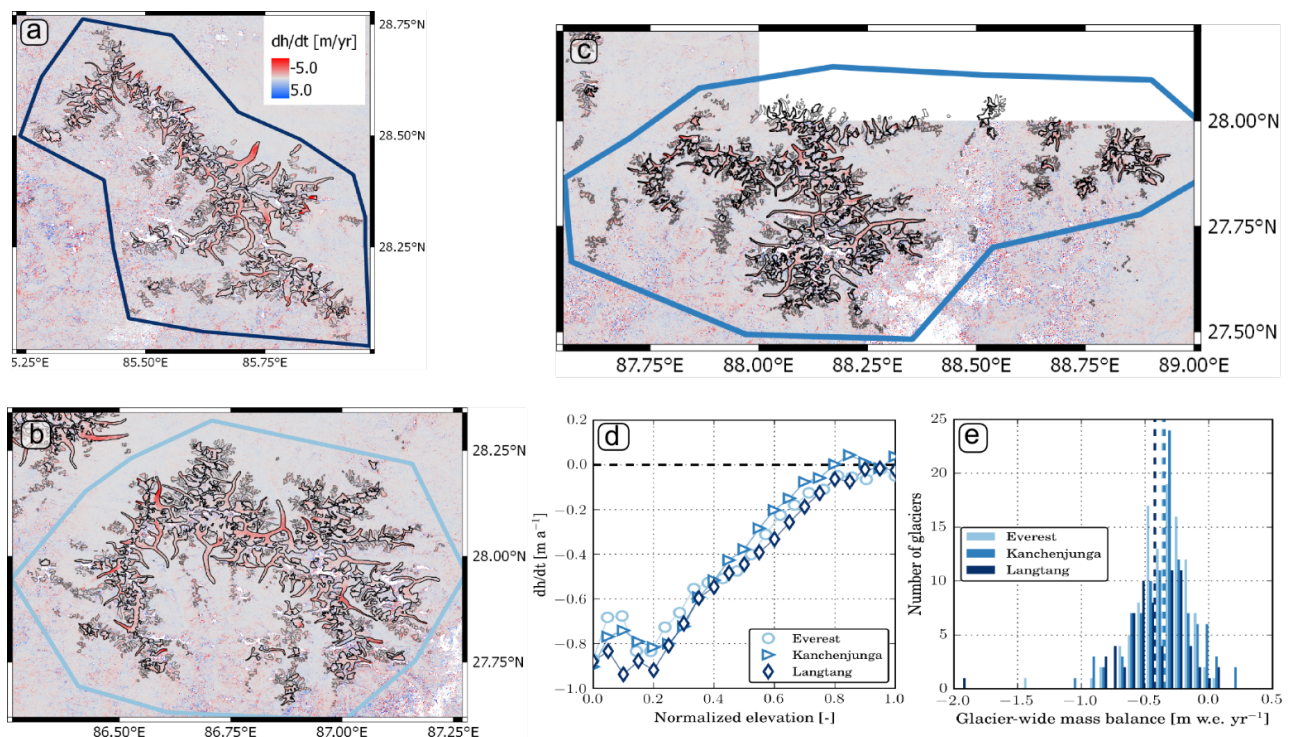


Figure 3.13: a, b, c- maps of rate of elevation change for Langtang, Everest, and Kanchenjunga, respectively. d- altitudinal distribution of thickness changes for the three sub-regions defined in Fig. 3.12 ; e- distribution of glacier-wide mass balances for individual glaciers larger than $2 km^2$ and for which more than 70 % of the surface is classified as good data. The vertical dashed lines represent the sub-region-wide mass balances.

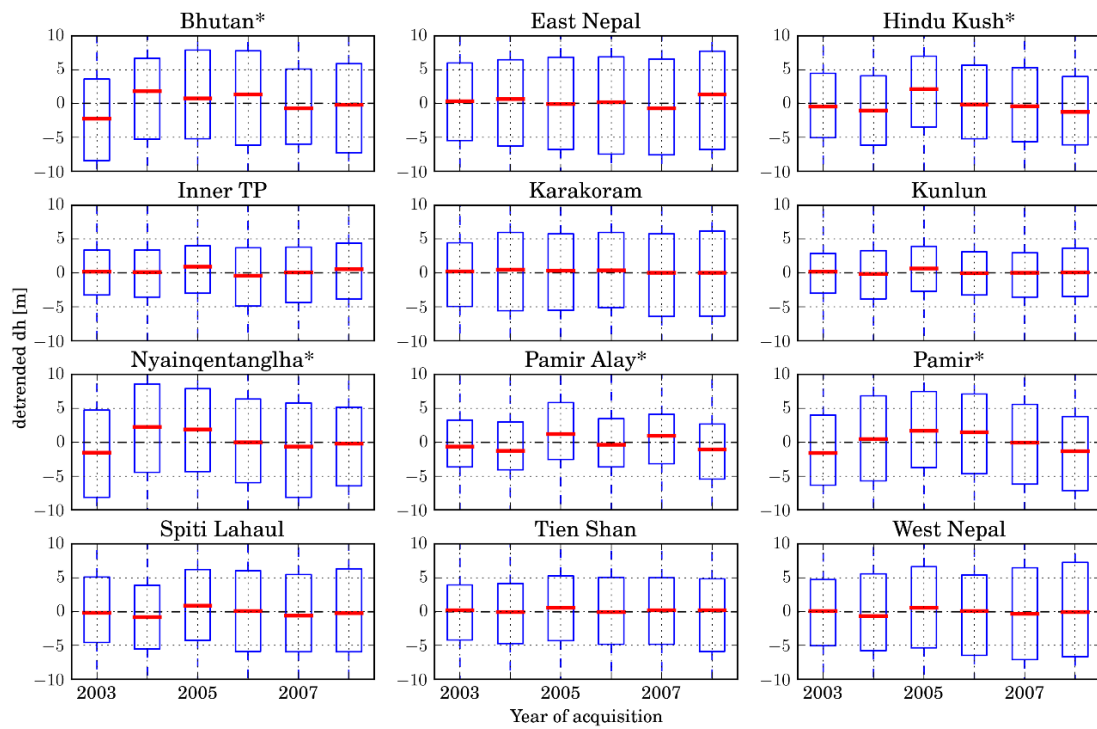


Figure 3.14: Boxplots of the detrended ICESat dh (ICESat elevation – SRTM) grouped by year of acquisition. The controversial regions are marked with an asterisk.

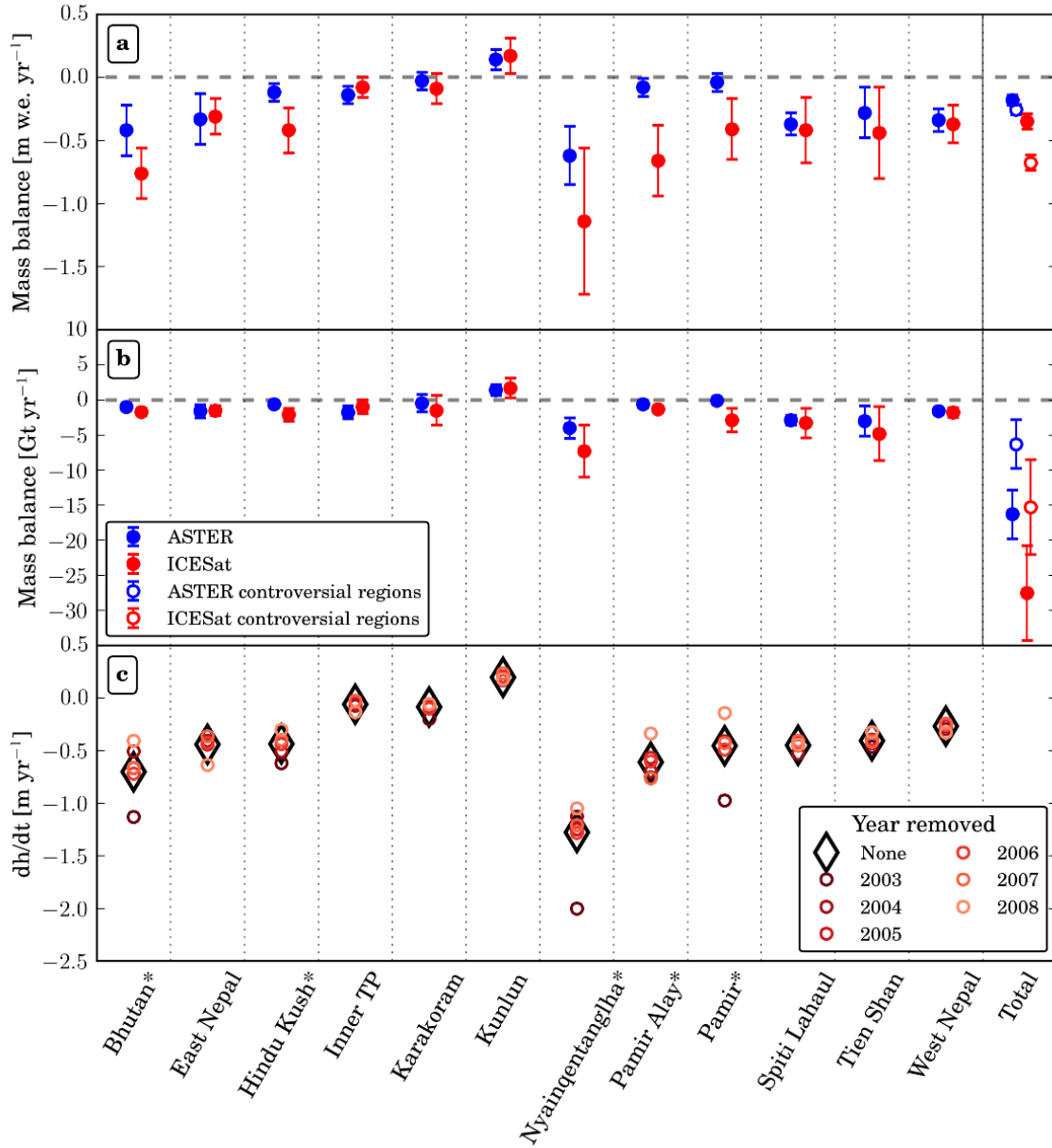


Figure 3.15: a- Region-wide specific mass balance (in m w.e. a⁻¹) for each region; b- Region-wide mass balance (in Gt a⁻¹) for each region; c- Results of the bootstrap test for each region. For a given region, the solid diamond represents the robust temporal fit through all ICESat dh (i.e. Elevation ICESat – SRTM) data and each of the colored circle represents the robust temporal fit of the ICESat dh excluding one year of acquisition. The controversial regions are marked with an asterisk.

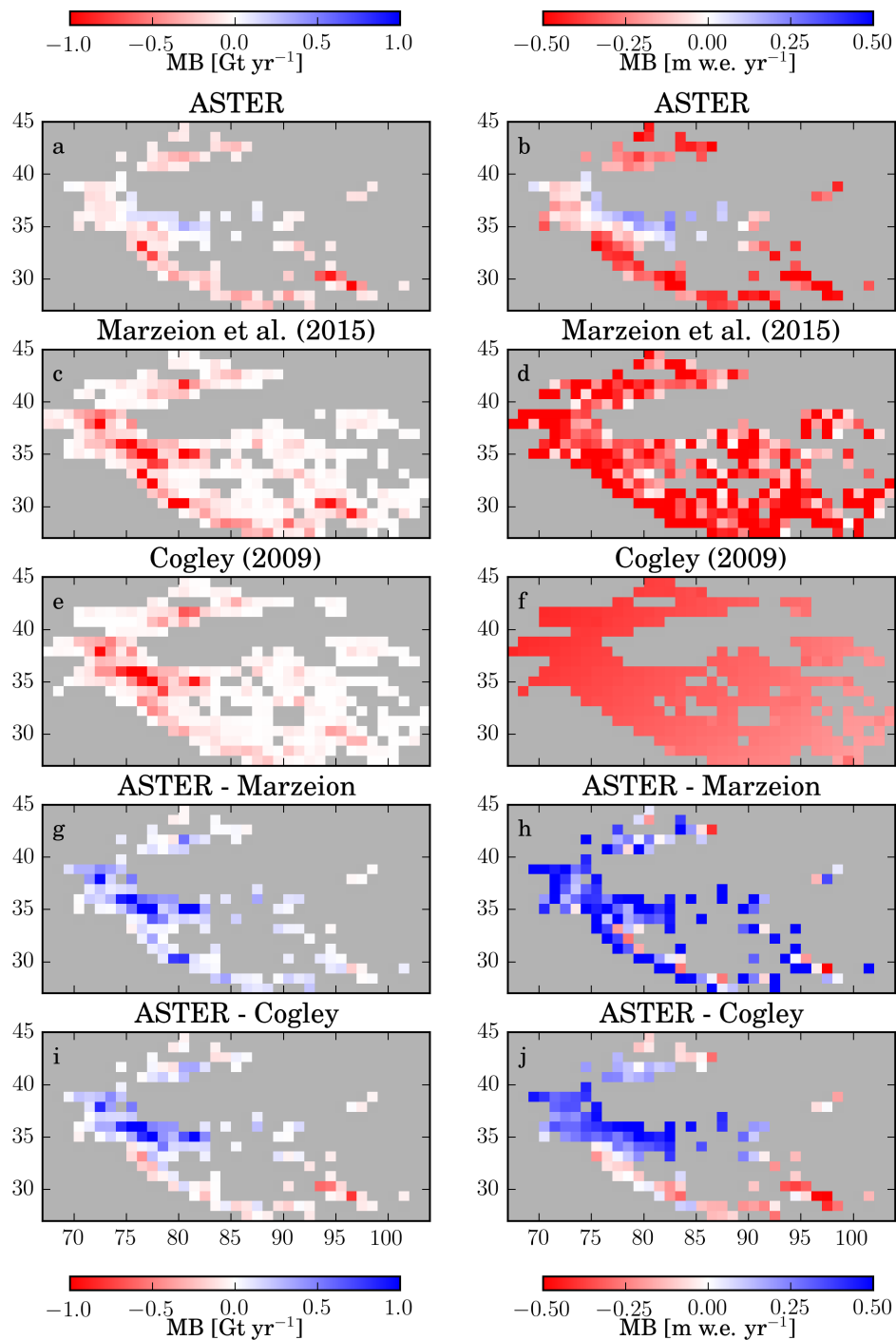


Figure 3.16: Mass balance in Gt a^{-1} (a, c, e, g, i) and in m w.e. a^{-1} (b, d, f, h, j) on a $1^\circ \times 1^\circ$ grid. Mass balance estimates are obtained from ASTER trends (a, b, this study), numerical modelling (c, d, *Marzeion et al. (2015)*) and interpolation (e, f, *Cogley (2009)*). g, h, i and j shows grid based comparisons of the different datasets.

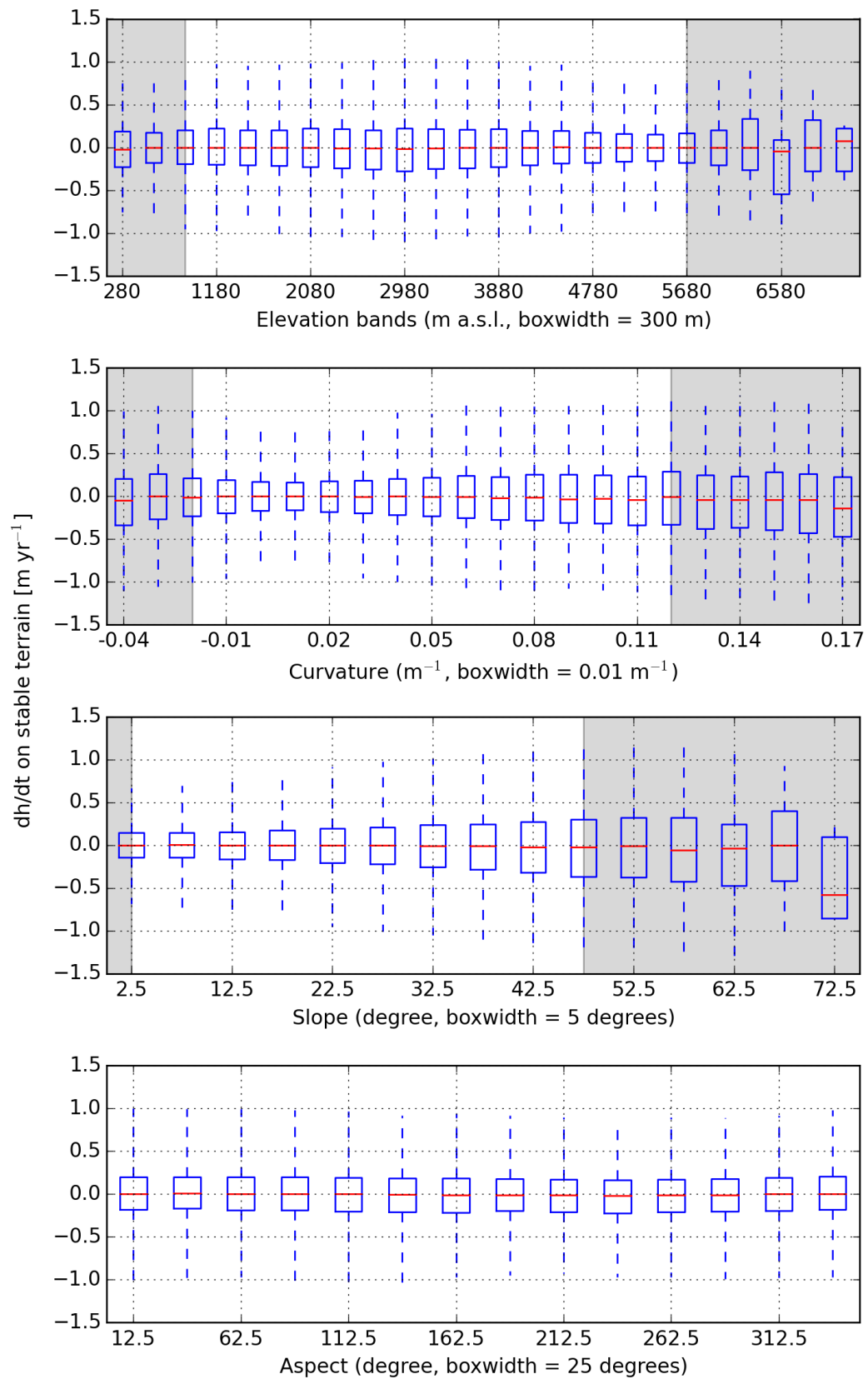


Figure 3.17: Rate of elevation change ($m\ a^{-1}$) on stable terrain for 132 000 randomly chosen points.

3.8 Going one step further

3.8.1 Towards an evaluation of the magnitude of the SRTM-C band penetration for the entire HMA?

This section is based on work in progress, which was presented at EGU 2018 in the session "Glacier Monitoring from In-situ and Remotely Sensed Observations".

The global SRTM-C band DEM is known to have a negative elevation bias over snow covered and glacierized areas (e.g., *Berthier et al.*, 2006, box 2.5). Currently, the penetration depth of the SRTM-C band signal into snow and ice is evaluated based on two main methods in HMA:

X-band method The X-band radar signal (9.65 GHz) penetrates less than the C-band radar signal (5.3 GHz) into snow and ice. Consequently, assuming a negligible penetration of the X-band signal, the difference between SRTM-C band DEM and SRTM-X band DEM gives an estimate of the SRTM-C band penetration (*Gardelle et al.*, 2012a). Then the elevation difference is aggregated by elevation band, which gives an estimate of the penetration as a function of elevation for a given region.

Extrapolation of ICESat trend The glacier thickness changes with ICESat are calculated by fitting linear temporal trends through dh values of a region, where dh are individual elevation differences between ICESat and SRTM. The difference between SRTM elevation and the elevation obtained by extrapolating the linear relationship of ICESat values (acquired during the 2003-2008 period) to the acquisition date of SRTM (February 2000) gives an estimate of SRTM penetration (*Kääb et al.*, 2012).

None of these methods is completely satisfying. The X-band method underestimates the penetration, as the X-band signal penetrates as well. Moreover, the SRTM-X band DEMs were not acquired everywhere. The ICESat method linearly extrapolates back in time 6-year trends of thickness changes to February 2000 (i.e., three years earlier than the first acquisition). The extrapolated value of SRTM elevation is thus poorly constrained and very sensitive to small changes or noise during the ICESat period. This method provides only region-wide averages. The results of these methods are summarized in Table 3.9.

Table 3.9: Existing SRTM-C penetration estimates in m, provided as hypsometric averages over the glacierized area. The estimates marked with an asterisk are from *Kääb et al.* (2015).

Sub-region	<i>Gardelle et al.</i> (2013)	<i>Kääb et al.</i> (2012)
Hengduan Shan/Nyainqentanglha	1.7	10*
Bhutan	2.4	6*
Everest	1.4	2.5 ± 0.5
West Nepal	N/A	1.5 ± 0.4
Spiti Lahaul	N/A	
Hindu Kush	N/A	2.4 ± 0.4
Karakoram	3.4	2.4 ± 0.3
Pamir	1.8	5-6*

Methods

Similarly to the ICESat data, ASTER rates of elevation changes can also be extrapolated back in time at the date of SRTM acquisition (*Wang and Kääb, 2015; Berthier et al., 2016; Dussailant et al., 2018*). The extrapolated trends are calculated pixel by pixel and are called the reconstructed SRTM, which is a raster with dimensions similar to the SRTM. The estimate of the penetration is obtained by subtracting the SRTM from the reconstructed SRTM.

The uncertainty on these estimates are high and not easy to assess. The best estimate is probably a ± 3 m for the ASTER penetration averaged over the glacierized area (*Berthier et al., 2016*).

In the following sections, we compare ASTER estimates with SPOT5-SRTM estimates (*Gardelle et al., 2013*). We work on the extent of *Gardelle et al. (2013)*, with the RGI 5.0. Despite temporal inconsistencies, we assume that the main source of difference in terms of rate of elevation changes (dh/dt) is the SRTM penetration. We focused specifically on two regions, Nyainqentanglha and Pamir, as these are regions where the previous estimates were in marked disagreement (*Kääb et al., 2015*). In particular, *Kääb et al. (2015)* suggested SRTM penetration estimates more than three times larger than the estimates of *Gardelle et al. (2013)*, in order to reconcile the geodetic mass balances.

Eastern Nyainqentanglha

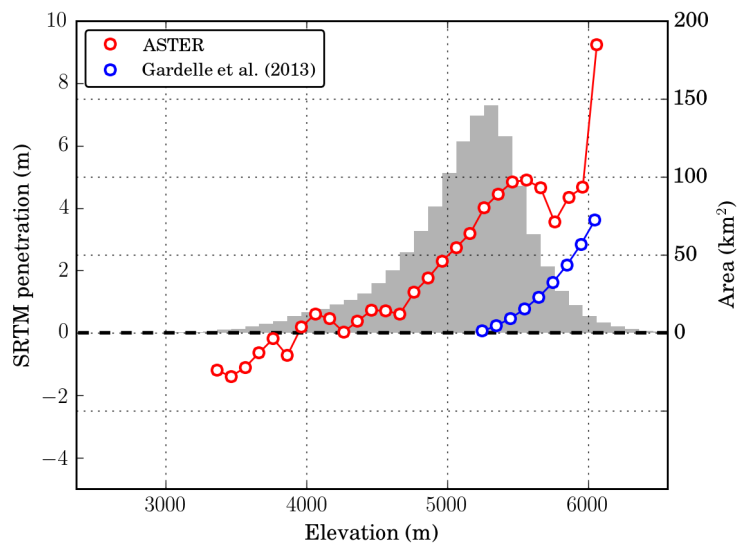


Figure 3.18: Estimates of SRTM penetration as a function of elevation from *Gardelle et al. (2013)* (blue curve) and ASTER extrapolation (red curve) for a sub-region of Nyainqentanglha. The shaded histogram represents the glacier hypsometry. The apparent negative penetration discussed in the text has almost no influence in this region as it concerns a very limited glacierized area.

In the sub-region studied in *Gardelle et al. (2013)*, the ASTER method gives a larger SRTM penetration estimate than the X-band method (Figure 3.18 and Table 3.10). The mean glacier penetration is 2.5 m, which is roughly twice as large as the X-band estimate. If we apply the ASTER correction to the SPOT5-SRTM estimate, the region-wide mass balances are in closer agreement with -0.38 ± 0.14 m w.e. a^{-1} for the SPOT5-SRTM estimate (instead of -0.29 ± 0.14 m w.e. a^{-1}) and -0.43 ± 0.23 m w.e. a^{-1} for the ASTER estimate.

It is likely that the 10 m of penetration estimated by *Kääb et al. (2015)*, is an overestimation of the actual penetration, due to an ICESat dh/dt trend that is far too negative (section 3.7).

Central Pamir

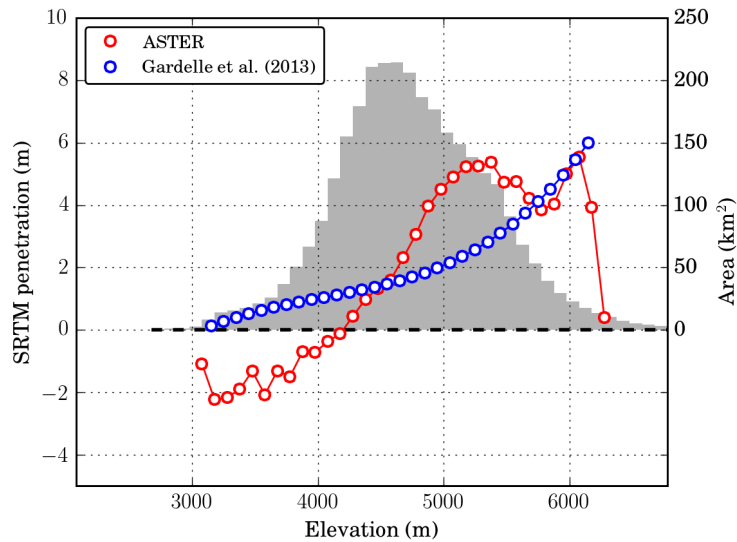


Figure 3.19: Estimates of SRTM penetration as a function of elevation from *Gardelle et al. (2013)* (blue curve) and ASTER extrapolation (red curve) for a sub-region of central Pamir. The shaded histogram represents the glacier hypsometry.

For the central Pamir, we obtain an apparent negative penetration with ASTER extrapolation (Figure 3.19). For the lower most part of the glacierized area, the extrapolation of ASTER trends resulted in a DEM with lower elevation than the SRTM. How can we explain such a negative apparent penetration? We have two main hypothesis: 1- the ASTER DEMs are acquired mainly in summer/fall, because of the frequent cloud cover in winter in this region; 2- there was probably a thick, and potentially wet, layer of snow in Pamir in February 2000, and consequently the surface reconstructed by ASTER could be lower than the surface seen by SRTM. This interpretation is supported by the large amplitude of seasonal glacier elevation fluctuations observed in this region (*Wang et al., 2017*). In order to test these hypothesis and to provide realistic uncertainty assessments on the penetration estimates, we plan to perform the following experiments:

- carefully find the ASTER DEMs that were acquired around February 2000, (almost) simultaneously with the SRTM (if they exist) for a direct comparison
- extrapolate the ASTER trends only from DEMs acquired between January and March
- use a WorldView DEM acquired around 2015 in winter (January to March) as a reference surface and apply the ASTER linear trend to evaluate the surface elevation in February 2000. This would provide an independent estimate of the penetration and thus help to quantify the uncertainty.

As I haven't done this work yet, I apply a very simple "seasonal correction", that consists in adding 2 m to the penetration, which represents the maximum of observed negative penetration, in order to have positive values of penetration only. This probably leads to an overestimation of the total penetration, if this problem of negative penetration is due to the

presence of wet snow, which is not present at higher elevations. The mean penetration on glaciers estimated by ASTER is 2.0 m without the seasonal correction and 4.0 m with the seasonal correction.

Table 3.10: Hypsometric averages of the SRTM penetration (mean glacier SRTM penetration) and their influence of the region-wide mass balance. The number in parenthesis beneath the SRTM penetration values from ASTER are the ASTER estimates plus the seasonal correction (see text). Case 1 corresponds to the SPOT5-SRTM estimates corrected with the X-band correction (*Gardelle et al., 2013*), case 2 corresponds to the SPOT5-SRTM estimates corrected with the ASTER correction (in parenthesis, when accounting for the seasonal correction) and case 3 corresponds to the ASTER mass balance estimates.

	SRTM penetration (m)		Mass balance (m w.e. a ⁻¹)		
	ASTER	<i>Gardelle et al. (2013)</i>	Case 1	Case 2	Case 3
Nyainqentanglha	2.5 (2.5)	1.7	-0.29 ± 0.14	-0.38 ± 0.14 (-0.38 ± 0.14)	-0.43 ± 0.23
Pamir	2.0 (4.0)	1.8	0.14 ± 0.14	0.12 ± 0.14 (-0.08 ± 0.14)	-0.07 ± 0.07

From ICESat, the penetration was estimated at 5-6 m for the Pamir (*Kääb et al., 2015*). This estimate is in relatively good agreement with the upper bound of the ASTER estimate (with seasonal correction). Moreover, the ICESat dh/dt trend is more negative than the ASTER trend for Pamir, and consequently the ICESat penetration estimate is probably too high.

The SPOT5-SRTM mass balance corrected with the ASTER penetration correction without the seasonal correction is very close to the original mass balance from *Gardelle et al. (2013)*, with 0.12 ± 0.14 m w.e. a⁻¹ versus 0.14 ± 0.14 . The SPOT5-SRTM mass balance corrected with ASTER penetration correction and the seasonal correction is -0.08 ± 0.14 , which is almost equal to the ASTER mass balance of -0.07 ± 0.07 (Table 3.10).

Application to the entire HMA?

The extrapolation of ASTER trends to estimate the biases in the SRTM-C DEM over glaciated areas is similar to the method of *Kääb et al. (2012)* developed for ICESat, but is extrapolated over shorter time, as the first ASTER images became available in spring 2000. Most of the geodetic studies about HMA glacier mass changes for the periods 1970s-2000 and 2000-2010s relied on the SRTM DEM. Consequently, regional estimates of the SRTM penetration are needed to re-evaluate these studies. These estimates cannot be based on ASTER trend extrapolation only because this method has a high uncertainty and is empirical. It should therefore be complemented with estimates based on firn modeling and/or interpretation of the SRTM backscatter signal intensity, which can be a good proxy for the presence of liquid water.

3.8.2 Glacier contribution to streamflow: balance versus imbalance contributions

The glacier seasonal delay can be calculated as the sum of the monthly differences between ablation and precipitation divided by the annual precipitation on glacier (*Kaser et al., 2010*).

According to this definition, the seasonal delay is a scalar between 0 and 1, 0 corresponding to a glacier which accumulates and melts exactly at the same time and 1 corresponding to a glacier which has totally distinct accumulation and ablation seasons. It is noteworthy that this definition includes the seasonal snow on glacier (and even on the non glacierized area of the catchments that are above the glacier terminus) and consequently it would still be non zero in absence of the glacier. In HMA, glaciers located in the monsoon influenced regions have a low seasonal delay, ranging from 0.17 to 0.33, whereas regions dominated by the westerlies have higher values, up to 0.79 for the Aral Sea (Table 3.11, values from *Kaser et al.*, 2010). This means that the river flow fluctuations in the latter regions (at least in the upper reaches of the catchments) are less prone to be influenced by year to year precipitation fluctuations, as the discharge is sustained by glacier melt during the dry season for catchments with a high seasonal delay. Conversely, in regions with a low seasonal delay the glaciers do not melt during the dry months and therefore do not provide the same service to the population living downstream. This seasonally delayed runoff can also be called glacier balance contribution to streamflow (*Pritchard*, 2017).

It is also possible to calculate the contribution to runoff from the long term change in the glacier storage. This is named the excess discharge (*Radić and Hock*, 2014) or the glacier imbalance contribution (*Pritchard*, 2017). The seasonality of the imbalance contribution is not clear, as it is a multi-annual average value. The special cases of glaciers with positive mass balance is counter intuitive, because the glacier cannot "pump" the water from the rivers, consequently it was suggested to set this contribution to 0, when it is negative (*Radić and Hock*, 2014).

The glacier imbalance contribution is larger than the balance contribution for the basins strongly influenced by the monsoon (Brahmaputra, Ganges, Salween and Yangtze) and lower for the Aral Sea basin, which has a strong seasonality. The contributions are of similar magnitude for the Indus basin. They are not comparable for the Tarim basin, because the glaciers are gaining mass (Table 3.11). These results are not directly comparable with those of *Huss et al.* (2017), as the latter included the snow water equivalent (SWE) in their quantification, which is the dominant term for most of the basins (often one or two orders of magnitude larger than the glacier imbalance contribution). Moreover, they did not include the glacier seasonal delay in their analysis, which should be negligible in front of the SWE, at least on the annual scale. Note that the glacier seasonal delay could be dominant at the monthly scale for some dry and winter type accumulation catchments (*Huss et al.*, 2017).

3.8.3 Spatially resolved geodetic observations, new data to calibrate and/or validate global glacier models

Global glacier models aim at answering a wide range of questions related to the climate-glacier relationship and the future of glaciers. This wide range of applications led to significant advances, such as the quantification of the anthropogenic contribution to recent glacier mass losses (*Marzeion et al.*, 2014), of the committed glacier mass losses (*Marzeion et al.*, 2018), of the glacier contribution to SLR under different climate scenarios (e.g., *Radić and Hock*, 2014) or of future glacier contribution to streamflow changes (*Huss and Hock*, 2018). However, there is still room for substantial improvements in the representation of glaciological processes and about the calibration strategy.

Global glacier models are relatively recent tools, as their performances were hampered by the lack of complete glacier inventories before 2012 (*Pfeffer et al.*, 2014). By necessity, global

Table 3.11: Glacier contribution to streamflow. The basin area, mean basin precipitation, mean glacier precipitation and seasonal delay are taken from *Kaser et al. (2010)*. The seasonal delay is defined as the sum of the monthly differences between the ablation and precipitation on glaciers divided by the annual precipitation on glaciers. The glacier area and imbalance contributions are from *Brun et al. (2017)*. The glacier balance contribution is re-calculated from the mean glacier precipitation, the seasonal delay and the glacier area.

Basin	Basin area [km ²]	Glacier area [km ²]	Mean basin precipitation [mm yr ⁻¹]	Mean glacier precipitation [mm yr ⁻¹]	Seasonal delay	Glacier balance contrib. [m ³ s ⁻¹]	Glacier imbalance contrib. [m ³ s ⁻¹]
Aral Sea	1234075	13120	309	657	0.79	216	41
Brahmaputra	527666	9513	1145	382	0.17	20	163
Ganges	1023609	8314	1118	349	0.33	30	84
Indus	1139814	24698	405	304	0.55	131	125
Salween	410376	1195	1775	797	0.25	8	24
Tarim	1053180	18409	87	129	0.38	29	-12
Yangtze	1746593	1422	1062	592	0.33	9	14

glacier models are very crude representations of the glaciological processes (e.g., *Radić and Hock, 2006; Marzeion et al., 2012; Huss and Hock, 2015*). Very few of them include frontal ablation at tide-water glacier terminus (with the exception of *Huss and Hock, 2015*) or melt beneath supraglacial debris. Glacier models need to include ice dynamics in order to simulate glacier geometry changes. The state-of-the-art option would be to solve for the ice flow equations using a finite element model, such as Elmer/Ice model (*Gagliardini et al., 2013*). Nevertheless, this solution is computationally too demanding at the moment and the technical issues related to the lack of constraints on the glacier bed geometry prevent the implementation of such models at the moment. Models including simplified, but physically-based, ice dynamics are promising alternative (*Clarke et al., 2015; Maussion et al., 2018*). Otherwise, most of the current models rely on a parametrized glacier geometry change, known as the Δh -parametrization (*Huss et al., 2010*) or through empirical area-volume scaling (*Bahr et al., 2015*).

The calibration strategies are different for each model. Some of them rely only on field measured point mass balances (*Radić and Hock, 2014*), whereas other rely on regional glacier mass balance geodetic estimates (*Huss and Hock, 2015*) or on the glacier geometry (*Marzeion et al., 2012*). All of these calibration strategies have some drawbacks. For instance, the calibration on field measured mass balances is a good strategy where the glacier measurements are numerous, but does not work where the measurements are sparse. The calibration on geodetic mass balances is possible globally, but it relies on the poorly spatially resolved estimates of *Gardner et al. (2013)*. The geometric calibration of *Marzeion et al. (2015)* could explain part of the discrepancies between the model outputs and the geodetic estimate for the 2000-2016 period (for the entire HMA, the model outputs were roughly three times as negative as the geodetic mass balance with -45 Gt yr^{-1} versus -16 Gt yr^{-1} , section 3.7).

An alternative calibration strategy could consist in calibrating individually the glaciers on their individual geodetic mass balances derived in this study (or on homogeneous groups of glaciers in order to reduce the geodetic estimate uncertainty). Obviously the model could not be validated with these geodetic observations, but it could be validated against past moraine extents or against geodetic estimates for the 1970s-2000 period, which are now

available in multiple regions of the world, and in particular in HMA (section 2.3).

Non ubiquitous influence of debris cover and proglacial lakes on the variability of the High Mountain Asia glacier mass balances

Contents

4.1	A short introduction	81
4.2	Abstract	82
4.3	Introduction	83
4.4	Data and methods	84
4.4.1	Glacier-wide mass balance and morphological data	84
4.4.2	Debris-covered glaciers and debris-free glaciers	87
4.4.3	Lake-terminating and land-terminating glaciers	87
4.4.4	Multivariate linear model	87
4.5	Results	88
4.5.1	Contrasted glacier morphologies in the different regions	88
4.5.2	Morphological variables and glacier-wide mass balance	88
4.5.3	No systematic difference between debris-covered and debris-free glaciers in terms of glacier-wide mass balance	89
4.5.4	Influence of proglacial lakes on glacier-wide mass balance	91
4.6	Discussion	91
4.6.1	Complex influence of the morphological variables and debris-cover on the glacier-wide mass balance	91
4.6.2	Specificities of debris-covered glaciers	93
4.6.3	Proglacial lake influence on glacier mass balance	93
4.6.4	Limitations of our analysis	93
4.7	Conclusion	94
4.8	Supplementary methods	94
4.9	Going one step further	96

This chapter is written after an article submitted to the *Journal of Geophysical Research: Earth Surface*:

Brun, F., P. Wagnon, E. Berthier, V. Jomelli, S. B. Maharjan, F. Shrestha, and P. Kraaijenbrink (2018a), Non ubiquitous influence of debris cover and proglacial lakes on the variability of the High Mountain Asia glacier mass balances, *in review at Journal of Geophysical Research: Earth Surface*

4.1 A short introduction

Individual glacier mass balances for the period 2000-2016 and glacier surface classifications became available almost simultaneously, from the work presented in the previous chapter (Brun *et al.*, 2017) and from the study of Kraaijenbrink *et al.* (2017). Consequently, it created the opportunity to address the following research question: are the debris-covered glaciers different from the debris-free glaciers in terms of glacier-wide mass balance? Despite its apparent simplicity, this question raised other tricky issues such as:

1. How can we define a debris-covered glacier?
2. What is the share of the climate influence in the mass balance variability? At which spatial scale should we work to dissociate the influence of the debris cover and the influence of the climate?
3. How to untangle the effect of the debris from the other morphological variables?

First, we need an acceptable definition of a debris-covered glacier. Such a definition is not available in the literature and, consequently, we had to build our own definition. The distinction between debris-free and debris-covered glaciers is somehow arbitrary, but is intuitive and very helpful for the analysis, therefore, we decided to use it.

Second, the question of the climate influence is also complicated to address, because of the strong link between climate and glacier-wide mass balance through the precipitation and surface energy balance. If we want to isolate the effect of the glaciers geometry, we need to work with populations of glaciers located in a homogeneous climate. We decided to work with the regions defined in Brun *et al.* (2017). The region-wide mass balances correlate well with the region mass balance sensitivity average calculated by Sakai and Fujita (2017) with $R^2 = 0.47$, showing relatively homogeneous conditions at this spatial scale (figure 4.1). Interestingly, the correlation between mass balance and mass balance sensitivity is not as good for the $1^\circ \times 1^\circ$ tiles, with $R^2 = 0.32$. This can be interpreted as a less significant effect of climate on these finer scale and further justify our choice.

Third, the morphology of glaciers is linked with their debris cover (Scherler *et al.*, 2011b), and consequently, one needs to use the appropriate statistical tools to assess the influence of each of these variables on the glacier mass balance. For this study, we use a multivariate linear model, which is easier to interpret than a principal component analysis.

This work was the opportunity to collaborate with Vincent Jomelli, a geomorphologist who came in the field with us in November 2017. His point of view was very relevant, especially for the interpretation of the statistical analysis, which is not a common approach in the field of glaciology. The collaboration with Sudan Maharjan and Finu Shrestha was very stimulated as well, as they work on glacial lakes, a topic which is timely in terms of hazard assessment and risk management. Last but not least, this study was made possible by the

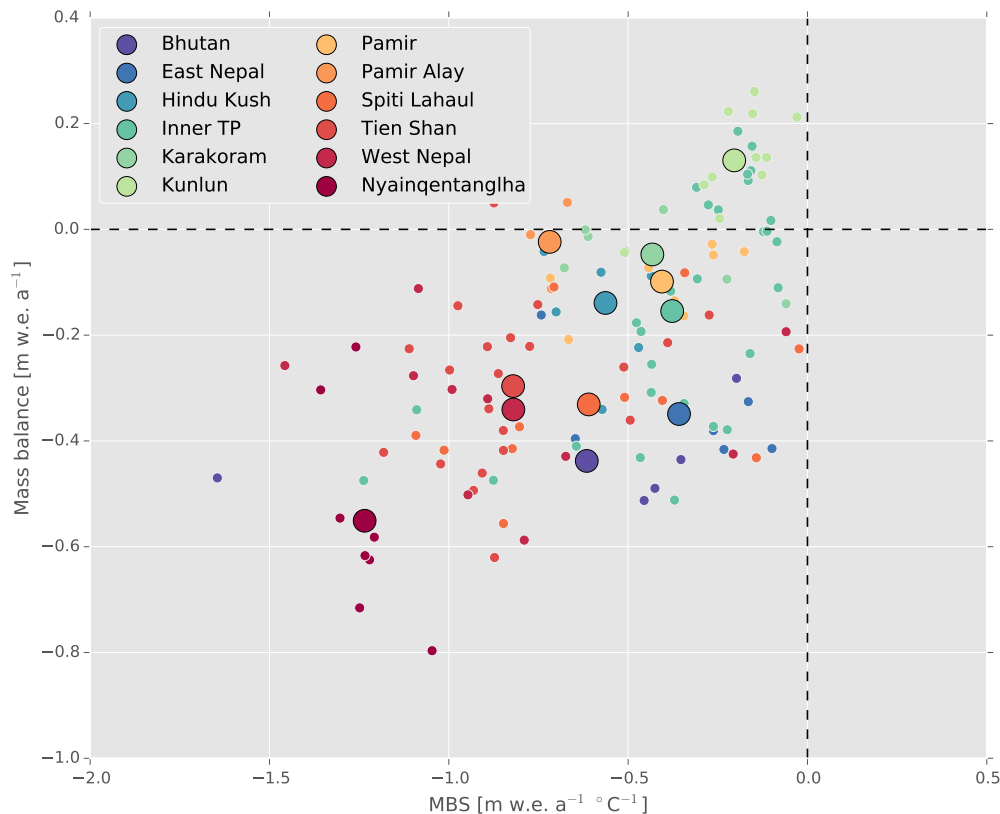


Figure 4.1: Mass balance as a function of MBS from *Sakai and Fujita (2017)*. Each small dot represents a $1^\circ \times 1^\circ$ tile and the large dots represent the regional averages.

impressive work of Philip Kraaijenbrink, who classified automatically thousands of Landsat images to produce maps of glacier surface classifications for the entire HMA.

4.2 Abstract

We analyze the 2000-2016 mean glacier-wide mass balance of 6 560 individual glaciers of High Mountain Asia larger than 2 km^2 in order to understand the drivers of the variability. We separate the dataset into 12 regions assumed to be climatically homogeneous. After a careful selection of the morphological variables which had the strongest influence on the mass balance, we find that the slope of the glacier tongue, mean glacier elevation, percentage of debris cover, pond density and avalanche contributing area all together explain a maximum of 46 % and a minimum of 8 % of the glacier-wide mass balance variability, within a given region. The best predictor of the glacier-wide mass balance is the slope of the glacier tongue and the mean glacier elevation for most regions, with the notable exception of the inner Tibetan Plateau, where debris cover is the best predictor. Within seven regions out of twelve, debris-free and debris-covered glaciers have non significantly different glacier-wide mass balance. Past studies assessed the influence of debris and surpaglacial ponds on glaciers with variables that are difficult to interpret (advance/retreat or tongue-wide thinning rate); we challenge some of their conclusions. Lake-terminating glaciers have more negative mass balances than the regional averages, the influence of lakes being stronger on small glaciers than on large glaciers.

4.3 Introduction

Mountain glaciers are widely recognized as sensitive indicators of climate change (Oerlemans, 1986). However the response of each individual glacier to climate variability is modulated by its climate sensitivity and its geometry, complicating the climatic interpretation. Recent studies showed the contrasted glacier mass changes at the scale of High Mountain Asia (HMA) for the beginning of the twenty-first century (e.g., Kääh *et al.*, 2015; Gardelle *et al.*, 2013; Gardner *et al.*, 2013; Brun *et al.*, 2017). Causes of these spatio-temporal changes are still not fully understood. The heterogeneous climatology (Maussion *et al.*, 2014) could be responsible for various glacier mass balance sensitivities to temperature, explaining partly the regional pattern of recent glacier mass changes (Sakai and Fujita, 2017). However the nature of glacier tongues (debris-free or debris-covered) and morphology of the glaciers and glacier catchments, that show large variations in HMA may also play a significant role, which is to our knowledge insufficiently explored in this region. In particular, the influence of the presence of debris at the surface of many HMA glaciers is the subject of an ongoing hot debate.

In the European Alps, annual fluctuations of glacier-wide mass balance are strongly correlated among themselves for a given region (e.g., Vincent *et al.*, 2017), and can be related to meteorological annual fluctuations (e.g., Rabatel *et al.*, 2013). Nevertheless, multi-decadal averages of individual glacier mass balances and the glacier geometry (or morphological variables) are linked (e.g., Paul and Haeberli, 2008; Huss, 2012; Huss *et al.*, 2012; Rabatel *et al.*, 2013; Fischer *et al.*, 2015; Rabatel *et al.*, 2016).

In HMA, Salerno *et al.* (2017) conducted a statistical analysis of the thinning rates of glaciers in the Everest region, in relationship with morphological variables. They found that the glacier tongue slope (named down gradient in their study), was the main morphological variable controlling the glacier thickness changes, and they suggested that this was partially explained by preferential development of glacial ponds on shallow slopes (e.g., Quincey *et al.*, 2007). They also found that the presence of debris-cover was not a significant contributor to differences in thinning rates among the studied glaciers. Nevertheless, they examined a restricted sample of glaciers (28) and analyzed only tongue-averaged thinning rates, which are less straightforward to interpret than glacier-wide mass balances as they are the sum of surface mass balance and emergence velocity (e.g., Cuffey and Paterson, 2010).

Additionally, compared with land-terminating glaciers, lake-terminating glaciers shrink faster in Sikkim (Basnett *et al.*, 2013), have more negative rates of elevation changes in Bhutan, Everest region and West Nepal (Gardelle *et al.*, 2013) and have more negative mass balances in the Everest region (King *et al.*, 2017). Terminal lakes develop when supraglacial ponds coalesce into a single lake dammed by a terminal moraine (e.g., Benn *et al.*, 2012; Thompson *et al.*, 2012). Eventually, the terminal lakes enhance the frontal ablation by dynamic thinning, calving and thermo-erosion (e.g., Benn *et al.*, 2012). To our knowledge, the only study quantifying the influence of terminal lake on glacier-wide mass balance was conducted on 32 glaciers (9 of them being lake-terminating glaciers) and restricted to the Everest region (King *et al.*, 2017).

In this study, we extend the work of Salerno *et al.* (2017) and King *et al.* (2017) to the entire HMA, by analyzing 6 560 individual glacier mass changes in relationship with morphological variables. For each of the twelve regions defined in Brun *et al.* (2017), we explore the variables which have a significant influence on the glacier-wide mass balance, with a focus on the differences between debris-covered and debris-free and between lake-terminating and land-terminating glaciers.

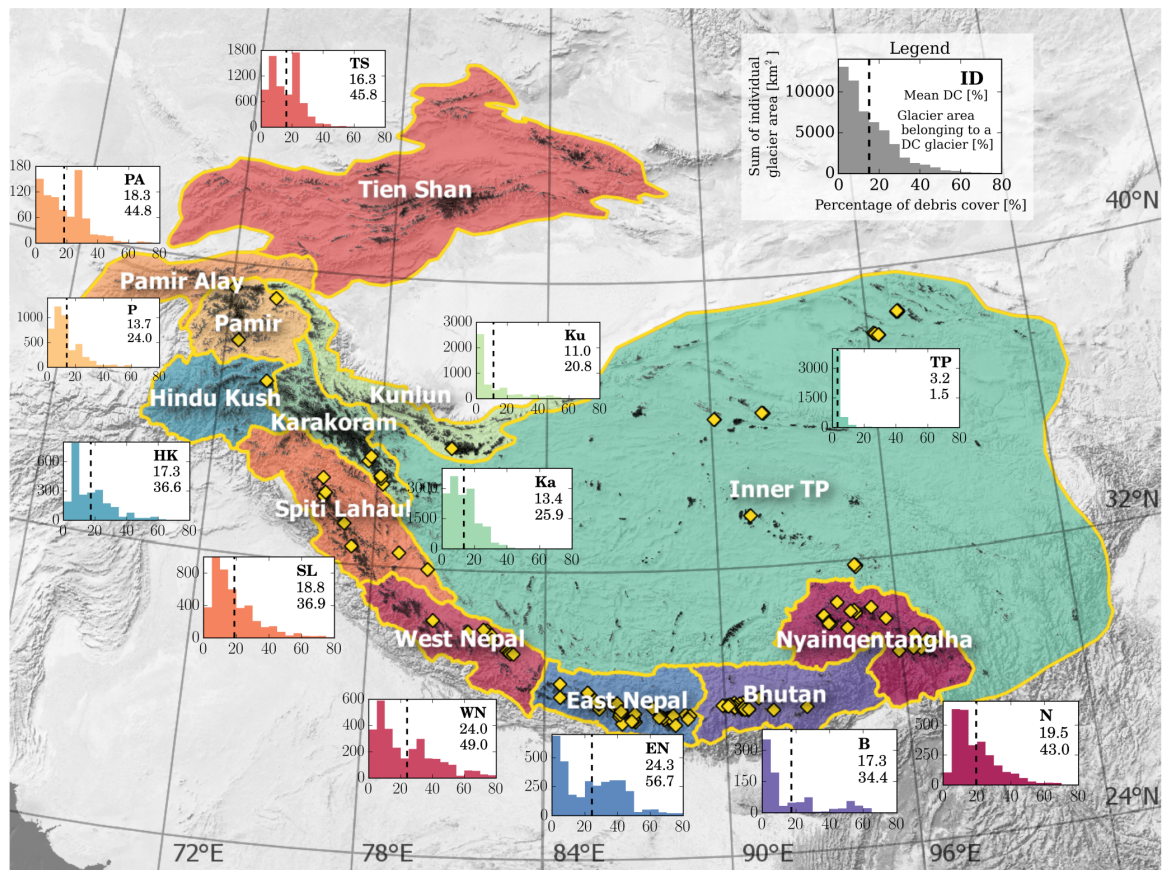


Figure 4.2: Distribution of the debris-covered and lake-terminating glaciers in HMA. Each bar of the histogram represents the total area of the glaciers which belong to this interval in terms of mean debris-cover. The vertical dashed bars represent the area weighted debris-cover average, which is also the upper number. The lower number represents the proportion of ice that belongs to a debris-covered glacier (with a debris threshold of 19 %). The yellow diamonds represent the locations of the lake-terminating glaciers.

4.4 Data and methods

4.4.1 Glacier-wide mass balance and morphological data

All the glacier-wide mass balance (\dot{M}) data are calculated from linear fit of multi-temporal digital elevation models (DEMs) obtained from the Advanced Spaceborne Thermal Emission and Reflection Radiometer (ASTER) satellite (Brun *et al.*, 2017). Only glaciers larger than 2 km² are included, because the random error on the glacier-wide mass balance decreases with the glacier area. The glaciers with less than 70 % of good data coverage are excluded from the analysis, leading to a total number of glaciers of 6 557. They represent 54 % of the total glacierized area of the HMA. The individual glacier mass balances have a median uncertainty of ± 0.22 m w.e. a⁻¹ (Brun *et al.*, 2017). The glacier-wide mass balances are calculated using the RGI 5.0 glacier mask (Pfeffer *et al.*, 2014).

Based on the literature (e.g., Huss, 2012; Fischer *et al.*, 2015; Salerno *et al.*, 2017), we explore glacier morphological variables that were shown to have a potential influence on \dot{M} : area, aspect, mean slope, slope of the lower 20 % (Tongue slope), mean elevation (Mean elev.), median elevation, minimum elevation, maximum elevation, percentage of debris-cover (DC), pond density (PD) and avalanche contributing area (Contrib. area). The glacier morpho-

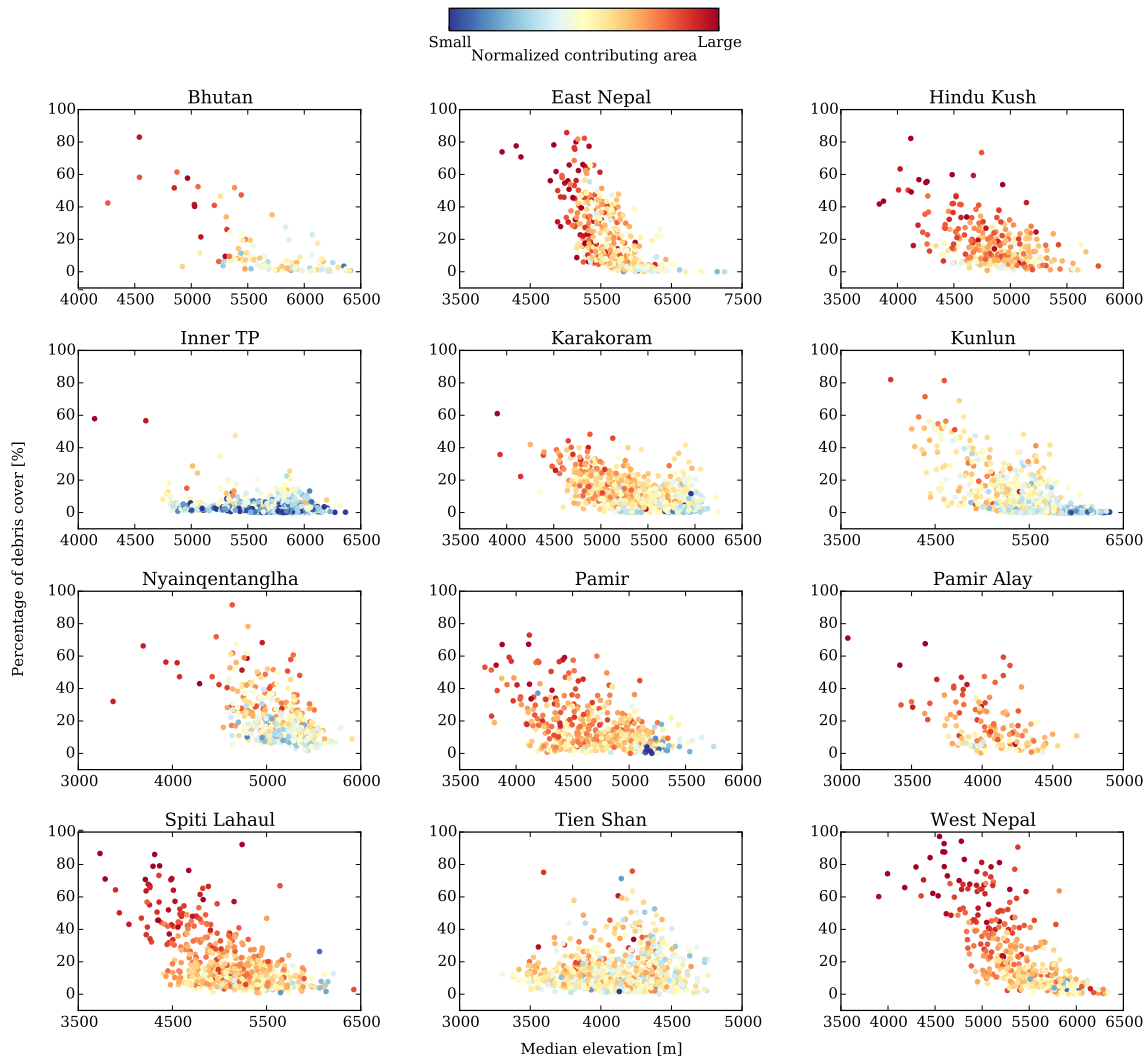


Figure 4.3: Percentage of the glacier debris-cover as a function of the glacier median elevation. The dots represent individual glaciers and are colored according to the logarithm of their normalized avalanche contributing area, defined as the ratio of the avalanche contributing area divided by the glacier area.

logical variables are calculated from the supplementary data of *Kraaijenbrink et al. (2017)*, meaning that they are computed on the basis of a 30 m grid clipped to the RGI 5.0 glacier extents. The percentage of debris-cover is calculated as the ratio of the glacier area classified as debris in *Kraaijenbrink et al. (2017)* divided by the total glacier area. The pond density is calculated as the number of pixels classified as ponds within the ablation area (defined as the area below the median elevation) divided by the percentage of the glacier ablation area covered by debris. If some pixels are classified as ponds but there is no pixel classified as debris below the median glacier elevation, then the pond density is assigned to zero. The avalanche contributing area is defined as the area in the catchment upstream of the glacier median elevation with slope higher than 30° . The catchment upstream of the median glacier elevation is calculated based on the Shuttle Radar Topographic Mission (SRTM) DEM (*Farr et al., 2007*) and the upslope area module (*Freeman, 1991*) implemented in the SAGA software (*Conrad et al., 2015*). Through the data analysis, we found some obvious outliers (10 glaciers), for instance glaciers which had a very low minimum elevation. These errors come from artifacts in the SRTM and we exclude these glaciers from the analysis, leading to a final number of 6 560 glaciers.

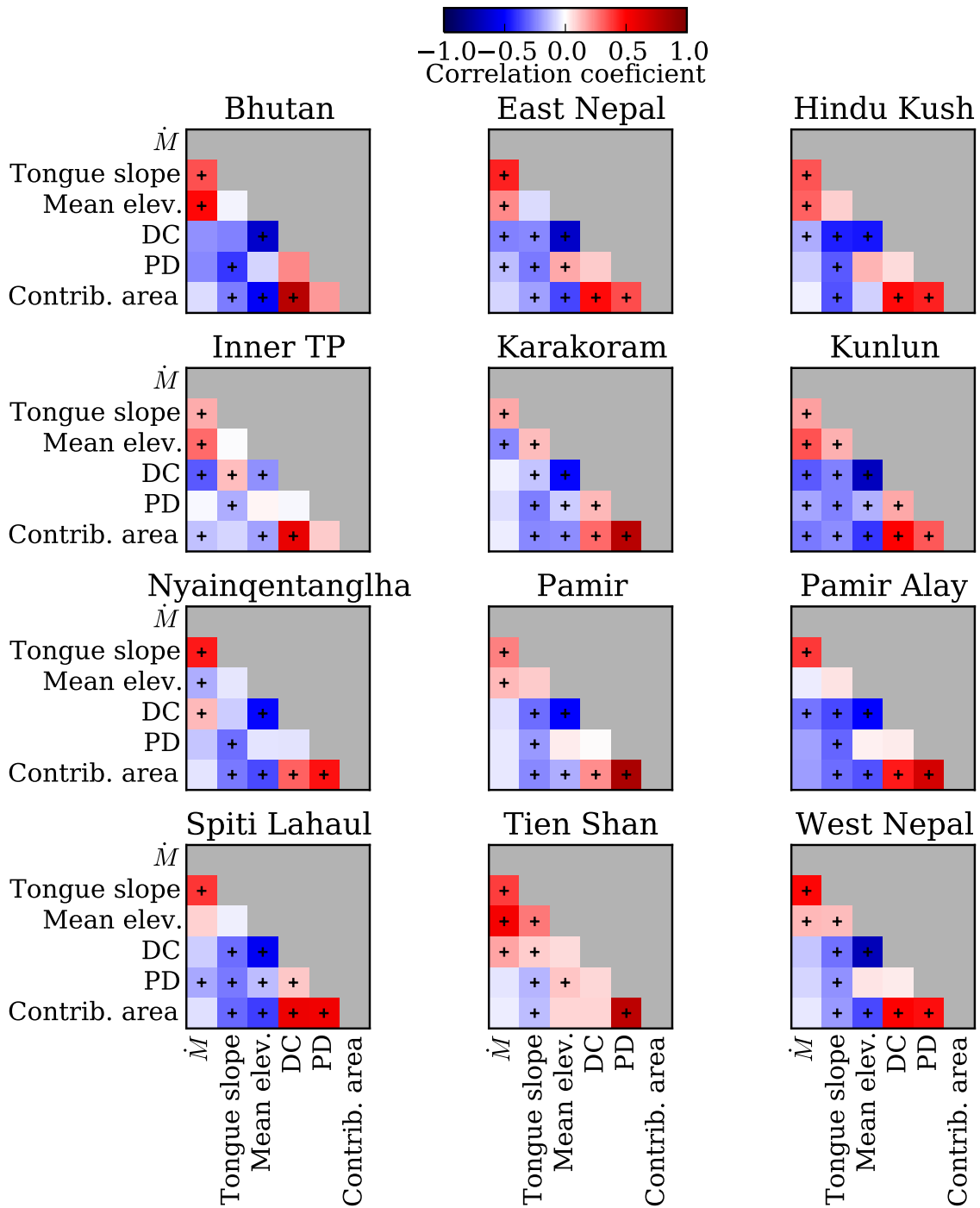


Figure 4.4: Pearson correlation coefficients between selected variables. The + denotes correlation significant at $p < 0.01$.

4.4.2 Debris-covered glaciers and debris-free glaciers

To our knowledge, there is no widely-accepted definition of what is a debris-covered glacier. For instance, *Xiang et al.* (2018) use a 5 % threshold for the debris-cover fraction (Yang Xiang, personal communication), whereas *Janke et al.* (2015) use a 25 % threshold to define the partially debris-covered glaciers. We determine an optimal threshold of 19 % of debris-cover, based on the classification of 100 randomly selected glaciers produced by five different operators (see Supplementary Text in section 4.8 and Figures 4.7 and 4.8). It is noteworthy that this distinction is somehow arbitrary, as there is a continuum between debris-covered and debris-free glaciers, however we find useful to make this categorization, as it simplifies the analysis. We comparing debris-covered and debris-free glaciers, we test the sensitivity to this threshold by testing 14 % and 24 % thresholds.

4.4.3 Lake-terminating and land-terminating glaciers

From a quality controlled lake inventory produced by ICIMOD (*Maharjan et al.*, 2018) and the glacial lake inventory produced by *Zhang et al.* (2017), we automatically select the glaciers in contact with lakes (within a 50 m buffer). Then from visual inspection of Google Earth imagery, we retain the 133 glaciers, which are actually lake-terminating glaciers. The lake inventory does not cover the Tien Shan and Pamir Alay regions and we find only 1, 1, 3 and 5 lake-terminating glaciers in Kunlun, Hindu Kush, Pamir and Karakoram, respectively. Consequently, we focus the analysis on the six remaining regions: Bhutan (21 lakes), East Nepal (47 lakes), inner Tibetan Plateau (TP, 16 lakes), Spiti Lahaul (7 lakes), West Nepal (11 lakes) and Nyainqentanglha (19 lakes). Eight of these glaciers are excluded from the analysis because their rate of elevation change coverage is not good enough.

4.4.4 Multivariate linear model

The multivariate linear model aims at finding the set of coefficients (a_1, a_2, \dots, a_n), which explain a maximum of the mass balance (\dot{M}), when multiplying the predictors (x_1, x_2, \dots, x_n), such as:

$$\dot{M} = a_1x_1 + a_2x_2 + \dots + a_nx_n \quad (4.1)$$

We worked with standardized predictors and standardized \dot{M} to allow for a direct comparison between the coefficients a_i . The standardized predictor X_s derived from the variable X is defined as:

$$X_s = \frac{X - \bar{X}}{\sqrt{V(X)}} \quad (4.2)$$

where \bar{X} is the variable regional average and $V(X)$ is its regional variance.

We explore the morphological variables that explain the maximum of the variance, but the selection of the different variables to include in the multivariate linear model is subjective and we could not find an optimal combination of variables which minimized the Akaike Information Criterion (AIC, *Akaike*, 1974), while maximizing the explained variance R^2 for all the regions simultaneously. Similarly, standard approach such as the forward selection and backward elimination (e.g., *Hocking*, 1976), gives different results for different regions, mainly because the variables were very redundant (for example the mean and the median elevation). Instead, we favor the variables which are often selected in the literature and/or

Table 4.1: Results of the multivariate linear regression to explain the glacier-wide mass balance for each region. The variables are standardized, and therefore the coefficients associated with each variable are directly representative of their relative influence on the glacier-wide mass balance. R^2 is the squared Pearson coefficient for the multivariate linear regression, including all the predictors. We reported only the coefficients of the variables statistically significant in predicting \dot{M} ($p < 0.01$). The dominant variable for each region is highlighted in bold font. The acronyms are the same one as used in Figure 4.2.

Region	B	EN	HK	TP	Ka	Ku	N	P	PA	SL	TS	WN
R^2	0.46	0.27	0.22	0.22	0.10	0.16	0.24	0.08	0.20	0.19	0.37	0.26
n	106	434	297	742	1196	717	398	552	141	679	881	417
Tongue slope [-]	0.44	0.45	0.36	0.23	0.18	-	0.47	0.26	0.28	0.43	0.24	0.51
Mean elev. [-]	0.73	0.35	0.36	0.23	-0.34	0.20	-	0.18	-	0.16	0.48	0.18
DC [-]	-	-	-	-0.41	-0.16	-0.13	0.16	-	-	-	0.12	-
PD [-]	-	-0.13	-	-	-	-	-	-	-	-0.14	-	-
Contrib. area [-]	0.36	0.17	-	0.18	-	-	-	-	-	0.19	-	-

variables we want to test, such as the debris cover, the pond density or the avalanche contributing area (*Huss et al., 2012; Salerno et al., 2017*).

All the calculations are performed using the `ols` tool from Python’s `pandas` package.

4.5 Results

4.5.1 Contrasted glacier morphologies in the different regions

The different regions have varying debris-cover, with mean debris cover ranging from 3.2 % in the inner TP to 24.3 % in the East Nepal (Figure 4.2). With a threshold of 19 % to distinguish between debris-free and debris-cover glaciers, we find that debris-covered glaciers occupy between 1.5 % in the inner TP and 56.7 % in the East Nepal of the total glacierized area (Figure 4.2). At first order, the debris-cover is controlled by the local relief, and in particular the area above the glacier, which contributes to the debris supply (*Scherler et al., 2011b*). We extend the analysis of *Scherler et al. (2011b)*, which cover only a limited number of glaciers (287) over selected regions (Hindu Kush, Karakoram, Kunlun, Spiti Lahaul, West Nepal, East Nepal, Bhutan), to the entire HMA: in most regions, the debris cover increases with the contributing area and decreases with the median elevation, as the insulating effect of debris allows for the existence of debris-covered tongues at low elevation (Figure 4.3). Very few glaciers are debris covered in the inner TP, where glaciers are often small ice caps (i.e. with no head-walls above their accumulation area). The glaciers located in Tien Shan do not follow the same distribution as in the other regions, as the debris cover is neither related with the median elevation, nor with the avalanche contributing area (Figure 4.3). The lake-terminating glaciers are mostly located in the south-eastern margin of the HMA (Figure 4.2).

4.5.2 Morphological variables and glacier-wide mass balance

For the different regions, the morphological variables have different influence on \dot{M} and different correlations among each others (Figure 4.4). Note that we do not present the results for all the initially selected variables. The aspect and area are not significant contributors to

\dot{M} for almost all of the regions. The median elevation, minimum elevation and maximum elevations are discarded because the mean elevation is a better predictor in most cases, and is less sensitive to the quality of the input DEM than the maximum and minimum elevation.

It is noteworthy that \dot{M} has always a significant ($p < 0.01$) positive correlation with the tongue slope (Figure 4.4), meaning the gentler the glacier slope, the more negative \dot{M} . The mean elevation is often significantly correlated with \dot{M} , most of the time positively, but sometimes negatively. For half of the regions, the DC is significantly and negatively correlated with \dot{M} , meaning the higher the debris-cover, the more negative the glacier-wide mass balance. However, for the other regions, it is the opposite (for the Nyainqentanglha and Tien Shan), or the correlation is not significant. The pond density and contributing area are usually not significantly and negatively correlated with \dot{M} .

The morphological variables are often correlated with each other. In particular, the debris-cover is always significantly negatively correlated with the mean glacier elevation, with the notable exception of the Tien Shan (Figures 4.3 and 4.4). The contributing area is often positively and significantly correlated with the debris-cover and pond density. The pond density is always significantly and negatively correlated with the tongue slope, because ponds develop preferentially on shallow slopes (Quincey *et al.*, 2007; Miles *et al.*, 2017b).

The multivariate linear model explains 8 to 46 % of \dot{M} variability (Table 4.1). The regions where the explained variability is the lowest are the Pamir, Karakoram and Kunlun. The regions where the explained variability is the highest are the Bhutan and Tien Shan. Except for the Kunlun region, the tongue slope is always a significant predictor of \dot{M} variability and for seven regions out of twelve, it is the predictor which has the strongest influence on \dot{M} variability. The mean elevation has a significant contribution to \dot{M} variability for ten regions out of twelve and is its dominating component for five regions. The debris-cover has a significant contribution to \dot{M} variability for five regions and is sometimes positive and sometimes negative. It is dominant only for the inner TP, with a negative value. In the other regions, it has a small contribution compared with the other predictors. The avalanche contributing area and the pond density are significant contributors to \dot{M} variability only for four and two regions, respectively. They have a small contribution compared with the other predictors (Table 4.1).

4.5.3 No systematic difference between debris-covered and debris-free glaciers in terms of glacier-wide mass balance

In terms of regional area weighted averages, the debris-covered glaciers have a \dot{M} significantly more negative than the debris-free glaciers in the East Nepal, inner TP, Kunlun and Pamir Alay. In the Tien Shan it is the opposite, and for all the other regions, the differences are not significant.

In terms of glacier-wide mass balance, for glaciers grouped by mean elevation (Figure 4.5), we can see differences between regions. For instance, in the East Nepal, Nyainqentanglha, Pamir Alay and in the inner TP, the debris-covered glaciers have more negative mass balances, whereas it is the opposite for Bhutan, Pamir and Tien Shan.

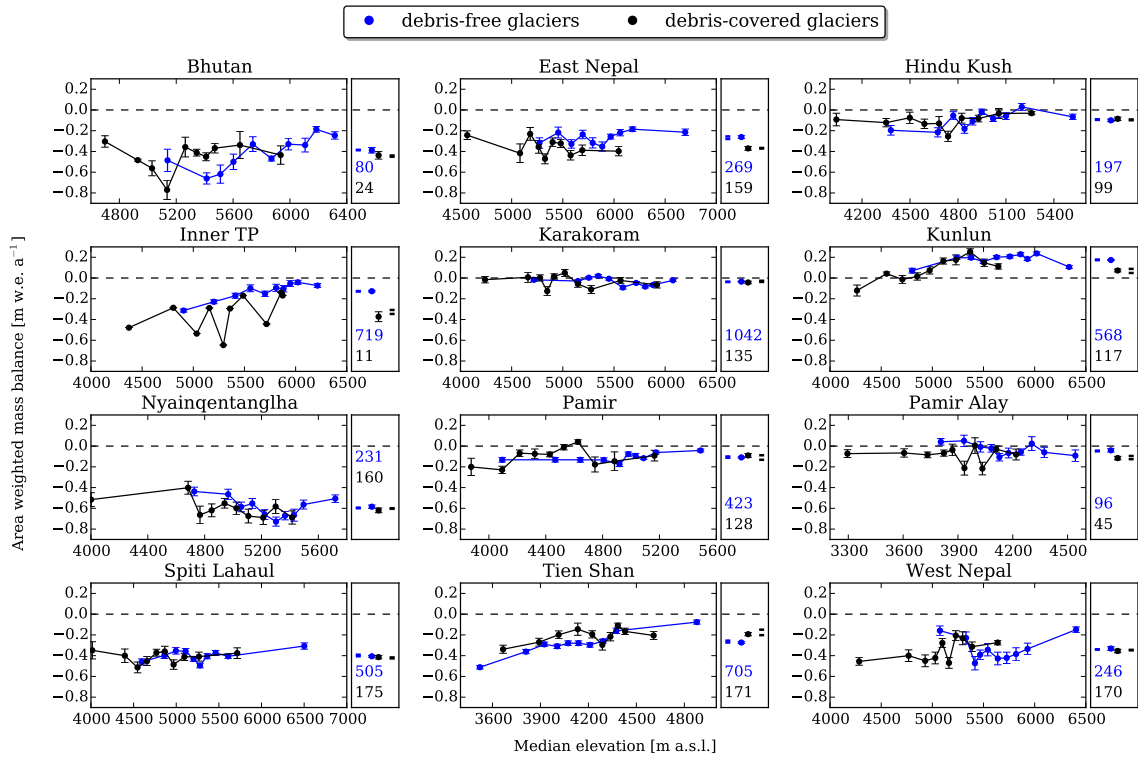


Figure 4.5: Glacier-wide mass balances for debris-covered and debris-free glaciers (threshold between debris-covered and debris-free glaciers is set to 19 % of debris cover). Each dot represents the area-weighted \dot{M} average of the glaciers with mean elevation belonging to a given 10 percentile of the glacier mean elevation. The error bars represent the uncertainty on the mean (i.e. the standard deviation of glacier-wide mass balances divided by the square root of the number of glaciers within the sample). The dots in the right hand side plots represent the regional averages (the errorbars show the uncertainty on the mean), and the horizontal dashes represent the same averages with a threshold between debris-covered and debris-free glaciers at 14 and 24 % of debris cover.

These results are not very sensitive to the threshold used to discriminate between debris-free and debris covered glaciers. Although the altitudinal distribution of debris-covered and debris-free glaciers is strongly modified if we use threshold of 14 or 24 % to discriminate debris-covered and debris-free glaciers, the differences of \dot{M} between debris-free and debris-covered glaciers are no different from the reference differences (with a 19 % threshold) to more than ± 0.05 m w.e. a⁻¹.

4.5.4 Influence of proglacial lakes on glacier-wide mass balance

In general, lake-terminating glaciers have more negative \dot{M} than the regional average (Figure 4.6). They regularly lie further than one standard deviation from the mean. They have mean \dot{M} that are between 0.11 to 0.32 m w.e. a⁻¹ more negative than the regional averages, in Nyainqentanglha and West Nepal, respectively. Nevertheless, the lake influence on \dot{M} is dampened by the glacier area, as the large lake-terminating glaciers tend to have \dot{M} closer to the regional average than the small lake-terminating glaciers (Figure 4.6).

4.6 Discussion

4.6.1 Complex influence of the morphological variables and debris-cover on the glacier-wide mass balance

With explained variances of \dot{M} ranging from 8 to 46 % (mean value of 23 %), the multiple regressions are in line with values obtained for the Alps. *Rabatel et al.* (2016) found that the slope of the tongue and the glacier median elevation explained 25 % of the variance of a serie of 30 glacier-wide mass balances averaged over 31 years. *Huss* (2012) found that a combination of 3 variables (area, median glacier elevation and slope of the tongue) explained 35 % of the variance of a serie of 50 glacier-wide mass balances averaged over 100 years. The explained variance reached 51 % when using a combination of 6 variables. The anti-correlation between the \dot{M} and the area, was found only for glaciers smaller than 0.1 km² in the Alps, and above this area, the 1980-2010 mass balances of Swiss glaciers was relatively constant with glacier size (*Fischer et al.*, 2015). Here we analyzed only glaciers larger than 2 km², explaining why we did not find such a link.

The multiple correlations among the predictors complicate the interpretation of the results, but the multivariate linear model can partially separate the contribution of each predictor (Table 4.1). For instance, the negative correlation between \dot{M} and the debris cover is surprising, because debris is expected to insulate the glacier tongue and reduce its ablation (e.g., *Østrem*, 1959). But this correlation is somehow artificial and driven by the correlations between the debris-cover and the mean elevation and tongue slope, which are themselves correlated with \dot{M} (Figure 4.4). The multivariate linear model shows that the dominant influences are the tongue slope and mean elevation, and that the negative correlation between the debris-cover and \dot{M} is only apparent. This is further supported by the fact that debris-covered glaciers and debris-free glaciers do not have systematic differences in terms of \dot{M} when they are grouped by mean elevation (Figure 4.5).

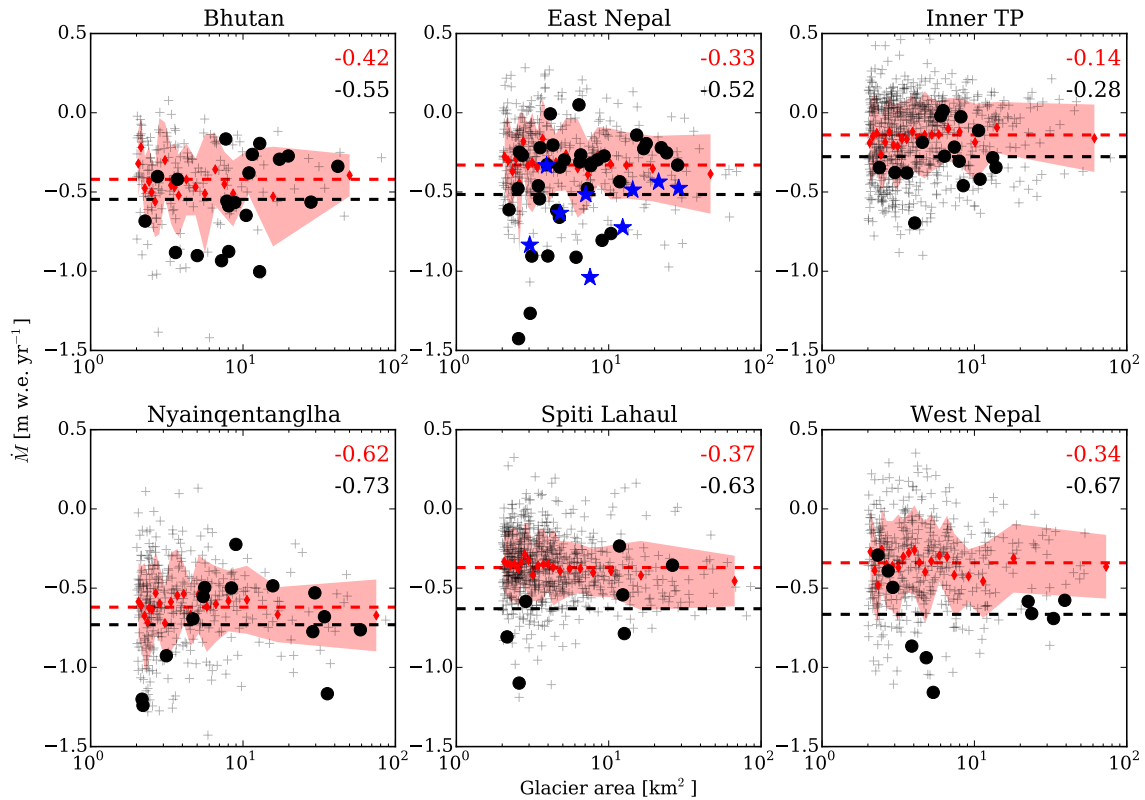


Figure 4.6: \dot{M} as a function of glacier area. The black crosses represent the land terminating glaciers and the large black dots the lake-terminating glaciers. The blue stars in East Nepal represent the nine lake-terminating glaciers studied by *King et al.* (2017). The red diamonds represent the 5 percentile averages of all glaciers (for instance, the first diamond represents the 0 to 5 percentile, centered on the 2.5 percentile). The red envelope represents the \pm one standard deviation from the mean, within a 5 percentile. The red number (and red horizontal dashed line) is the region-wide mass balance, and the black number (and black horizontal dashed line) is the mean of the lake-terminating glacier mass balances. The plots were cut at 10² km², as all the lake-terminating glaciers have an area smaller than this value. Note that for East Nepal, one lake-terminating glacier (with a size of 2.6 km²) has a mass balance of -1.9 m w.e. yr⁻¹ and therefore is missing on the plot.

4.6.2 Specificities of debris-covered glaciers

The pond density has a non significant influence on \dot{M} , except for the East Nepal (where Salerno *et al.* (2017) found a similar result) and Spiti Lahaul. This result is surprising as an abundant literature highlighted the role of supraglacial ponds as entry points for the energy for debris-covered glaciers (e.g., Sakai *et al.*, 2000; Miles *et al.*, 2016). Consequently, the conclusions of Salerno *et al.* (2017), who suggested an important control of the ponds on the glacier surface lowering, were reproduced for the East Nepal region in this study, but cannot be extended to the entire HMA.

Even though we did not document glacier front position changes, it was already shown for selected regions of HMA that the debris-covered tongues experience limited retreat compared with debris-free tongues (e.g., Scherler *et al.*, 2011a; Xiang *et al.*, 2018). However, debris-covered and debris-free glaciers have mostly similar \dot{M} , meaning that they have to respond through different mechanisms to climate changes. The debris-covered glaciers thin differently from the debris-free glaciers: debris-covered glacier thinning is distributed over their lower reaches independently of the elevation, whereas debris-free glaciers experience front retreat (Rowan *et al.*, 2015; Rowan, 2017; Salerno *et al.*, 2017). Consequently, the ice dynamics play a major role for the evolution of debris-covered tongues, and the stable front positions of debris-covered glaciers should not be interpreted as balance mass budget (Scherler *et al.*, 2011a).

4.6.3 Proglacial lake influence on glacier mass balance

Lake-terminating glaciers have \dot{M} that are more negative than the regional average, in most cases. However, the lake influence depends on the glacier size and the lake's stage of development (Benn *et al.*, 2012; King *et al.*, 2017). The glacier sample of King *et al.* (2017) has a mean \dot{M} of -0.61 ± 0.11 m w.e. a^{-1} (versus -0.70 ± 0.27 m w.e. a^{-1} in their study), which is slightly more negative than the average of all lake-terminating glacier of East Nepal (Figure 4.6). The results presented in this study are a first step, and more studies should be conducted on specific lake-terminating glaciers to better understand the lake influence on the glacier dynamics and mass balance (King *et al.*, 2018). Local studies are even more needed because of the risk of glacial lake outburst floods (GLOFs) associated (Haritashya *et al.*, 2018).

4.6.4 Limitations of our analysis

The statistical analysis presented here is sensitive to outliers, biases and uncertainties in the data. The individual mass balances data have themselves a relatively high level of uncertainty with a median uncertainty of 0.22 m w.e. a^{-1} (ranging from 0.14 to 0.78 m w.e. a^{-1}), depending on the glacier area, on the proportion of the glacier surface surveyed and on the number of DEMs available to extract a reliable rate of elevation change signal (Brun *et al.*, 2017).

The other data sources are also subject to uncertainty in the glacier delineation (Paul *et al.*, 2013), which, in turn, introduces large uncertainties in the debris-cover extent, as formerly glacierized area would be classified as debris-covered area. The overall accuracy of the

glacier surface classification is 91 % (*Kraaijenbrink et al.*, 2017). Moreover, the avalanche contributing area is sensitive to the quality of the DEM used to determine the upstream area of each glaciers (*Tribe*, 1992). These intrinsic limitations should be kept in mind, however the quality of the data is high enough to conduct the analysis presented here.

The separation of the glaciers into debris-covered and debris-free glaciers is a bit artificial and arbitrary. Nevertheless, the choice of different thresholds has a limited influence on the results (Figure 4.5), and therefore the classification is still insightful.

Another limitation of our study is the separation of glaciers into regions that we assumed homogeneous in terms of climate. The regions considered in this study have much larger spatial extent than the Swiss or French Alps (< 300 and 200 km long, respectively), as they spread from ~ 300 km (Pamir) to more than 2 000 km (Inner TP). Regional divisions remain arbitrary and alternative delineations could be provided. This is especially true for regions such as the Tibetan Plateau and the Tien Shan, where we put together glaciers that are under very different climate influences (e.g., *Sakai and Fujita*, 2017).

4.7 Conclusion

We assessed the main morphological controls on glacier-wide mass balances of HMA glaciers for the period 2000-2016. The morphological variables have various influences over our twelve studied regions and they explain more than one quarter of the mass balance variability for one third of the regions. The influence of the debris is not completely clear and complicated to untangle from the effect of the other morphological variables, because heavily debris-covered tongues are often situated at lower elevation than debris-free tongues, where ablation is higher. Overall, we did not observe systematic differences between debris-free and debris-covered glaciers in terms of glacier-wide mass balances.

The lake-terminating glaciers have more negative mass balances than the region average. Nevertheless, this effect is not systematic and specific studies need to be conducted on these glaciers to better quantify the lake influence and assess the GLOF hazard.

4.8 Supplementary methods

Finding a threshold on the debris cover relative area to classify the glaciers into two categories: debris-covered and non debris-covered To create a reference database, we asked five operators to classify 100 randomly selected glaciers, into two categories: debris-covered (DC) or non debris-covered (non DC), based on Google Earth images. The sum of the votes for each glacier will thus vary from 0 to 5. For the rest of the study, we will consider that any glacier with three votes or more is DC and is non DC otherwise. Individually, the different operators classified between 15 and 30 glaciers as DC. In total, 21 glaciers were classified as DC.

The link between the number of votes and the debris threshold is not straightforward (Figure 4.7). This is due to three main factors. First, the separation of the glaciers into two categories is somehow arbitrary and the different operators have different perceptions of

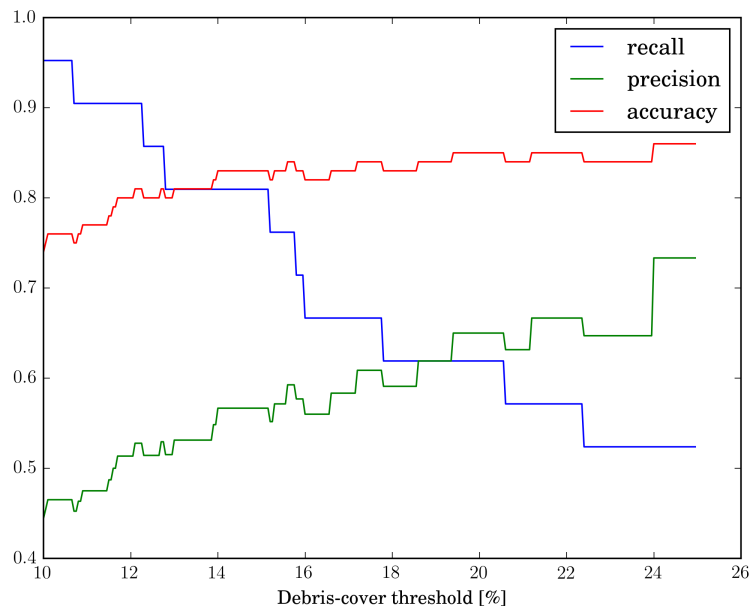


Figure 4.8: Recall, precision and accuracy as a function of the threshold used to categorized the glaciers on DC or non DC.

A good test method should ideally minimize and balance FP and FN. Additional quantities can be defined:

- recall $\frac{TP}{TP+FN}$ is the rate of detection of DC relative to the total number of DC
- precision $\frac{TP}{TP+FP}$ is the probability for a glacier detected as DC of being actually a DC
- accuracy $\frac{TP+TN}{TP+FP+TN+FN}$ is the success rate of the method

Ideally, all the above mentioned quantities should be as close to 1 as possible. In practice, the optimal threshold is obtained where the precision and the recall are equal (e.g., *Herreid and Pellicciotti, 2018*). We tested relative debris-covered area thresholds ranging from 10 to 25 % and found an optimal around 19 % (Figure 4.8). The accuracy of the test method for this threshold is 84 %.

4.9 Going one step further

The statistical analysis presented in this chapter is not fully satisfying, as it does not provide definitive explanations in terms of glaciological processes. I guess that I was also a bit disappointed by the weakness of the conclusions, whereas I would have expected more contrast among the different categories of glaciers. However, the enthusiasm of Vincent Jomelli gave me a different point of view about the strength of these results, and I deeply thank him for this!

One remaining limitation of this study is the fact that we did not take into account the climate influence and assumed climatically homogeneous regions, even though we know that they are not completely homogeneous. Future work should be based on a collaboration with HMA climate specialists. They would bring new perspectives about the problem and could help us to refine the region divisions. Another direction could be the study of the surface

mass balance of neighboring large debris-free and debris-covered tongues. *Vincent et al.* (2016) showed that the tongue-wide ablation of the debris-covered Changri Nup Glacier was reduced compared with a near-by debris-free tongue. However, this is based on a single glacier tongue and such a comparison would benefit from being repeated. Based on large scale glacier surface velocity products (e.g., *Dehecq et al.*, 2015), ice thickness estimates (e.g., *Huss and Farinotti*, 2012) and glacier rate of elevation changes, it is possible to estimate the ablation of debris-covered tongues and to compare them with debris-free tongues. However, the thickness estimates by *Huss and Farinotti* (2012) rely on a mass balance gradient hypothesis, and one should be careful not to produce only a circular reasoning.

Ice cliff contribution to the tongue-wide ablation of Changri Nup Glacier, Nepal, Central Himalaya

Contents

5.1	A short introduction	101
5.2	Abstract	101
5.3	Introduction	102
5.4	Study area	104
5.5	Data	104
5.5.1	Terrestrial photogrammetry	104
5.5.2	UAV photogrammetry	105
5.5.3	Pléiades tri-stereo photogrammetry	106
5.5.4	Update of existing datasets	109
5.6	Methods	110
5.6.1	Emergence velocity	110
5.6.2	Ice cliff backwasting calculation	112
5.6.3	Sources of uncertainty on the ice cliff backwasting	114
5.7	Results	117
5.7.1	Comparison of TIN based and DEM based estimates	117
5.7.2	Sensitivity to the emergence velocity	121
5.7.3	Importance of the glacier flow corrections	121
5.7.4	Total contribution of ice cliffs to the glacier tongue net ablation for the period November 2015–November 2016	123
5.7.5	Total contribution of ice cliffs to the glacier tongue net ablation for the period November 2016–November 2017	123
5.8	Discussion	124
5.8.1	Cliff evolution and comparison of two years of acquisition	124
5.8.2	Influence of emergence velocity and glacier flow correction on f_C and f_C^*	125

5.8.3	Ice cliff ablation and the debris-cover anomaly	126
5.8.4	Applicability to other glaciers	128
5.9	Conclusions	129
5.10	Going one step further	131

This chapter is written after an article published in the journal *The Cryosphere*:

Brun, F., P. Wagnon, E. Berthier, J. M. Shea, W. W. Immerzeel, P. D. A. Kraaijenbrink, C. Vincent, C. Reverchon, D. Shrestha, and Y. Arnaud (2018b), Ice cliff contribution to the tongue-wide ablation of Changri Nup Glacier, Nepal, central Himalaya, *The Cryosphere*, 12(11), 3439–3457, doi: 10.5194/tc-12-3439-2018

5.1 A short introduction

Ablation at ice cliffs is probably one of the main processes contributing significantly to the ablation of a debris-covered tongue. It is possible to measure the volume losses of individual cliffs due to their backwasting (*Brun et al.*, 2016). However, previous attempts were based on very high resolution data (terrestrial photogrammetry), which require extensive field work, preventing the application of this method at the scale of a glacier tongue. Consequently, this study had initially three main objectives:

1. providing the first observation-based assessment of the ice cliff contribution to the ablation of a debris-covered glacier tongue
2. applying the initial method to lower resolution and gridded data, such as UAV and Pléiades DEMs in order to cover larger areas
3. improving the treatment of the emergence velocity

This study is based on three months of field work, which represented a substantial part of my PhD. All these expeditions were great human adventures and taught me a lot about Himalayan glaciers. None of this work could have been done without Patrick Wagnon, who organized all the logistics and gathered the people with the skills needed for such campaigns. He even learned how to fly a drone! In 2011, Christian Vincent and Patrick Wagnon collected precious ice thickness data. The Utrecht University team (Walter Immerzeel and Philip Kraaijenbrink) and Joe Shea (ICIMOD and now at Prince Georges University) did most of the UAV acquisition and processing. Etienne Berthier acquired the Pléiades images and we exchanged a lot about the processing. Etienne Berthier, Sonam Sherpa and Dibas Shrestha were all very skillful field assistants for the (extremely boring) task of surveying ice cliffs from terrestrial photogrammetry. The experiment design of cliff monitoring was first suggested by colleagues from ETHZ (Pascal Buri, Jakob Steiner, Evan Miles, Francesca Pellicciotti), and refined by myself. Camille Reverchon worked as an intern under my supervision and processed the first set of images used for the terrestrial photogrammetry. I presented this work at the Alpine Glaciology Meeting 2018 (Chamonix) and at the European Geoscience Union meeting 2018 (Vienna), where it was awarded an Outstanding Student Poster and Pico (OSPP) award.

5.2 Abstract

Ice cliff backwasting on debris-covered glaciers is recognized as an important mass loss process that is potentially responsible for the so-called "debris-cover anomaly", i.e. the fact that debris-covered and debris-free glacier tongues appear to have similar thinning rates in Himalaya. In this study, we quantify the total contribution of ice cliff backwasting to

the net ablation of the tongue of Changri Nup Glacier, Nepal, between 2015 and 2017. Detailed backwasting and surface thinning rates were obtained from terrestrial photogrammetry collected in November 2015 and 2016, unmanned air vehicle (UAV) surveys conducted in November 2015, 2016 and 2017, and Pléiades tri-stereo imagery obtained in November 2015, 2016, and 2017. UAV- and Pléiades-derived ice cliff volume loss estimates were, respectively, 3 and 7% less than the value calculated from the reference terrestrial photogrammetry. Ice cliffs cover between 7 and 8% of the total map view area of the Changri Nup tongue. Yet from November 2015 to November 2016 (November 2016 to November 2017), ice cliffs contributed to 23 +/- 5% (24 +/- 5%) of the total ablation observed on the tongue. Ice cliffs therefore have a net ablation rate 3.1 ± 0.6 (resp. 3.0 ± 0.6) times higher than the average glacier tongue surface. However, on Changri Nup Glacier, ice cliffs still cannot compensate for the reduction of ablation due to debris-cover. In addition to cliffs enhancement, a combination of reduced ablation and lower emergence velocities could be responsible for the debris covered anomaly on debris-covered tongues.

5.3 Introduction

Ablation areas in High Mountain Asia (HMA) are heavily debris-covered, meaning that a potentially large part of melt water originates from ice ablation of debris-covered glacier tongues (Kraaijenbrink *et al.*, 2017). Numerous studies have demonstrated that a debris layer thicker than 5–10 cm has a dominant insulating effect and dampens the ablation of ice beneath it (e.g., Østrem, 1959; Nicholson and Benn, 2006; Reid and Brock, 2010; Reznichenko *et al.*, 2010; Lejeune *et al.*, 2013). Yet counter-intuitively, similar thinning rates (change in glacier surface elevation over time) have been observed for clean ice and debris-covered ice at similar elevations across HMA (Gardelle *et al.*, 2013; Kääh *et al.*, 2012). This ‘debris-cover anomaly’ (Pellicciotti *et al.*, 2015) has been observed in the Khumbu region (Nuimura *et al.*, 2012), the Kangri Karpo Mountains (Wu *et al.*, 2018), and at Kanchenjunga (Lamsal *et al.*, 2017) and Siachen (Agarwal *et al.*, 2017) glaciers.

Two main hypotheses have been proposed to explain this anomaly. First, while ablation rates are reduced by thick debris, ice cliffs act as local hot spots for melt and thus could contribute disproportionately to the tongue-averaged ablation (Sakai *et al.*, 1998, 2002; Reid and Brock, 2014; Immerzeel *et al.*, 2014a; Pellicciotti *et al.*, 2015; Steiner *et al.*, 2015; Buri *et al.*, 2016b). Additionally, other processes linked to supraglacial and englacial water systems could lead to substantial ablation (e.g., Sakai *et al.*, 2000; Miles *et al.*, 2016, 2018; Benn *et al.*, 2017; Watson *et al.*, 2018). Second, debris-covered tongues likely have a lower emergence velocity compared with debris-free tongues (Anderson and Anderson, 2016; Banerjee, 2017). As a result, similar thinning rates (surface mass balance rate minus emergence velocity) could potentially be observed for debris-covered and clean ice glaciers, though the measured mass balance rates would be more negative for clean ice.

In order to partially test the first hypothesis, there is a need to calculate the total contribution of the additional melt processes to the tongue-wide surface mass balance. In this work, we focus on the ice cliff contributions, as the processes related to the glacial water system are currently not quantifiable at the scale of a glacier tongue. For simplicity, hereafter we use the term *net ablation* instead of surface mass balance as we focus only on the ablation areas. We introduce the variable f_C , defined as the spatially integrated ratio between the net ablation from all ice cliffs and the net glacier tongue ablation, to quantify the enhanced

ablation due to the presence of ice cliffs:

$$f_C = \frac{\dot{b}_C}{\dot{b}_T} = \frac{\Delta V_C}{A_C} \times \frac{A_T}{\Delta V_T} \quad (5.1)$$

where \dot{b} is the net ablation, ΔV is the volume loss, A is the area, and the subscript refers to the cliffs (C) or the glacier tongue (T). Additionally, we define the quantity f_C^* , which is the spatially integrated ratio between net ablation from all ice cliffs, and the net ablation on all non-cliff areas on the glacier tongue (noted with the subscript NC):

$$f_C^* = \frac{\dot{b}_C}{\dot{b}_{NC}} = \frac{\Delta V_C}{A_C} \times \frac{A_{NC}}{\Delta V_{NC}} = \frac{\Delta V_C}{A_C} \times \frac{A_T - A_C}{\Delta V_T - \Delta V_C} = f_C \frac{\Delta V_T}{\Delta V_T - \Delta V_C} \frac{A_T - A_C}{A_T} \quad (5.2)$$

f_C^* has the advantage of not including the ice cliff contributions in the total tongue ablation, it is thus useful for modeling studies where sub-debris and cliff ablation are estimated independently or in order to scale the ice cliff ablation from the sub-debris ablation. f_C has the advantage of being directly linked to the total ice cliff contributions to ablation. f_C^* is expected to be larger than f_C , and both terms refer to a glacier-wide value.

Previous model-based estimates of f_C range between 6 and 14 (Sakai *et al.*, 2000; Reid and Brock, 2014; Buri *et al.*, 2016a), while values of f_C^* range between 7 (Juen *et al.*, 2014) and 12 (Sakai *et al.*, 2000). Two studies have quantified f_C using direct observations: Brun *et al.* (2016) found $f_C = 6$ over Lirung Glacier by extrapolating volume losses measured from very high resolution photogrammetry on a limited number of cliffs and Thompson *et al.* (2016) found a value of 8 by digital elevation model (DEM) differencing at Ngozumpa Glacier in the Nepalese Himalaya.

Emergence velocities (w_e) significantly greater than zero have been found previously on debris-covered glaciers, but w_e has been neglected in the calculation of f_C in all the above-mentioned studies. Values of w_e equal to $5.1\text{--}5.9 \pm 0.28 \text{ m a}^{-1}$ (Nuimura *et al.*, 2011), $0.41 \pm 0.05 \text{ m a}^{-1}$ (Vincent *et al.*, 2016) and $0.00\text{--}0.35 \pm 0.10 \text{ m a}^{-1}$ (Nuimura *et al.*, 2017) have been found for, respectively, the debris-covered tongues of Khumbu, Changri Nup and Lirung glaciers in Nepal. However, we stress the fact that these emergence velocities have been measured at different locations of these debris-covered tongues (in particular close to the clean ice/debris transition on Khumbu Glacier), on glaciers with very different dynamics. Neglecting the emergence velocities (i.e., comparing thinning rates instead of ablation rates) introduces a systematic overestimation of f_C . This is due to the fact that cliffs ablate at higher rates than the rest of the glacier tongue: ice cliff thinning rates are thus less influenced than the thinning rates of debris-covered ice when neglecting the emergence velocity. As a consequence, the ratio of the cliff thinning rate divided by the mean tongue thinning rate will overestimate f_C . To correctly estimate f_C and the fraction of total ice cliff net ablation, thinning rates need to be corrected with the emergence velocity.

Recent studies advocate the use of terrestrial photogrammetry to understand patterns of ice cliff retreat (e.g., Watson *et al.*, 2017a). Nevertheless, these data can only be collected in the field with some difficulty, and thus can only be acquired on a limited number of cliffs. Remote sensing platforms (unmanned aerial vehicles [UAVs], satellites) offer the potential to provide high resolution topographic data with a glacier-wide or region-wide coverage but have not yet been evaluated for detailed multi-temporal monitoring of ice cliffs. Here we test the possibility to use gridded elevation data (i.e. DEMs) obtained from both UAV and Pléiades imagery to assess the total ice cliff contribution to the tongue-wide net ablation.

In this study, we use three very high resolution topographic datasets based on terrestrial photogrammetry, UAV imagery, and Pléiades imagery collected over the tongue of Changri Nup Glacier, Nepal between 2015 and 2017. From the terrestrial photogrammetry, 3D models of 12 cliffs are created to calculate reference ice cliff volume losses from 2015 to 2016. We introduce a new method to calculate ice volume losses based on DEM differencing and geometric changes (e.g. ice emergence) induced by glacier flow. The new method is validated with terrestrial photogrammetric estimates of ice cliff volume loss and applied to the entire Changri Nup Glacier tongue to estimate the fraction of tongue-wide net ablation due to ice cliffs.

5.4 Study area

This study focuses on the debris-covered part of the tongue of the Changri Nup Glacier, located in the Everest region of Nepal (Fig. 5.1). The glacier accumulates mass partly through avalanche deposition from the surrounding steep slopes (up to ~ 6700 m a.s.l.) and flows down to 5250 m a.s.l. The local equilibrium line altitude (ELA) calculated for the nearby debris-free West Changri Nup Glacier is approximately 5600 m (*Sherpa et al.*, 2017). We use the same glacier tongue outline as *Vincent et al.* (2016), which was derived from a combination of UAV imagery, velocities measured on the ground and field observations. This outline is substantially different from the outline available in the Randolph Glacier Inventory 6.0 (*Pfeffer et al.*, 2014), which erroneously connects the debris-covered Changri Nup Glacier and the debris-free West Changri Nup Glacier.

Debris covers an area of 1.49 ± 0.16 km² (Fig. 5.1) on the tongue of Changri Nup Glacier. Twelve ice cliffs were ground-surveyed (Table 5.1 and Fig. 5.1), and the analysis was then extended to more than 140 ice cliffs of various sizes (Fig. 5.1). The map view area of all ice cliffs was $70 \pm 14 \times 10^3$ m², $72 \pm 14 \times 10^3$ m² and $70 \pm 14 \times 10^3$ m² in November 2015, in November 2016 and in November 2017, respectively (see section 4.4.4 for the uncertainty assessment of the cliff map view areas).

5.5 Data

5.5.1 Terrestrial photogrammetry

Terrestrial photographs of 12 ice cliffs (Table 5.1) were collected during two field campaigns: 24–28 November 2015 and 9–12 November 2016, using survey methods similar to those described in *Brun et al.* (2016) and *Watson et al.* (2017a). Between 200 and 400 photographs of each ice cliff were taken from various camera positions using a Canon EOS5D Mark II digital reflex camera with a Canon 50 mm f/2.8 fixed focal length lens (*Vincent et al.*, 2016). For each ice cliff, we derived point clouds (PCs) and triangulated irregular networks (TINs) with Agisoft Photoscan 1.3.4 Professional (*Agisoft*, 2017). In order to align the photographs and georeference the final point clouds and derived products, between 7 and 17 ground control points (GCPs) made of pink fabric were spread around each cliff. GCP positions were surveyed with a Topcon differential global positioning system (DGPS) unit with a precision of ~ 0.10 m. All markers were used as GCPs and therefore no independent markers were available for validation. After optimization of the photographs alignment, the marker residuals

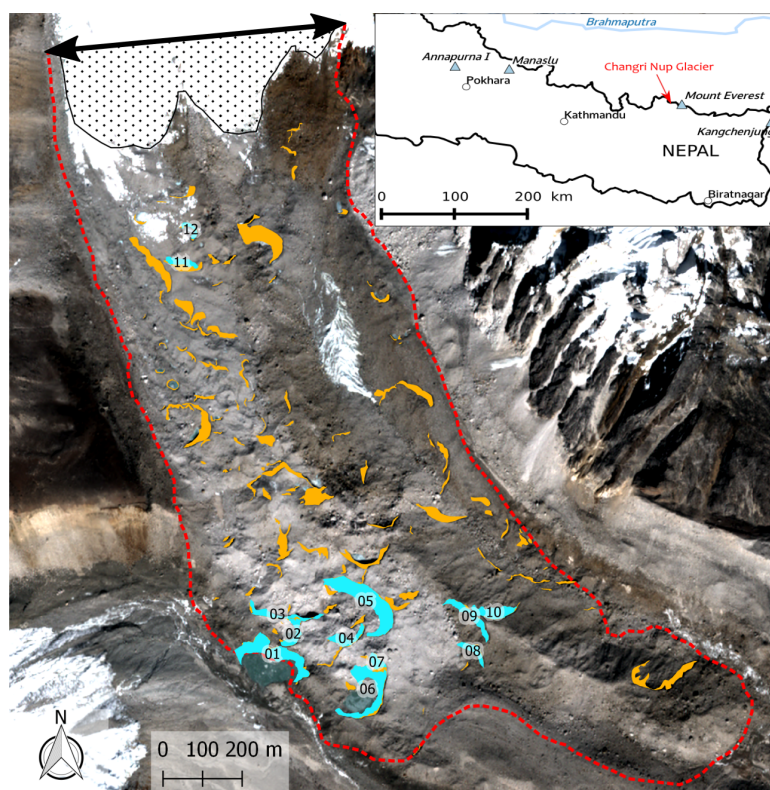


Figure 5.1: Map of Changri Nup Glacier tongue (red outline). The light blue shapes are the twelve cliffs surveyed with the terrestrial photogrammetry and the orange shapes are all the cliffs of the tongue. The background image is the Pléiades images of November 2016 (copyright: CNES 2016, Distribution Airbus D&S). The ice thickness was measured along the upper line of the glacier tongue outline in 2011 (Vincent *et al.*, 2016). The dotted area is the debris-free part of the tongue (measured on November 2017).

were on average 0.27 m for the 2015 campaign and 0.18 m for the 2016 campaign. The 3D area of the surveyed cliffs ranged from 600 m² to more than 11 000 m² (Table 5.1).

5.5.2 UAV photogrammetry

UAV imagery of Changri Nup Glacier was obtained in November 2015, November 2016, and November 2017 using the Sony Cyber-shot WX DSC-WX220 mounted on the fixed-wing eBee UAV manufactured by senseFly (Table 5.4). Aerial imagery was processed using a Structure from Motion (SfM) procedure in Agisoft Photoscan (see Vincent *et al.* (2016) and Kraaijenbrink *et al.* (2016a) for details) to produce dense point clouds. Orthomosaics (0.10 m resolution) and DEMs (0.20 m resolution) were produced for each year. Additional mission and processing details for each year are given below.

In 2015, five separate eBee flights between 22 –24 November were flown to cover the surface of the glacier. The data were georeferenced using a set of 24 GCPs that were spatially well-distributed and measured using the Topcon DGPS (Fig. 5.2). Based on 10 additional independent GCPs, the error of the 2015 UAV product was determined to be 0.04 m horizontal and 0.10 m vertical, which is in the range of expected accuracy (Gindraux *et al.*, 2017).

On 10 November 2016, Changri Nup was surveyed with three eBee flights. To georeference the 2016 UAV imagery, we distributed a total of 17 markers on the glacier and measured

Table 5.1: Characteristics of the 12 surveyed cliffs. The 3D mean area was calculated as the mean of the November 2015 and 2016 areas, which were measured from the PCs obtained with the terrestrial photogrammetry on CloudCompare. The perimeter was calculated from the cliff footprint of November 2015 and 2016. The backwasting rate was calculated as the ratio between the cliff backwasting volume obtained from terrestrial photogrammetry and the 3D mean area, for the period November 2015–November 2016. The cliffs are usually not perfectly planar and they exhibit multiple aspects. The main aspects were calculated by fitting a plan through the cliff PC or through parts of the PC in CloudCompare, the main aspect is in bold when it was possible to determine it.

Cliff ID	3D mean area [m ²]	Cliff footprint [m ²]	Footprint perimeter [m]	Elevation [m a.s.l.]	Backwasting rate [m a ⁻¹]	Main aspects (slope [degree])
Cliff 01	7543	6575	711	5330	7.5 ± 0.6	SW (44°) / S (46°) / W (39°) / NE (59°)
Cliff 02	1315	1406	260	5343	4.4 ± 0.5	SW (25°) / NW (29°)
Cliff 03	3033	1821	479	5347	4.9 ± 0.5	N (69°)
Cliff 04	1851	1774	286	5352	3.1 ± 0.4	N (42°) / NW (57°) / E (36°)
Cliff 05	11294	8592	607	5353	4.4 ± 0.5	SW (44°) / NW (51°)
Cliff 06	5267	5064	639	5331	5.9 ± 0.5	N (60°) / W (52°) / S (45°) / SW (86°)
Cliff 07	752	979	153	5350	5.6 ± 0.5	SW (41°)
Cliff 08	1282	1307	227	5325	5.8 ± 0.5	S (58°) / SW (59°)
Cliff 09	2408	2263	386	5350	5.4 ± 0.5	SW (60°) / S (46°)
Cliff 10	2426	2521	284	5338	4.5 ± 0.5	N (35°)
Cliff 11	775	630	194	5452	1.2 ± 0.4	N (38°)
Cliff 12	587	653	165	5464	2.5 ± 0.4	W (58°) / SW (50°) / S (40°)

their coordinates with the Topcon DGPS. Unfortunately, due to time constraints, the resulting spatial distribution of the markers was suboptimal (Fig. 5.2). Using only these markers as GCPs had considerable consequences for processing accuracy, and we therefore defined 16 additional virtual tie points. Tie point coordinates were sampled from the November 2015 UAV orthomosaic and DEM (Fig. 5.2), and we selected specific features on boulders that were (a) clearly identifiable on both the 2015 and 2016 image sets, and (b) located on stable terrain (*Immerzeel et al.*, 2014a), which we determined from visual inspection of the Pléiades orthoimages and DEMs.

In 2017, three separate flights were used to survey the glacier on 23 November, and 30 GCPs were collected (Fig. 5.2). Residuals, based on 6 independent check points, were 0.10 m in horizontal and 0.14 m in vertical.

5.5.3 Pléiades tri-stereo photogrammetry

Three triplets of Pléiades images were acquired over the study area on 22 November 2015, 13 November 2016, and 24 October 2017 (Table 5.5). The along-track angles of the acquisitions gave base-to-height ratios that ensured suitable stereo capabilities (e.g., *Belart et al.*, 2017). For each acquisition, we derived a 2 m DEM and a 0.5 m orthoimage using the Ames Stereo Pipeline (ASP; *Shean et al.*, 2016) using only the rational polynomial coefficients (RPCs) provided with the imagery (no GCPs) and the same processing parameters as *Marti et al.* (2016). We used the *stereo* routine of ASP to derive one PC from each triplet of images, which was gridded into a single 2 m DEM using the *point2dem* routine. Orthoimages were generated from the image closest to the nadir using the *mapproject* function and a 2 m resolution DEM, which was gap-filled with 4 and 8 m DEM resolutions derived similarly. This ensured sharp and gap-free images.

Each Pléiades orthoimage was co-registered to the corresponding UAV orthomosaic by visually matching boulders on stable ground. The accuracy of this co-registration was ex-

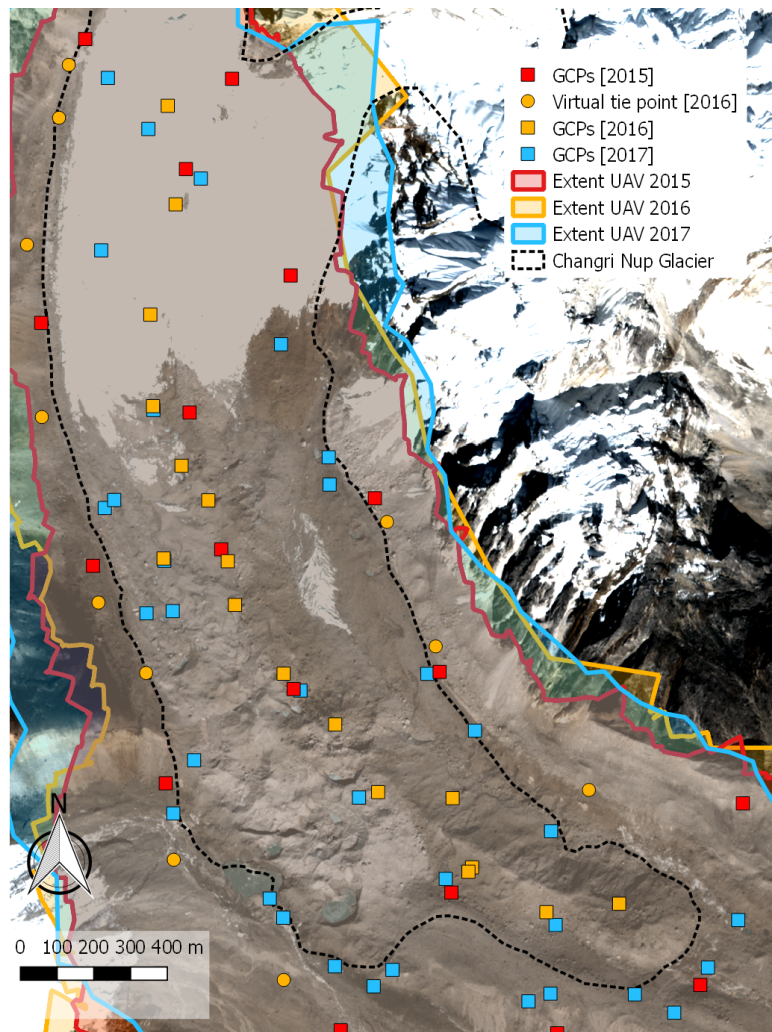


Figure 5.2: Map of Changri Nup Glacier showing the extent of the UAV DEMs and the location of the markers used. The background image is the multispectral Pléiades image of November 2016 (copyright: CNES 2016, distribution Airbus D&S).

amined by calculating the median displacement on a 2.4 km^2 area of stable terrain located off-glacier. An east to west residual displacement of 0.05 m and a north to south residual displacement of -0.09 m was identified after co-registration. This absolute co-registration was needed to compare the UAV and Pléiades datasets, but would not be necessary while working with Pléiades data only. In the latter case, the robustness of the Pléiades processing based only on RPCs would be sufficient to co-register the images and DEMs relatively using automatic co-registration methods.

Each Pléiades DEM was shifted with the same horizontal displacement as the corresponding orthoimage (Table 5.5). Automatic co-registration methods applied to the manually-shifted DEMs (Berthier *et al.*, 2007; Nuth and Kääb, 2011) resulted in no improvement of the standard deviation of elevation changes on stable terrain. Thus, no further horizontal shift was applied. The vertical shift between the two Pléiades DEMs, calculated as the median elevation change on stable terrain, was equal to -7.43 m and -3.31 m for the periods November 2015–November 2016 and November 2016–November 2017, respectively. These vertical offsets are quite large but expected, as the DEMs are derived from the orbital parameters only (Berthier *et al.*, 2014). We corrected these offsets by subtracting them from the elevation difference map. Elevation changes over stable terrain have no relation to the slope, aspect or curvature (Fig. 5.3).

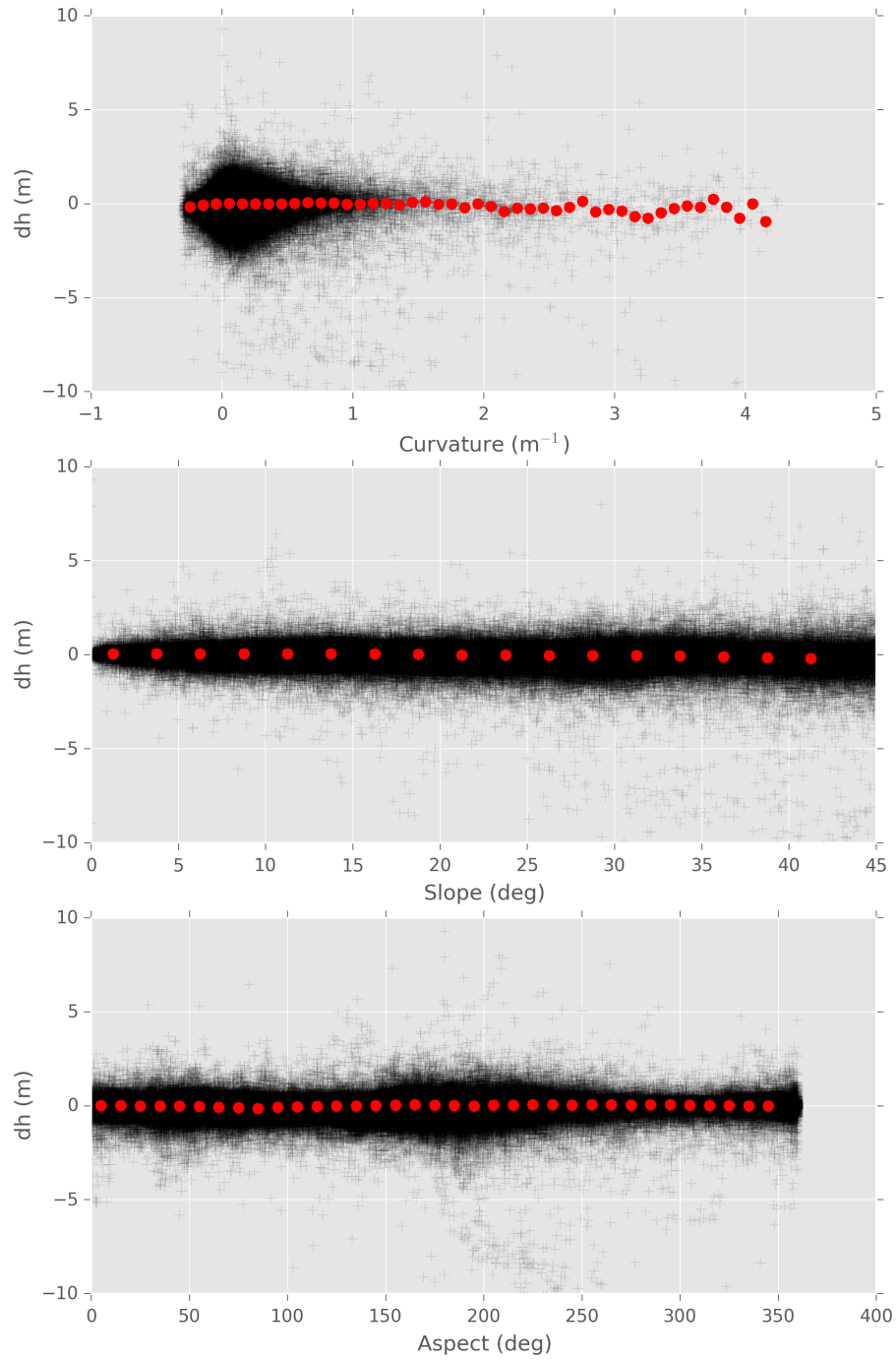


Figure 5.3: Elevation changes on stable terrain from Pléiades DEMs of November 2015 and November 2016 as a function of curvature, slope and aspect.

For these three satellite-based datasets, the duration between acquisition dates was 350 to 381 days. All displacements and volumes were linearly adjusted (divided by the number of days between the acquisition dates and multiplying by the total number of days in a year) to obtain annual velocities and change rates.

5.5.4 Update of existing datasets

We updated two datasets from *Vincent et al.* (2016): the glacier surface velocity and the cross sectional ice thickness data.

Surface velocity fields

Surface velocity fields were derived from the correlation of the Pléiades orthoimages and UAV orthomosaics using COSI-corr (*Leprince et al.*, 2007). The UAV orthomosaics were re-sampled to a resolution of 0.5 m to match the Pléiades orthoimages. For both data sets we choose an initial correlation window size of 256 pixels and a final size of 16 pixels (*Kraaijenbrink et al.*, 2016a). The step was set to 16 pixels, leading to a final grid spacing of 8 m.

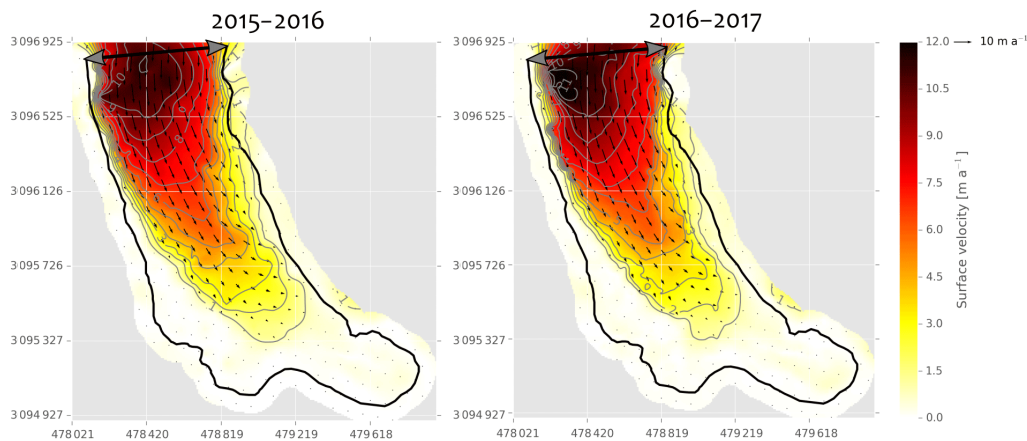


Figure 5.4: Annual horizontal velocity fields deduced from the correlation of Pléiades orthoimages. The field is linearly interpolated in the area of missing data.

The raw correlation outputs were filtered to retain pixels with a signal to noise ratio larger than 0.9. We manually removed pixels at ice cliff locations, as cliff retreat lead to large geometric changes and therefore poor correlation. These outputs were filtered with a 9×9 pixel window moving median filter and then gap-filled with a bilinear interpolation (Fig. 5.4). The patterns of displacement from UAV and Pléiades are in very good agreement. The velocities measured with Pléiades match well with the field data (ablation stake displacements measured with a DGPS between November 2015 and November 2016), with the notable exception of a stake located where the velocity gradient is high and for which the Pléiades images could not be correlated due to snow, leading to a poor bilinear interpolation (Fig. 5.5). Nevertheless, the maximum displacement in the remote sensing data (around 11 m a^{-1}) is less than that observed in the 2011–2015 field data (around 12 m a^{-1} ; *Vincent et al.*, 2016). This is due to a slowdown of the glacier that is also observed also in the 2015–2016 field data.

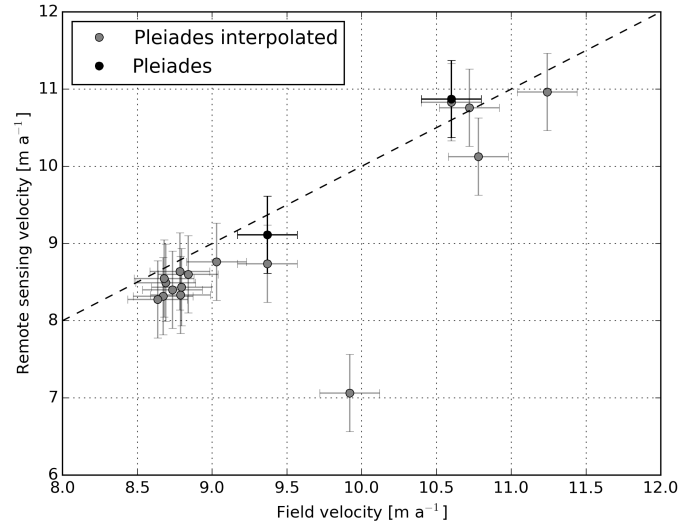


Figure 5.5: Comparison of the field measured velocity with the Pléiades measured velocity. The dashed line is the 1:1 line.

Cross section ice thickness

A cross sectional profile of ice thickness was measured upstream of the debris-covered tongue (Fig. 5.1) in October 2011, with a ground penetrating radar (GPR) working at a frequency of 4.2 MHz (Vincent *et al.*, 2016). The original cross-sectional area was 79 300 m² in 2011 and 78 200 m² in 2015 (Vincent *et al.*, 2016). Between November 2015–November 2016 and November 2016–November 2017, the cross sectional area decreased from $S_{2015-2016} = 76\,900\text{ m}^2$ to $S_{2016-2017} = 76\,340\text{ m}^2$ (with $S_{\text{yr1-yr2}}$ being the mean cross sectional area between the year 1 and 2), based on the 0.86 m a^{-1} thinning rate measured over the November 2015–November 2017 period along the profile. Following Azam *et al.* (2012), who measured the ice thickness of Chhota Shigri Glacier (15.48 km² flowing from 5830 to 4050 m a.s.l. with a maximum measured ice thickness of $\sim 270\text{ m}$) using the same methods, we estimated that the absolute uncertainty on the ice thickness is $\pm 15\text{ m}$, which leads to an uncertainty on the cross sectional area (σ_S) of $\pm 10\,000\text{ m}^2$, as the length of the cross-section is 670 m.

5.6 Methods

5.6.1 Emergence velocity

The emergence velocity refers to the upward flux of ice relatively to the glacier surface in an Eulerian reference system (Cuffey and Paterson, 2010). For the case of a glacier in steady-state (i.e., no volume change at the annual scale), the emergence velocity balances exactly the net ablation for any point of the glacier ablation area (Hooke, 2005). For a glacier out of its steady state (such as Changri Nup Glacier) the thinning rate in the ablation area is the sum of the net ablation and the emergence velocity (Hooke, 2005). On debris-covered glaciers, while the thinning rate is relatively straightforward to measure from DEM differences, for example, the ablation is highly variable in space and difficult to measure (e.g., Vincent *et al.*, 2016). In order to evaluate the mean net ablation of Changri Nup Glacier tongue from the thinning rate, we estimate mean emergence velocities (w_e) for November 2015–November 2016 and

November 2016–November 2017 using the flux gate method of *Vincent et al.* (2016). As the ice flux at the glacier front is 0, the average emergence velocity downstream of a cross-section can be calculated as the ratio of the ice flux through the cross-section (Φ in $\text{m}^3 \text{a}^{-1}$), divided by the glacier area downstream of this cross-section (A_T in m^2):

$$w_e = \frac{\Phi}{A_T} \quad (5.3)$$

This method requires an estimate of ice flux through a cross-section of the glacier, and is based here on measurements of ice depth and surface velocity along a profile upstream of the debris-covered tongue (Figs. 5.1 and 5.4). The ice flux is the product of the depth-averaged velocity (\bar{u} in m a^{-1}) and the cross-sectional area. For the periods November 2015–November 2016 and November 2016–November 2017, centerline velocities were equal to 10.8 m a^{-1} and 11.1 m a^{-1} , respectively. Assuming that mean surface velocity is usually 70 to 80 % of the centerline velocity (e.g., *Azam et al.*, 2012; *Berthier and Vincent*, 2012), this gives mean surface velocities along the upstream profile of $8.1 \pm 0.6 \text{ m a}^{-1}$ in 2015–2016, and $8.3 \pm 0.6 \text{ m a}^{-1}$ for 2016–2017. We used the relationship between the centerline velocity and the mean velocity, instead of an average of the velocity field along the cross section, because the image correlation was not successful on a relatively large fraction ($\sim 30\%$) of the cross section.

Converting the surface velocity into a depth-averaged velocity requires assumptions about basal sliding and a flow law (*Cuffey and Paterson*, 2010). Little is known about the basal conditions of Changri Nup Glacier, but *Vincent et al.* (2016) assumed a cold base, and therefore no sliding. This leads to \bar{u} being approximated as 80 % of the surface velocity, assuming $n = 3$ in Glen's flow law (*Cuffey and Paterson*, 2010). As an end-member case, assuming that the motion is entirely by slip implies \bar{u} equals to the surface velocity (*Cuffey and Paterson*, 2010). Consequently, we followed *Vincent et al.* (2016) and assumed no basal sliding, but we took the difference between the two above-mentioned cases as the uncertainty on \bar{u} . This gives $\bar{u} = 6.5 \pm 1.6 \text{ m a}^{-1}$ for 2015–2016 and $\bar{u} = 6.6 \pm 1.7 \text{ m a}^{-1}$ for 2016–2017.

Assuming that cross-sectional area (σ_S) and the depth-averaged velocity ($\sigma_{\bar{u}}$) are independent, uncertainty in the ice flux (σ_Φ) can be estimated as:

$$\frac{\sigma_\Phi}{\Phi} = \sqrt{\frac{\sigma_{\bar{u}}^2}{\bar{u}} + \frac{\sigma_S^2}{S}} \quad (5.4)$$

Given the above mentioned values for the depth-averaged velocity, the cross-sectional area and the associated uncertainties, the relative uncertainty in the estimated ice flux is $\sim 30\%$. As a result, for the November 2015–November 2016 and November 2016–November 2017 periods, the ice flux was $499\,700 \pm 150\,000 \text{ m}^3 \text{a}^{-1}$ and $503\,840 \pm 150\,000 \text{ m}^3 \text{a}^{-1}$, respectively. The glacier tongue area was considered unchanged at $1.49 \pm 0.16 \text{ km}^2$, corresponding to $w_e = 0.33 \pm 0.11 \text{ m a}^{-1}$ for 2015–2016 and $w_e = 0.34 \pm 0.11 \text{ m a}^{-1}$ for 2016–2017.

It is notoriously difficult to delineate debris-covered glacier tongues (e.g., *Frey et al.*, 2012). Uncertainty in the outline position of $\pm 20 \text{ m}$ leads to a relative uncertainty in the glacier area of 11 %, which is higher than the 5 % given by *Paul et al.* (2013). In this case, the uncertainty on the glacier outline is not the main source of uncertainty in w_e . However, if we had used automatically delineated outlines, this would be an important source of uncertainty. The updated emergence velocity is $\sim 20\%$ lower than estimated for the 2011–2015 period (*Vincent et al.*, 2016), due to both the thinning and deceleration of the glacier at the cross-section. As the difference in w_e between November 2015–November 2016 and

November 2016–November 2017 is insignificant, we consider w_e to be constant and equal to $w_e = 0.33 \pm 0.11 \text{ m a}^{-1}$ for the rest of this study. It is noteworthy that w_e is likely to be spatially variable, however, we have no means to assess its spatial variability.

5.6.2 Ice cliff backwasting calculation

Point cloud deformation

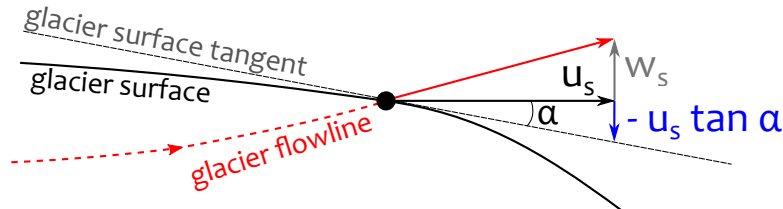


Figure 5.6: Definition of the different flow components, adapted from *Hooke* (2005).

Every point on the glacier surface moves with a horizontal velocity u_s , along a surface slope α and is advected upwards following the vertical velocity w_s (Fig. 5.6; *Hooke*, 2005; *Cuffey and Paterson*, 2010):

$$w_s = u_s \tan \alpha + w_e \quad (5.5)$$

When DEM differencing is applied, observed thinning rates at every point on the glacier surface is a combination of net ablation and displacement caused by glacier flow. In order to exclusively measure the volume loss associated with the net ablation, we deformed the PCs by displacing individual points for the datasets acquired in November 2015 and in November 2016. This accounts for three-dimensional glacier flow between November 2015 and November 2016 and between November 2016 and November 2017, respectively. For the terrestrial photogrammetry and UAV data, we applied these deformations directly to each point in the PCs. For the Pléiades data, we artificially oversampled the DEM on a 0.5 m resolution grid and converted this DEM to a PC, using the `gdal_translate` function. All the points of the PCs were displaced in x , y and z direction:

$$\begin{cases} x_{t+dt} = x_t + u_{s,x} dt \\ y_{t+dt} = y_t + u_{s,y} dt \\ z_{t+dt} = z_t + w_s dt \end{cases} \quad (5.6)$$

where $u_{s,x}$ and $u_{s,y}$ are the x and y components of the horizontal velocity, dt is the duration between the two acquisitions and z is the glacier surface elevation.

Even though w_e is likely to be spatially variable, we consider it to be homogeneous over the whole ablation tongue. The horizontal velocity u_s was directly taken from the bilinear interpolation of the Pléiades velocity field (Fig. 5.4). The term $u_s \tan \alpha$, can be expressed as:

$$u_s \tan \alpha = \frac{z(x + u_{s,x} dt, y + u_{s,y} dt) - z(x, y)}{dt} \quad (5.7)$$

As the ice flows along the longitudinal gradient instead of the rough local surface slope, we extracted z from a version of the Shuttle Radar Topography Mission (SRTM) DEM smoothed with a Gaussian filter using a 30 pixel kernel size (Fig. 5.7).

For the Pléiades and UAV data, we then gridded the deformed PCs using the `point2dem` ASP function (*Shean et al.*, 2016) and derived the associated maps of elevation changes (Figs. 5.9 and 5.10).

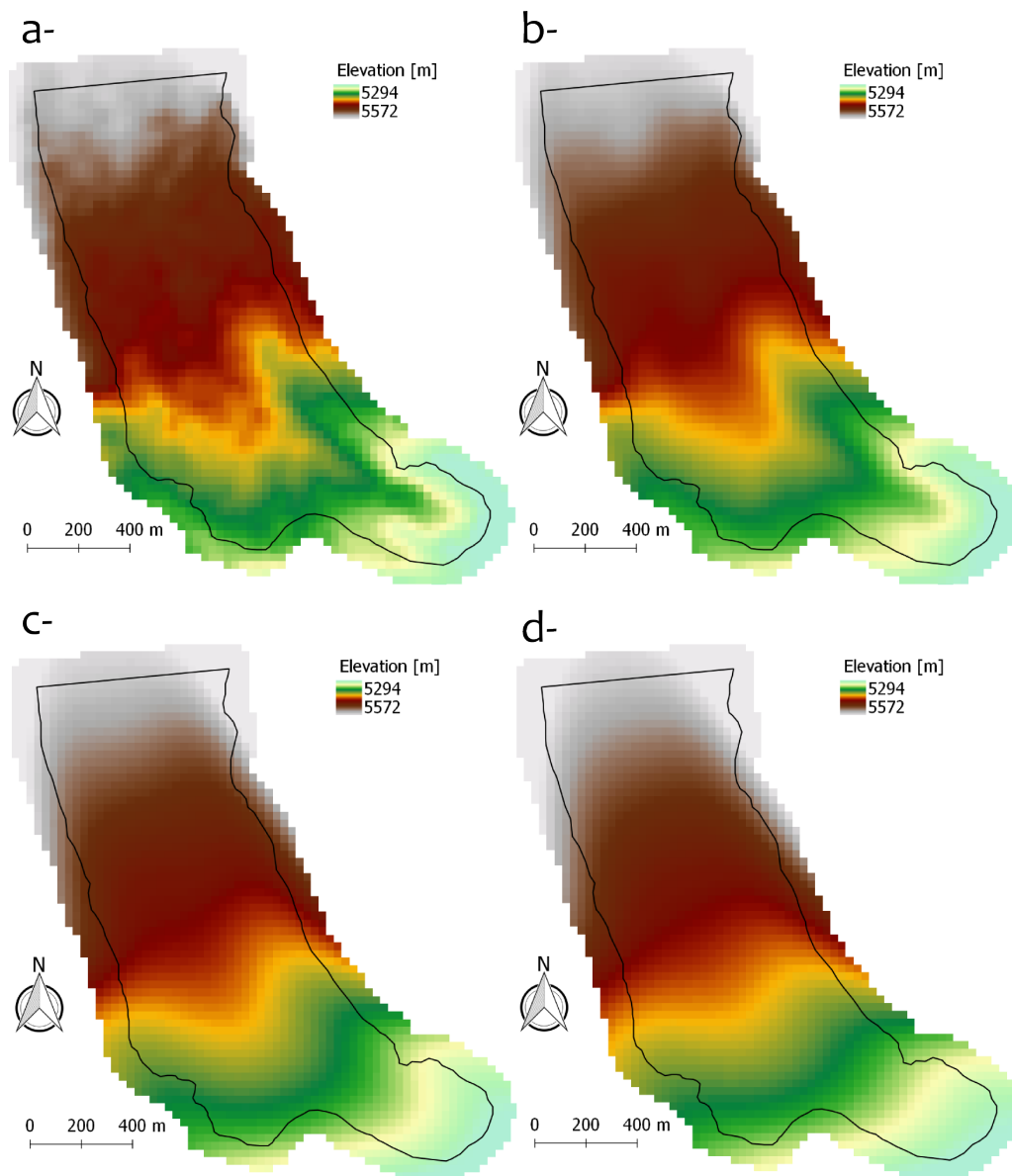


Figure 5.7: Maps of elevation of Changri Nup Glacier (black outline) obtained from the original SRTM DEM (a) and from the SRTM DEM blurred with a five (b), thirty (c) and sixty (d) pixel Gaussian kernel.

Ice cliff volume change from TINs

In order to measure the volume changes due to cliff retreat from the TINs derived from terrestrial photos, we applied the method from *Brun et al.* (2016) with some methodological improvements. First, the field of displacement was assumed to be homogeneous at the cliff scale in *Brun et al.* (2016). In this study, we use interpolated values of the local field of displacement with a resolution of 8 m. This would be an important methodological refinement for ice cliffs on fast flowing glaciers with a rotational component, but has minor influence for the cliffs of interest in this study (Fig. 5.8a). Second, we added more analogous points in the cliff edge triangulation method. Analogous points are points that are assumed to match in the two acquisitions (e.g. the corners of cliffs; Fig. 5.8b). *Brun et al.* (2016) discretized the triangulation problem assuming that the final number of points was equal on the upper and on the lower side of the cliff outline (i.e. implicitly assuming that the two corners of the cliffs were the only analogous points). In this study, the operator can choose how many analogous points are needed to link the two cliff outlines. Consequently, the method is now able to handle larger geometry changes than previously, under the assumption that some analogous parts of the cliffs are identifiable on both cliff outlines.

Ice cliff volume change from DEMs

To calculate ice cliff volume change from the DEMs, the mean elevation change was corrected for glacier flow below a cliff mask multiplied by the projected map view area of the mask. The cliff mask was defined as the union of the shapefiles of the cliff outlines, and is called the cliff footprint and noted A_{2D} hereafter. The cliff outlines were manually delineated both on the Pléiades and UAV orthoimages for November 2015, November 2016 and November 2017. For each acquisition, we used deformed outlines of November 2015 and November 2016 cliffs when working with the corresponding deformed DEM difference. We manually edited the cliff mask to make sure we included the terrain along which the cliff retreated. In particular, this implied linking the corners of the cliff outlines of the two acquisitions in many cases (Fig. 5.8c).

5.6.3 Sources of uncertainty on the ice cliff backwasting

The main sources of uncertainties on the volume loss estimates are (1) the uncertainty on the spatial distribution of the emergence velocity (σ_e); (2) uncertainties of the horizontal surface displacement (σ_d); (3) uncertainty introduced by the displacement along the slope (σ_w); (4) uncertainties of the cliff outlines delineation (σ_m) and (5) uncertainties of the various representations of the glacier surface in TINs and DEMs (σ_z). The first, second and third sources of uncertainties are common to the three datasets and the third and fourth ones are specific to each dataset. We assume these five sources of uncertainty to be independent.

Emergence velocity

We calculated a mean emergence velocity for the tongue of $0.33 \pm 0.11 \text{ m a}^{-1}$, but as the spatial variability was unknown extreme values of emergence velocities were tested to estimate σ_e . We choose 0.00 m a^{-1} as a lower limit because the emergence velocity is positive in the ablation area (*Hooke, 2005; Cuffey and Paterson, 2010*). For a thinning glacier, the net

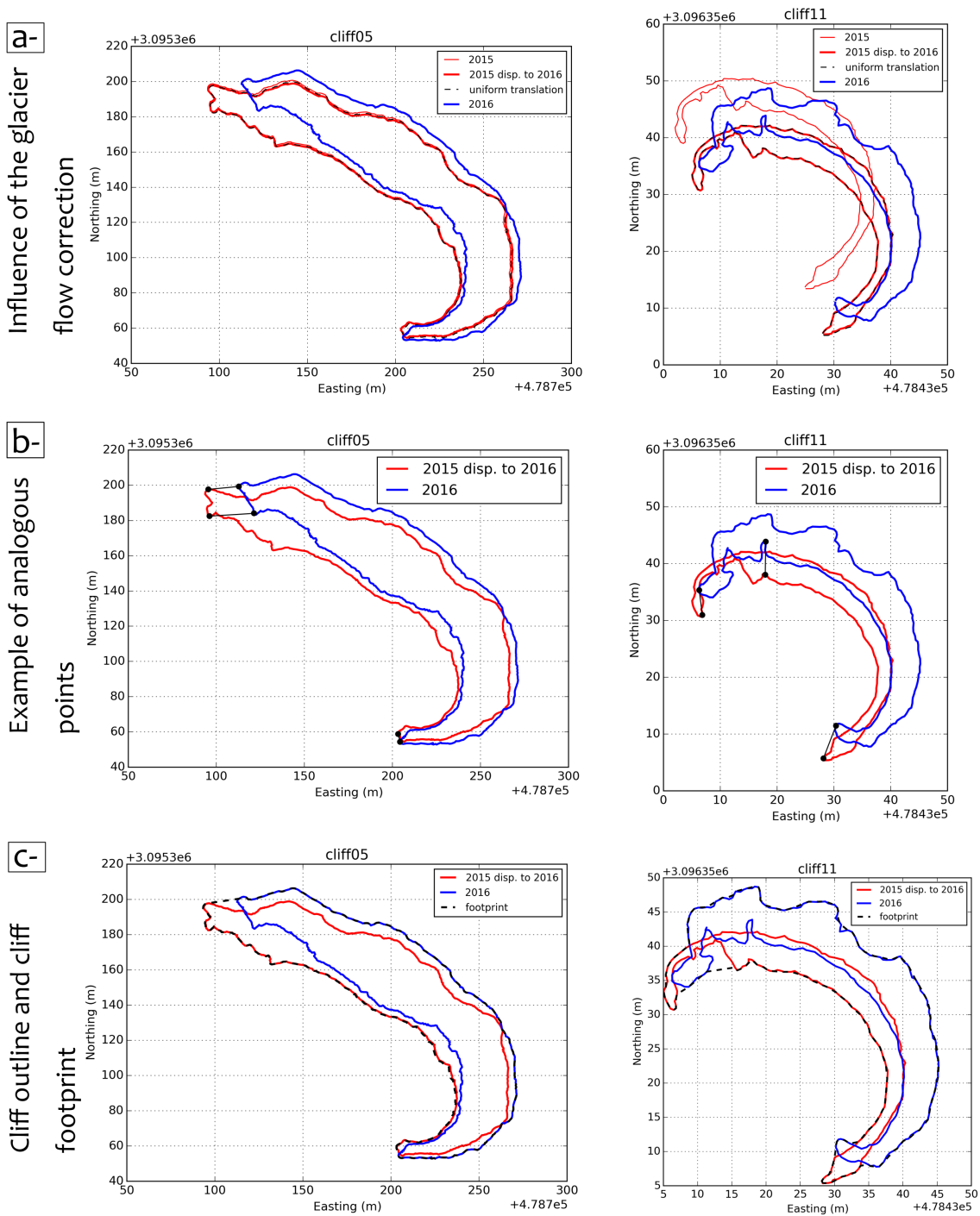


Figure 5.8: Examples of the methodological processing for cliff 05, located on a slow flowing area (left panels) and cliff 11, located in a fast flowing area (right panels). For all the panels the cliff outlines are represented in UTM45/WGS84. a- influence of the glacier flow correction, and comparison with a uniform translation. B- example of analogous points needed for the triangulation regularization. c- difference between the individual cliff outlines and the cliff footprint needed to calculate the cliff contribution for gridded data (DEMs).

ablation is higher than the emergence velocity (e.g., *Hooke, 2005*), consequently, the net ablation can be used as a proxy for the upper bound for the emergence velocity. The maximum net ablation measured with stakes within the period 2014–2016 on the tongue of Changri Nup (2.22 m a^{-1}) was chosen as the upper limit (*Vincent et al., 2016*). We tested these values on the terrestrial photogrammetry-based volume change estimate of each cliff (Fig. 5.11a). Except for cliff 11, the relative volume change that resulted from the test was always below +40 % for an increase in the emergence velocity and -5 % for a decrease in the emergence velocity. Cliff 11 likely exhibits a high sensitivity to the emergence velocity due to its relatively shallow slope and its very small volume loss (Tables 5.1 and 5.2). The tested range of values of emergence velocities is rather extreme for the case of Changri Nup Glacier, and we therefore assumed that the uncertainty due to the emergence velocity was equal to the median of the relative volume change for an increase in the emergence velocity (23 %). As a consequence, $\sigma_e = 0.23V$, where V is the cliff volume change.

Horizontal displacement

The quality of the horizontal surface displacement derived from Pléiades orthoimages was evaluated by comparison with field measurements of the surface displacement. The median of the absolute difference between the 16 field measurements (stakes and marked rocks) and the corresponding Pléiades measurements was 30.8 cm. We therefore assumed that the uncertainty introduced by the horizontal displacement (σ_d) is 30 cm. The conversion into volumetric uncertainty, σ_d , was made by multiplying this uncertainty by the cliff 3D area (A_{3D}) for the terrestrial photogrammetry and by the cliff footprint area (A_{2D}) for the UAV and Pléiades (Table 5.1).

Displacement along the glacier slope

The uncertainty on $u_s \tan \alpha$ depends mostly on the uncertainty on the mean slope of the surrounding glacierized surface (*Hooke, 2005*). Kernel sizes of 5 and 60 pixels used to filter the SRTM DEM produced respective mean elevation changes on the cliff mask of -0.51 and -0.33 m a^{-1} . As these values correspond to relatively sharp and very smooth DEMs, half of the difference between these two values (10 cm) is a good proxy for the uncertainty due to this correction. We converted this uncertainty into a volumetric uncertainty (σ_w) by multiplying it by the cliff 3D area (A_{3D}) for the terrestrial photogrammetry and by the cliff footprint area (A_{2D}) for the UAV and Pléiades.

Cliff mapping

The uncertainty on the cliff mapping from Pléiades orthoimages was empirically assessed by asking eight different operators (most of the co-authors of this study) to map six cliffs for which we had reference outlines from the terrestrial photogrammetry. The operators had access to the Pléiades orthoimage of November 2016 and to the corresponding slope map. We calculated a normalized length difference defined as the difference between the area mapped by the operator and the reference area divided by the outline perimeter. The median normalized length difference ranged between -0.7 and 1.7 m , and was on average equal to 0.6 m , meaning that the operators systematically overestimated the cliff area. The mean of the absolute value of the median normalized length difference was 0.8 m , which

was used as an estimate for the cliff area delineation uncertainty. We conservatively assumed the same value for the Pléiades orthoimages and UAV orthomosaics, even though it should be lower for the UAV orthomosaics because of their higher resolution. For the terrestrial photogrammetry data, we assumed no uncertainty on the cliff area. The volumetric uncertainty σ_m was obtained by multiplying this value by the perimeter of cliff footprint and by the mean elevation change from DEM differences for UAV and Pléiades.

Accuracy of the topographic data

The uncertainty on the vertical accuracy of the terrestrial photogrammetry was directly estimated as the mean of the GCPs residual of all cliffs (0.21 m). For the UAV and Pléiades orthoimages we followed the classical assumption of partially correlated errors (*Fischer et al.*, 2015; *Rolstad et al.*, 2009) and therefore σ_z is given by:

$$\sigma_z = \begin{cases} A_{2D}\sigma_{\Delta h}\sqrt{\frac{A_{cor}}{5A_{2D}}} & ; A_{2D} \geq A_{cor} \\ A_{2D}\sigma_{\Delta h} & ; A_{2D} < A_{cor} \end{cases} \quad (5.8)$$

where $A_{cor} = \pi L^2$, with L being the decorrelation length and $\sigma_{\Delta h}$ being the normalized median of absolute difference (NMAD; *Höhle and Höhle*, 2009) of the elevation difference on stable ground. We experimentally determined $L = 150$ m for both the UAV and Pléiades data, even though the spherical model was not fitting the Pléiades semi-variogram very well. We found $\sigma_{\Delta h} = 0.27$ m for the UAV and 0.36 m for Pléiades.

Under the assumption that the different sources of uncertainty are independent, the final uncertainty on the volume estimate σ_V is:

$$\sigma_V = \sqrt{\sigma_e^2 + \sigma_d^2 + \sigma_w^2 + \sigma_m^2 + \sigma_z^2} \quad (5.9)$$

5.7 Results

5.7.1 Comparison of TIN based and DEM based estimates

The volume changes estimated from terrestrial photogrammetry (our reference) and from UAV / Pléiades data are in good agreement and within error bars (Table 5.2 and Fig. 5.12). The total volume loss estimated for these twelve cliffs for the period November 2015–November 2016 is $193\,453 \pm 19\,647 \text{ m}^3 \text{ a}^{-1}$ using terrestrial photogrammetry and $188\,270 \pm 20\,417 \text{ m}^3 \text{ a}^{-1}$ and $181\,744 \pm 19\,436 \text{ m}^3 \text{ a}^{-1}$ using UAV and Pléiades, respectively. The total relative difference is therefore -3 % for the UAV and -7 % for Pléiades, which is smaller than the uncertainty on each estimate (~ 10 %, calculated as the quadratic sum of the twelve individual cliff uncertainty estimates, assumed to be independent). The total Pléiades and UAV estimates are lower than the reference estimate, nevertheless, this is probably due to the estimate of the largest cliff (cliff 01), as there is no systematic under estimation of the volume for individual cliffs (Fig. 5.12).

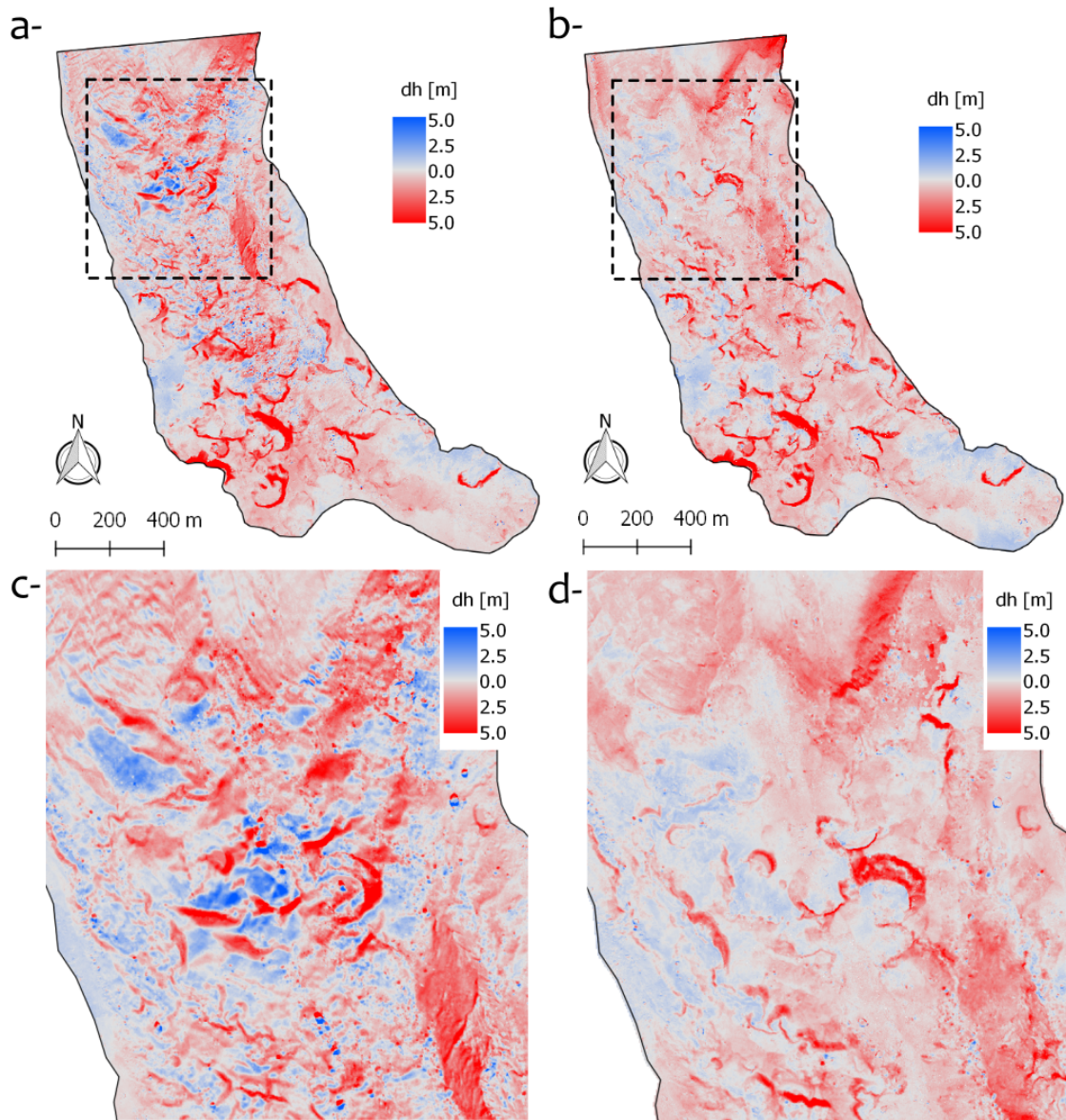


Figure 5.9: Panels showing maps of: raw elevation change for UAV (a, c), elevation change corrected from flow for UAV (b, d). The panels c and d correspond to a zoom in the dashed rectangle (a).

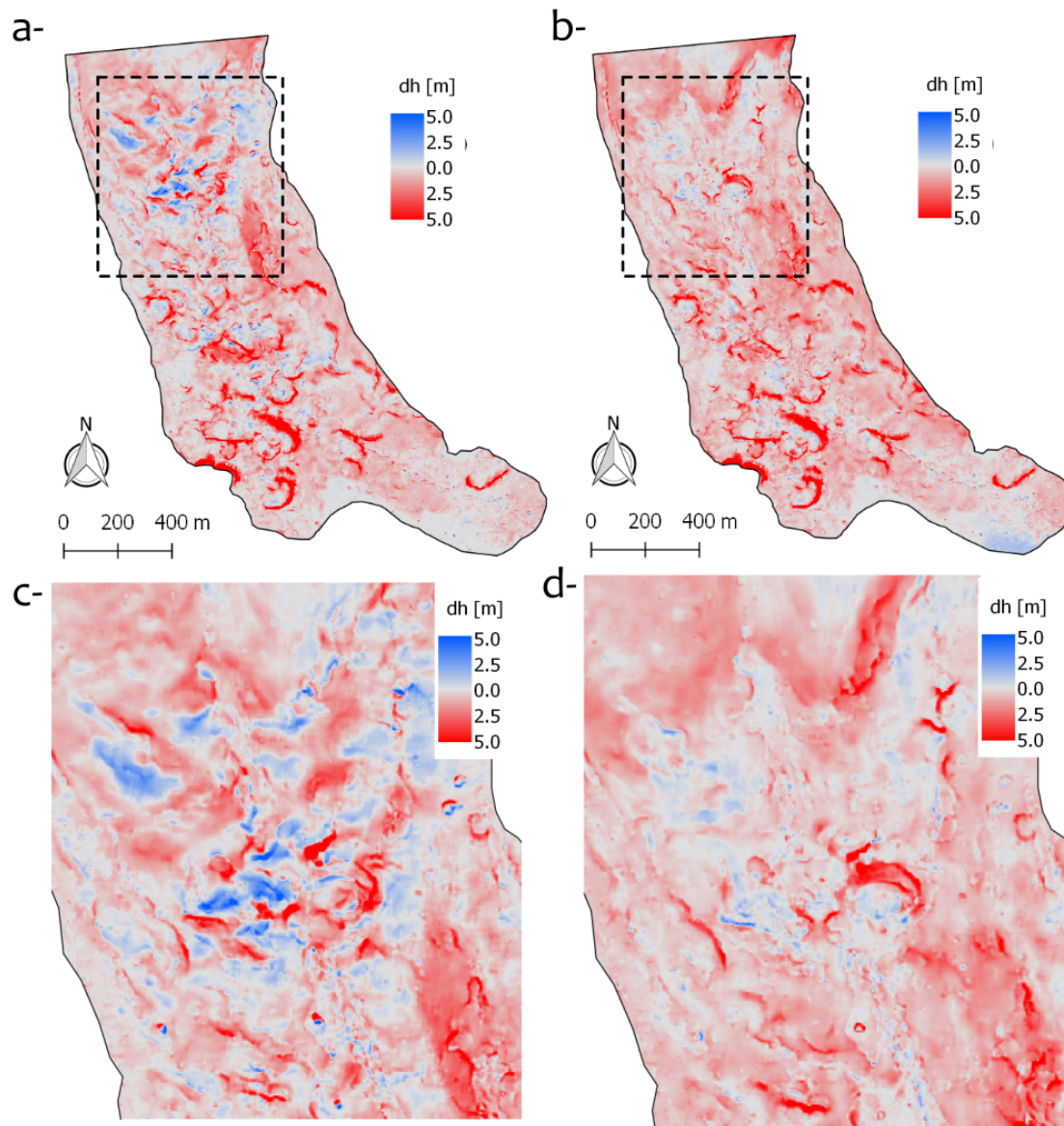


Figure 5.10: Panels showing maps of: raw elevation change for Pléiades (a, c), elevation change corrected from flow for Pléiades (b, d). The panels c and d correspond to a zoom in the dashed rectangle (a).

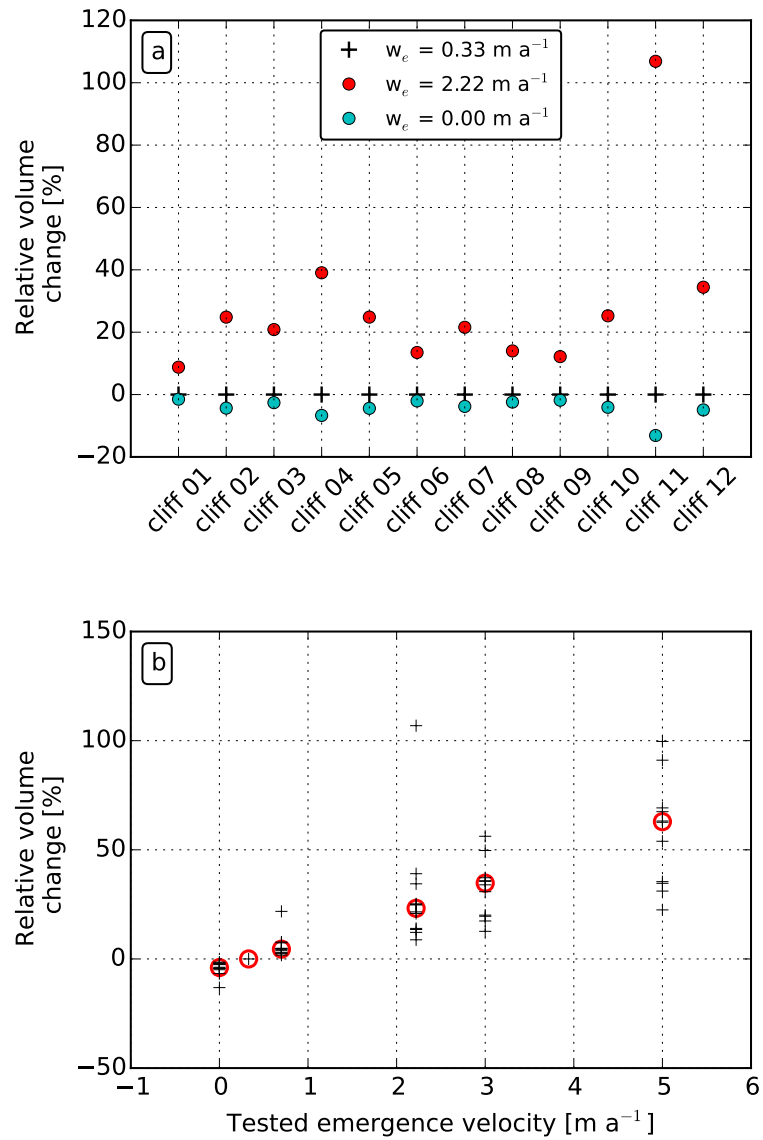


Figure 5.11: Sensitivity of the normalized volume change estimate to the emergence velocity for each cliff with two tested emergence velocities (a) and for all cliffs with various emergence velocities tested (b). In the latter, each cross represent a cliff and the open circles represent the median, note that cliff 11 relative volume change is not visible for emergence velocities higher than 2.2 m a^{-1} , because it is more than 150 %. The volume estimates are from terrestrial photogrammetry data.

Table 5.2: Volume loss from the three methods for each cliff

Cliff ID	Volume terrestrial photogrammetry [m ³ a ⁻¹]	Volume UAV [m ³ a ⁻¹]	Volume Pléiades [m ³ a ⁻¹]
Cliff 01	54066 ± 12735	51587 ± 12946	44259 ± 11303
Cliff 02	5538 ± 1361	5726 ± 1664	6464 ± 1877
Cliff 03	14374 ± 3486	9460 ± 3038	10345 ± 3318
Cliff 04	47771 ± 11733	49691 ± 12258	48075 ± 12066
Cliff 05	5543 ± 1442	6136 ± 1767	6802 ± 1975
Cliff 06	12562 ± 3020	13224 ± 3651	13459 ± 3736
Cliff 07	7146 ± 1709	7496 ± 2080	7762 ± 2169
Cliff 08	29685 ± 7092	29315 ± 7635	28748 ± 7596
Cliff 09	4034 ± 967	4203 ± 1167	3838 ± 1104
Cliff 10	10439 ± 2559	9143 ± 2472	10485 ± 2845
Cliff 11	1398 ± 386	1747 ± 595	1000 ± 431
Cliff 12	899 ± 350	542 ± 311	507 ± 339
Total	193453 ± 19647	188270 ± 20417	181744 ± 19436

5.7.2 Sensitivity to the emergence velocity

As Changri Nup Glacier is a slow flowing glacier, the emergence velocity is small and the associated uncertainty is low (Fig. 5.11a). Nevertheless, with our dataset it is possible to explore more extreme emergence velocities up to 5 m a⁻¹, which is a value inferred for a part of the Khumbu Glacier tongue and which is also the maximum emergence velocity measured on a debris-covered tongue (*Nuimura et al.*, 2011). Our results show that, as a rule of thumb, every 1 m a⁻¹ error on the emergence velocity would increase the one-year volume change estimate by 10 % (Fig. 5.11b). It is noteworthy that the main source of uncertainty on the cliff volume change is the uncertainty on the emergence velocity.

5.7.3 Importance of the glacier flow corrections

In order to check the internal consistency of the glacier flow correction, we calculated mean net ablation over the glacier tongue (the mean rate of elevation change minus the emergence velocity) before and after corrections. For the period November 2015–November 2016, without flow correction the mean tongue net ablation was equal to -1.07 ± 0.27 m a⁻¹ and -1.18 ± 0.36 m a⁻¹ for the UAV and Pléiades DEM differences, respectively. After the glacier flow correction (Eq. 5.6), the mean tongue net ablation was equal to -1.10 ± 0.27 m a⁻¹ and -1.20 ± 0.36 m a⁻¹ for the UAV and Pléiades data, respectively. The very good consistency between each estimate lends confidence to the fact that our glacier flow correction conserves mass. The same consistency was found for the period November 2016–November 2017.

For individual cliffs, the contribution of the glacier flow corrections were small relative to the uncertainties (Fig. 5.12), except for cliff 11 and 12 that experienced a small volume change. These two cliffs are also located in the fastest flowing part of the glacier tongue. The low magnitude of the glacier flow correction is a result of (1) the small displacements of most of the cliffs and (2) the vertical displacement due to slope, which tended to compensate for the emergence velocity (Fig. 5.6). Nevertheless, for the two smallest and fast moving cliffs

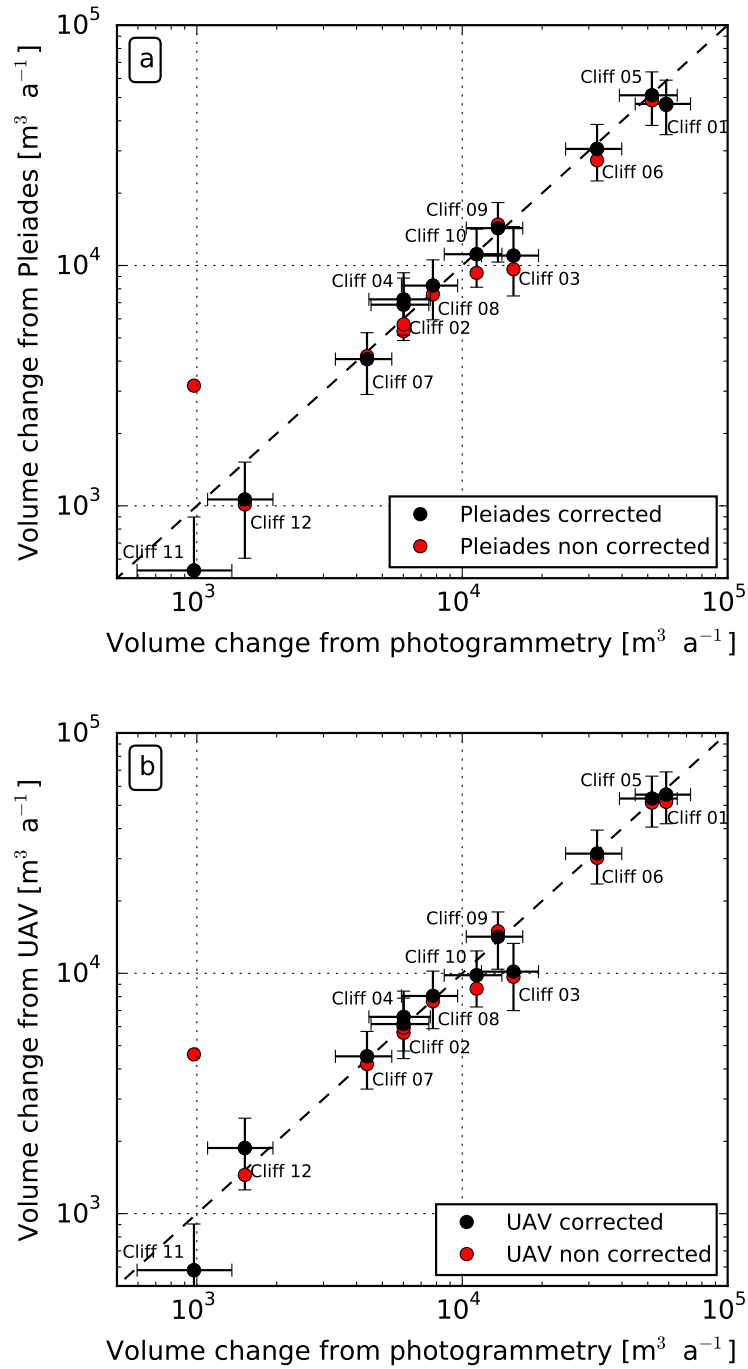


Figure 5.12: Comparison of the ice cliff volume changes estimated from DEM differences between Pléiades (a) or UAV (b) and terrestrial photogrammetry. Note the log scale. For each panel, "corrected" means taking into account the geometric corrections due to glacier flow and "non corrected" means neglecting them.

(cliffs 11 and 12), these corrections were much larger and resulted in improved estimates of volume change for both Pléiades and UAV data (Fig. 5.12).

5.7.4 Total contribution of ice cliffs to the glacier tongue net ablation for the period November 2015–November 2016

In addition to the 12 cliffs mapped in the field, we manually mapped 132 additional ice cliffs from the Pléiades and UAV orthoimages and slope maps. The total map view cliff footprint area from November 2015 and November 2016 was $113 \pm 21 \times 10^3 \text{ m}^2$, i.e. 7.4 % of the total tongue map view area. Averaged over this cliff mask, the UAV (respectively Pléiades) rate of elevation change corrected from glacier flow and emergence was $-3.88 \pm 0.27 \text{ m a}^{-1}$ (respectively $-3.91 \pm 0.36 \text{ m a}^{-1}$). This corresponds to a total average volume loss at ice cliffs of $440 \pm 54 \times 10^3 \text{ m}^3 \text{ a}^{-1}$.

The three largest cliffs contribute to almost 40 % of the total net ablation from cliffs (Fig. 5.13). As there is some variability in the rate of cliff thinning, the volume change of each cliff is not always directly related to its area (Figs. 5.13 and 5.14). Nevertheless, the largest cliffs dominate the volume loss, as 80 % of the total cliff contribution originates from the 20 largest cliffs in our study and all the cliffs below $2\,000 \text{ m}^2$ (i.e., the 120 smallest cliffs) contribute to less than 20 % of the total volume loss (Fig. 5.13).

For the same period the tongue-averaged rate of elevation change was $-0.79 \pm 0.21 \text{ m a}^{-1}$ (average of the UAV and Pléiades thinning rates). After adding the emergence velocity, this corresponds to a net glacier tongue ablation of $1.12 \pm 0.21 \text{ m a}^{-1}$ or a volume loss of $1.9 \pm 0.2 \times 10^6 \text{ m}^3 \text{ a}^{-1}$. Consequently, the fraction of total net glacier tongue ablation due to cliffs was $23 \pm 5 \%$, these cliffs covered only 7.4 % of the tongue area. The factors f_C and f_C^* were thus equal to 3.1 ± 0.6 and 3.7 ± 0.7 , respectively.

5.7.5 Total contribution of ice cliffs to the glacier tongue net ablation for the period November 2016–November 2017

For the period November 2016–November 2017, we relied on the Pléiades and UAV data only. The cliff footprint area from November 2016 and November 2017 was $120 \pm 21 \times 10^3 \text{ m}^2$, i.e. 7.8 % of the total tongue area. Averaged over this cliff mask, the UAV (respectively Pléiades) rate of elevation change corrected for glacier flow and emergence was $-4.76 \pm 0.27 \text{ m a}^{-1}$ ($-4.43 \pm 0.36 \text{ m a}^{-1}$). The average from the Pléiades and UAV data gives a total ice cliff volume loss of $550 \pm 66 \times 10^3 \text{ m}^3 \text{ a}^{-1}$.

The average thinning rate over the terminus was $-1.18 \pm 0.21 \text{ m a}^{-1}$ (average of the UAV and Pléiades thinning rates). This corresponds to a net glacier tongue ablation of $1.51 \pm 0.21 \text{ m a}^{-1}$, after correction for the emergence, or a total volume loss of $2.3 \pm 0.2 \times 10^6 \text{ m}^3 \text{ a}^{-1}$. Consequently, between 2016 and 2017 ice cliffs contributed to $24 \pm 5 \%$ of the net glacier tongue ablation. The factors f_C and f_C^* were thus equal to 3.0 ± 0.6 and 3.6 ± 0.7 , respectively.

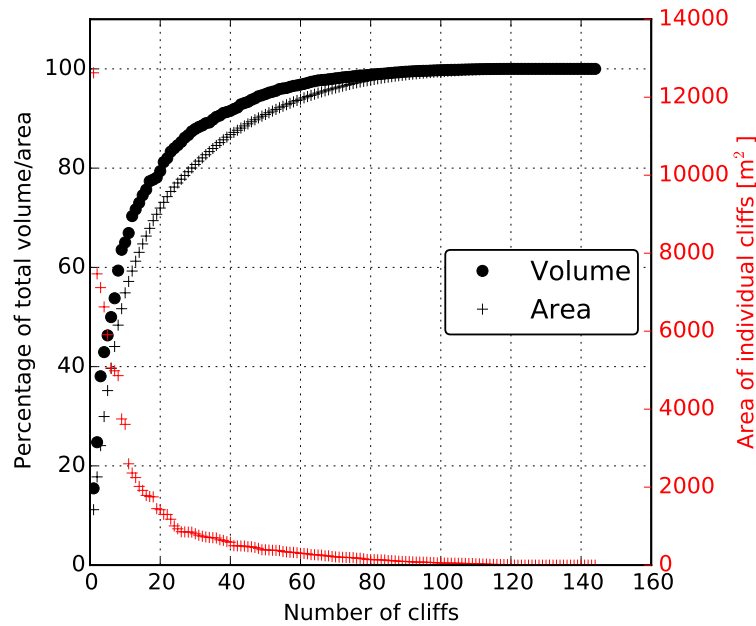


Figure 5.13: Individual ice cliff contributions for the period November 2015–November 2016 based on the UAV data. The left axis shows the cumulative volume (black dots) and area (black crosses), expressed as a percentage of the total volume or area, respectively.

5.8 Discussion

5.8.1 Cliff evolution and comparison of two years of acquisition

The total area covered by ice cliffs did not vary significantly from year to year, ranging from $70 \pm 14 \times 10^3 \text{ m}^2$ in November 2015 and 2017 to $71 \pm 14 \times 10^3 \text{ m}^2$ in November 2016. The twelve individual cliffs surveyed showed substantial variations in area within the course of one year, with a maximum increase of 57 % for the large cliff 06 and a decrease of 34 % for cliffs 03 and 09 (Table 5.3). The total area of these twelve cliffs increased by 8 % in one year. Interestingly, over the same period, *Watson et al.* (2017a) observed only declining ice cliff area on the tongue of Khumbu Glacier ($\sim 6 \text{ km}$ away), suggesting a lack of regional consistency. All the large cliffs (most of them are included in the twelve cliffs surveyed with the terrestrial photogrammetry) persisted over two years of survey, including the south or south-west facing ones (Table 5.1), although south facing cliffs are known to persist less than non south facing ones (*Buri and Pellicciotti, 2018*). However, we observed the appearance and disappearance of small cliffs, and terrain that was difficult to classify as cliff or non-cliff, highlighting the challenge in mapping regions covered by thin debris (e.g., *Herreid and Pellicciotti, 2018*).

We calculated backwasting rates for the twelve cliffs monitored with terrestrial photogrammetry for the period November 2015–November 2016 (Table 5.1). The backwasting rate is sensitive to cliff area changes (because it is calculated as the rate of volume change divided by the mean 3D area) and should be interpreted with caution for cliffs that underwent large area changes (e.g., cliffs 01, 02, 03, 06, 09 and 11; Table 5.3). The backwasting rates ranged from 1.2 ± 0.4 to $7.5 \pm 0.6 \text{ m a}^{-1}$, reflecting the variability in terms of ablation rates among the terrain classified as cliff (Fig. 5.14). The lowest backwasting rates are observed for cliffs 11 and 12, located on the upper part of the tongue, roughly 100 m higher than the other cliffs (Fig. 5.1 and Table 5.1). The largest backwasting rates were observed for cliff 01,

Table 5.3: 3D area changes of the twelve field monitored cliffs

Cliff ID	Area 2015 [m ²]	Area 2016 [m ²]	Relative area change (%)
Cliff 01	6126	8961	46
Cliff 02	1135	1496	32
Cliff 03	3650	2415	-34
Cliff 04	1915	1788	-7
Cliff 05	11323	11265	-1
Cliff 06	4099	6435	57
Cliff 07	749	756	1
Cliff 08	1286	1278	-1
Cliff 09	2897	1918	-34
Cliff 10	2659	2192	-18
Cliff 11	466	707	52
Cliff 12	818	732	-11
Total	37124	39942	8

which expanded significantly between November 2015 and November 2016. The backwasting rates are lower than those reported by *Brun et al.* (2016) on Lirung Glacier (Langtang catchment) for the period May 2013–October 2014, which ranged from 6.0 to 8.4 m a⁻¹ and lower than those reported by *Watson et al.* (2017a) on Khumbu Glacier for the period November 2015–October 2016, which ranged from 5.2 to 9.7 m a⁻¹ (we reported the values for cliffs which survived over their entire study period only). These differences are likely due to temperature differences between sites. Indeed, the cliffs studied here are at higher elevation (5320–5470 m a.s.l.) than the two other studies (4050–4200 m a.s.l. for Lirung Glacier and 4923–4939 m a.s.l. for Khumbu Glacier).

While a comparison between only two years of data cannot be used to extrapolate our results in time, we note the similarity between the total ice cliff contribution to net ablation (23 ± 5 % and 24 ± 5 % in November 2015–November 2016 and November 2016–November 2017, respectively). In contrast, total net ablation of the Changri Nup Glacier tongue was ~25 % higher for the period November 2016–November 2017 than for the period November 2015–November 2016. While a difference in meteorological conditions between these two years is a likely cause of the greater ablation totals, the ice cliffs seem to contribute a constant share to the total ablation.

5.8.2 Influence of emergence velocity and glacier flow correction on f_C and f_C^*

In most studies quantifying ice cliff ablation (*Brun et al.*, 2016; *Thompson et al.*, 2016), the glacier thinning rate was assumed to be directly equal to the net ablation rate, i.e. emergence velocity was assumed to be zero. If we make the same assumption (but still include the corrections for horizontal displacement and the vertical displacement due to the slope), we find a mean thinning rate of 0.80 ± 0.10 m a⁻¹ for the tongue and of 3.59 ± 0.17 m a⁻¹ for the cliffs (average of UAV and Pléiades data) for the period November 2015–November 2016. This results in calculated values of $f_C = 4.5 \pm 0.6$ (and $f_C^* = 5.4 \pm 0.7$), which is 50 % higher than the actual value. Ice cliffs would thus contribute to ~34 % of the total tongue ablation. For the period November 2016–November 2017, the same assumption results in $f_C = 3.6 \pm 0.6$ (and $f_C^* = 4.3 \pm 0.7$), and an ice cliff contribution of ~29 % to the total tongue

ablation. Neglecting w_e might partially explain why previous studies found significantly higher values of f_C , and our results stress need to estimate and take into account ice flow emergence, even for nearly-stagnant glacier tongues like Changri Nup Glacier (see Discussion below).

Values of f_C and f_C^* not corrected for the emergence velocity can be compared to the previous observational estimates. Both *Brun et al. (2016)* and *Thompson et al. (2016)* found values higher than our estimates. Part of the difference might arise from the different climatological settings, as Lirung and Ngozumpa glaciers are located at lower elevation than Changri Nup Glacier.

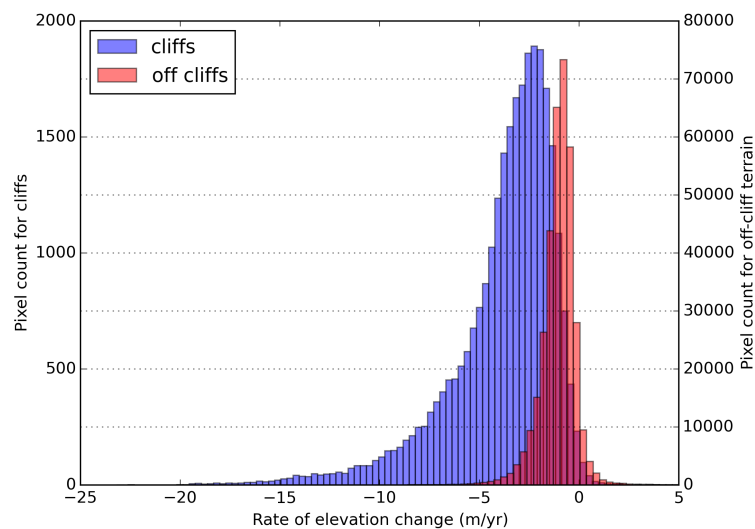


Figure 5.14: Rate of glacier surface elevation change for cliff and off-cliff terrain (Pléiades DEM difference November 2015–November 2016, corrected from flow). Note the strongly different Y axis.

5.8.3 Ice cliff ablation and the debris-cover anomaly

Between November 2011 and November 2015, *Vincent et al. (2016)* quantified the reduction of area-averaged net ablation over the glacier tongue due to debris-cover. They obtained a tongue-wide net ablation of $-1.2 \text{ m w.e. a}^{-1}$ and $-3.0 \text{ m w.e. a}^{-1}$ with and without debris, respectively. As demonstrated in this study, ice cliffs ablate at $-3.5 \text{ m w.e. a}^{-1}$, ~ 3.6 times faster than the non-cliff terrain of the debris-covered tongue for the period November 2015–November 2016, and ~ 1.2 times faster than the tongue if it was entirely debris-free. Consequently, approximately 75 % of the tongue would have to be covered by ice cliffs to compensate for the lower ablation rate under debris and to achieve the same overall ablation rate as a clean ice glacier under similar conditions. Since ice cliffs typically cover a very limited area (*Herreid and Pellicciotti, 2018*), it is unlikely that they can enhance the ablation of debris-covered tongues enough to reach the level of ablation of ice-free tongues.

Other ablation-related processes such as supra-glacial ponds (*Miles et al., 2016*) or englacial ablation (*Benn et al., 2012*) may contribute to higher ablation rates than what can be expected on the basis of the Østrem curve. Yet the contribution of these processes is not sufficient to enhance the ablation of the debris-covered tongue of Changri Nup Glacier at the level of clean ice ablation, as *Vincent et al. (2016)* already showed that the insulating effect of debris

dominates for this glacier. As a consequence, and based on this case study, we hypothesize that the reason for similar thinning rates over debris-covered and debris-free areas, i.e. the "debris-cover anomaly", is largely related to a reduced emergence velocity compensating for a reduced ablation due to the debris mantle.

This hypothesis currently applies to the Changri Nup Glacier tongue only, and it is unclear if it can be extended to the debris cover anomaly identified at larger scales. The high quality data available for Changri Nup Glacier are not available for other glaciers at the moment, and we thus provide a theoretical discussion below.

The mass conservation equation (e.g., *Cuffey and Paterson, 2010*) gives the link between thinning rate ($\overline{\frac{\partial h}{\partial t}}$ in m a^{-1}), ablation rate and emergence velocity for a glacier tongue:

$$\overline{\frac{\partial h}{\partial t}} = -\frac{1}{\rho} \dot{b} + \frac{\Phi}{A} \quad (5.10)$$

where Φ ($\text{m}^3 \text{a}^{-1}$) is the ice flux entering in the tongue of area A (m^2), ρ is the ice density (kg m^{-3}), and \dot{b} is the area-averaged tongue net ablation ($\text{kg m}^{-2} \text{a}^{-1}$ or m w.e. a^{-1}).

Consider two glaciers with tongues that are either debris-covered (case 1- referred hereafter as "DC") or debris-free (case 2 – referred hereafter as "DF"), and similar ice fluxes entering at the ELA i.e., $\Phi_{\text{DC}} = \Phi_{\text{DF}}$. The ice flux at the ELA is expected to be driven by accumulation processes, and it is reasonable to assume similarity for both debris-covered and debris-free glaciers. There is a clear link between the glacier tongue area and its mean emergence velocity: the larger the tongue, the lower the emergence velocity. These theoretical considerations have been developed by *Banerjee (2017)* and *Anderson and Anderson (2016)*, the latter demonstrating that debris-covered glacier lengths could double, depending on the debris effect on ablation in their model. Real-world evidence for such differences in debris-covered and debris-free glacier geometry remain largely qualitative. For instance, *Scherler et al. (2011b)* found lower accumulation-area ratios for debris-covered than debris-free glaciers. Additionally, based on the data of *Kraaijenbrink et al. (2017)*, we found a negative correlation ($r = -0.36$, $p < 0.01$) between the glacier minimum elevation and the percentage of debris cover (Fig. 5.15). The combination of these two observations hints at both reduced ablation and a larger tongue for debris-covered glaciers.

Consequently, the qualitative picture we can draw is that the ablation area of glaciers with considerable debris-cover is usually larger than for debris-free glaciers ($A_{\text{DC}} > A_{\text{DF}}$). This results in lower emergence velocities ($w_{e,\text{DC}} = \Phi/A_{\text{DC}} < \Phi/A_{\text{DF}} = w_{e,\text{DF}}$). If the glacier is in mass and dynamical equilibrium, in both debris-covered and debris-free cases, the thinning rate at any elevation is 0, because the emergence velocity compensates the surface mass balance. However, both w_e and \dot{b} will be lower for the debris-covered tongue (Fig. 5.16). In an unbalanced regime with consistent negative mass balances, as mostly observed in High Mountain Asia (*Brun et al., 2017*), similar thinning rates between debris-free and debris-covered tongues could be the combination of reduced emergence velocities and lower ablation for debris-covered glaciers (Fig. 5.16). Evidence for reduced debris-covered glacier velocities and loss of connectivity between accumulation and ablation areas (*Neckel et al., 2017*) will lead to further reductions in both ice fluxes and w_e .

In conclusion, our field evidence shows that enhanced ice cliff ablation alone could not lead to a similar level of ablation for debris-covered and debris-free tongues. While other processes can substantially increase the ablation of debris-covered tongues, we highlight the potentially important role of the neglected emergence velocity in the explanation of the so-called 'debris-cover anomaly'.

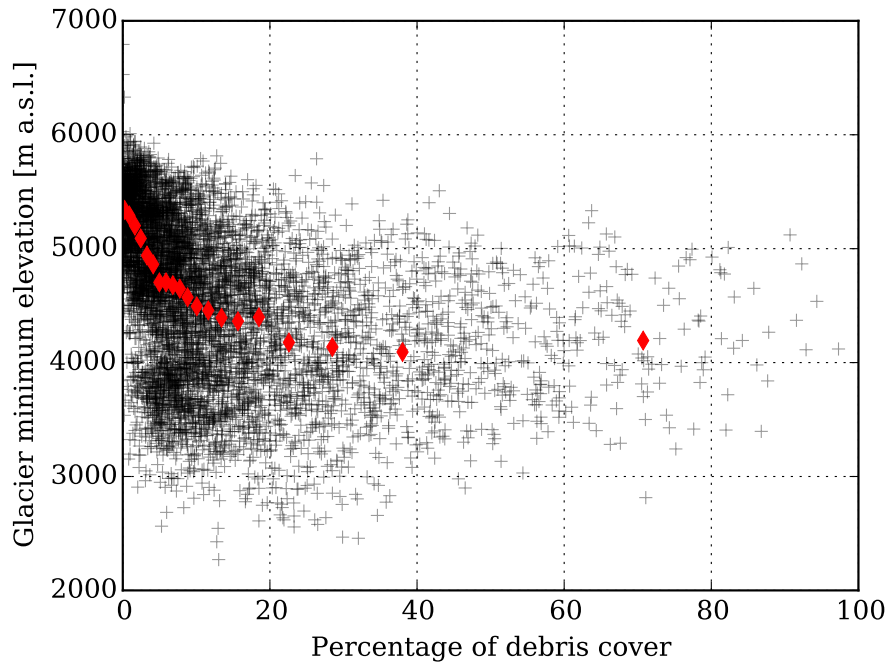


Figure 5.15: Glacier minimum elevation as a function of the percentage of debris cover for the glaciers larger than 2 km^2 in High Mountain Asia (6571 glaciers in total). The black crosses represent individual glaciers and the red diamonds shows the mean of the glacier minimum elevation for each five percentile of debris cover. For instance, the first diamond represent the mean of the glacier minimum elevation for glaciers with a percentage of debris cover between 0 (minimum) and 0.51 % (5th percentile).

5.8.4 Applicability to other glaciers

Determining the total ice cliff contribution to the net ablation of the tongue (i.e., the f_C factor defined in this study) of a single glacier has limited value by itself, because we do not know the variability between glaciers. In particular, it is too early to conclude if the range of f_C values reported in the literature reflects inconsistencies amongst the different methods, or is actually a reflection of variability between glaciers. For instance, model-based f_C values (Sakai *et al.*, 1998; Juen *et al.*, 2014; Buri *et al.*, 2016a; Reid and Brock, 2014) are not directly comparable with the observations (Brun *et al.*, 2016; Thompson *et al.*, 2016), because they usually require additional assumptions about e.g., the sub-debris ablation or emergence velocity. The definition of debris-covered tongues, the nature of their surface, and their hypsometry might also have a considerable effect on f_C .

A significant obstacle to applying our method to other glaciers is the need to estimate the emergence velocity, which requires an accurate determination of the ice fluxes entering the glacier tongues. The measurement of ice thickness with GPR systems is already challenging for debris-free glaciers, as it requires transmitter, receiver and antennae must be pulled along transects on the glacier surface. It is even more challenging for debris-covered glaciers, as the hummocky surface prevents the operators from dragging a sledge. More field campaigns dedicated to ice thickness and velocity measurements (Nuimura *et al.*, 2011, 2017) or the development of airborne ice thickness retrievals through debris are needed, as stressed by the outcome of the Ice Thickness Models Intercomparison eXperiment (Farinotti *et al.*, 2017). The precise retrieval of emergence velocity pattern using a network of ablation stakes combined with DGPS is a promising alternative, in particular if combined with detailed ice flow modeling (e.g., Gilbert *et al.*, 2016).

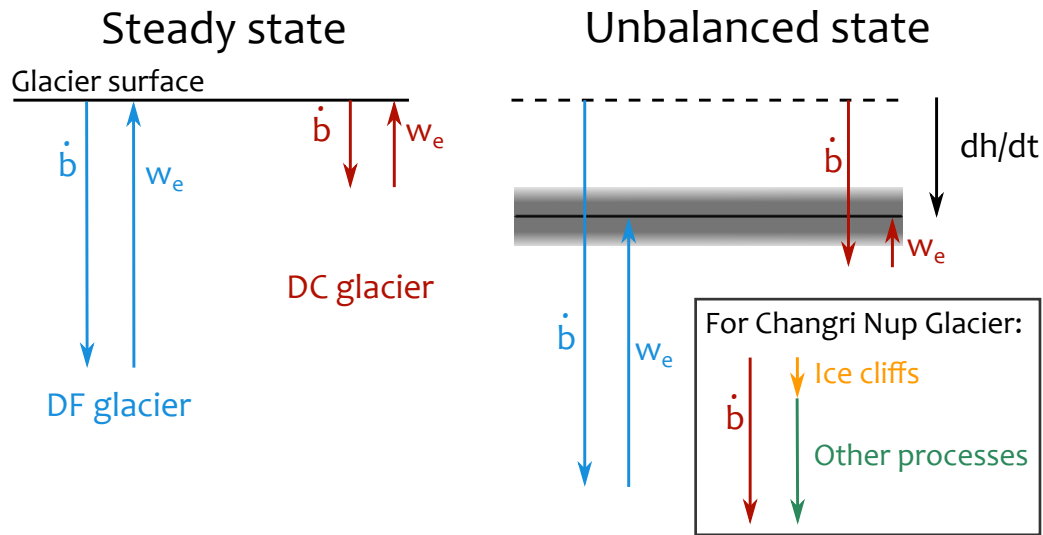


Figure 5.16: Conceptual representation of the interplay of net ablation (\dot{b}) and emergence velocity (w_e) for debris-free (DF, blue color) and debris-covered (DC, brown color) glacier tongues. In the left panel both glaciers are at equilibrium (no thinning) and in the right panel their tongues are thinning at roughly the same rate $\overline{\partial h/\partial t}$, shown by the grey shaded area. In the unbalanced state, the values are scaled according to Vincent *et al.* (2016). For the steady state, we assumed a similar emergence velocity for the debris-free tongue. The inset shows the share of the ice cliffs versus the other processes for the tongue-wide ablation on Changri Nup Glacier tongue. It is noteworthy that this representation is only conceptual, that it is based on our current understanding of the interplay of ablation and ice dynamics of a single, small glacier tongue (Changri Nup), and that the emergence velocity values are very poorly constrained.

5.9 Conclusions

In this study, we estimate the total contribution of ice cliff to the total net ablation of a debris-covered glacier tongue for two consecutive years, taking into account the emergence velocity. Ice cliffs are responsible for $23\text{-}24 \pm 5\%$ of the total net ablation for both years, despite a tongue-wide net ablation approximately 25% higher in the second year. On Changri Nup Glacier, the fraction of total net ablation from ice cliffs is too low to explain the so-called "debris-cover anomaly". Other contributions, such as ablation from supra-glacial lakes, or along englacial conduits, are potentially large and have yet to be quantified. For the specific case of Changri Nup Glacier they are likely not large enough to compensate for the reduced ablation (Vincent *et al.*, 2016). Consequently, we hypothesize that the "debris-cover anomaly" could be a result of lower emergence velocities and reduced ablation, which leads to *thinning rates* comparable to those observed on clean ice glaciers. However, ice cliffs are still hot-spots of ablation and consequently of enhanced thinning; without them, the thinning rates of debris-covered and clean ice might not be similar.

Our method requires high-resolution UAV or satellite stereo imagery, and is restricted to glaciers where thickness estimates at a cross section upstream of the debris-covered tongue are available, and emergence velocity can be estimated. A comparison of cliff ablation enhancement factor (f_C or f_C^*) values calculated for other debris-covered glaciers under our suggested framework would be informative, in order to compare estimates of ice cliff ablation for other and potentially much larger debris-covered tongues. Though our results cover only two years of data where net ablation totals differed by 25%, the area occupied by ice cliffs and their relative contribution to ablation (f_C) remained almost constant. A main limitation of our study is its short spatial and temporal extent, and it would be worth-

while to obtain longer-term estimates of the relative ice-cliff contribution to net ablation at multiple sites. These estimates would lead to the development of empirical relationships for cliff enhanced ablation that could be included in debris-covered glacier mass balance models.

In line with a previous study (*Vincent et al., 2016*), we stress the need for more research about the emergence velocity of debris-covered (and nearby debris-free) tongues, as the assumption that thinning rates are equal to net ablation rates is incorrect, and can lead to inaccurate conclusions. Two research directions could be (a) to measure cross sectional ice thicknesses for multiple debris-covered glaciers and (b) to install dense networks of ablation stakes to assess the spatial variability of ice flow emergence.

Table 5.4: Characteristics of the three UAV flights. The horizontal and vertical residuals are assessed on independent additional GCPs (*Agisoft, 2017*).

Date of acquisition	Number of images	Number of GCPs	Number of virtual GCPs	Horizontal residuals (cm)	Vertical residuals (cm)
22–24/11/2015	582	24	0	4	10
16/11/2016	475	17	16	N/A	N/A
23/11/2017	390	30	0	11	14

Table 5.5: Characteristics and IDs of the Pléiades images. Horizontal shifts relative to the UAV ortho-images are also given.

Date of acquisition	B/H	Shift eastward (m)	Shift northward (m)
22/11/2015	0.36;0.26;0.10	-4.3	0.3
13/11/2016	0.47;0.28;0.20	6.6	3.7
24/10/2017	0.34;0.25;0.09	1.0	4.2

5.10 Going one step further

This work has potential widespread application to other debris-covered glacier tongues. It requires very high resolution satellite images, such as Pléiades or WorldView images which are now almost routinely used in glaciology (e.g. *Berthier et al.*, 2014). However, it also requires ice thickness data (at least one cross section). The collection of ice thickness data is labor intensive and ice thickness measurements are extremely sparse in HMA, and there is a real need to collect more ice thickness data to better understand the dynamics of debris-covered glacier tongues.

Fortunately, the ice thickness of Khumbu Glacier has been measured (*Gades et al.*, 2000) and used to tune an ice dynamics model (*Rowan et al.*, 2015). Consequently, it is worth trying to apply similar methods to this glacier tongue and assess whether the ice cliffs contribute similarly as on Changri Nup Glacier tongue.

Conclusions and outlook

Contents

6.1	Summary of the results	135
6.2	Outlook for future research	137
6.2.1	About debris-covered glaciers	137
6.2.2	About HMA climatology	138
6.2.3	About methodological developments	139

6.1 Summary of the results

The aim of this work was to explore the influence of debris on the glacier mass balance in HMA, by taking advantage of the different spatial scales. Below, I summarize some partial responses to the questions raised at the end of chapter 2.

Question 1 What are the recent changes of glaciers at the scale of HMA? Can we produce homogeneous glacier elevation change data with a resolution high enough to capture individual glacier mass balances?

In chapter 3, we processed more than 50 000 individual ASTER DEMs in order to extract time series of elevation, which were then converted into rate of elevation changes. The method was not novel by itself (e.g., *Willis et al.*, 2012; *Nuimura et al.*, 2012), but it is the first time it was applied over such a large area. My main contribution to this work was the automation of existing procedures (*Nuth and Kääb*, 2011; *Gardelle et al.*, 2012a; *Berthier et al.*, 2016) and the careful validations against published and unpublished individual glacier geodetic mass balances estimates. Additional comparison with high resolution glacier-wide geodetic estimates in central Asia showed good agreement with ASTER based estimates (*Barandun et al.*, 2018). Within the same framework, we managed to produce a quasi exhaustive geodetic estimate of HMA glacier mass changes, and individual glacier mass balances for more than 6 500 glaciers larger than 2 km².

Our individual glaciers estimates were recognized as timely and potentially very useful for glacier modeling studies (*Farinotti*, 2017; *Barandun et al.*, 2018). These data were later used to understand the local context of glacier mass changes associated with the collapse of the Aru-Co glaciers in summer 2016 (*Kääb et al.*, 2018). They were also used to assess the glacier contribution to the increasing lake volume of the Tibetan Plateau (*Zhang et al.*, in prep.), to untangle the glacier contribution in the endorheic basins of HMA to changes in the terrestrial water storage (*Wang et al.*, 2018) and were used to show that the twenty-first century slowdown of glaciers in HMA (derived from the automatic processing of Landsat archive, *Dehecq et al.*, 2015) is driven by the driving stress reduction induced by the glacier thinning (*Dehecq et al.*, 2018). These data were included in a compilation as the reference for the 2000-2016 HMA glacier contribution to SLR (*Bamber et al.*, 2018).

Question 2 What is the influence of the debris cover on the glacier-wide mass balance? Is it possible to quantify this influence? Are the debris-covered and debris-free glaciers different in terms of glacier-wide mass balances?

In chapter 4, we showed that the percentage of debris cover has sometimes a positive correlation with the mass balance and sometimes a negative correlation. In terms of quantitative contribution to the mass balance variability, we found that this variable was always a small contributor in the multivariate linear model, with the exception of the inner TP. The influence of the debris on the glacier mass balance is not completely clear and complicated to untangle from the effect of the other morphological variables.

One of the limitations of this study is the use of the debris cover extent as an input variable. The debris thickness would make more sense from a physical point of view, but the debris thickness maps derived from satellite thermal imagery and available at the scale of HMA are suspected to underestimate the debris thickness, as it was shown by the rejection of the article of *Sasaki et al.* (2016). If realistic maps of debris thickness become available at the scale of HMA, it would be interesting to conduct a new analysis with these data.

We investigated the glacier-wide mass balance, which is influenced by processes in the ablation area (i.e. the ice melt beneath debris), but is also influenced by processes related to the accumulation. For instance, we assumed in chapter 4 that the investigated regions were climatically homogeneous. This hypothesis is probably not verified everywhere and especially the precipitation can be highly variable in space and time within short distances in mountainous areas.

Debris-covered and debris-free glaciers have non significantly different mass balances for seven regions out of twelve. For four regions debris-covered glaciers have significantly more negative mass balances than debris-free glaciers (because they are located at lower elevations), and for the remaining region it is the opposite. On average, field based mass balance measurements are biased towards too negative mass balances in HMA, but our new results suggest that it is not due to the fact that only debris-free glaciers are monitored, as sometimes suggested (e.g., *Azam et al.*, 2018).

Question 3 Which terms of the ablation budget of a debris-covered tongue are quantifiable from remote sensing and field observations?

In chapter 5, we showed that it was possible to quantify the influence of ice cliffs at the scale of a single small glacier-tongue. This is clearly one step forward compared to previous studies, which showed larger thinning rates on areas of glacier tongues covered by cliff than on areas with less cliffs, but did not estimate the exact ice cliff contribution to ablation (*Ragettli et al.*, 2016b; *Watson et al.*, 2017b; *Huang et al.*, 2018). We found that over two contrasted years, the ice cliffs contributed to 23 and 24 ± 5 % of the total net ablation of Changri Nup Glacier tongue, even though they occupied only 7 to 8 % of the tongue surface.

This study demonstrated the need of cross-sectional ice thickness measurements to complement the surface elevation changes measured from satellite platforms. For Changri Nup Glacier, ice thickness measurements consist in a single cross section measure, located ~ 200 m upstream of the clean ice/debris transition. It would be useful to have multiple measurements downstream of this one, in order to calculate ice flux through multiple gates and therefore refine our hypothesis about the distribution of the emergence for the glacier tongue. However, it is extremely challenging to measure ice thickness with a GPR on the portions of the glacier that are heavily debris-covered because it is tough to drag it on the ground due to the rocks and ice cliffs.

From this study, we concluded that the ice cliffs should occupy ~ 75 % of the glacier tongue area in order to have the same mass balance as a nearby debris-free tongue. This means that ice cliffs matter, but they are likely insufficient to compensate for the insulating effect of debris. However, this conclusion remains valid for the tongue of Changri Nup Glacier only and we cannot extrapolate it to other glaciers.

We targeted the process (ice cliff retreat) that is the easiest to quantify at the scale of a debris-covered glacier tongue. The other processes would require more intensive field campaigns. For instance, the quantification of the ice melt beneath debris would require a precise knowledge of the debris thickness on the entire tongue, which is not achievable at the moment. The quantification of the pond and englacial melt is even more challenging, as only indirect measurements are possible.

To summarize, two major contributions of this PhD work can be distinguished. First, I showed that neither the debris cover, nor the supraglacial pond density were good predictors of glacier mass balance. This means that the large scale influence of debris cover

and supraglacial features is not clear, and that more research is needed to understand the respective influence of these features. Second, we showed that ice cliffs, despite contributing to a substantial part of the ablation, were not the dominant term of the ablation budget, due to their limited spatial extent.

6.2 Outlook for future research

Based on the literature review, the results and methodological developments presented in this manuscript, the very insightful discussions with colleagues, but also based on the difficulties, wrong tracks, and other detours, I can attempt to give seven research directions for future work, grouped into three major themes.

6.2.1 About debris-covered glaciers

Direction 1: closing the ablation budget of a debris-covered glacier tongue This is a real need in order to validate models, but also possibly to derive empirical relationships among the pond or/and cliff extents and the ablation. However, this quantification would require multiple prerequisites. First of all, knowing the ice flux entering the glacier tongue is required, in order to calculate the net ablation rate and not only the rate of thinning (Vincent *et al.*, 2016). The ice flux through a cross sectional gate is calculated from the glacier surface velocity and the mean ice thickness along a cross section. The glacier surface velocity is relatively easy to access from satellite products (e.g., Dehecq *et al.*, 2015; Usman and Furuya, 2018). However, ice thickness cannot be measured from satellite platforms, and, to my knowledge, in HMA, ice thickness data are available for few debris-covered glaciers, which are Changri Nup, Lirung and Khumbu glaciers (Vincent *et al.*, 2016; Nuimura *et al.*, 2017; Gades *et al.*, 2000). Second, the cliff contribution quantification requires high resolution topographic data. In chapter 5, we demonstrated that tri-stereo Pléiades data are suitable to measure ice cliff backwasting, even without GCPs. Pléiades data can virtually be acquired anywhere, and consequently I plan to reproduce the work done on Changri Nup Glacier tongue on Khumbu Glacier tongue, which should be more challenging than this early work, as Khumbu Glacier is larger and flowing faster than Changri Nup Glacier.

In term of surface and englacial hydrology, Lirung, Ngozumpa and Khumbu glaciers are relatively well understood (e.g., Miles *et al.*, 2017c; Benn *et al.*, 2017; Watson *et al.*, 2018). As a consequence, it is possible that Lirung Glacier will be the first debris-covered glacier on which all processes could be quantified, despite an accumulation through snow avalanches which is not well constrained.

Direction 2: better understanding the ice dynamics of debris-covered tongues Ice dynamics controls the englacial debris transport (Wirbel *et al.*, 2018) and needs to be accounted for if ones wants to interpret rates of thickness changes in terms of surface mass balance (chapter 5). It is also likely that ice dynamics plays a role in the development of ice cliffs and/or supraglacial ponds, but this research direction has barely been explored yet.

Consequently, more ice thickness measurements are needed and 3D ice flow modeling, for instance with community used codes such as Elmer/Ice model (Gagliardini *et al.*, 2013), is a promising research direction. Indeed, glacier flow modeling is a relevant tool to assess the relationship between thickness changes, surface mass balance and ice dynamics (e.g.,

Gilbert et al., 2016). It could help extending the work of *Vincent et al.* (2016), to assess the bulk debris effect on surface mass balance.

Direction 3: quantifying the long term debris supply and its link with the erosion In this dissertation, I explored only very short time scales of debris-covered glacier evolution and changes; I ignored the longer timescales. However, the glaciers, and in particular the debris-covered glaciers, play the role of conveyor belts that remove debris from the foot of the head-walls, allowing them to further retreat through frost-cracking (*Scherler et al.*, 2011b; *Ward and Anderson*, 2011; *Scherler*, 2014). The process of frost-cracking is highly sensitive to the temperature (*Scherler*, 2014). In terms of ablation processes, the formation of ice cliffs is not yet clearly understood (*Benn et al.*, 2012), nor is their temporal evolution on the long run.

It is generally accepted that, over decadal timescales, the debris supply is controlled by mass movement (e.g., landslides or rockfalls). Nevertheless, over longer (centennial to millennial) timescales the debris supply rate is expected to be influenced by the erosion rate and therefore by the climate and tectonic uplift (e.g., *Gibson et al.*, 2017). Consequently, as on the longer run, the debris supply has a potentially strong influence on glacier mass balance and ice dynamics (*Rowan et al.*, 2015; *Anderson and Anderson*, 2016), it is important to better constrain the current rates of debris supply (e.g., *Gibson et al.*, 2017) and to assess how they evolve in relationship with climate, for future projections but also for palaeoclimate interpretations.

6.2.2 About HMA climatology

Direction 4: improving the quality of the high altitude precipitation products The hydrological cycle of major rivers of HMA is largely influenced by the high altitude precipitations, partly through snow and glacial processes (e.g., *Lutz et al.*, 2014). However, due to extreme topographic gradients and lack of observations, the variability and amount of high altitude precipitations are poorly known in HMA and the different datasets (observational or modeled with assimilated data) are often in strong disagreement (*Palazzi et al.*, 2013; *Ceglar et al.*, 2017).

Usually, the high altitude precipitation are underestimated (*Palazzi et al.*, 2013). The glaciers can be used as natural pluviometers, and the accumulation can be estimated by the opposite method of *Kaser et al.* (2010). The ablation is assumed as a function of elevation and the precipitation vertical structure is tuned, until the accumulation matches the ablation (*Immerzeel et al.*, 2012a, 2015; *Sakai et al.*, 2015). However, these studies relied on simplified assumptions, including a balanced mass budget for the glaciers (*Immerzeel et al.*, 2012a), or glacier mass changes derived at the region scale from ICESat (*Immerzeel et al.*, 2015). The incorporation of more resolved glacier mass balances (chapter 3) could improve such inversions. Moreover, the use of highly resolved atmospheric models, such as WRF or MAR, is now frequent in HMA (e.g., *Ménégoz et al.*, 2013; *Collier et al.*, 2013; *Collier and Immerzeel*, 2015; *Kumar et al.*, 2015; *Maussion et al.*, 2014; *de Kok et al.*, 2018) and they can be used to make more reasonable assumptions about the vertical distribution of precipitations.

Direction 5: applying the albedo or snowline methods to gain insights about the annual variability of glacier mass balances The glacier end-of-summer snowlines, used as proxies for the ELA, have successfully been used to study the glacier/climate relationship (*Clare*

et al., 2002; *Chinn et al.*, 2005; *Rabatel et al.*, 2013). The albedo method, which consists in tracking the glacier mean albedo to find its annual minimum, and link it to the glacier-wide mass balance is also a promising approach (*Dumont et al.*, 2012; *Brun et al.*, 2015; *Davaze et al.*, 2018). These methods and the geodetic method complement one another (*Barandun et al.*, 2018). However, they are currently limited by the lack of fully automatic and reliable procedures to retrieve end-of-summer or transient snowlines in a full satellite archive. The aim of Lucas Davaze's PhD project (2016-2019) is to produce such a method. Two other limitations could prevent the use of these methods at the scale of HMA: the persistent cloud cover during the ablation season for the monsoon influenced regions prevent from reliable observations of the snowline and the interpretation of the snowlines in a context of summer accumulation type glacier is not completely clear (e.g., *Rabatel et al.*, 2012; *Brun et al.*, 2015).

6.2.3 About methodological developments

Direction 6: assessing the SRTM-C penetration bias The potential and limitations of ASTER trend extrapolation to estimate the SRTM-C DEM penetration bias has been discussed extensively in section 3.8.1. The extrapolation of ASTER trends would be an improvement compared with the ICESat trend extrapolations or X-band method estimates, which are currently widely used in the literature (section 3.8.1). However, the understanding of this bias requires a much larger effort, involving multidisciplinary skills. It remains likely that the best effort would still lead to estimates provided large uncertainties.

Direction 7: using the ASTER glacier-wide mass balances for model calibration or validation The geodetic method based on timeseries of ASTER DEMs is not a new method (e.g., *Willis et al.*, 2012; *Nuimura et al.*, 2012; *Wang and Käähb*, 2015), but it is now highly automated (based on the developments made by myself and by Romain Hugonnet) and has the potential to be applied at the scale of the globe. It was recently applied to the Northern Patagonian Icefield (*Dussaillant et al.*, 2018), in Alaska (*Berthier et al.*, 2018) and is currently applied to the entire Andes (PhD project of Ines Dussaillant 2016-2019). There is room for methodological improvements, for example the implementation of the MMASTER suite in Mic-Mac software could potentially improve the quality of ASTER DEMs (*Girod et al.*, 2017). However, this method relies on optical images, which are degraded by the presence of clouds, preventing its application in some regions (for instance there was only one good ASTER image acquired for Brøggerhalvøya Glacier, Ny Ålesund, over 16 years; Luc Girod personal communication). The global monitoring of ice changes for the beginning of the twenty-first century will potentially be performed by Romain Hugonnet, within the framework of the putative ASTERIX project¹. This new global estimate would be more than welcome for glacier model calibration, as it would ensure a consistent, global (except in the regions that are too cloudy) and spatially resolved glacier mass change estimate (section 3.8.3).

The ASTER archive has been largely populated through the GLIMS project, and it has been fully open in April 2016, enabling our work on HMA glacier mass balances. Moreover, the revisit of such archives benefits from the continuous development and improvement of image processing algorithm, such as ASP (*Shean et al.*, 2016). The automatic processing of massive amount of data is now very frequent in glaciology, and will likely become more and more standard (e.g., *Dehecq et al.*, 2015; *Maurer et al.*, 2016; *Mouginot et al.*, 2017). The full

¹ASTER-based monitoring of Ice in eXtinction

release of SPOT5 raw stereo images, acquired within the SPIRIT project (*Korona et al.*, 2009), could lead to major progresses in glaciology, because the algorithm correlation routines have been substantially improved and show better performances over low contrast terrain, such as Greenland and Antarctica glaciers, than the earlier ones. Similarly, Pléiades data acquired within the ISIS projects, and in particular the targeted acquisitions of the WGMS reference glaciers, are now free for all users. In the same line, the release of the High Mountain Asia 8m DEM (*Shean*, 2017), based on WorldView images acquired mainly from 2013 to 2016 will likely trigger a massive production of glacier mass changes data.

Among these different research directions, some are more appealing to me than others. After these three years of PhD, I would like to shift a bit my focus and the research direction 4 is my favorite. Through collaborations with hydrologists (*Mimeau et al.*, 2018), and participation to field campaigns, which include glaciological mass balance and GPS measurements on Mera Glacier within the CRYOBS-CLIM² framework, but also maintenance of automatic weather stations, I have developed a feel that high altitude precipitation measurement and modeling will be a major challenge for the coming years. During this PhD work, I learned that satellites are fantastic tools, but they are even more appropriate when complemented with ground observations (e.g., *Vincent et al.*, 2016; *Sherpa et al.*, 2017). I also realized the importance of long term glacier mass balance monitoring programs, and I am happy that I (modestly!) contributed to the monitoring of Mera Glacier. I also realized that going back and forth between large scale and small scale studies was a true enrichment to my research and reflection, and I hope to have the possibility to work in such stimulating context in the future!

²La CRYosphère, un Observatoire du CLIMat

Additional Publication

The next pages consist in an article based on my master's thesis work (*Brun et al.*, 2016). As it is the basis of chapter 5, I decided to include it in this dissertation.

Quantifying volume loss from ice cliffs on debris-covered glaciers using high-resolution terrestrial and aerial photogrammetry

FANNY BRUN,^{1,2,3} PASCAL BURI,¹ EVAN S. MILES,⁴ PATRICK WAGNON,^{2,5}
JAKOB STEINER,¹ ETIENNE BERTHIER,⁶ SILVAN RAGETTLI,¹ PHILIP KRAAIJENBRINK,⁷
WALTER W. IMMERZEEL,⁷ FRANCESCA PELLICCIOTTI^{8,1}

¹Institute of Environmental Engineering, ETH Zurich, Zurich, Switzerland

²Univ. Grenoble Alpes, CNRS, IRD, LTHE, UMR5564, Grenoble, France

³Geosciences Department, ENS, Paris, France

⁴Scott Polar Research Institute, University of Cambridge, Cambridge, UK

⁵International Centre for Integrated Mountain Development, Kathmandu, Nepal

⁶LEGOS, Université de Toulouse, CNES, CNRS, IRD, UPS, Toulouse, France

⁷Department of Physical Geography, Utrecht University, Utrecht, Netherlands

⁸Department of Geography, Northumbria University, Newcastle Upon Tyne, UK

Correspondence: Fanny Brun <fanny.brun@ujf-grenoble.fr>

ABSTRACT. Mass losses originating from supraglacial ice cliffs at the lower tongues of debris-covered glaciers are a potentially large component of the mass balance, but have rarely been quantified. In this study, we develop a method to estimate ice cliff volume losses based on high-resolution topographic data derived from terrestrial and aerial photogrammetry. We apply our method to six cliffs monitored in May and October 2013 and 2014 using four different topographic datasets collected over the debris-covered Lirung Glacier of the Nepalese Himalayas. During the monsoon, the cliff mean backwasting rate was relatively consistent in 2013 (3.8 ± 0.3 cm w.e. d^{-1}) and more heterogeneous among cliffs in 2014 (3.1 ± 0.7 cm w.e. d^{-1}), and the geometric variations between cliffs are larger. Their mean backwasting rate is significantly lower in winter (October 2013–May 2014), at 1.0 ± 0.3 cm w.e. d^{-1} . These results are consistent with estimates of cliff ablation from an energy-balance model developed in a previous study. The ice cliffs lose mass at rates six times higher than estimates of glacier-wide melt under debris, which seems to confirm that ice cliffs provide a large contribution to total glacier melt.

KEYWORDS: debris-covered glaciers, ice cliffs, terrestrial and aerial photogrammetry, structure for motion, ice volume losses

1. INTRODUCTION

Debris-covered glaciers are notable features in the Pamir-Karakoram-Himalaya (PKH) region (e.g. Scherler and others, 2011; Bolch and others, 2012), covering ~10% of the glacierized area (Bolch and others, 2012), and are of importance for melt and mass balance because they normally lay at low elevations. Despite an insulating effect of debris when thick enough (e.g. Østrem, 1959; Nicholson and Benn, 2006; Reid and Brock, 2010; Lejeune and others, 2013), recent large-scale studies based on remote sensing have provided evidence that they might be losing mass at rates comparable with those of debris-free ice (e.g. Käb and others, 2012; Nuimura and others, 2012; Gardelle and others, 2013; Holzer and others, 2015), which has been referred to as the debris-covered glacier anomaly (e.g. Pellicciotti and others, 2015).

A number of pioneering (e.g. Sakai and others, 2000, 2002) and more recent studies (Steiner and others, 2015; Buri and others, 2016; Miles and others, 2016) have suggested that supraglacial lakes and cliffs are responsible for larger than expected volume losses. These features have low albedo and are exposed directly to the atmosphere, enhancing the radiative transfer and turbulent energy fluxes at the glacier surface (Buri and others, 2016; Miles and others, 2016). Due to their steep slopes (commonly $>45^\circ$ and

sometimes overhanging) and the complex topography of debris-covered glaciers, the cliffs also receive additional long-wave radiation emitted from the surrounding debris-covered terrain, thus further enhancing their melt (Reid and Brock, 2014; Steiner and others, 2015; Buri and others, 2016).

However, actual quantitative estimates of the total contribution of ice cliffs backwasting (i.e. the volume loss at cliff scale) to the total mass balance of debris-covered glaciers do not exist. Modelling studies are still in their infancy and cannot be yet used to quantify the total contribution of cliffs to the glacier mass balance. Most numerical models (based on calculation of the energy balance at the cliff surface) have been developed at the point scale (Sakai and others, 1998, 2000; Han and others, 2010; Reid and Brock, 2014; Steiner and others, 2015) and some have quantified the total contribution of cliffs to melt by extrapolation of point estimates of backwasting (Sakai and others, 1998, 2000; Han and others, 2010; Reid and Brock, 2014). Most of these models were validated only against point scale measurements and over short periods of time given the difficulty of maintaining ablation stakes on cliffs (Reid and Brock, 2014; Steiner and others, 2015) or against cliff edge retreat measurements (Sakai and others, 1998; Han and others, 2010). A recent attempt has been made to develop a fully distributed model of cliff backwasting that could provide estimates of total cliff

backwasting volumes and patterns (Buri and others, 2016), but that model focuses on mass losses due to the energy exchange with the atmosphere and still does not include all relevant processes contributing to cliff volume changes. In addition, numerical models need validation through distributed ground data that, to our knowledge, are not yet available.

Thus, this paper's main aim is to develop a method that allows calculation of total backwasting volumes of supraglacial cliffs from dense point clouds of glacier and cliff topography obtained via terrestrial and aerial photogrammetry, using Structure from Motion (SfM) techniques (Westoby and others, 2012) or, alternatively using dGPS measurements of the cliff outline, which are comparable with the type of data that may be obtained from very-high-resolution optical satellite photogrammetry. The volumetric change estimates obtained in this way can be used both to quantify total volume losses and to validate the models currently being developed.

In formulating the new method proposed here, we focus on an approach to provide total volume losses, but not the spatial pattern of backwasting. Several methods have been proposed to estimate temporal changes of complex surfaces. One of the most refined methods is the M3C2 algorithm implemented in the Cloud Compare open-source software (Lague and others, 2013). This method enables computation of distances between two point clouds. Its main strength is that it does not require a priori information on the surface orientation, as it calculates local normals to the surface using neighboring points. However, a consequence of the method's practicality is that the surface change is measured perpendicular to the surface, which presents a challenge for ice cliff backwasting, where sloped features undergo a linear translation. Given the limitation of tools like M3C2, we developed a specific method to estimate volumetric change associated with ice cliff backwasting, which we applied to selected cliffs on the debris-covered tongue of Lirung Glacier in the Nepalese Himalaya. We used an existing dataset of triangulated irregular networks (TINs) obtained from unmanned aerial vehicle (UAV) surveys (Immerzeel and others, 2014; Kraaijenbrink and others, 2016) and a novel TIN dataset derived from terrestrial photogrammetric survey. We calculate cliff backwasting over two monsoon seasons (May–October 2013 and May–October 2014) and one winter season (October 2013–May 2014). We then compare these estimates with those obtained with a simpler approximation similar to the method of Han and others (2010) and discuss whether simplified geometry assumptions can produce a realistic estimate of backwasting. We also document the cliff evolution as inferred from our detailed estimates of cliff geometry and volumetric loss and discuss the possible processes responsible for the observed evolution.

2. STUDY AREA

Lirung Glacier (28.24°N; 85.56°E) is a debris-covered glacier located in the Upper Langtang Valley of the Central Nepalese Himalayas (Fig. 1, inset). It flows from Langtang Lirung peak (7234 m a.s.l.) down to ~4000 m a.s.l. (e.g. Sakai and others, 1998; Immerzeel and others, 2014; Buri and others, 2016). In this study, we focus on the lower ablation zone (ranging between 4000 and 4450 m a.s.l.), which is entirely covered by a heterogeneous debris layer and is detached from the glacier upper area (Ragetti and others, 2015).

Ice cliffs on Lirung Glacier have been monitored during four field campaigns in May 2013, October 2013, May

2014 and October 2014. The monitored cliffs have a height ranging between 10 and 30 m, a width ranging between 40 and 200 m and a mean slope ~45° (Table 1). For the remainder of this study, we focus on the cliffs indicated as cliff 1–5 (Fig. 1; Table 1). Cliff 4' indicates the western side of cliff 4, which was observed for the first time in October 2013 (this area was previously covered by debris) and has been surveyed since May 2014.

3. DATA

3.1. Differential GPS data

The dGPS measurements are based on simultaneous use of two GPS devices: a base station and a rover. The relative accuracy between both devices is usually better than 5 cm, in the horizontal and vertical (Immerzeel and others, 2014). During the May 2014 field campaign, 13 cliff outlines were mapped by dGPS on Lirung Glacier (Fig. 1); in October 2014 two cliffs were fully mapped and three were partially mapped (i.e. only the upper edge was mapped; Fig. 1). To map a cliff outline, one dGPS point was recorded every 5 m for all debris/ice margins. The cliff edge was measured as accurately as possible, but it was not always possible to map the exact edge, it being too hazardous due to unstable terrain and rockfall. In cases where a supraglacial pond was present at the foot of the cliff, the cliff bottom was not surveyed.

The dGPS points have two main uses: to reconstruct the cliff surface from its outline and to serve as ground control points (GCPs) for the photogrammetric models.

3.2. High-resolution topographic data

The topographic data were utilized as TINs from terrestrial or airborne (UAV) SfM photogrammetry. All the terrestrial and aerial photographs were processed using the commercial Agisoft software (Agisoft, 2013), which uses an SfM workflow (e.g. Westoby and others, 2012; Immerzeel and others, 2014; Passalacqua and others, 2015; Kraaijenbrink and others, 2016). The first step of SfM workflow is based on keypoint (i.e. matching features) extraction from the images collected in the field. This is achieved by feature recognition algorithms, such as the Scale Invariant Feature Transform method (e.g. Snavely and others, 2008). These keypoints allow for the derivation of a first low-density point cloud and constrain the camera pose (so-called bundle block adjustment). The cloud densification is done by a pair-wise depth map computation algorithm (Furukawa and Ponce, 2009). It is finally triangulated to obtain an irregularly triangulated mesh, also called a TIN.

In May and October 2013, the topographic data were obtained by UAV photogrammetry (Immerzeel and others, 2014; Kraaijenbrink and others, 2016). Despite a high viewing angle, there was enough overlap in the photographs to resolve the overhanging sections of the cliffs on the final TINs. The flight altitude was chosen in order to obtain images with a ground resolution ~4–7 cm (Kraaijenbrink and others, 2016). A step-by-step description of the processing workflow is available in Kraaijenbrink and others (2016). The extraction of the cliff surfaces from the TIN representing the whole glacier is based on visual inspection of the TIN. The resulting TINs have an original point density ranging from 2.3 to 7.8 points m⁻². The TINs representing cliff 2

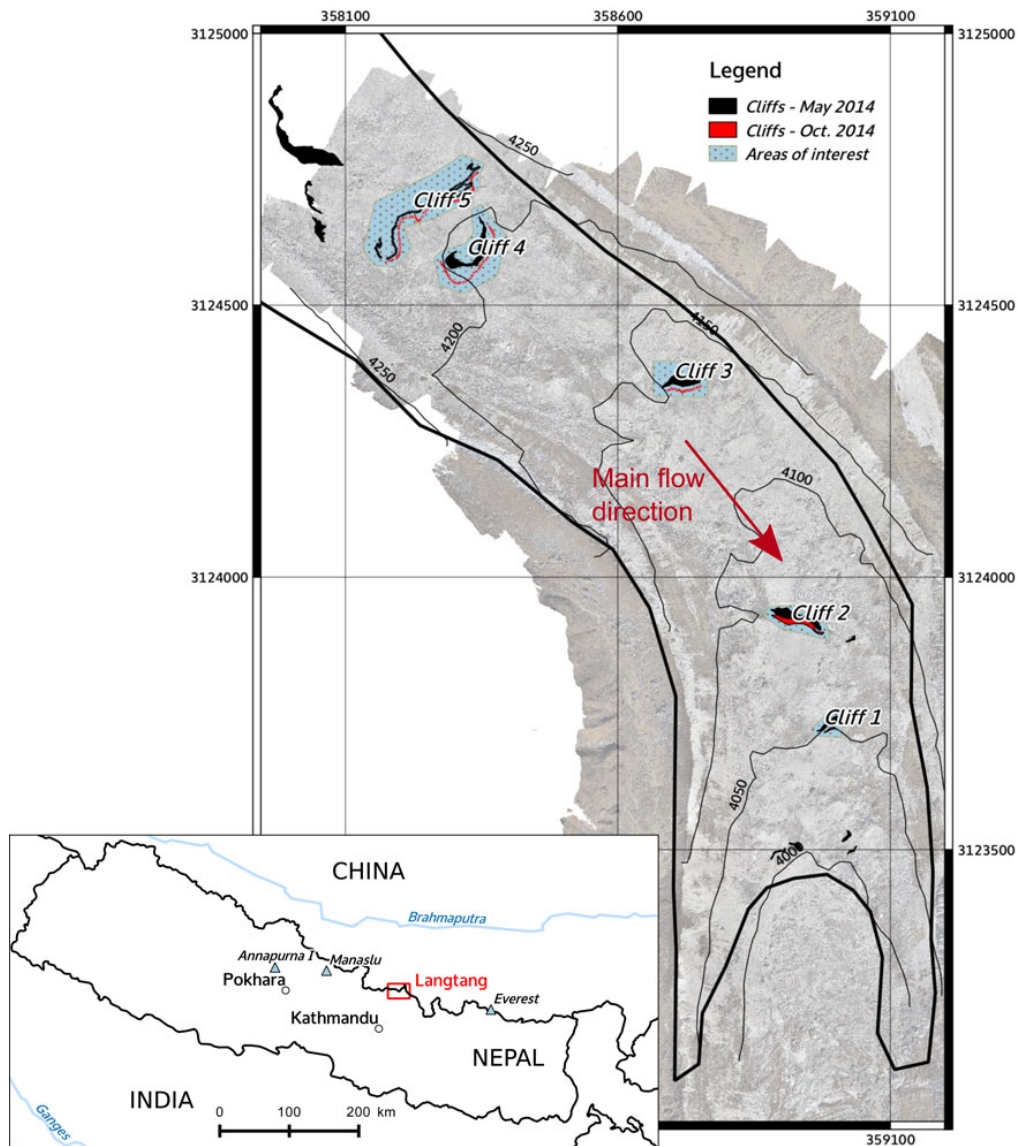


Fig. 1. Map of Lirung Glacier tongue showing the cliffs surveyed in May 2014 (black polygons and dots) and in October 2014 (red polygons and dots). The blue polygons show the areas where terrestrial photographs were taken to measure ice cliff backwasting. The background is an orthophoto taken in October 2013 (Immerzeel and others, 2014). The black thick line represents the glacier outline, manually delineated based on the May 2013 UAV-based orthophoto (Immerzeel and others, 2014). All the coordinates are in UTM 45N/WGS84 (m). The inset shows the location of the Langtang catchment in Nepal.

and cliff 3 in May 2013 were linearly re-sampled at 10 points m^{-2} to facilitate the manual delineation of the cliff.

In May and October 2014, the topography of the cliffs was obtained from terrestrial photographs using SfM. We processed between 10 and 200 pictures to generate each cliff TIN. We filtered the sparse point clouds by removing ~15–20 % of the points with the highest reprojection error and reconstruction uncertainty. The TINs were derived from the dense point clouds using a number of triangle elements with the same order of magnitude as the number of points in the cloud. The final TINs from the terrestrial photogrammetry had a much higher point density than the UAV TINs, ranging from 14 to 243 points m^{-2} . We used 4–8 distinguishable features (such as a high point on the cliff, or a cliff corner) as GCPs for each cliff in order to properly

georeference the SfM output. The GCPs were chosen among the dGPS points forming the cliff outline. We then manually extracted the cliff outline from the TIN, which we compared with the full set of dGPS observations for validation of the SfM TIN (Fig. 2; Table 2).

3.3. Displacement data

As the avalanche-fed and nearly-flat tongue of Lirung Glacier is disconnected from its steep accumulation zone, the ice flows very slowly. Immerzeel and others (2014) measured surface velocities between $\sim 0 m a^{-1}$ (almost stagnant terminus) to $5 m a^{-1}$.

Between May 2014 and October 2014, marked rocks near the cliffs were monitored with a dGPS to track the glacier

Table 1. Characteristics of the studied cliffs

Cliff ID	Height m	Width m	Area m ²	Slope °	Aspect °
Cliff 1	9	42	381	45	321 (NW)
Cliff 2	21	102	1921	48	31 (NE)
Cliff 3	21	80	1494	47	351 (N)
Cliff 4	11	72	1117	43	265 (W)
Cliff 4*	32	65	1369	39	47 (NE)
Cliff 5	21	245	6441	43	313 (NW)

For all cliffs we present the mean value of multiple years of observations (Fig. 7a for dates). The mean slope and aspect is calculated from 20 cm DEMs derived from the cliff TINs and therefore are only indicative (because for an equal area a steep slope is represented by fewer pixels).

Cliff 4 indicates the western side of cliff 4, which was observed for the first time in October 2013 and has been surveyed since May 2014.

surface displacement. The surface displacement data used in this study are listed in Table 3. All cliff outlines are translated horizontally and vertically down-glacier to the October 2014 base to remove glacier motion from the volume calculations (Fig. 3). The local displacement for each cliff is assumed to be equal to the median of the measured velocities in a 50 m buffer around the cliff outlines, excluding the cliffs themselves.

4. METHODS

4.1. Underlying principle

Ice cliff retreat can be idealized as in Figure 4, where cliff backwasting between t_i and t_{i+1} is the volume represented

by the shaded area (cross-sectional view). In this case, the cliff backwasting can be seen as the volume sandwiched between the cliff surfaces at different times after correction of the cliff position for glacier flow. We developed two methods to calculate this volume: (1) the ‘dGPS method’ triangulates the dGPS outline of the cliffs to produce two interpolated surfaces, and the outlines of the two surfaces are then triangulated to enclose a volume; (2) the ‘TIN method’ is based on the extraction of the cliff triangulated surface (i.e. TIN) obtained by photogrammetry. Then the outlines of the cliff at t_1 are triangulated with those at t_5 to enclose a volume (Figs 5, 6).

The TIN method is expected to provide the most realistic volume estimates, as it does not require assumptions on the cliff surface geometry. Nevertheless, the dGPS method has the advantage that it can be applied to very high-resolution satellite images or airborne data, and thus offers greater potential for future applications at regional scale.

4.2. Surface reconstruction and volume calculation

4.2.1. dGPS method

The main assumption we make to triangulate the surface from the outlines is that the cliff surface is mostly flat so that it is consistent to link the upper edge of the cliff with the bottom edge. As the dGPS points are not equally spaced (especially when parts of the outlines cannot be reached because they are too steep or bordered by a lake), we interpolate along the surveyed cliff edge to obtain cliff outlines of 500 nodes on the upper and lower edges for 1:1

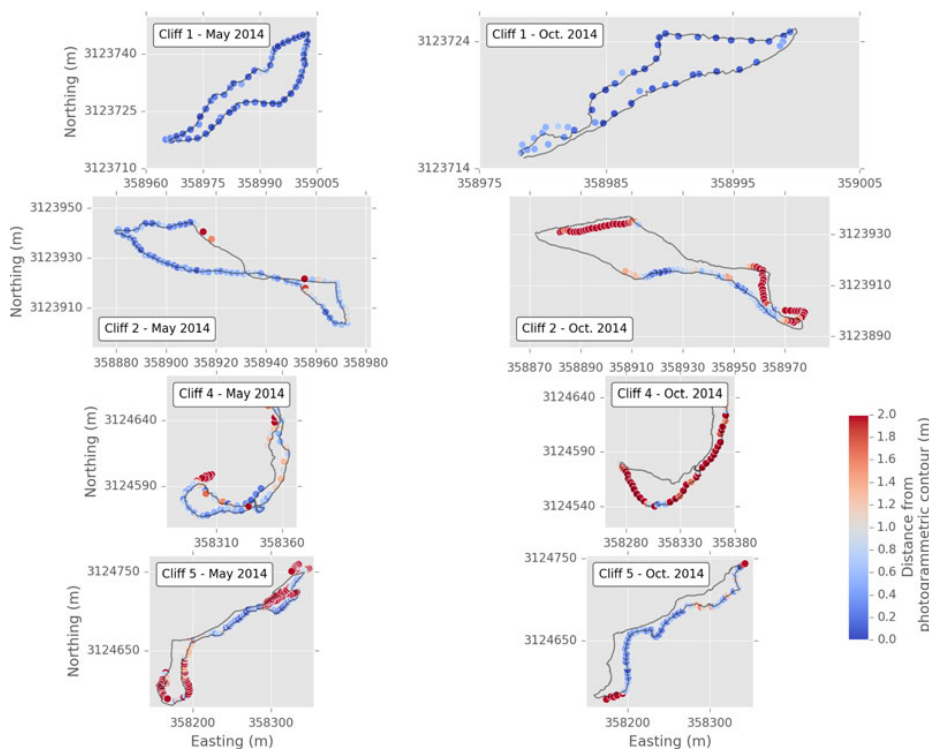


Fig. 2. Distance (3-D) between the field dGPS mapped cliff outlines (dots) and the generated TIN cliff outlines (black). The dots are coloured as a function of the distance to the closest point in the TIN outline. All the coordinates are in UTM 45N/WGS84. Note the difference in horizontal scale between the different cliffs. Cliff 4 is poorly aligned for October 2014, partially due to the lack of dGPS points at the bottom of the cliff. dGPS points are very helpful in aligning the 3-D models and constraining the photogrammetric processing.

Table 2. Differences between dGPS and TINs cliff outlines

Cliff ID	Δx		Δy		Δz		Distance		Number of dGPS points
	Median m	Std m	Median m	Std m	Median m	Std m	Median m	Std m	
Cliff 1 – May 2014	0.2	0.2	0.1	0.2	0.1	0.1	0.3	0.2	57
Cliff 1 – Oct 2014	0.1	0.1	0.1	0.2	0.1	0.1	0.3	0.2	47
Cliff 2 – May 2014	0.3	0.3	0.2	0.3	0.4	0.4	0.7	0.5	79
Cliff 2 – Oct 2014	0.2	0.7	0.7	0.9	0.8	0.5	1.6	1.0	108
Cliff 4 – May 2014	0.7	1.1	0.9	1.5	0.7	0.5	1.4	1.7	78
Cliff 4 – Oct 2014	0.8	0.7	0.4	0.9	0.7	0.9	1.5	1.3	46
Cliff 5 – May 2014	1.0	1.8	1.2	2.0	1.5	1.6	2.2	2.6	170
Cliff 5 – Oct 2014	0.3	0.8	0.4	0.7	0.5	0.7	0.8	1.2	76
Median	0.3	0.7	0.4	0.8	0.6	0.5	1.1	1.1	

All the values correspond to the absolute difference between the cliff TIN outline and dGPS outline. Table based on the same data as Figure 2.

correspondence between outlines. The number of points interpolated between two adjacent dGPS points is a function of the distance between these points normalized by the median distance between adjacent dGPS points along this cliff edge. The upper and lower cliff edges are separated manually. Once the outline is interpolated, we triangulate it according to the rule illustrated in Figure 6a. The point number $(i - 1)$ of the bottom edge (y_{i-1}) is linked with the point number i of the bottom edge (y_i) and with the point number i of the upper edge (x_i). Then x_i is linked with y_i and x_{i+1} .

4.2.2. TIN method

For the TIN method the cliff surface is delineated and extracted based on visual inspection of the coloured TIN and of the raw photographs (the cliff has different color and texture than the surrounding terrain).

In both cases we obtain a TIN that contains the cliff surface. These TINs are linearly translated down-glacier to the position where they would have been in October 2014 if the glacier was motionless (Fig. 3). We used for this the velocity data of Table 3.

The triangulation of the ice volume loss is similar to the triangulation of the surface from the dGPS outline (Fig. 6b). For the TIN method, the original cliff outline extracted from the TIN is also interpolated to produce a cliff outline of 1000 points.

The final three meshes (cliff at t_1 , cliff at t_2 displaced to October 2014 base and the mesh obtained by joining the

two cliff outlines) are imported into the open-source software MeshLab (Cignoni and others, 2008). In Meshlab, the face normals are oriented outwards and merged into a single mesh, from which the volume is calculated according to Mirtich (1996).

4.3. Uncertainty assessment

The main sources of uncertainties in our methods are: (1) the emergence velocity, which is not taken into account, (2) uncertainty of the cliff outline position as determined from the TIN vertices, (3) uncertainty and spatial variability of the glacier surface displacement field and (4) uncertainty of the georeferencing.

It is difficult to assess the uncertainty associated with the first and second sources of errors. The emergence velocity can be estimated by calculating the ice flow through a cross section of the glacier. This can be performed by measuring the ice surface velocity (and assuming a given ice velocity profile) and the ice thickness along the cross section. The surface velocity can be estimated from our data (either from the UAV or the dGPS data), but the ice thickness is unknown. However, the emergence velocity was previously estimated to be $\sim 0.18 \text{ m a}^{-1}$ (Naito and others, 1998), which is low compared with the 1.1 m a^{-1} average lowering of the glacier surface (Immerzeel and others, 2014). The discrimination between cliff and non-cliff surfaces is a potential source of error ((2) above), but it is usually straightforward to distinguish between vertical bare ice and the surrounding rocks because they have different colors and the cliff surface

Table 3. Glacier surface displacement corresponding to each cliff

Cliff ID	May–Oct. 2013			Oct. 2013–May 2014			May–Oct. 2014		
	D_x m	D_y m	D_z m	D_x m	D_y m	D_z m	D_x m	D_y m	D_z m
Cliff 1	–0.1	–0.4	–0.8	0.2	–0.4	–	0.3	–0.7	–1.2
Cliff 2	0.1	–0.8	–1.0	0.4	–0.2	–	0.2	–0.3	–1.6
Cliff 3	1.3	–0.3	–0.5	–	–	–	1.2	–0.2	–0.6
Cliff 4	1.8	–0.1	–1.0	–	–	–	1.6	–0.7	–1.1
Cliff 5	–	–	–	–	–	–	0.7	–1.4	–0.7
Median	0.7	–0.3	–0.9	0.3	–0.3	–	0.7	–0.7	–1.1

D_x and D_y are increasing towards the east and north, respectively. D_z is the difference in elevation. The data from May–October 2014 are obtained by tracking marked rocks with dGPS. The May–October 2013 data and the October 2013–May 2014 come from feature tracking on UAV orthophotos and DEMs (Immerzeel and others, 2014).

Brun and others: Quantifying volume loss from ice cliffs on debris-covered glaciers using high-resolution terrestrial and aerial photogrammetry 689

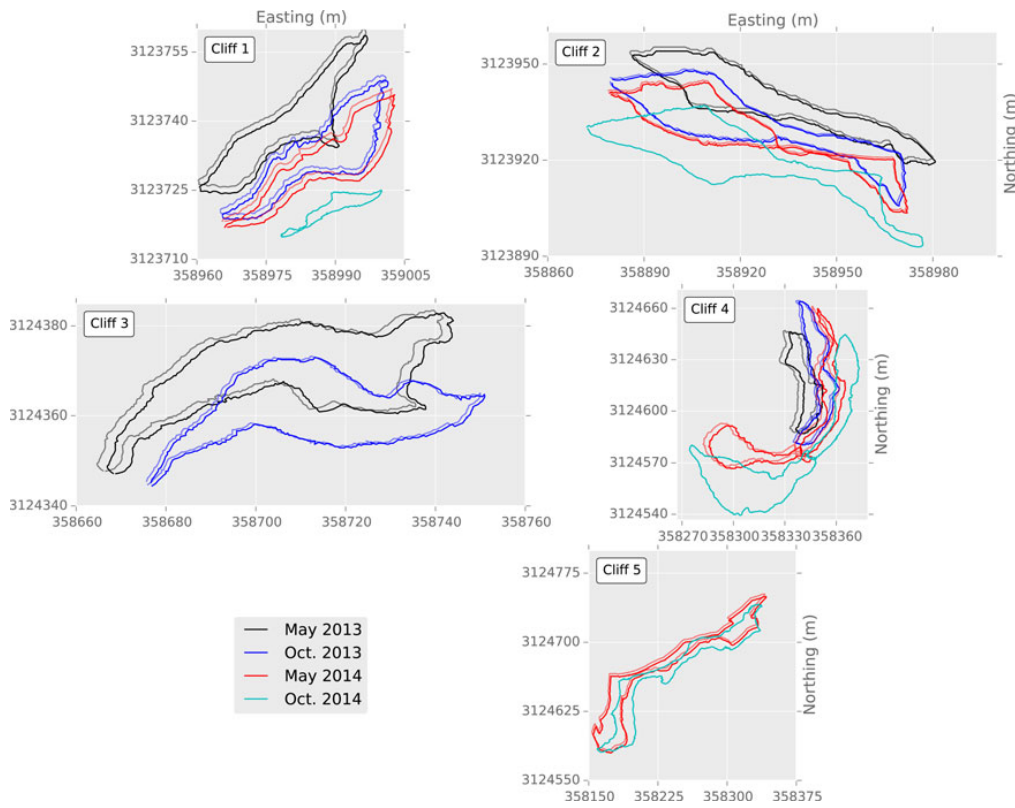


Fig. 3. Cliff outlines from May 2013 to October 2014. The light coloured outlines are the original cliff outlines and the darker outlines are after correction for the glacier flow according to the October 2014 base. All the coordinates are in UTM 45N/WGS84 system (m). Note the difference in the horizontal scale.

is smooth and flat compared with the surrounding environment.

Uncertainty on cliff displacement due to glacier motion ((3) above) is not easy to assess. Our method assumes that the local displacement field is homogeneous within the cliff. This is a reasonable assumption for small cliffs (e.g. cliff 1) but is more questionable for larger cliffs, even though they are mostly perpendicular to the flow. The larger cliffs (almost as large as the glacier width) are very likely to experience some differential flow. The glacier-wide boulder tracking study of (Immerzeel and others, 2014) showed that the 147 boulders have a mean displacement (horizontal and vertical) of 1.1 m with a standard deviation of 0.7 m over the study period. Assuming the uncertainty in the displacement is equal to the ratio of the standard deviation to the average, we obtain an uncertainty

of 60%. The displacements between May and October, and October and May are, on average 1.4 and 0.4 m, respectively (Table 3; for May–October we use the average over the two periods May–October 2013 and May–October 2014). This leads to uncertainties in displacement, $\Delta_{\text{displacement}}$ of 0.8 m between May and October and 0.2 m between October and May.

The main uncertainty remains the location of the cliff outlines as derived from the SfM workflow and by dGPS measurement ((4) above). The absolute median distance between each point of the cliff dGPS outline and of the closest point of the cliff TIN outline is higher in z (0.6 m) than in x and y (0.4 and 0.4 m, respectively; Table 2). We also take into account the intrinsic uncertainty on dGPS location, which is assumed to be ± 0.3 m. The total uncertainty on the cliff location can be calculated as the quadratic sum of

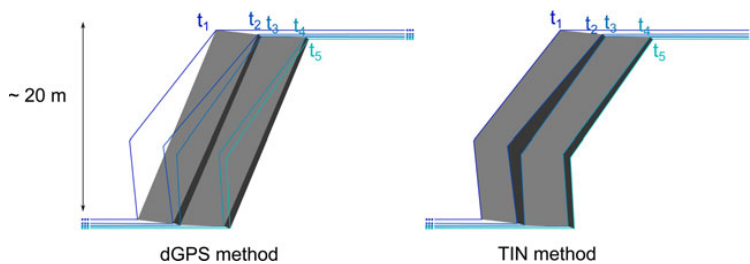


Fig. 4. Idealized cross-section views of a retreating cliff between times t_1 and t_5 . The cliff backwasting is represented by the grey shaded areas (projections of the backwasting volumes).

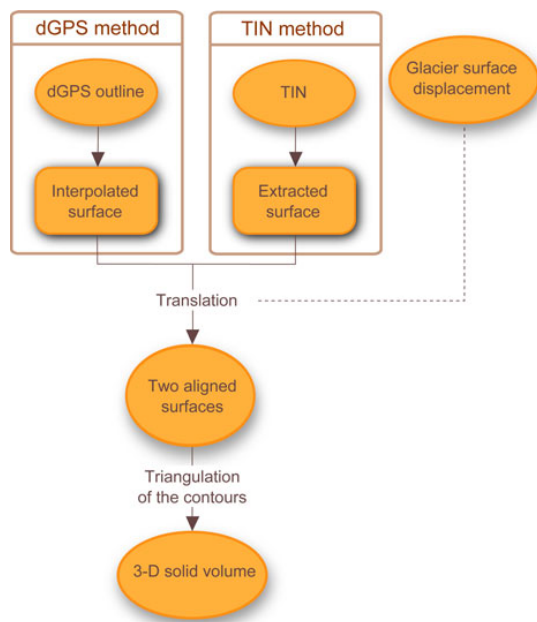


Fig. 5. Chart of the workflow.

these errors, which leads to an uncertainty in outline location, Δ_{outline} , of 0.9 m.

Assuming that both errors in displacement and location are independent, the overall uncertainty in the location is calculated as:

$$\begin{aligned} \Delta_{\text{overall}} &= \sqrt{\Delta_{\text{displacement}}^2 + \Delta_{\text{outline}}^2} \\ &= \begin{cases} 1.2 & m \text{ between May and October} \\ 0.9 & m \text{ between October and May} \end{cases} \quad (1) \end{aligned}$$

It is difficult to assess whether this overall error in location has preferential directions, so we use it as the upper bound for the worst-case scenario (i.e. we take the error to be exactly in the backwasting direction). Using typical values 6 m of backwasting (D_{bw}) over the monsoon season, and 2 m over the winter, obtained with our method (Table 4), we obtain the following relative uncertainties:

$$\Delta_{\text{bw}} = \frac{\Delta_{\text{overall}}}{D_{\text{bw}}} = \begin{cases} 20\% & \text{between May and October} \\ 45\% & \text{between October and May} \end{cases} \quad (2)$$

The uncertainty on the cliff area ((2) above) is negligible in comparison, so we represent the maximum uncertainty of volume calculations using Δ_{bw} .

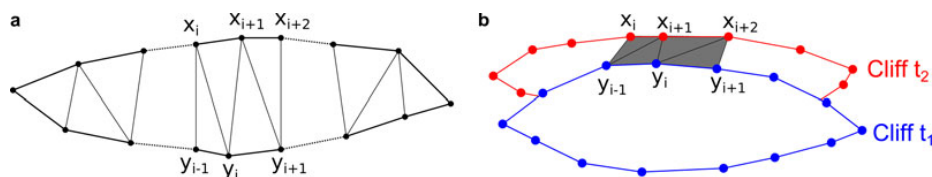


Fig. 6. Schematic of the principle of the triangulation (a) of a cliff outline (used in the dGPS method) and (b) between two cliff outlines to calculate the melted ice volume. For the sake of readability, the density of points is reduced. In real cases, the points are closer and more evenly distributed along each outline.

5. RESULTS

We calculate a normalized volume loss, called hereafter average cliff backwasting rate, as the volume loss between t_1 and t_2 divided by the average of the cliff areas at t_1 and t_2 , converted to cm w.e. assuming an ice density of 900 km m^{-3} . Figure 7 and Table 4 show the backwasting rate calculated with the TIN method for all cliffs and seasons investigated. This normalization is useful for comparing cliff changes within different areas (Fig. 7a), but it may not be appropriate to normalize by the mean area when the area changes drastically between the two dates (for instance cliff 1 and cliff 4' between May and October 2014; Fig. 7). Cliffs lose mass at much faster rates between May and October ($3.8 \pm 0.3 \text{ cm w.e. d}^{-1}$ in 2013 and $3.1 \pm 0.7 \text{ cm w.e. d}^{-1}$ in 2014) than between October and May ($1.0 \pm 0.3 \text{ cm w.e. d}^{-1}$; Table 4), in agreement with Steiner and others (2015). We suspect that a large part of the measured melt between October and May happens just after observations in October or just before observations in April/May, corresponding to the end and start of the melt season in Langtang catchment (Steiner and others, 2015). The consistency in the backwasting rates between the two monsoon seasons suggests similar controls of backwasting. Cliffs with area spanning over two orders of magnitude lose mass at similar rates (Fig. 7). The reduced backwasting rate during winter is expected and can be explained by a reduction in the total energy reaching the cliff surface, especially the incoming shortwave and longwave radiation, which are the two main energy fluxes (Steiner and others, 2015). In winter, the solar elevation angle is lower, reducing incoming shortwave radiation over the entire glacier tongue, and especially affecting the cliff surfaces due to their northerly aspects and steep slopes. The incoming longwave radiation from the surrounding debris is also reduced due to the lower average temperature of the debris surfaces. In addition, refreezing may play a strong role in the reduction of melt in winter (Steiner and others, 2015).

The backwasting rates obtained using the TIN method are compared with the backwasting rates obtained using the dGPS method in Table 4. The data are sufficient to apply the latter only for cliff 1 and cliff 2 between May and October 2014. The cliff outlines were fully mapped for cliff 3, 4 and 4' in May 2014 as well, but lack of time did not allow the survey to be repeated in October 2014. Cliff 5's bottom edge has never been accessible because of a large supraglacial lake. For cliff 1 the agreement is very good and the volume loss estimated with the dGPS method is $<1.5\%$ lower than the TIN method's result. On the other hand for cliff 2 the agreement is not as good and the dGPS method underestimates the volume loss by 9%. This is within the uncertainty of the TIN method and could be due either to the complex geometry of cliff 2 (which exhibits an

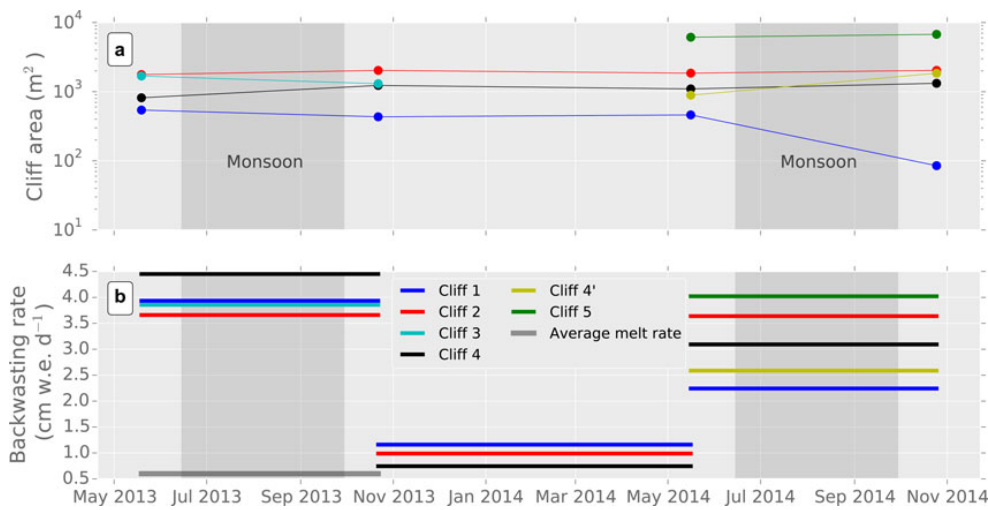


Fig. 7. Area change (a) and backwasting rate (b) of all cliffs as a function of time. The backwasting rate is defined as the volume change between t_1 and t_2 divided by the number of days and the mean cliff area. The average melt rate (grey) is from Immerzeel and others (2014). Note that the y-axis for the upper panel has a logarithmic scale. Shaded areas in both panels indicate the monsoon period (15 June–30 September).

overhanging face) or the incomplete dGPS outline of cliff 2 (Fig. 2), which leads to an underestimation of the volume loss. As they are, these results are insufficient to reach a conclusion about the dGPS method’s accuracy.

6. DISCUSSION

6.1. Method’s limitations and comparison with M3C2 method

The method developed in this paper has the potential to provide estimates of cliff backwasting that can be used to validate melt models and/or to provide a direct estimate of cliff contribution to total glacier mass balance. The method requires several steps of manual processing: delineating the cliff outlines, merging the different TINs and calculating the volume of the mesh. This was not a limiting factor in this study, but it will be useful to automate some of these steps to apply the method more systematically.

The TIN and dGPS methods are not suitable for estimating backwasting rates for cases, in which the cliff geometry changes significantly, as for cliff 1, which shrank between May and October 2014 (Fig. 7a). Despite the high confidence

in the volume loss estimate, we can obtain a backwasting rate of 0.7 or 3.8 cm w.e. d⁻¹ if we normalize by the cliff area of May 2014 or October 2014, respectively. A similar effect can be observed for cliff 4, which expanded between May and October 2014.

The method is also intrinsically limited by the accuracy of the topographic data and it can only be applied to calculate backwasting rates over periods long enough to measure changes that are significantly higher than the uncertainty of the method.

Another main limitation of the TIN and dGPS methods is the fact that they provide only estimates of total volume loss, and cannot be used to calculate the spatial distribution or patterns of cliff backwasting. A promising alternative method is the M3C2 algorithm, which was developed to measure distances between point clouds (Lague and others, 2013). This method is based on calculation of local normals to the initial surface, which are then used to calculate distances from the other surface. This algorithm was tested without success on our data, which describe the geometry of the cliff surface alone. However, the test was unsuccessful for two reasons. First, as the backwasting is usually not perpendicular to the cliff face, mismatches occur

Table 4. Volume loss obtained for all cliffs over the study period

Method	May–Oct. 2013			Oct. 2013–May 2014			May–Oct. 2014		
	D_{bw}	Rate	Volume	D_{bw}	Rate	Volume	D_{bw}	Rate	Volume
	m	cm w.e. d ⁻¹	m ³	m	cm w.e. d ⁻¹	m ³	m	cm w.e. d ⁻¹	m ³
Cliff 1 TIN	6.0	3.8 (3.6)	3241	2.4	1.2	1189	3.6	2.2	1103.1
Cliff 1 dGPS	–	–	–	–	–	–	3.6	2.2	1113
Cliff 2 TIN	5.7	3.7 (3.1)	12 050	2.0	1.0	4393	5.9	3.6	12 728
Cliff 2 dGPS	–	–	–	–	–	–	5.2	3.2	11 251
Cliff 3 TIN	6.0	3.9	9986	–	–	–	–	–	–
Cliff 4 TIN	6.9	4.5	7901	1.5	0.7	1984	5.0	3.1	6733
Cliff 4’ TIN	–	–	–	–	–	–	4.2	2.6	6372
Cliff 5 TIN	–	–	–	–	–	–	6.5	4.0	46 627

The bracketed May–October 2013 values for cliff 1 and cliff 2 are the estimates of Buri and others (2016).

between normals calculated at the cliff surface at t_1 , which frequently miss the cliff surface at t_2 . Based on our attempts with the algorithm, this results in a loss of up to 82% of points, with the highest efficacy when the backwasting is smallest (winter). Second, interpretation of spatial patterns of backwasting are subjected to high relative georeferencing errors – a slight lateral shift in the position of cliff geometry observed at t_2 may emphasize backwasting at one part of the cliff over another; the volume estimate will not be affected so heavily but the spatial patterns may be very sensitive to such a change. Finally, computation of volumetric change from M3C2 distances is not a trivial undertaking (Lague and others, 2013). As a result, we believe that the method presented here has value as an alternate approach to assess volumetric change of ice cliffs.

However, algorithms for cloud comparison are fast developing and the M3C2 method is very promising for future analyses of the spatial patterns of backwasting, especially for short-return time intervals. Thus, we present here some recommendations for data collection targeting M3C2 use, and highlight the challenges that future applications will face. First, to maximize the likelihood of surface normals from t_1 intercepting the surface at t_2 , we suggest a closed-volume approach to terrestrial SfM. This entails measuring the entire ice cliff depression, as well behind the cliffs (rather than the cliff geometry alone), such that the area of volumetric change is fully enclosed by the two point clouds. Second, the georeferencing needs to be more accurate than was performed for this study. Therefore, we recommend georeferencing of the TINs on artificial GCPs (i.e. painted rocks for instance) instead of natural features, for easier identification and stronger constraint in the SfM processing. Third, we recommend more frequent surveys of cliff geometry, studying changes over shorter time intervals

than used for this study and maximizing the usable area of the cliff.

6.2. Comparison with a simplified approach

Both the TIN and dGPS methods require collection of substantial field data. It is beneficial to determine the minimum amount of input data required to obtain a satisfying estimate of cliff backwasting rate. To estimate ice cliff backwasting, Han and others (2010) measured the distance between the cliff edge and a distinguishable fixed boulder at t_1 , and measured it again at t_2 (1 month later in their case). We adapted their method and measured the horizontal distance between the cliff upper edge at t_1 and at t_2 on the ortho-photos. For comparison, we calculated the backwasting distance (i.e. volume loss divided by the cliff average area with no density correction (m)) taking into account the cliff geometry provided by our topographic dataset. Interpolating the two cliff edges to obtain the same number of points along each edge, we took the median distance between these pairs of points as the distance between the edges. After correcting for glacier flow and excluding cliff 4' from the analysis because its shape changed too much, we compared the horizontal distance between the edges with our estimate of the perpendicular backwasting (called backwasting distance; Fig. 8 – left panel). The horizontal distance is higher than the backwasting distance (mean bias of 2.9 m). If we calculate the horizontal backwasting by projecting the backwasting distance (i.e. by dividing the backwasting distance by the sine of the slope), the mean bias is reduced (0.9 m) but the correlation is slightly worse ($R^2 = 0.58$ after projection versus 0.66 without correction; Fig. 8). Even if the agreement between the two methods is not fully satisfying, it has the potential to be used widely because cliff edges are visible on

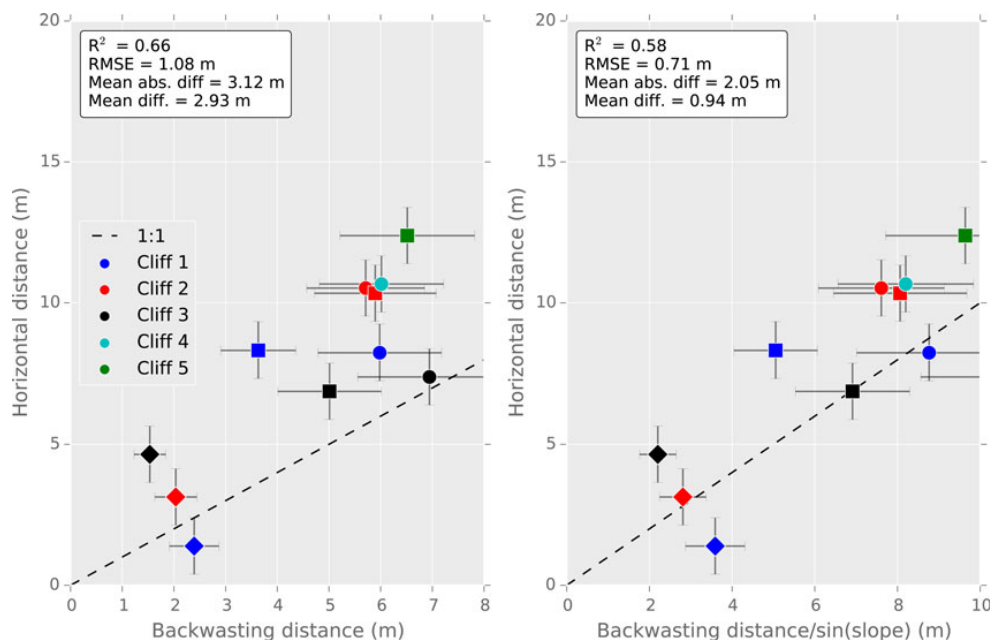


Fig. 8. Comparison of the cliff backwasting measured with our method (x-axis) and the horizontal displacement of the cliff edge (y-axis). The circles correspond to the period May–October 2013, the diamonds to the period October 2013–May 2014 and the squares to the period May–October 2014. The dashed line is the 1:1 line. The backwasting distance is calculated as the volume loss divided by the cliff area. Note that cliff 4' is excluded from the analysis. The x error bars are calculated assuming 15% uncertainty in the volume loss results and the y error bars correspond to 1 m of error in the edge backwasting observation.

very high-resolution satellite imagery. However, a major drawback of this method is that it cannot provide estimates of the volume loss (because the cliff area and slope are a priori unknown) and is therefore of limited interest.

6.3. Comparison with model results

The present study derives mass losses from cliff backwasting that can be used to validate models. Buri and others (2016) developed a distributed energy balance model that calculates melt for each grid cell of a high-resolution DEM of the cliff. They applied the model to cliff 1 and 2 of Lirung Glacier for 8 May–23 October 2013. The model was forced with data from an AWS located on-glacier. Buri and others (2016) ran the model on a 20 cm grid extracted from an UAV DEM (Immerzeel and others, 2014; Buri and others, 2016). Buri and others (2016) calculated average melt rates of 3.6 and 3.1 cm w.e. d⁻¹ for cliff 1 and 2 respectively, results consistent with ours: 3.8 ± 0.8 and 3.7 ± 0.7 cm w.e. d⁻¹, respectively (Table 4). The volume losses calculated with the TIN method are slightly higher than the model estimates (even if the uncertainties on both are still large). This can be explained by the fact that Buri and others (2016) calculated only the volume losses associated with melt due to energy exchange with the atmosphere, whereas other processes, such as the contribution to radiative fluxes of a lake or thermoerosion at the base of the cliff, may also contribute to cliff backwasting.

6.4. Insight into mechanisms of cliff area changes

The repeated high-resolution topographic surveys are very useful for documenting cliff evolution. The expansion of cliff 4, with the appearance of a new cliff on its western side (cliff 4'), or the shrinkage of cliff 1 are striking behaviours, in contrast to cliff 2 and 5, which maintain a constant shape (Figs 3, 9). The most interesting change observed in this study is the shrinkage of cliff 1, which nearly disappeared between May and October 2014 (Figs 3, 7, 9).

A first possible mechanism responsible for the disappearance of cliff 1 may be the absence of a lake at its foot. The lake contributes to the ice cliff radiation budget and maintains the steep slope at the lower section of the cliff through thermoerosional undercutting (Miles and others, 2016). Field evidence suggests that a pond was present during May–October 2013, which then disappeared, triggering the substantial changes in cliff 1 from May to October 2014.

A second possible mechanism may be the limiting volume of the topography behind the cliff. We analyzed the surrounding terrain within a 2 m buffer around the upper cliff edge. For cliff 1, we observed that a small ridge, parallel to the cliff edge and located ~1 m from the edge in the north-eastern side of the cliff disappeared between October 2013 and May 2014. It is likely that its disappearance limited the amount of ice available for melt.

These process-oriented hypotheses remain qualitative and speculative, but our method has produced one of the first quantitative datasets of cliff evolution over several seasons,

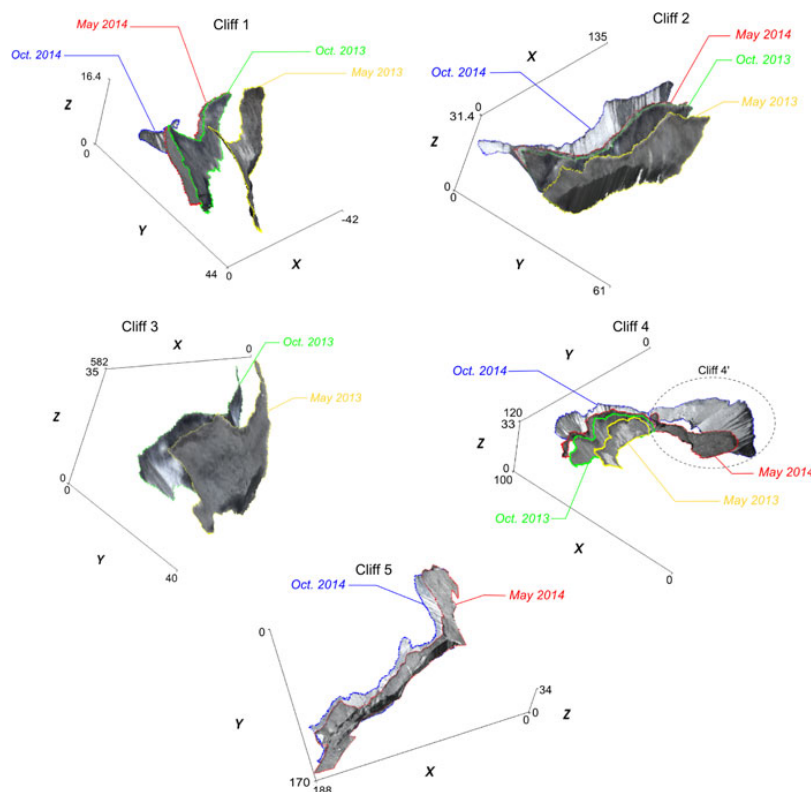


Fig. 9. Evolution of the cliffs between May 2013 and October 2014. The X, Y and Z coordinates are in meters with arbitrary origins. X and Y correspond to the easting and northing, respectively. All the TINs from which these figures are produced are shifted to the October 2014 base to correct for the ice flow.

showing interesting phenomena of growth and decay that should be incorporated into advanced numerical models of cliff evolution.

7. CONCLUSIONS

In this study we have developed a method based on high-resolution topographic data to assess volume loss due to ice cliff backwasting, and applied the method to selected ice cliffs of Lirung Glacier (Langtang Valley, Nepal). Our results confirm the significant contribution of ice cliffs to total mass loss, with backwasting rates of $3.5 \pm 0.7 \text{ cm d}^{-1}$ over the monsoon. This rate is 6 times higher than the average glacier ablation rate over the same period (Immerzeel and others, 2014), thus substantiating a potential explanation for the so-called debris-covered anomaly. This is, to our knowledge, the first accurate, high-resolution estimate of ice cliff backwasting from ground data, and is important as a confirmation of the results of the few existing modelling studies (Han and others, 2010; Reid and Brock, 2014; Steiner and others, 2015; Buri and others, 2016).

We have provided the first time series of cliff 3-D changes, encompassing a period of two monsoon seasons and one winter season. This time series shows geometric developments that are not uniform, with some cliffs exhibiting few changes and a striking persistence over the two monsoon seasons, while others grow or shrink substantially. These variable observations point to the heterogeneity of the processes controlling cliff evolution and dynamics, even on a relatively small glacier such as Lirung Glacier, and to the need for process-based modelling studies of cliff developments.

While there is some evidence that cliffs form preferentially on stagnant tongues, we still lack an understanding of their distribution, formation and future change. The datasets in this study can provide the necessary basis for numerical studies of cliff evolution.

In addition, the existing energy balance models of cliff backwasting are still affected by parametric uncertainties and errors due to the poorly understood variability of meteorological forcing at the cliff's local scale (Steiner and others, 2015; Buri and others, 2016). Availability of accurate, high-resolution datasets of 3-D cliff backwasting such as presented here can help to significantly constrain these uncertainties and inform model development. While assessment of ice cliff volume changes with this method is not practical at the scale of large glaciers or basins, more datasets of the type presented in this paper can provide critical calibration and validation data for numerical model development, and be used to test simplified methods of cliff volume change estimates based on satellite images. These data are now easier to collect and process thanks to the recent advances in UAVs and photogrammetric software.

ACKNOWLEDGEMENTS

We thank Tek Rai, Ibai Rico, Anna Chesnokova and Bhanu Thakur for help with dGPS and photogrammetric data collection. All the participants in the four field campaigns made this work possible and are gratefully acknowledged, as all are the Nepali helpers who supported our work in a great way. We thank Joe Shea and the International Centre for Integrated Mountain Development (ICIMOD) for administrative and logistical support in Kathmandu. We thank Dimitri Lague

and Matt Westoby for precious advice on M3C2 algorithm use. This study is funded by the Swiss National Science Foundation (SNF) project UNCOMUN (Understanding Contrasts in High Mountain Hydrology in Asia) and by the USAID High Mountain Glacier Watershed Programs Climber-Scientist (Grant No. CCRDCS0010), which are warmly acknowledged for their support. E. B. acknowledges support from the French Space Agency (CNES) through the TOSCA and ISIS programs. We thank Duncan Quincey and an anonymous reviewer who made very helpful comments on an earlier version of this manuscript, which greatly improved the final paper. This project has received funding from the European Research Council (ERC) under the European Union's Horizon 2020 research and innovation program (grant agreement No 676819).

REFERENCES

- Agisoft (2013) *PhotoScan Professional 1.0.0 user manual*. St Petersburg
- Bolch T and 11 others (2012) The state and fate of Himalayan glaciers. *Science*, **336**, 310–314 (doi: 10.1126/science.1215828)
- Buri P, Pellicciotti F, Steiner J, Miles E and Immerzeel W (2016) A grid-based model of backwasting of supraglacial ice cliffs on debris-covered glaciers. *Ann. Glaciol.*, **57**(71), 199–210 (doi: 10.3189/2016aog71a059)
- Cignoni P, Corsini M and Ranzuglia G (2008) Meshlab: an open-source 3d mesh processing system. *Ercim News*, **73**, 45–46
- Furukawa Y and Ponce J (2009) Accurate camera calibration from multi-view stereo and bundle adjustment. *Int. J. Comput. Vis.*, **84**(3), 257–268, ISSN 0920-5691 (doi: 10.1007/s11263-009-0232-2)
- Gardelle J, Berthier E, Arnaud Y and Käab A (2013) Region-wide glacier mass balances over the Pamir-Karakoram-Himalaya during 1999–2011. *Cryosphere*, **7**(4), 1263–1286 (doi: 10.5194/tc-7-1263-2013)
- Han H, Wang J, Wei J and Liu S (2010) Backwasting rate on debris-covered Koxkar glacier, Tuomuer mountain, China. *J. Glaciol.*, **56**, 287–296 (doi: 10.3189/002214310791968430)
- Holzer N and 5 others (2015) Four decades of glacier variations at Muztag Ata (Eastern Pamir): a multi-sensor study including Hexagon KH-9 and Pléiades data. *Cryosphere Discuss.*, **9**(2), 1811–1856 (doi: 10.5194/tcd-9-1811-2015)
- Immerzeel W and 6 others (2014) High-resolution monitoring of Himalayan glacier dynamics using unmanned aerial vehicles. *Remote Sens. Environ.*, **150**, 93–103 (doi: 10.1016/j.rse.2014.04.025)
- Käab A, Berthier E, Nuth C, Gardelle J and Arnaud Y (2012) Contrasting patterns of early twenty-first-century glacier mass change in the Himalayas. *Nature*, **488**(7412), 495–498 (doi: 10.1038/nature11324)
- Kraaijenbrink P and 5 others (2016) Seasonal surface velocities of a Himalayan glacier derived by automated correlation of unmanned aerial vehicle imagery. *Ann. Glaciol.*, **57**(61), 103–113 (doi: 10.3189/2016aog71a072)
- Lague D, Brodu N and Leroux J (2013) Accurate 3D comparison of complex topography with terrestrial laser scanner: application to the Rangitikei canyon (N-Z). *ISPRS J. Photogramm. Remote Sens.*, **82**, 10–26, ISSN 0924-2716 (doi: 10.1016/j.isprsjprs.2013.04.009)
- Lejeune Y, Bertrand JM, Wagnon P and Morin S (2013) A physically based model of the year-round surface energy and mass balance of debris-covered glaciers. *J. Glaciol.*, **59**, 327–344 (doi: 10.3189/2013JoG12J149)
- Miles E and 5 others (2016) Refined energy-balance modelling of a supraglacial pond, Langtang Khola, Nepal. *Ann. Glaciol.*, **57**(71), 29–39

Brun and others: Quantifying volume loss from ice cliffs on debris-covered glaciers using high-resolution terrestrial and aerial photogrammetry 695

- Mirtich B (1996) Fast and accurate computation of polyhedral mass properties. *J. Graphics Tools*, **1**(2), 31–50 (doi: 10.1080/10867651.1996.10487458)
- Naito N and 8 others (1998) Surface flow on the ablation area of the Lirung Glacier in Langtang Valley, Nepal Himalayas. *Bull. Glacier Res.*, **16**, 67–73
- Nicholson L and Benn DI (2006) Calculating ice melt beneath a debris layer using meteorological data. *J. Glaciol.*, **52**, 463–470 (doi: 10.3189/172756506781828584)
- Nuimura T, Fujita K, Yamaguchi S and Sharma RR (2012) Elevation changes of glaciers revealed by multitemporal digital elevation models calibrated by GPS survey in the Khumbu region, Nepal Himalaya, 1992–2008. *J. Glaciol.*, **58**(210), 648–656 (doi: 10.3189/2012JoG11J061)
- Østrem G (1959) Ice melting under a thin layer of moraine, and the existence of ice cores in moraine ridges. *Geogr. Ann.*, **41**(4), 228–230, ISSN 16513215
- Passalacqua P and 15 others (2015) Analyzing high resolution topography for advancing the understanding of mass and energy transfer through landscapes: a review. *Earth-Sci. Rev.*, **148**, 174–193, ISSN 0012-8252 (doi: 10.1016/j.earscirev.2015.05.012)
- Pellicciotti F and 5 others (2015) Mass-balance changes of the debris-covered glaciers in the Langtang Himal, Nepal, from 1974 to 1999. *J. Glaciol.*, **61**(226), 373–386 (doi: 10.3189/2015jog13j237)
- Ragetti S and 9 others (2015) Unraveling the hydrology of a Himalayan catchment through integration of high resolution in situ data and remote sensing with an advanced simulation model. *Adv. Water Res.*, **78**, 94–111, ISSN 0309-1708 (doi: 10.1016/j.advwatres.2015.01.013)
- Reid T and Brock B (2014) Assessing ice-cliff backwasting and its contribution to total ablation of debris-covered Miage glacier, Mont Blanc massif, Italy. *J. Glaciol.*, **60**(219), 3–13 (doi: 10.3189/2014JoG13J045)
- Reid TD and Brock BW (2010) An energy-balance model for debris-covered glaciers including heat conduction through the debris layer. *J. Glaciol.*, **56**, 903–916 (doi: 10.3189/002214310794457218)
- Sakai A, Nakawo M and Fujita K (1998) Melt rate of ice cliffs on the Lirung Glacier, Nepal Himalayas, 1996. *Bull. Glacier Res.*, **16**, 57–66, ISSN 09134190
- Sakai A, Takeuchi N, Fujita K and Nakawo M (2000) Role of supraglacial ponds in the ablation process of a debris-covered glacier in the Nepal Himalayas. In *Debris-covered Glaciers (Proceedings of a Workshop Held at Seattle, Washington, USA, September 2000)*, vol. **265**
- Sakai A, Nakawo M and Fujita K (2002) Distribution characteristics and energy balance of ice cliffs on debris-covered glaciers, Nepal Himalaya. *Arct. Antarct. Alp. Res.*, **34**(1), 12–19
- Scherler D, Bookhagen B and Strecker MR (2011) Spatially variable response of Himalayan glaciers to climate change affected by debris cover. *Nat. Geosci.*, **4**, 156–159 (doi: 10.1038/ngeo1068)
- Snavely N, Seitz S and Szeliski R (2008) Modeling the world from internet photo collections. *Int. J. Comput. Vis.*, **80**(2), 189–210, ISSN 0920-5691 (doi: 10.1007/s11263-007-0107-3)
- Steiner J and 5 others (2015) Modelling ice cliff backwasting on a debris covered glacier in the Nepalese Himalayas. *J. Glaciol.*, **61**(229), 889–907
- Westoby M, Brasington J, Glasser N, Hambrey M and Reynolds J (2012) Structure-from-motion photogrammetry: a low-cost, effective tool for geoscience applications. *Geomorphology*, **179**, 300–314, ISSN 0169-555X (doi: 10.1016/j.geomorph.2012.08.021)

MS received 27 July 2015 and accepted in revised form 4 February 2016; first published online 13 May 2016

Bibliography

- Agarwal, V., T. Bolch, T. H. Syed, T. Pieczonka, T. Strozzi, and R. Nagaich (2017), Area and mass changes of Siachen Glacier (East Karakoram), *Journal of Glaciology*, 63, 148–163, doi: 10.1017/jog.2016.127.
- Agisoft, L. (2017), Agisoft PhotoScan User Manual: Professional Edition, Version 1.3.
- Akaike, H. (1974), A new look at the statistical model identification, *IEEE transactions on automatic control*, 19(6), 716–723.
- Akhtar, M., N. Ahmad, and M. J. Booij (2008), The impact of climate change on the water resources of Hindukush–Karakorum–Himalaya region under different glacier coverage scenarios, *Journal of hydrology*, 355(1-4), 148–163.
- Alexander, D., J. Shulmeister, and T. Davies (2011), High basal melting rates within high-precipitation temperate glaciers, *Journal of Glaciology*, 57(205), 789–795, doi: 10.3189/002214311798043726.
- Andermann, C., S. Bonnet, and R. Gloaguen (2011), Evaluation of precipitation data sets along the Himalayan front, *Geochemistry, Geophysics, Geosystems*, 12, Q07,023, doi: 10.1029/2011GC003513.
- Andermann, C., L. Longuevergne, S. Bonnet, A. Crave, P. Davy, and R. Gloaguen (2012), Impact of transient groundwater storage on the discharge of Himalayan rivers, *Nature Geoscience*, 5, 127.
- Anderson, L. S., and R. S. Anderson (2016), Modeling debris-covered glaciers: response to steady debris deposition, *The Cryosphere*, 10(3), 1105–1124, doi: 10.5194/tc-10-1105-2016.
- Andreassen, L. M., H. Elvehøy, B. Kjølmoen, and R. V. Engeset (2016), Reanalysis of long-term series of glaciological and geodetic mass balance for 10 Norwegian glaciers, *The Cryosphere*, 10(2), 535–552, doi: 10.5194/tc-10-535-2016.
- Azam, M. F., P. Wagnon, A. Ramanathan, C. Vincent, P. Sharma, Y. Arnaud, A. Linda, J. G. Pottakkal, P. Chevallier, V. B. Singh, and E. Berthier (2012), From balance to imbalance: a shift in the dynamic behaviour of Chhota Shigri glacier, western Himalaya, India, *Journal of Glaciology*, 58, 315–324, doi: 10.3189/2012JoG11J123.
- Azam, M. F., P. Wagnon, C. Vincent, A. Ramanathan, V. Favier, A. Mandal, and J. G. Pottakkal (2014a), Processes governing the mass balance of Chhota Shigri Glacier (western Himalaya, India) assessed by point-scale surface energy balance measurements, *The Cryosphere*, 8(6), 2195–2217, doi: 10.5194/tc-8-2195-2014.
- Azam, M. F., P. Wagnon, C. Vincent, A. Ramanathan, A. Linda, and V. B. Singh (2014b), Reconstruction of the annual mass balance of Chhota Shigri glacier, Western Himalaya, India, since 1969, *Annals of Glaciology*, 55, 69–80, doi: 10.3189/2014AoG66A104.

- Azam, M. F., A. Ramanathan, P. Wagnon, C. Vincent, A. Linda, E. Berthier, P. Sharma, A. Mandal, T. Angchuk, V. B. Singh, and J. G. Pottakkal (2016), Meteorological conditions, seasonal and annual mass balances of Chhota Shigri Glacier, western Himalaya, India, *Annals of Glaciology*, 57(71), 328–338, doi: 10.3189/2016aog71a570.
- Azam, M. F., P. Wagnon, E. Berthier, C. Vincent, K. Fujita, and J. S. Kargel (2018), Review of the status and mass changes of Himalayan-Karakoram glaciers, *Journal of Glaciology*, pp. 1–14, doi: 10.1017/jog.2017.86.
- Bahr, D. B., W. T. Pfeffer, and G. Kaser (2015), A review of volume-area scaling of glaciers, *Reviews of Geophysics*, 53, 95–140, doi: 10.1002/2014RG000470.
- Bajracharya, S. R., and B. Shrestha (2011), *The Status of Glaciers in the Hindu Kush-Himalayan Region*, International Centre for Integrated Mountain Development, Kathmandu, Nepal.
- Bajracharya, S. R., S. B. Maharjan, and F. Shrestha (2014), The status and decadal change of glaciers in Bhutan from the 1980s to 2010 based on satellite data, *Annals of Glaciology*, 55, 159–166, doi: 10.3189/2014AoG66A125.
- Bamber, J., R. M. Westaway, B. Marzeion, and B. Wouters (2018), The land ice contribution to sea level during the satellite era, *Environmental Research Letters*.
- Banerjee, A. (2017), Brief communication: Thinning of debris-covered and debris-free glaciers in a warming climate, *The Cryosphere*, 11(1), 133–138, doi: 10.5194/tc-11-133-2017.
- Barandun, M., M. Huss, L. Sold, D. Farinotti, E. Azisov, N. Salzmann, R. Usubaliev, A. Merkushkin, and M. Hoelzle (2015), Re-analysis of seasonal mass balance at Abramov glacier 1968–2014, *Journal of Glaciology*, 61, 1103–1117, doi: 10.3189/2015JoG14J239.
- Barandun, M., M. Huss, R. Usubaliev, E. Azisov, E. Berthier, A. Käab, T. Bolch, and M. Hoelzle (2018), Multi-decadal mass balance series of three Kyrgyz glaciers inferred from modelling constrained with repeated snow line observations, *The Cryosphere*, 12(6), 1899–1919, doi: 10.5194/tc-12-1899-2018.
- Basnett, S., A. V. Kulkarni, and T. Bolch (2013), The influence of debris cover and glacial lakes on the recession of glaciers in Sikkim Himalaya, India, *Journal of Glaciology*, 59, 1035–1046, doi: 10.3189/2013JoG12J184.
- Belart, J. M. C., E. Berthier, E. Magnússon, L. S. Anderson, F. Pálsson, T. Thorsteinsson, I. M. Howat, G. Aðalgeirsdóttir, T. Jóhannesson, and A. H. Jarosch (2017), Winter mass balance of Drangajökull ice cap (NW Iceland) derived from satellite sub-meter stereo images, *The Cryosphere*, 11(3), 1501–1517, doi: 10.5194/tc-11-1501-2017.
- Benn, D., T. Bolch, K. Hands, J. Gulley, A. Luckman, L. Nicholson, D. Quincey, S. Thompson, R. Toumi, and S. Wiseman (2012), Response of debris-covered glaciers in the Mount Everest region to recent warming, and implications for outburst flood hazards, *Earth-Science Reviews*, 114(1–2), 156–174, doi: 10.1016/j.earscirev.2012.03.008.
- Benn, D. I., S. Wiseman, and K. A. Hands (2001), Growth and drainage of supraglacial lakes on the debris-mantled Ngozumpa Glacier, Khumbu Himal, Nepal, *Journal of Glaciology*, 47, 626–638, doi: 10.3189/172756501781831729.
- Benn, D. I., S. Thompson, J. Gulley, J. Mertes, A. Luckman, and L. Nicholson (2017), Structure and evolution of the drainage system of a Himalayan debris-covered glacier, and its relationship with patterns of mass loss, *The Cryosphere*, 11(5), 2247–2264, doi: 10.5194/tc-11-2247-2017.
- Berthier, E., and C. Vincent (2012), Relative contribution of surface mass-balance and ice-flux changes to the accelerated thinning of Mer de Glace, French Alps, over 1979–2008, *Journal of Glaciology*, 58, 501–512, doi: 10.3189/2012JoG11J083.

- Berthier, E., Y. Arnaud, C. Vincent, and F. Rémy (2006), Biases of SRTM in high-mountain areas: Implications for the monitoring of glacier volume changes, *Geophysical Research Letters*, 33, L08,502, doi: 10.1029/2006GL025862.
- Berthier, E., Y. Arnaud, R. Kumar, S. Ahmad, P. Wagnon, and P. Chevallier (2007), Remote sensing estimates of glacier mass balances in the Himachal Pradesh (Western Himalaya, India), *Remote Sensing of Environment*, 108(3), 327–338, doi: 10.1016/j.rse.2006.11.017.
- Berthier, E., E. Schiefer, G. K. C. Clarke, B. Menounos, and F. Rémy (2010), Contribution of Alaskan glaciers to sea-level rise derived from satellite imagery, *Nature Geoscience*, 3, 92–95, doi: 10.1038/ngeo737.
- Berthier, E., C. Vincent, E. Magnússon, P. Gunnlaugsson, P. Pitte, E. Le Meur, M. Masiokas, L. Ruiz, F. Pálsson, J. M. C. Belart, and P. Wagnon (2014), Glacier topography and elevation changes derived from Pléiades sub-meter stereo images, *The Cryosphere*, 8(6), 2275–2291, doi: 10.5194/tc-8-2275-2014.
- Berthier, E., V. Cabot, C. Vincent, and D. Six (2016), Decadal region-wide and glacier-wide mass balances derived from multi-temporal ASTER satellite digital elevation models. Validation over the Mont-Blanc area, *Frontiers in Earth Science*, 4(63), doi: 10.3389/feart.2016.00063.
- Berthier, E., C. Larsen, W. J. Durkin, M. J. Willis, and M. E. Pritchard (2018), Brief communication: Unabated wastage of the Juneau and Stikine icefields (southeast Alaska) in the early 21st century, *The Cryosphere*, 12(4), 1523–1530, doi: 10.5194/tc-12-1523-2018.
- Bhambri, R., T. Bolch, R. K. Chaujar, and S. C. Kulshreshtha (2011), Glacier changes in the Garhwal Himalaya, India, from 1968 to 2006 based on remote sensing, *Journal of Glaciology*, 57, 543–556, doi: 10.3189/002214311796905604.
- Bhattacharya, A., T. Bolch, K. Mukherjee, T. Pieczonka, J. Kropáček, and M. F. Buchroithner (2016), Overall recession and mass budget of Gangotri Glacier, Garhwal Himalayas, from 1965 to 2015 using remote sensing data, *Journal of Glaciology*, 62, 1115–1133, doi: 10.1017/jog.2016.96.
- Bolch, T., M. Buchroithner, T. Pieczonka, and A. Kunert (2008), Planimetric and volumetric glacier changes in the Khumbu Himal, Nepal, since 1962 using Corona, Landsat TM and ASTER data, *Journal of Glaciology*, 54, 592–600, doi: 10.3189/002214308786570782.
- Bolch, T., T. Pieczonka, and D. I. Benn (2011), Multi-decadal mass loss of glaciers in the Everest area (Nepal Himalaya) derived from stereo imagery, *The Cryosphere*, 5(2), 349–358, doi: 10.5194/tc-5-349-2011.
- Bolch, T., A. Kulkarni, A. Käab, C. Huggel, F. Paul, J. G. Cogley, H. Frey, J. S. Kargel, K. Fujita, M. Scheel, S. Bajracharya, and M. Stoffel (2012), The State and Fate of Himalayan Glaciers, *Science*, 336, 310–314, doi: 10.1126/science.1215828.
- Bolch, T., T. Pieczonka, K. Mukherjee, and J. Shea (2017), Brief communication: Glaciers in the Hunza catchment (Karakoram) have been nearly in balance since the 1970s, *The Cryosphere*, 11(1), 531–539, doi: 10.5194/tc-11-531-2017.
- Bolch, T., J. M. Shea, L. Shiyin, M. F. Azam, Y. Gao, S. Gruber, W. W. Immerzeel, A. Kulkarni, H. Li, A. A. Tahir, G. Zhang, Y. Zhang, A. Banerjee, E. Berthier, F. Brun, A. Kaab, P. Kraaijenbrink, G. Moholdt, L. Nicholson, N. Pepin, and A. Racoviteanu (2018), Chapter 7: Status and Change of the HKH-TP Cryosphere, in *Hindu Kush Himalayan Monitoring and Assessment Program (HIMAP)*.
- Bookhagen, B., and D. W. Burbank (2006), Topography, relief, and TRMM-derived rainfall variations along the Himalaya, *Geophysical Research Letters*, 33, L08,405, doi: 10.1029/2006GL026037.
- Bookhagen, B., and D. W. Burbank (2010), Toward a complete Himalayan hydrological budget: Spatiotemporal distribution of snowmelt and rainfall and their impact on river discharge, *Journal of Geophysical Research: Earth Surface*, 115(F3), F03,019, doi: 10.1029/2009JF001426.

- Braithwaite, R. J., S. C. B. Raper, and K. Chutko (2006), Accumulation at the equilibrium-line altitude of glaciers inferred from a degree-day model and tested against field observations, *Annals of Glaciology*, 43, 329–334, doi: 10.3189/172756406781812366.
- Brock, B. W., C. Mihalcea, M. P. Kirkbride, G. Diolaiuti, M. E. J. Cutler, and C. Smiraglia (2010), Meteorology and surface energy fluxes in the 2005–2007 ablation seasons at the Miage debris-covered glacier, Mont Blanc Massif, Italian Alps, *Journal of Geophysical Research: Atmospheres*, 115, D09,106, doi: 10.1029/2009JD013224.
- Brun, F., M. Dumont, P. Wagnon, E. Berthier, M. F. Azam, J. M. Shea, P. Sirguey, A. Rabatel, and A. Ramanathan (2015), Seasonal changes in surface albedo of Himalayan glaciers from MODIS data and links with the annual mass balance, *The Cryosphere*, 9(1), 341–355, doi: 10.5194/tc-9-341-2015.
- Brun, F., P. Buri, E. S. Miles, P. Wagnon, J. F. Steiner, E. Berthier, S. Ragetti, P. Kraaijenbrink, W. Immerzeel, and F. Pellicciotti (2016), Quantifying volume loss from ice cliffs on debris-covered glaciers using high-resolution terrestrial and aerial photogrammetry, *Journal of Glaciology*, 62(234), 684–695, doi: 10.1017/jog.2016.54.
- Brun, F., E. Berthier, P. Wagnon, A. Kääb, and D. Treichler (2017), A spatially resolved estimate of High Mountain Asia glacier mass balances from 2000 to 2016, *Nature Geoscience*, 10, 668–673.
- Brun, F., P. Wagnon, E. Berthier, V. Jomelli, S. B. Maharjan, F. Shrestha, and P. Kraaijenbrink (2018a), Non ubiquitous influence of debris cover and proglacial lakes on the variability of the High Mountain Asia glacier mass balances, *in review at Journal of Geophysical Research: Earth Surface*.
- Brun, F., P. Wagnon, E. Berthier, J. M. Shea, W. W. Immerzeel, P. D. A. Kraaijenbrink, C. Vincent, C. Reverchon, D. Shrestha, and Y. Arnaud (2018b), Ice cliff contribution to the tongue-wide ablation of Changri Nup Glacier, Nepal, central Himalaya, *The Cryosphere*, 12(11), 3439–3457, doi: 10.5194/tc-12-3439-2018.
- Burbank, D. W., B. Bookhagen, E. J. Gabet, and J. Putkonen (2012), Modern climate and erosion in the Himalaya, *Comptes Rendus Geoscience*, 344(11), 610 – 626, doi: <https://doi.org/10.1016/j.crte.2012.10.010>.
- Buri, P., and F. Pellicciotti (2018), Aspect controls the survival of ice cliffs on debris-covered glaciers, *Proceedings of the National Academy of Sciences*, p. 201713892.
- Buri, P., F. Pellicciotti, J. F. Steiner, E. S. Miles, and W. W. Immerzeel (2016a), A grid-based model of backwasting of supraglacial ice cliffs on debris-covered glaciers, *Annals of Glaciology*, 57(71), 199–211, doi: 10.3189/2016aog71a059.
- Buri, P., E. S. Miles, J. F. Steiner, W. W. Immerzeel, P. Wagnon, and F. Pellicciotti (2016b), A physically based 3-D model of ice cliff evolution over debris-covered glaciers, *Journal of Geophysical Research: Earth Surface*, 121, 2471–2493, doi: 10.1002/2016JF004039.
- Carenzo, M., F. Pellicciotti, J. Mabillard, T. Reid, and B. W. Brock (2016), An enhanced temperature index model for debris-covered glaciers accounting for thickness effect, *Advances in Water Resources*, 94, 457 – 469, doi: <https://doi.org/10.1016/j.advwatres.2016.05.001>.
- Casey, K. A., A. Kääb, and D. I. Benn (2012), Geochemical characterization of supraglacial debris via in situ and optical remote sensing methods: a case study in Khumbu Himalaya, Nepal, *The Cryosphere*, 6(1), 85–100, doi: 10.5194/tc-6-85-2012.
- Ceglar, A., A. Toreti, G. Balsamo, and S. Kobayashi (2017), Precipitation over Monsoon Asia: A Comparison of Reanalyses and Observations, *Journal of Climate*, 30, 465–476, doi: 10.1175/JCLI-D-16-0227.1.
- Chambers, D. P., A. Cazenave, N. Champollion, H. Dieng, W. Llovel, R. Forsberg, K. von Schuckmann, and Y. Wada (2017), Evaluation of the Global Mean Sea Level Budget between 1993 and 2014, *Surveys in Geophysics*, 38(1), 309–327, doi: 10.1007/s10712-016-9381-3.

- Chanard, K., J. P. Avouac, G. Ramillien, and J. Genrich (2014), Modeling deformation induced by seasonal variations of continental water in the Himalaya region: Sensitivity to Earth elastic structure, *Journal of Geophysical Research: Solid Earth*, 119(6), 5097–5113, doi: 10.1002/2013JB010451.
- Chinn, T. J., C. Heydenrych, and M. J. Salinger (2005), Use of the ELA as a practical method of monitoring glacier response to climate in New Zealand's Southern Alps, *Journal of Glaciology*, 51(172), 85–95, doi: 10.3189/172756505781829593.
- Church, J., P. Clark, A. Cazenave, J. Gregory, S. Jevrejeva, A. Levermann, M. Merrifield, G. Milne, R. Nerem, P. Nunn, A. Payne, W. Pfeffer, D. Stammer, and A. Unnikrishnan (2013), Sea Level Change, in *Climate Change 2013: The Physical Science Basis. Contribution of Working Group I to the Fifth Assessment Report of the Intergovernmental Panel on Climate Change*, edited by T. Stocker, D. Qin, G.-K. Plattner, M. Tignor, S. Allen, J. Boschung, A. Nauels, Y. Xia, V. Bex, and P. Midgley, pp. 1137–1216, Cambridge University Press, Cambridge, United Kingdom and New York, NY, USA, doi: 10.1017/CBO9781107415324.026.
- Clare, G. R., B. B. Fitzharris, T. J. H. Chinn, and M. J. Salinger (2002), Interannual variation in end-of-summer snowlines of the Southern Alps of New Zealand, and relationships with Southern Hemisphere atmospheric circulation and sea surface temperature patterns, *International Journal of Climatology*, 22, 107–120, doi: 10.1002/joc.722.
- Clarke, G. K. C., A. H. Jarosch, F. S. Anslow, V. Radić, and B. Menounos (2015), Projected deglaciation of western Canada in the twenty-first century, *Nature Geoscience*, 8, 372–377, doi: 10.1038/ngeo2407.
- Cogley, J., R. Hock, L. Rasmussen, A. Arendt, A. Bauder, R. Braithwaite, P. Jansson, G. Kaser, M. Möller, L. Nicholson, et al. (2011), Glossary of glacier mass balance and related terms, *IHP-VII technical documents in hydrology*, 86, 965.
- Cogley, J. G. (2009), Geodetic and direct mass-balance measurements: comparison and joint analysis, *Annals of Glaciology*, 50, 96–100, doi: 10.3189/172756409787769744.
- Cogley, J. G. (2016), Glacier shrinkage across High Mountain Asia, *Annals of Glaciology*, 57(71), 41–49, doi: 10.3189/2016AoG71A040.
- Cogley, J. G., J. S. Kargel, G. Kaser, and C. J. van der Veen (2010), Tracking the Source of Glacier Misinformation, *Science*, 327, 522–522, doi: 10.1126/science.327.5965.522-a.
- Collier, E., and W. W. Immerzeel (2015), High-resolution modeling of atmospheric dynamics in the Nepalese Himalaya, *Journal of Geophysical Research: Atmospheres*, 120, 9882–9896, doi: 10.1002/2015JD023266.
- Collier, E., T. Mölg, F. Maussion, D. Scherer, C. Mayer, and A. B. G. Bush (2013), High-resolution interactive modelling of the mountain glacier–atmosphere interface: an application over the Karakoram, *The Cryosphere*, 7(3), 779–795, doi: 10.5194/tc-7-779-2013.
- Collier, E., L. I. Nicholson, B. W. Brock, F. Maussion, R. Essery, and A. B. G. Bush (2014), Representing moisture fluxes and phase changes in glacier debris cover using a reservoir approach, *The Cryosphere*, 8(4), 1429–1444, doi: 10.5194/tc-8-1429-2014.
- Conrad, O., B. Bechtel, M. Bock, H. Dietrich, E. Fischer, L. Gerlitz, J. Wehberg, V. Wichmann, and J. Böhrner (2015), System for Automated Geoscientific Analyses (SAGA) v. 2.1.4, *Geoscientific Model Development*, 8(7), 1991–2007, doi: 10.5194/gmd-8-1991-2015.
- Conway, H., and L. Rasmusen (2000), Summer temperature profiles within supraglacial debris on Khumbu Glacier, Nepal, *IAHS-AISH publication*, pp. 89–97.
- Cuffey, K. M., and W. S. B. Paterson (2010), *The physics of glaciers*, Academic Press.

- Dall, J., S. N. Madsen, K. Keller, and R. Forsberg (2001), Topography and penetration of the greenland ice sheet measured with airborne SAR interferometry, *Geophysical Research Letters*, 28(9), 1703–1706, doi: 10.1029/2000gl011787.
- Davaze, L., A. Rabatel, Y. Arnaud, P. Sirguey, D. Six, A. Letreguilly, and M. Dumont (2018), Monitoring glacier albedo as a proxy to derive summer and annual surface mass balances from optical remote-sensing data, *The Cryosphere*, 12(1), 271–286, doi: 10.5194/tc-12-271-2018.
- de Kok, R. J., O. A. Tuinenburg, P. N. J. Bonekamp, and W. W. Immerzeel (2018), Irrigation as a Potential Driver for Anomalous Glacier Behavior in High Mountain Asia, *Geophysical Research Letters*, 45, 2047–2054, doi: 10.1002/2017GL076158.
- Dee, D. P., S. M. Uppala, A. J. Simmons, P. Berrisford, P. Poli, S. Kobayashi, U. Andrae, M. A. Balmaseda, G. Balsamo, P. Bauer, P. Bechtold, A. C. M. Beljaars, L. van de Berg, J. Bidlot, N. Bormann, C. Delsol, R. Dragani, M. Fuentes, A. J. Geer, L. Haimberger, S. B. Healy, H. Hersbach, E. V. Hólm, L. Isaksen, P. Kallberg, M. Köhler, M. Matricardi, A. P. McNally, B. M. Monge-Sanz, J.-J. Morcrette, B.-K. Park, C. Peubey, P. de Rosnay, C. Tavolato, J.-N. Thépaut, and F. Vitart (2011), The ERA-Interim reanalysis: configuration and performance of the data assimilation system, *Quarterly Journal of the Royal Meteorological Society*, 137, 553–597, doi: 10.1002/qj.828.
- Dehecq, A., N. Gourmelen, and E. Trouve (2015), Deriving large-scale glacier velocities from a complete satellite archive: Application to the Pamir–Karakoram–Himalaya, *Remote Sensing of Environment*, 162, 55–66, doi: 10.1016/j.rse.2015.01.031.
- Dehecq, A., R. Millan, E. Berthier, N. Gourmelen, E. Trouvé, and V. Vionnet (2016), Elevation Changes Inferred From TanDEM-X Data Over the Mont-Blanc Area: Impact of the X-Band Interferometric Bias, *IEEE Journal of Selected Topics in Applied Earth Observations and Remote Sensing*, 9(8), 3870–3882, doi: 10.1109/JSTARS.2016.2581482.
- Dehecq, A., N. Gourmelen, A. S. Gardner, F. Brun, D. Goldberg, P. Nienow, E. Berthier, C. Vincent, P. Wagnon, and E. Trouvé (2018), Twenty-first century glacier slowdown driven by mass loss in High Mountain Asia, *in press. Nature Geoscience*.
- Deline, P. (2005), Change in surface debris cover on Mont Blanc massif glaciers after the ‘Little Ice Age’ termination, *The Holocene*, 15, 302–309, doi: 10.1191/0959683605hl809rr.
- Drewry, D. J. (1972), A quantitative assessment of dirt-cone dynamics, *Journal of Glaciology*, 11, 431–446, doi: 10.1017/S0022143000022383.
- Duethmann, D., T. Bolch, D. Farinotti, D. Kriegel, S. Vorogushyn, B. Merz, T. Pieczonka, T. Jiang, B. Su, and A. Güntner (2015), Attribution of streamflow trends in snow and glacier melt-dominated catchments of the Tarim River, Central Asia, *Water Resources Research*, 51, 4727–4750, doi: 10.1002/2014WR016716.
- Dumont, M., J. Gardelle, P. Sirguey, A. Guillot, D. Six, A. Rabatel, and Y. Arnaud (2012), Linking glacier annual mass balance and glacier albedo retrieved from MODIS data, *The Cryosphere*, 6(6), 1527–1539, doi: 10.5194/tc-6-1527-2012.
- Dussaillant, I., E. Berthier, and F. Brun (2018), Geodetic Mass Balance of the Northern Patagonian Icefield from 2000 to 2012 Using Two Independent Methods, *Frontiers in Earth Science*, 6, 8, doi: 10.3389/feart.2018.00008.
- Eeckman, J., P. Chevallier, A. Boone, L. Neppel, A. De Rouw, F. Delclaux, and D. Koirala (2017), Providing a non-deterministic representation of spatial variability of precipitation in the Everest region, *Hydrology and Earth System Sciences*, 21(9), 4879–4893, doi: 10.5194/hess-21-4879-2017.
- Evatt, G. W., I. D. Abrahams, M. Heil, C. Mayer, J. Kingslake, S. L. Mitchell, A. C. Fowler, and C. D. Clark (2015), Glacial melt under a porous debris layer, *Journal of Glaciology*, 61(229), 825–836, doi: 10.3189/2015JG14J235.

- Farinotti, D. (2017), Cryospheric science: Asia's glacier changes, *Nature Geoscience*, 10, 621–622, doi: 10.1038/ngeo2995.
- Farinotti, D., L. Longuevergne, G. Moholdt, D. Duethmann, T. Mölg, T. Bolch, S. Vorogushyn, and A. Guntner (2015), Substantial glacier mass loss in the Tien Shan over the past 50 years, *Nature Geoscience*, 8(9), 716–722.
- Farinotti, D., D. J. Brinkerhoff, G. K. C. Clarke, J. J. Fürst, H. Frey, P. Gantayat, F. Gillet-Chaulet, C. Girard, M. Huss, P. W. Leclercq, A. Linsbauer, H. Machguth, C. Martin, F. Maussion, M. Morlighem, C. Mosbeux, A. Pandit, A. Portmann, A. Rabatel, R. Ramsankaran, T. J. Reerink, O. Sanchez, P. A. Stentoft, S. Singh Kumari, W. J. J. van Pelt, B. Anderson, T. Benham, D. Binder, J. A. Dowdeswell, A. Fischer, K. Helfricht, S. Kutuzov, I. Lavrentiev, R. McNabb, G. H. Gudmundsson, H. Li, and L. M. Andreassen (2017), How accurate are estimates of glacier ice thickness? Results from IT-MIX, the Ice Thickness Models Intercomparison eXperiment, *The Cryosphere*, 11(2), 949–970, doi: 10.5194/tc-11-949-2017.
- Farr, T. G., P. A. Rosen, E. Caro, R. Crippen, R. Duren, S. Hensley, M. Kobrick, M. Paller, E. Rodriguez, L. Roth, D. Seal, S. Shaffer, J. Shimada, J. Umland, M. Werner, M. Oskin, D. Burbank, and D. Alsdorf (2007), The Shuttle Radar Topography Mission, *Reviews of Geophysics*, 45(2), doi: 10.1029/2005RG000183.
- Fischer, M., M. Huss, and M. Hoelzle (2015), Surface elevation and mass changes of all Swiss glaciers 1980–2010, *The Cryosphere*, 9(2), 525–540, doi: 10.5194/tc-9-525-2015.
- Forsythe, N., H. J. Fowler, X.-F. Li, S. Blenkinsop, and D. Pritchard (2017), Karakoram temperature and glacial melt driven by regional atmospheric circulation variability, *Nature Climate Change*, 7, 664–670, doi: 10.1038/nclimate3361.
- Foster, L., B. Brock, M. Cutler, and F. Diotri (2012), A physically based method for estimating supraglacial debris thickness from thermal band remote-sensing data, *Journal of Glaciology*, 58(210), 677–691, doi: 10.3189/2012jog11j194.
- Freeman, T. G. (1991), Calculating catchment area with divergent flow based on a regular grid, *Computers & Geosciences*, 17(3), 413 – 422, doi: [https://doi.org/10.1016/0098-3004\(91\)90048-I](https://doi.org/10.1016/0098-3004(91)90048-I).
- Frey, H., F. Paul, and T. Strozzi (2012), Compilation of a glacier inventory for the western Himalayas from satellite data: methods, challenges, and results, *Remote Sensing of Environment*, 124, 832 – 843, doi: <http://dx.doi.org/10.1016/j.rse.2012.06.020>.
- Fujii, Y. (1977), Field experiment on glacier ablation under a layer of debris cover, *Journal of the Japanese Society of Snow and Ice*, 39(Special), 20–21.
- Fujita, K., and T. Nuimura (2011), Spatially heterogeneous wastage of Himalayan glaciers, *AGU Fall Meeting Abstracts*, pp. C43A–08.
- Fujita, K., and A. Sakai (2014), Modelling runoff from a Himalayan debris-covered glacier, *Hydrology and Earth System Sciences*, 18(7), 2679–2694, doi: 10.5194/hess-18-2679-2014.
- Fyffe, C. L., T. D. Reid, B. W. Brock, M. P. Kirkbride, G. Diolaiuti, C. Smiraglia, and F. Diotri (2014), A distributed energy-balance melt model of an alpine debris-covered glacier, *Journal of Glaciology*, 60(221), 587–602, doi: 10.3189/2014jog13j148.
- Gades, A., H. Conway, N. Nereson, N. Naito, and T. Kadota (2000), Radio echo-sounding through supraglacial debris on Lirung and Khumbu Glaciers, Nepal Himalayas, *IAHS PUBLICATION*, pp. 13–24.
- Gagliardini, O., T. Zwinger, F. Gillet-Chaulet, G. Durand, L. Favier, B. de Fleurian, R. Greve, M. Malinen, C. Martín, P. R'va aback, J. Ruokolainen, M. Sacchettini, M. Schäfer, H. Seddik, and J. Thies (2013), Capabilities and performance of Elmer/Ice, a new-generation ice sheet model, *Geoscientific Model Development*, 6(4), 1299–1318, doi: 10.5194/gmd-6-1299-2013.

- Gardelle, J., E. Berthier, and Y. Arnaud (2012a), Impact of resolution and radar penetration on glacier elevation changes computed from DEM differencing, *Journal of Glaciology*, 58(208), 419–422, doi: doi:10.3189/2012JoG11J175.
- Gardelle, J., E. Berthier, and Y. Arnaud (2012b), Slight mass gain of Karakoram glaciers in the early twenty-first century, *Nature geoscience*, 5(5), 322–325.
- Gardelle, J., E. Berthier, Y. Arnaud, and A. Kääb (2013), Region-wide glacier mass balances over the Pamir-Karakoram-Himalaya during 1999–2011, *The Cryosphere*, 7(4), 1263–1286, doi: 10.5194/tc-7-1263-2013.
- Gardent, M., A. Rabatel, J.-P. Dedieu, and P. Deline (2014), Multitemporal glacier inventory of the French Alps from the late 1960s to the late 2000s, *Global and Planetary Change*, 120, 24–37, doi: 10.1016/j.gloplacha.2014.05.004.
- Gardner, A. S., G. Moholdt, J. G. Cogley, B. Wouters, A. A. Arendt, J. Wahr, E. Berthier, R. Hock, W. T. Pfeffer, G. Kaser, S. R. M. Ligtenberg, T. Bolch, M. J. Sharp, J. O. Hagen, M. R. van den Broeke, and F. Paul (2013), A Reconciled Estimate of Glacier Contributions to Sea Level Rise: 2003 to 2009, *Science*, 340, 852–857, doi: 10.1126/science.1234532.
- Gibson, M. J., N. F. Glasser, D. J. Quincey, C. Mayer, A. V. Rowan, and T. D. L. Irvine-Fynn (2017), Temporal variations in supraglacial debris distribution on Baltoro Glacier, Karakoram between 2001 and 2012, *Geomorphology*, 295, 572 – 585, doi: <https://doi.org/10.1016/j.geomorph.2017.08.012>.
- Gilbert, A., G. E. Flowers, G. H. Miller, B. T. Rabus, W. Van Wychen, A. S. Gardner, and L. Copland (2016), Sensitivity of Barnes Ice Cap, Baffin Island, Canada, to climate state and internal dynamics, *Journal of Geophysical Research: Earth Surface*, 121, 1516–1539, doi: 10.1002/2016JF003839.
- Gindraux, S., R. Boesch, and D. Farinotti (2017), Accuracy Assessment of Digital Surface Models from Unmanned Aerial Vehicles' Imagery on Glaciers, *Remote Sensing*, 9(2), doi: 10.3390/rs9020186.
- Girod, L., C. Nuth, A. Kääb, R. McNabb, and O. Galland (2017), MMASTER: Improved ASTER DEMs for Elevation Change Monitoring, *Remote Sensing*, 9(7), 704.
- Glaciers_cci consortium (2015), Climate Research Data Package (CRDP) Technical Document.
- Gulley, J., and D. I. Benn (2007), Structural control of englacial drainage systems in Himalayan debris-covered glaciers, *Journal of Glaciology*, 53, 399–412, doi: 10.3189/002214307783258378.
- Gulley, J. D., D. I. Benn, D. Müller, and A. Luckman (2009), A cut-and-closure origin for englacial conduits in uncrevassed regions of polythermal glaciers, *Journal of Glaciology*, 55, 66–80, doi: 10.3189/002214309788608930.
- Guo, W., S. Liu, J. Xu, L. Wu, D. Shangguan, X. Yao, J. Wei, W. Bao, P. Yu, Q. Liu, and Z. Jiang (2015), The second Chinese glacier inventory: data, methods and results, *Journal of Glaciology*, 61, 357–372, doi: 10.3189/2015JoG14J209.
- Hagg, W., C. Mayer, A. Lambrecht, and A. Helm (2008), Sub-debris melt rates on southern Inylchek Glacier, central Tian Shan, *Geografiska Annaler: Series A, Physical Geography*, 90(1), 55–63, doi: 10.1111/j.1468-0459.2008.00333.x.
- Han, H., Y. Ding, and S. Liu (2006), A simple model to estimate ice ablation under a thick debris layer, *Journal of Glaciology*, 52(179), 528–536, doi: 10.3189/172756506781828395.
- Han, H., J. Wang, J. Wei, and S. Liu (2010), Backwasting rate on debris-covered Koxkar glacier, Tuomuer mountain, China, *Journal of Glaciology*, 56, 287–296, doi: 10.3189/002214310791968430.
- Haritashya, U. K., J. S. Kargel, D. H. Shugar, G. J. Leonard, K. Strattman, C. S. Watson, D. Shean, S. Harrison, K. T. Mandli, and D. Regmi (2018), Evolution and Controls of Large Glacial Lakes in the Nepal Himalaya, *Remote Sensing*, 10(5), doi: 10.3390/rs10050798.

- Heid, T., and A. Kääb (2012), Repeat optical satellite images reveal widespread and long term decrease in land-terminating glacier speeds, *The Cryosphere*, 6(2), 467–478, doi: 10.5194/tc-6-467-2012.
- Herreid, S., and F. Pellicciotti (2018), Automated detection of ice cliffs within supraglacial debris cover, *The Cryosphere*, 12(5), 1811–1829, doi: 10.5194/tc-12-1811-2018.
- Herreid, S., F. Pellicciotti, A. Ayala, A. Chesnokova, C. Kienholz, J. Shea, and A. Shrestha (2015), Satellite observations show no net change in the percentage of supraglacial debris-covered area in northern Pakistan from 1977 to 2014, *Journal of Glaciology*, 61(227), 524–536, doi: 10.3189/2015jog14j227.
- Hewitt, K. (2005), The Karakoram anomaly? Glacier expansion and the ‘elevation effect’, Karakoram Himalaya, *Mountain Research and Development*, 25(4), 332–340.
- Höhle, J., and M. Höhle (2009), Accuracy assessment of digital elevation models by means of robust statistical methods, *{ISPRS} Journal of Photogrammetry and Remote Sensing*, 64(4), 398 – 406, doi: <http://dx.doi.org/10.1016/j.isprsjprs.2009.02.003>.
- Hocking, R. R. (1976), The Analysis and Selection of Variables in Linear Regression, *Biometrics*, 32(1), 1–49, doi: 10.2307/2529336.
- Hoelzle, M., E. Azisov, M. Barandun, M. Huss, D. Farinotti, A. Gafurov, W. Hagg, R. Kenzhebaev, M. Kronenberg, H. Machguth, A. Merkushev, B. Moldobekov, M. Petrov, T. Saks, N. Salzmann, T. Schöne, Y. Tarasov, R. Usabaliev, S. Vorogushyn, A. Yakovlev, and M. Zemp (2017), Re-establishing glacier monitoring in Kyrgyzstan and Uzbekistan, Central Asia, *Geoscientific Instrumentation, Methods and Data Systems*, 6(2), 397–418, doi: 10.5194/gi-6-397-2017.
- Holzer, N., S. Vijay, T. Yao, B. Xu, M. Buchroithner, and T. Bolch (2015), Four decades of glacier variations at Muztagh Ata (eastern Pamir): a multi-sensor study including Hexagon KH-9 and Pléiades data, *The Cryosphere*, 9(6), 2071–2088, doi: 10.5194/tc-9-2071-2015.
- Hooke, R. L. (2005), *Principles of glacier mechanics*, Cambridge university press.
- Huang, L., Z. Li, B. S. Tian, H. D. Han, Y. Q. Liu, J. M. Zhou, and Q. Chen (2017), Estimation of supraglacial debris thickness using a novel target decomposition on L-band polarimetric SAR images in the Tianshan Mountains, *Journal of Geophysical Research: Earth Surface*, 122, 925–940, doi: 10.1002/2016JF004102.
- Huang, L., Z. Li, H. Han, B. Tian, and J. Zhou (2018), Analysis of thickness changes and the associated driving factors on a debris-covered glacier in the Tianshan Mountain, *Remote Sensing of Environment*, 206, 63 – 71, doi: <https://doi.org/10.1016/j.rse.2017.12.028>.
- Huss, M. (2011), Present and future contribution of glacier storage change to runoff from macroscale drainage basins in Europe, *Water Resources Research*, 47, W07,511, doi: 10.1029/2010WR010299.
- Huss, M. (2012), Extrapolating glacier mass balance to the mountain-range scale: the European Alps 1900–2100, *The Cryosphere*, 6(4), 713–727, doi: 10.5194/tc-6-713-2012.
- Huss, M. (2013), Density assumptions for converting geodetic glacier volume change to mass change, *The Cryosphere*, 7(3), 877–887, doi: 10.5194/tc-7-877-2013.
- Huss, M., and D. Farinotti (2012), Distributed ice thickness and volume of all glaciers around the globe, *Journal of Geophysical Research: Earth Surface*, 117(F4), F04,010, doi: 10.1029/2012JF002523.
- Huss, M., and R. Hock (2015), A new model for global glacier change and sea-level rise, *Frontiers in Earth Science*, 3, 54, doi: 10.3389/feart.2015.00054.
- Huss, M., and R. Hock (2018), Global-scale hydrological response to future glacier mass loss, *Nature Climate Change*, 8(2), 135–140, doi: 10.1038/s41558-017-0049-x.

- Huss, M., G. Jouvett, D. Farinotti, and A. Bauder (2010), Future high-mountain hydrology: a new parameterization of glacier retreat, *Hydrology and Earth System Sciences*, 14(5), 815–829, doi: 10.5194/hess-14-815-2010.
- Huss, M., R. Hock, A. Bauder, and M. Funk (2012), Conventional versus reference-surface mass balance, *Journal of Glaciology*, 58(208), 278–286, doi: 10.3189/2012JoG11J216.
- Huss, M., B. Bookhagen, C. Huggel, D. Jacobsen, R. S. Bradley, J. J. Clague, M. Vuille, W. Buytaert, D. R. Cayan, G. Greenwood, B. G. Mark, A. M. Milner, R. Weingartner, and M. Winder (2017), Toward mountains without permanent snow and ice, *Earth's Future*, 5, 418–435, doi: 10.1002/2016EF000514.
- Immerzeel, W., F. Pellicciotti, and M. Bierkens (2013), Rising river flows throughout the twenty-first century in two Himalayan glacierized watersheds, *Nature Geoscience*, 6(9), 742–745, doi: 10.1038/NGEO1896.
- Immerzeel, W., P. Kraaijenbrink, J. Shea, A. Shrestha, F. Pellicciotti, M. Bierkens, and S. de Jong (2014a), High-resolution monitoring of Himalayan glacier dynamics using unmanned aerial vehicles, *Remote Sensing of Environment*, 150, 93–103, doi: 10.1016/j.rse.2014.04.025.
- Immerzeel, W. W., L. P. H. van Beek, and M. F. P. Bierkens (2010), Climate Change Will Affect the Asian Water Towers, *Science*, 328(5984), 1382–1385, doi: 10.1126/science.1183188.
- Immerzeel, W. W., F. Pellicciotti, and A. B. Shrestha (2012a), Glaciers as a Proxy to Quantify the Spatial Distribution of Precipitation in the Hunza Basin, *Mountain Research and Development*, 32(1), 30–38.
- Immerzeel, W. W., L. van Beek, M. Konz, A. Shrestha, and M. Bierkens (2012b), Hydrological response to climate change in a glacierized catchment in the Himalayas, *Climatic Change*, 110(3-4), 721.
- Immerzeel, W. W., L. Petersen, S. Ragettli, and F. Pellicciotti (2014b), The importance of observed gradients of air temperature and precipitation for modeling runoff from a glacierized watershed in the Nepalese Himalayas, *Water Resour. Res.*, 50(3), 2212–2226, doi: 10.1002/2013wr014506.
- Immerzeel, W. W., N. Wanders, A. F. Lutz, J. M. Shea, and M. F. P. Bierkens (2015), Reconciling high-altitude precipitation in the upper Indus basin with glacier mass balances and runoff, *Hydrology and Earth System Sciences*, 19(11), 4673–4687, doi: 10.5194/hess-19-4673-2015.
- Irvine-Fynn, T. D. L., P. R. Porter, A. V. Rowan, D. J. Quincey, M. J. Gibson, J. W. Bridge, C. S. Watson, A. Hubbard, and N. F. Glasser (2017), Supraglacial Ponds Regulate Runoff From Himalayan Debris-Covered Glaciers, *Geophysical Research Letters*, 44, 11, doi: 10.1002/2017GL075398.
- Jacob, T., J. Wahr, W. T. Pfeffer, and S. Swenson (2012), Recent contributions of glaciers and ice caps to sea level rise, *Nature*, 482(7386), 514–518, doi: 10.1038/nature10847.
- Janke, J. R., A. C. Bellisario, and F. A. Ferrando (2015), Classification of debris-covered glaciers and rock glaciers in the Andes of central Chile, *Geomorphology*, 241, 98–121, doi: 10.1016/j.geomorph.2015.03.034.
- Jin, Q., and C. Wang (2017), A revival of Indian summer monsoon rainfall since 2002, *Nature Climate Change*, 7, 587–594, doi: 10.1038/nclimate3348.
- Juen, M., C. Mayer, A. Lambrecht, H. Han, and S. Liu (2014), Impact of varying debris cover thickness on ablation: a case study for Koxkar Glacier in the Tien Shan, *The Cryosphere*, 8(2), 377–386, doi: 10.5194/tc-8-377-2014.
- Kääb, A., E. Berthier, C. Nuth, J. Gardelle, and Y. Arnaud (2012), Contrasting patterns of early twenty-first-century glacier mass change in the Himalayas, *Nature*, 488(7412), 495–498, doi: 10.1038/nature11324.

- Kääb, A., D. Treichler, C. Nuth, and E. Berthier (2015), Brief Communication: Contending estimates of 2003–2008 glacier mass balance over the Pamir–Karakoram–Himalaya, *The Cryosphere*, 9(2), 557–564, doi: 10.5194/tc-9-557-2015.
- Kääb, A., S. Leinss, A. Gilbert, Y. Bühler, S. Gascoin, S. G. Evans, P. Bartelt, E. Berthier, F. Brun, W.-A. Chao, D. Farinotti, F. Gimbert, W. Guo, C. Huggel, J. S. Kargel, G. J. Leonard, L. Tian, D. Treichler, and T. Yao (2018), Massive collapse of two glaciers in western Tibet in 2016 after surge-like instability, *Nature Geoscience*, 11(2), 114–120, doi: 10.1038/s41561-017-0039-7.
- Kapnick, S. B., T. L. Delworth, M. Ashfaq, S. Malyshev, and P. C. D. Milly (2014), Snowfall less sensitive to warming in Karakoram than in Himalayas due to a unique seasonal cycle, *Nature Geoscience*, 7, 834–840, doi: 10.1038/ngeo2269.
- Kaser, G., M. Großhauser, and B. Marzeion (2010), Contribution potential of glaciers to water availability in different climate regimes, *Proceedings of the National Academy of Sciences*, 107(47), 20,223, doi: 10.1073/pnas.1008162107.
- Kayastha, R. B., Y. Takeuchi, M. Nakawo, and Y. Ageta (2000), Practical prediction of ice melting beneath various thickness of debris cover on Khumbu Glacier, Nepal, using a positive degree-day factor, *IAHS Publication*, pp. 71–82.
- King, O., D. J. Quincey, J. L. Carrivick, and A. V. Rowan (2017), Spatial variability in mass loss of glaciers in the Everest region, central Himalayas, between 2000 and 2015, *The Cryosphere*, 11(1), 407–426, doi: 10.5194/tc-11-407-2017.
- King, O., A. Dehecq, D. Quincey, and J. Carrivick (2018), Contrasting geometric and dynamic evolution of lake and land-terminating glaciers in the central Himalaya, *Global and Planetary Change*, 167, 46–60, doi: 10.1016/j.gloplacha.2018.05.006.
- Kirkbride, M. P., and P. Deline (2013), The formation of supraglacial debris covers by primary dispersal from transverse englacial debris bands, *Earth Surface Processes and Landforms*, 38(15), 1779–1792, doi: 10.1002/esp.3416.
- Korona, J., E. Berthier, M. Bernard, F. Rémy, and E. Thouvenot (2009), SPIRIT. SPOT 5 stereoscopic survey of Polar Ice: Reference Images and Topographies during the fourth International Polar Year (2007–2009), *ISPRS Journal of Photogrammetry and Remote Sensing*, 64, 204–212, doi: 10.1016/j.isprsjprs.2008.10.005.
- Kraaijenbrink, P., S. W. Meijer, J. M. Shea, F. Pellicciotti, S. M. D. Jong, and W. W. Immerzeel (2016a), Seasonal surface velocities of a Himalayan glacier derived by automated correlation of unmanned aerial vehicle imagery, *Annals of Glaciology*, 57(71), 103–113, doi: 10.3189/2016aog71a072.
- Kraaijenbrink, P. D. A., J. M. Shea, F. Pellicciotti, S. M. d. Jong, and W. W. Immerzeel (2016b), Object-based analysis of unmanned aerial vehicle imagery to map and characterise surface features on a debris-covered glacier, *Remote Sensing of Environment*, 186(Supplement C), 581 – 595, doi: <https://doi.org/10.1016/j.rse.2016.09.013>.
- Kraaijenbrink, P. D. A., M. F. P. Bierkens, A. F. Lutz, and W. W. Immerzeel (2017), Impact of a global temperature rise of 1.5 degrees Celsius on Asia glaciers, *Nature*, 549, 257–260, doi: 10.1038/nature23878.
- Kraaijenbrink, P. D. A., J. M. Shea, M. Litt, J. F. Steiner, D. Treichler, I. Koch, and W. W. Immerzeel (2018), Mapping Surface Temperatures on a Debris-Covered Glacier With an Unmanned Aerial Vehicle, *Frontiers in Earth Science*, 6, 64, doi: 10.3389/feart.2018.00064.
- Kumar, P., S. Kotlarski, C. Moseley, K. Sieck, H. Frey, M. Stoffel, and D. Jacob (2015), Response of Karakoram-Himalayan glaciers to climate variability and climatic change: A regional climate model assessment, *Geophysical Research Letters*, 42, 1818–1825, doi: 10.1002/2015GL063392.

- Lambrecht, A., and C. Mayer (2009), Temporal variability of the non-steady contribution from glaciers to water discharge in western Austria, *Journal of Hydrology*, 376(3–4), 353 – 361, doi: <http://dx.doi.org/10.1016/j.jhydrol.2009.07.045>.
- Lambrecht, A., C. Mayer, W. Hagg, V. Popovnin, A. Rezepkin, N. Lomidze, and D. Svanadze (2011), A comparison of glacier melt on debris-covered glaciers in the northern and southern Caucasus, *The Cryosphere*, 5, 525–538, doi: 10.5194/tc-5-525-2011.
- Lambrecht, A., C. Mayer, V. Aizen, D. Floricioiu, and A. Surazakov (2014), The evolution of Fedchenko glacier in the Pamir, Tajikistan, during the past eight decades, *Journal of Glaciology*, 60(220), 233–244, doi: 10.3189/2014JoG13J110.
- Lamsal, D., K. Fujita, and A. Sakai (2017), Surface lowering of the debris-covered area of Kanchenjunga Glacier in the eastern Nepal Himalaya since 1975, as revealed by Hexagon KH-9 and ALOS satellite observations, *The Cryosphere*, 11(6), 2815–2827, doi: 10.5194/tc-11-2815-2017.
- Leclercq, P. W., J. Oerlemans, H. J. Basagic, I. Bushueva, A. J. Cook, and R. Le Bris (2014), A data set of worldwide glacier length fluctuations, *The Cryosphere*, 8(2), 659–672, doi: 10.5194/tc-8-659-2014.
- Lehner, B., and P. Döll (2004), Development and validation of a global database of lakes, reservoirs and wetlands, *Journal of Hydrology*, 296(1–4), 1 – 22, doi: <http://dx.doi.org/10.1016/j.jhydrol.2004.03.028>.
- Lejeune, Y., J.-M. Bertrand, P. Wagnon, and S. Morin (2013), A physically based model of the year-round surface energy and mass balance of debris-covered glaciers, *Journal of Glaciology*, 59, 327–344, doi: 10.3189/2013JoG12J149.
- Leprince, S., F. Ayoub, Y. Klingert, and J.-P. Avouac (2007), Co-Registration of Optically Sensed Images and Correlation (COSI-Corr): an operational methodology for ground deformation measurements, in *Geoscience and Remote Sensing Symposium, 2007. IGARSS 2007. IEEE International*, pp. 1943–1946, doi: 10.1109/IGARSS.2007.4423207.
- Li, G., and H. Lin (2017), Recent decadal glacier mass balances over the Western Nyainqentanglha Mountains and the increase in their melting contribution to Nam Co Lake measured by differential bistatic SAR interferometry, *Global and Planetary Change*, 149, 177–190, doi: 10.1016/j.gloplacha.2016.12.018.
- Li, G., H. Lin, and Q. Ye (2018), Heterogeneous decadal glacier downwasting at the Mt. Everest (Qomolangma) from 2000 to 2012 based on multi-baseline bistatic SAR interferometry, *Remote Sensing of Environment*, 206, 336 – 349, doi: <https://doi.org/10.1016/j.rse.2017.12.032>.
- Li, J., Z.-W. Li, J.-J. Zhu, X. Li, B. Xu, Q.-J. Wang, C.-L. Huang, and J. Hu (2017), Early 21st century glacier thickness changes in the Central Tien Shan, *Remote Sensing of Environment*, 192, 12–29, doi: 10.1016/j.rse.2017.02.003.
- Lin, H., G. Li, L. Cuo, A. Hooper, and Q. Ye (2017), A decreasing glacier mass balance gradient from the edge of the Upper Tarim Basin to the Karakoram during 2000–2014, *Scientific Reports*, 7(1), 6712, doi: 10.1038/s41598-017-07133-8.
- Lliboutry, L. (1965), *Traité de glaciologie: Glaciers, variations du climat, sols gelés*, vol. 2, Masson.
- Longuevergne, L., C. R. Wilson, B. R. Scanlon, and J. F. Crétaux (2013), GRACE water storage estimates for the Middle East and other regions with significant reservoir and lake storage, *Hydrology and Earth System Sciences*, 17(12), 4817–4830, doi: 10.5194/hess-17-4817-2013.
- Lutz, A. F., W. W. Immerzeel, A. B. Shrestha, and M. F. P. Bierkens (2014), Consistent increase in High Asia's runoff due to increasing glacier melt and precipitation, *Nature Clim. Change*, 4(7), 587–592.
- Lutz, A. F., W. W. Immerzeel, P. D. A. Kraaijenbrink, A. B. Shrestha, and M. F. P. Bierkens (2016),

- Climate Change Impacts on the Upper Indus Hydrology: Sources, Shifts and Extremes, *PLOS ONE*, 11(11), 1–33, doi: 10.1371/journal.pone.0165630.
- Maharjan, S. B., P. K. Mool, W. Lizong, G. Xiao, F. Shrestha, R. Shrestha, N. Khanal, S. R. Bajracharya, S. Joshi, S. Shai, and P. Baral (2018), The status of glacial lakes in the Hindu Kush Himalaya, *Tech. rep.*, ICIMOD, Kathmandu.
- Malsy, M., T. aus der Beek, and M. Flörke (2015), Evaluation of large-scale precipitation data sets for water resources modelling in Central Asia, *Environmental Earth Sciences*, 73(2), 787–799.
- Marti, R., S. Gascoïn, E. Berthier, M. de Pinel, T. Houet, and D. Laffly (2016), Mapping snow depth in open alpine terrain from stereo satellite imagery, *The Cryosphere*, 10(4), 1361–1380, doi: 10.5194/tc-10-1361-2016.
- Marzeion, B., A. H. Jarosch, and M. Hofer (2012), Past and future sea-level change from the surface mass balance of glaciers, *The Cryosphere*, 6(6), 1295–1322, doi: 10.5194/tc-6-1295-2012.
- Marzeion, B., J. G. Cogley, K. Richter, and D. Parkes (2014), Attribution of global glacier mass loss to anthropogenic and natural causes, *Science*, 345(6199), 919, doi: 10.1126/science.1254702.
- Marzeion, B., P. W. Leclercq, J. G. Cogley, and A. H. Jarosch (2015), Brief Communication: Global reconstructions of glacier mass change during the 20th century are consistent, *The Cryosphere*, 9(6), 2399–2404, doi: 10.5194/tc-9-2399-2015.
- Marzeion, B., N. Champollion, W. Haeberli, K. Langley, P. Leclercq, and F. Paul (2017), Observation-Based Estimates of Global Glacier Mass Change and Its Contribution to Sea-Level Change, *Surveys in Geophysics*, 38(1), 105–130, doi: 10.1007/s10712-016-9394-y.
- Marzeion, B., G. Kaser, F. Maussion, and N. Champollion (2018), Limited influence of climate change mitigation on short-term glacier mass loss, *Nature Climate Change*, 8, 305–308, doi: 10.1038/s41558-018-0093-1.
- Matsuo, K., and K. Heki (2010), Time-variable ice loss in Asian high mountains from satellite gravimetry, *Earth and Planetary Science Letters*, 290, 30–36, doi: 10.1016/j.epsl.2009.11.053.
- Maurer, J. M., S. B. Rupper, and J. M. Schaefer (2016), Quantifying ice loss in the eastern himalayas since 1974 using declassified spy satellite imagery, *The Cryosphere*, 10(5), 2203–2215, doi: 10.5194/tc-10-2203-2016.
- Maussion, F., D. Scherer, T. Mölg, E. Collier, J. Curio, and R. Finkelburg (2014), Precipitation Seasonality and Variability over the Tibetan Plateau as Resolved by the High Asia Reanalysis, *Journal of Climate*, 27(5), 1910–1927, doi: 10.1175/JCLI-D-13-00282.1.
- Maussion, F., A. Butenko, J. Eis, K. Fourteau, A. H. Jarosch, J. Landmann, F. Oesterle, B. Recinos, T. Rothenpieler, A. Vlug, C. T. Wild, and B. Marzeion (2018), The Open Global Glacier Model (OGGM) v1.0, *Geoscientific Model Development Discussions*, 2018, 1–33, doi: 10.5194/gmd-2018-9.
- Mayer, C., A. Lambrecht, M. Belò, C. Smiraglia, and G. Diolaiuti (2006), Glaciological characteristics of the ablation zone of Baltoro glacier, Karakoram, Pakistan, *Annals of Glaciology*, 43, 123–131, doi: 10.3189/172756406781812087.
- McCarthy, M., H. D. Pritchard, I. Willis, and E. King (2017), Ground-penetrating radar measurements of debris thickness on Lirung Glacier, Nepal, *Journal of Glaciology*, 63(239), 543–555, doi: 10.1017/jog.2017.18.
- Mihalcea, C., C. Mayer, G. Diolaiuti, A. Lambrecht, C. Smiraglia, and G. Tartari (2006), Ice ablation and meteorological conditions on the debris-covered area of Baltoro glacier, Karakoram, Pakistan, *Annals of Glaciology*, 43, 292–300, doi: 10.3189/172756406781812104.
- Mihalcea, C., B. Brock, G. Diolaiuti, C. D’Agata, M. Citterio, M. Kirkbride, M. Cutler, and C. Smiraglia (2008a), Using ASTER satellite and ground-based surface temperature measurements to derive

- supraglacial debris cover and thickness patterns on Miage Glacier (Mont Blanc Massif, Italy), *Cold Regions Science and Technology*, 52(3), 341–354, doi: 10.1016/j.coldregions.2007.03.004.
- Mihalcea, C., C. Mayer, G. Diolaiuti, C. D'Agata, C. Smiraglia, A. Lambrecht, E. Vuillermoz, and G. Tartari (2008b), Spatial distribution of debris thickness and melting from remote-sensing and meteorological data, at debris-covered Baltoro glacier, Karakoram, Pakistan, *Annals of Glaciology*, 48, 49–57, doi: 10.3189/172756408784700680.
- Miles, E. S., F. Pellicciotti, I. C. Willis, J. F. Steiner, P. Buri, and N. S. Arnold (2016), Refined energy-balance modelling of a supraglacial pond, Langtang Khola, Nepal, *Annals of Glaciology*, 57, 29–40, doi: 10.3189/2016AoG71A421.
- Miles, E. S., J. F. Steiner, and F. Brun (2017a), Highly variable aerodynamic roughness length (z_0) for a hummocky debris-covered glacier, *Journal of Geophysical Research: Atmospheres*, 122(16), 2017JD026,510, doi: 10.1002/2017JD026510.
- Miles, E. S., I. C. Willis, N. S. Arnold, J. Steiner, and F. Pellicciotti (2017b), Spatial, seasonal and interannual variability of supraglacial ponds in the Langtang Valley of Nepal, 1999–2013, *Journal of Glaciology*, 63(237), 88–105, doi: 10.1017/jog.2016.120.
- Miles, E. S., J. Steiner, I. Willis, P. Buri, W. W. Immerzeel, A. Chesnokova, and F. Pellicciotti (2017c), Pond Dynamics and Supraglacial-Englacial Connectivity on Debris-Covered Lirung Glacier, Nepal, *Frontiers in Earth Science*, 5, 69, doi: 10.3389/feart.2017.00069.
- Miles, E. S., I. Willis, P. Buri, J. Steiner, N. S. Arnold, and F. Pellicciotti (2018), Surface pond energy absorption across four Himalayan glaciers accounts for 1/8 of total catchment ice loss, *Geophysical Research Letters*, 0(ja), doi: 10.1029/2018GL079678.
- Milner, A. M., K. Khamis, T. J. Battin, J. E. Brittain, N. E. Barrand, L. Füreder, S. Cauvy-Fraunié, G. Már Gíslason, D. Jacobsen, D. M. Hannah, A. J. Hodson, E. Hood, V. Lencioni, J. S. Ólafsson, C. T. Robinson, M. Tranter, and L. E. Brown (2017), Glacier shrinkage driving global changes in downstream systems, *Proceedings of the National Academy of Science*, 114, 9770–9778, doi: 10.1073/pnas.1619807114.
- Mimeau, L., M. Esteves, I. Zin, H.-W. Jacobi, F. Brun, P. Wagnon, D. Koirala, and Y. Arnaud (2018), Quantification of different flow components in a high-altitude glacierized catchment (Dudh Koshi, Nepalese Himalaya), *Hydrology and Earth System Sciences Discussions*, 2018, 1–35, doi: 10.5194/hess-2018-34.
- Mölg, N., T. Bolch, P. Rastner, T. Strozzi, and F. Paul (2018), A consistent glacier inventory for the Karakoram and Pamir regions derived from Landsat data: distribution of debris cover and mapping challenges, *Earth System Science Data Discussions*, 2018, 1–44, doi: 10.5194/essd-2018-35.
- Mölg, T., F. Maussion, W. Yang, and D. Scherer (2012), The footprint of Asian monsoon dynamics in the mass and energy balance of a Tibetan glacier, *The Cryosphere*, 6(6), 1445–1461, doi: 10.5194/tc-6-1445-2012.
- Mölg, T., F. Maussion, and D. Scherer (2013), Mid-latitude westerlies as a driver of glacier variability in monsoonal High Asia, *Nature Climate Change*, 4, 68.
- Mölg, T., F. Maussion, E. Collier, J. C. H. Chiang, and D. Scherer (2017), Prominent Midlatitude Circulation Signature in High Asia's Surface Climate During Monsoon, *Journal of Geophysical Research: Atmospheres*, 122(23), 2017JD027,414, doi: 10.1002/2017JD027414.
- Ménégoz, M., H. Gallée, and H. W. Jacobi (2013), Precipitation and snow cover in the Himalaya: from reanalysis to regional climate simulations, *Hydrology and Earth System Sciences*, 17, 3921–3936, doi: 10.5194/hess-17-3921-2013.
- Moholdt, G., C. Nuth, J. O. Hagen, and J. Kohler (2010), Recent elevation changes of Svalbard glaciers

- derived from ICESat laser altimetry, *Remote Sensing of Environment*, 114, 2756–2767, doi: 10.1016/j.rse.2010.06.008.
- Moore, P. L. (2018), Stability of supraglacial debris, *Earth Surface Processes and Landforms*, 43(1), 285–297.
- Mouginot, J., E. Rignot, B. Scheuchl, and R. Millan (2017), Comprehensive Annual Ice Sheet Velocity Mapping Using Landsat-8, Sentinel-1, and RADARSAT-2 Data, *Remote Sensing*, 9, 364, doi: 10.3390/rs9040364.
- Mukherjee, K., A. Bhattacharya, T. Pieczonka, S. Ghosh, and T. Bolch (2018), Glacier mass budget and climate reanalysis data indicate a climatic shift around 2000 in Lahaul-Spiti, western Himalaya, *Climatic Change*, doi: 10.1007/s10584-018-2185-3.
- Nakawo, M., and G. J. Young (1981), Field experiments to determine the effect of a debris layer on ablation of glacier ice, *Annals of Glaciology*, 2, 85–91, doi: 10.3189/172756481794352432.
- Nakawo, M., and G. J. Young (1982), Estimate of glacier ablation under a debris layer from surface temperature and meteorological variables, *Journal of Glaciology*, 28, 29–34, doi: 10.1017/S002214300001176X.
- Nakawo, M., S. Iwata, O. Watanabe, and M. Yoshida (1985), Processes which distribute supraglacial debris on the Khumbu Glacier, Nepal Himalaya, *Annals of Glaciology*, 8, 129–131.
- Neckel, N., A. Braun, J. Kropáček, and V. Hochschild (2013), Recent mass balance of the Purogongri Ice Cap, central Tibetan Plateau, by means of differential X-band SAR interferometry, *The Cryosphere*, 7(5), 1623–1633, doi: 10.5194/tc-7-1623-2013.
- Neckel, N., J. Kropáček, T. Bolch, and V. Hochschild (2014), Glacier mass changes on the Tibetan Plateau 2003–2009 derived from ICESat laser altimetry measurements, *Environmental Research Letters*, 9(1), 014,009.
- Neckel, N., D. Loibl, and M. Rankl (2017), Recent slowdown and thinning of debris-covered glaciers in south-eastern Tibet, *Earth and Planetary Science Letters*, 464, 95–102, doi: 10.1016/j.epsl.2017.02.008.
- Nepal, S., P. Krause, W.-A. Flügel, M. Fink, and C. Fischer (2014), Understanding the hydrological system dynamics of a glaciated alpine catchment in the Himalayan region using the J2000 hydrological model, *Hydrological Processes*, 28, 1329–1344, doi: 10.1002/hyp.9627.
- Nicholson, L., and D. I. Benn (2006), Calculating ice melt beneath a debris layer using meteorological data, *Journal of Glaciology*, 52, 463–470, doi: 10.3189/172756506781828584.
- Nicholson, L., and D. I. Benn (2012), Properties of natural supraglacial debris in relation to modelling sub-debris ice ablation, *Earth Surf. Process. Landforms*, 38(5), 490–501, doi: 10.1002/esp.3299.
- Nicholson, L., and J. Mertes (2017), Thickness estimation of supraglacial debris above ice cliff exposures using a high-resolution digital surface model derived from terrestrial photography, *Journal of Glaciology*, 63(242), 989–998.
- Nicholson, L. I., M. McCarthy, H. Pritchard, and I. Willis (2018), Supraglacial debris thickness variability: Impact on ablation and relation to terrain properties, *The Cryosphere Discussions*, 2018, 1–30, doi: 10.5194/tc-2018-83.
- Nuimura, T., K. Fujita, K. Fukui, K. Asahi, R. Aryal, and Y. Ageta (2011), Temporal Changes in Elevation of the Debris-Covered Ablation Area of Khumbu Glacier in the Nepal Himalaya since 1978, *Arctic, Antarctic, and Alpine Research*, 43(2), 246–255, doi: 10.1657/1938-4246-43.2.246.
- Nuimura, T., K. Fujita, S. Yamaguchi, and R. R. Sharma (2012), Elevation changes of glaciers revealed by multitemporal digital elevation models calibrated by GPS survey in the Khumbu region, Nepal Himalaya, 1992–2008, *Journal of Glaciology*, 58(210), 648–656, doi: 10.3189/2012JoG11J061.

- Nuimura, T., A. Sakai, K. Taniguchi, H. Nagai, D. Lamsal, S. Tsutaki, A. Kozawa, Y. Hoshina, S. Takenaka, S. Omiya, K. Tsunematsu, P. Tshering, and K. Fujita (2015), The GAMDAM glacier inventory: a quality-controlled inventory of Asian glaciers, *The Cryosphere*, 9(3), 849–864, doi: 10.5194/tc-9-849-2015.
- Nuimura, T., K. Fujita, and A. Sakai (2017), Downwasting of the debris-covered area of Lirung Glacier in Langtang Valley, Nepal Himalaya, from 1974 to 2010, *Quaternary International*, doi: <http://dx.doi.org/10.1016/j.quaint.2017.06.066>.
- Nussbaumer, S., H. Zumbühl, and D. Steiner (2007), Fluctuations of the Mer de Glace (Mont Blanc area, France) AD 1500–2050. Part I: The history of the Mer de Glace AD 1570–2003 according to pictorial and written documents, *Zeitschrift für Gletscherkunde und Glazialgeologie*, 40(2005&2006), 5–140.
- Nuth, C., and A. Kääb (2011), Co-registration and bias corrections of satellite elevation data sets for quantifying glacier thickness change, *The Cryosphere*, 5(1), 271–290, doi: 10.5194/tc-5-271-2011.
- Oerlemans, J. (1986), Glaciers as indicators of a carbon dioxide warming, *Nature*, 320(6063), 607–609, doi: 10.1038/320607a0.
- Oerlemans, J. (2013), A note on the water budget of temperate glaciers, *The Cryosphere*, 7(5), 1557–1564, doi: 10.5194/tc-7-1557-2013.
- Oerlemans, J., and B. K. Reichert (2000), Relating glacier mass balance to meteorological data by using a seasonal sensitivity characteristic, *Journal of Glaciology*, 46(152), 1–6, doi: 10.3189/172756500781833269.
- Østrem, G. (1959), Ice Melting under a Thin Layer of Moraine, and the Existence of Ice Cores in Moraine Ridges, *Geografiska Annaler*, 41(4), pp. 228–230.
- Palazzi, E., J. von Hardenberg, and A. Provenzale (2013), Precipitation in the Hindu-Kush Karakoram Himalaya: Observations and future scenarios, *Journal of Geophysical Research: Atmospheres*, 118(1), 85–100, doi: 10.1029/2012JD018697.
- Paul, F., and W. Haeberli (2008), Spatial variability of glacier elevation changes in the Swiss Alps obtained from two digital elevation models, *Geophysical Research Letters*, 35(21), doi: 10.1029/2008GL034718.
- Paul, F., N. E. Barrand, S. Baumann, E. Berthier, T. Bolch, K. Casey, H. Frey, S. P. Joshi, V. Konovalov, R. Le Bris, N. Mölg, G. Nosenko, C. Nuth, A. Pope, A. Racoviteanu, P. Rastner, B. Raup, K. Scharrer, S. Steffen, and S. Winsvold (2013), On the accuracy of glacier outlines derived from remote-sensing data, *Annals of Glaciology*, 54, 171–182, doi: 10.3189/2013AoG63A296.
- Paul, F., T. Bolch, A. Kääb, T. Nagler, C. Nuth, K. Scharrer, A. Shepherd, T. Strozzi, F. Ticconi, R. Bhambri, E. Berthier, S. Bevan, N. Gourmelen, T. Heid, S. Jeong, M. Kunz, T. R. Lauknes, A. Luckman, J. P. M. Boncori, G. Moholdt, A. Muir, J. Neelmeijer, M. Rankl, J. VanLooy, and T. V. Niel (2015), The glaciers climate change initiative: Methods for creating glacier area, elevation change and velocity products, *Remote Sensing of Environment*, 162, 408 – 426, doi: <http://dx.doi.org/10.1016/j.rse.2013.07.043>.
- Pellicciotti, F., B. Brock, U. Strasser, P. Burlando, M. Funk, and J. Corripio (2005), An enhanced temperature-index glacier melt model including the shortwave radiation balance: development and testing for Haut Glacier d’Arolla, Switzerland, *Journal of Glaciology*, 51, 573–587, doi: 10.3189/172756505781829124.
- Pellicciotti, F., C. Buergi, W. W. Immerzeel, M. Konz, and A. B. Shrestha (2012), Challenges and uncertainties in hydrological modeling of remote Hindu Kush–Karakoram–Himalayan (HKH) basins: suggestions for calibration strategies, *Mountain Research and Development*, 32(1), 39–50.

- Pellicciotti, F., C. Stephan, E. Miles, S. Herreid, W. W. Immerzeel, and T. Bolch (2015), Mass-balance changes of the debris-covered glaciers in the Langtang Himal, Nepal, from 1974 to 1999, *Journal of Glaciology*, 61(226), 373–386, doi: 10.3189/2015jog13j237.
- Pfeffer, W. T., A. A. Arendt, A. Bliss, T. Bolch, J. G. Cogley, A. S. Gardner, J.-O. Hagen, R. Hock, G. Kaser, C. Kienholz, E. S. Miles, G. Moholdt, N. Mölg, F. Paul, V. Radic, P. Rastner, B. H. Raup, J. Rich, and M. J. Sharp (2014), The Randolph Glacier Inventory: a globally complete inventory of glaciers, *Journal of Glaciology*, 60, 537–552, doi: 10.3189/2014JoG13J176.
- Pieczonka, T., and T. Bolch (2015), Region-wide glacier mass budgets and area changes for the Central Tien Shan between ~1975 and 1999 using Hexagon KH-9 imagery, *Global and Planetary Change*, 128, 1–13, doi: 10.1016/j.gloplacha.2014.11.014.
- Pieczonka, T., T. Bolch, W. Junfeng, and L. Shiyin (2013), Heterogeneous mass loss of glaciers in the Aksu-Tarim Catchment (Central Tien Shan) revealed by 1976 KH-9 Hexagon and 2009 SPOT-5 stereo imagery, *Remote Sensing of Environment*, 130, 233–244, doi: 10.1016/j.rse.2012.11.020.
- Pohl, E., R. Gloaguen, C. Andermann, and M. Knoche (2017), Glacier melt buffers river runoff in the Pamir Mountains, *Water Resources Research*, 53, 2467–2489, doi: 10.1002/2016WR019431.
- Pritchard, H. D. (2017), Asia's glaciers are a regionally important buffer against drought, *Nature [retracted in 2018]*, 545(7653), 169–174, doi: 10.1038/nature22062.
- Qian, W., and D.-K. Lee (2000), Seasonal march of Asian summer monsoon, *International Journal of Climatology*, 20, 1371–1386, doi: 10.1002/1097-0088(200009)20:11<1371::AID-JOC538>3.3.CO;2-M.
- Quincey, D., M. Smith, D. Rounce, A. Ross, O. King, and C. Watson (2017), Evaluating morphological estimates of the aerodynamic roughness of debris covered glacier ice, *Earth Surface Processes and Landforms*, 42(15), 2541–2553, doi: 10.1002/esp.4198.
- Quincey, D. J., S. D. Richardson, A. Luckman, R. M. Lucas, J. M. Reynolds, M. J. Hambrey, and N. F. Glasser (2007), Early recognition of glacial lake hazards in the Himalaya using remote sensing datasets, *Global and Planetary Change*, 56, 137–152, doi: 10.1016/j.gloplacha.2006.07.013.
- Quincey, D. J., A. Luckman, and D. Benn (2009), Quantification of Everest region glacier velocities between 1992 and 2002, using satellite radar interferometry and feature tracking, *Journal of Glaciology*, 55, 596–606, doi: 10.3189/002214309789470987.
- Rabatel, A., J.-P. Dedieu, and C. Vincent (2005), Using remote-sensing data to determine equilibrium-line altitude and mass-balance time series: validation on three French glaciers, 1994–2002, *Journal of Glaciology*, 51, 539–546, doi: 10.3189/172756505781829106.
- Rabatel, A., A. Bermejo, E. Loarte, A. Soruco, J. Gomez, G. Leonardini, C. Vincent, and J. E. Sicart (2012), Can the snowline be used as an indicator of the equilibrium line and mass balance for glaciers in the outer tropics?, *Journal of Glaciology*, 58(212), 1027–1036, doi: 10.3189/2012JoG12J027.
- Rabatel, A., A. Letréguilly, J.-P. Dedieu, and N. Eckert (2013), Changes in glacier equilibrium-line altitude in the western Alps from 1984 to 2010: evaluation by remote sensing and modeling of the morpho-topographic and climate controls, *The Cryosphere*, 7(5), 1455–1471, doi: 10.5194/tc-7-1455-2013.
- Rabatel, A., J. P. Dedieu, and C. Vincent (2016), Spatio-temporal changes in glacier-wide mass balance quantified by optical remote sensing on 30 glaciers in the French Alps for the period 1983–2014, *Journal of Glaciology*, 62(236), 1153–1166, doi: 10.1017/jog.2016.113.
- Racoviteanu, A., F. Paul, B. Raup, S. Khalsa, and R. Armstrong (2009), Challenges in glacier mapping from space: recommendations from the Global Land Ice Measurements from Space (GLIMS) initiative, *Annals of Glaciology*, 50(53), 53–69.

- Racoviteanu, A. E., R. Armstrong, and M. W. Williams (2013), Evaluation of an ice ablation model to estimate the contribution of melting glacier ice to annual discharge in the Nepal Himalaya, *Water Resources Research*, 49, 5117–5133, doi: 10.1002/wrcr.20370.
- Radić, V., and R. Hock (2006), Modeling future glacier mass balance and volume changes using ERA-40 reanalysis and climate models: A sensitivity study at Storglaciären, Sweden, *Journal of Geophysical Research: Earth Surface*, 111, F03,003, doi: 10.1029/2005JF000440.
- Radić, V., and R. Hock (2014), Glaciers in the Earth's Hydrological Cycle: Assessments of Glacier Mass and Runoff Changes on Global and Regional Scales, *Surveys in Geophysics*, 35, 813–837, doi: 10.1007/s10712-013-9262-y.
- Radić, V., A. Bliss, A. C. Beedlow, R. Hock, E. Miles, and J. G. Cogley (2014), Regional and global projections of twenty-first century glacier mass changes in response to climate scenarios from global climate models, *Climate Dynamics*, 42, 37–58, doi: 10.1007/s00382-013-1719-7.
- Ragettli, S., F. Pellicciotti, W. Immerzeel, E. Miles, L. Petersen, M. Heynen, J. Shea, D. Stumm, S. Joshi, and A. Shrestha (2015), Unraveling the hydrology of a Himalayan catchment through integration of high resolution in situ data and remote sensing with an advanced simulation model, *Advances in Water Resources*, 78(0), 94–111, doi: 10.1016/j.advwatres.2015.01.013.
- Ragettli, S., W. W. Immerzeel, and F. Pellicciotti (2016a), Contrasting climate change impact on river flows from high-altitude catchments in the Himalayan and Andes Mountains, *Proceedings of the National Academy of Science*, 113, 9222–9227, doi: 10.1073/pnas.1606526113.
- Ragettli, S., T. Bolch, and F. Pellicciotti (2016b), Heterogeneous glacier thinning patterns over the last 40 years in Langtang Himal, Nepal, *The Cryosphere*, 10(5), 2075–2097, doi: 10.5194/tc-10-2075-2016.
- Ramillien, G., J. S. Famiglietti, and J. Wahr (2008), Detection of Continental Hydrology and Glaciology Signals from GRACE: A Review, *Surveys in Geophysics*, 29(4), 361–374, doi: 10.1007/s10712-008-9048-9.
- Rankl, M., and M. Braun (2016), Glacier elevation and mass changes over the central Karakoram region estimated from TanDEM-X and SRTM/X-SAR digital elevation models, *Annals of Glaciology*, 57(71), 273–281, doi: 10.3189/2016aog71a024.
- Reager, J. T., A. S. Gardner, J. S. Famiglietti, D. N. Wiese, A. Eicker, and M.-H. Lo (2016), A decade of sea level rise slowed by climate-driven hydrology, *Science*, 351(6274), 699, doi: 10.1126/science.aad8386.
- Reid, T., and B. Brock (2014), Assessing ice-cliff backwasting and its contribution to total ablation of debris-covered Miage glacier, Mont Blanc massif, Italy, *Journal of Glaciology*, 60(219), 3–13, doi: 10.3189/2014JoG13J045.
- Reid, T. D., and B. W. Brock (2010), An energy-balance model for debris-covered glaciers including heat conduction through the debris layer, *Journal of Glaciology*, 56, 903–916, doi: 10.3189/002214310794457218.
- Reznichenko, N., T. Davies, J. Shulmeister, and M. McSaveney (2010), Effects of debris on ice-surface melting rates: an experimental study, *Journal of Glaciology*, 56, 384–394, doi: 10.3189/002214310792447725.
- Röhl, K. (2006), Thermo-erosional notch development at fresh-water-calving Tasman Glacier, New Zealand, *Journal of Glaciology*, 52(177), 203–213, doi: 10.3189/172756506781828773.
- Rignot, E., K. Echelmeyer, and W. Krabill (2001), Penetration depth of interferometric synthetic-aperture radar signals in snow and ice, *Geophysical Research Letters*, 28, 3501–3504, doi: 10.1029/2000GL012484.

- Robson, B. A., C. Nuth, S. O. Dahl, D. Hölbling, T. Strozzi, and P. R. Nielsen (2015), Automated classification of debris-covered glaciers combining optical, SAR and topographic data in an object-based environment, *Remote Sensing of Environment*, 170, 372–387, doi: 10.1016/j.rse.2015.10.001.
- Robson, B. A., C. Nuth, P. R. Nielsen, L. Girod, M. Hendrickx, and S. O. Dahl (2018), Spatial Variability in Patterns of Glacier Change across the Manaslu Range, Central Himalaya, *Frontiers in Earth Science*, 6, doi: 10.3389/feart.2018.00012.
- Rolstad, C., T. Haug, and B. Denby (2009), Spatially integrated geodetic glacier mass balance and its uncertainty based on geostatistical analysis: application to the western Svartisen ice cap, Norway, *Journal of Glaciology*, 55(192), 666–680, doi: 10.3189/002214309789470950.
- Rounce, D. R., and D. C. McKinney (2014), Debris thickness of glaciers in the Everest area (Nepal Himalaya) derived from satellite imagery using a nonlinear energy balance model, *The Cryosphere*, 8(4), 1317–1329, doi: 10.5194/tc-8-1317-2014.
- Rounce, D. R., D. J. Quincey, and D. C. McKinney (2015), Debris-covered glacier energy balance model for Imja–Lhotse Shar Glacier in the Everest region of Nepal, *The Cryosphere*, 9(6), 2295–2310, doi: 10.5194/tc-9-2295-2015.
- Rounce, D. R., O. King, M. McCarthy, D. E. Shean, and F. Salerno (2018), Quantifying debris thickness of debris-covered glaciers in the Everest region of Nepal through inversion of a sub-debris melt model, *Journal of Geophysical Research: Earth Surface*.
- Rowan, A. V. (2017), The 'Little Ice Age' in the Himalaya: A review of glacier advance driven by Northern Hemisphere temperature change, *The Holocene*, 27, 292–308, doi: 10.1177/0959683616658530.
- Rowan, A. V., D. L. Egholm, D. J. Quincey, and N. F. Glasser (2015), Modelling the feedbacks between mass balance, ice flow and debris transport to predict the response to climate change of debris-covered glaciers in the Himalaya, *Earth and Planetary Science Letters*, 430, 427–438, doi: 10.1016/j.epsl.2015.09.004.
- Réveillet, M. (2016), Sensibilité du bilan de masse des glaciers alpins aux variables atmosphériques et topographiques: Observations et simulations, PhD Thesis, Univ. Grenoble Alpes, 175 p.
- Réveillet, M., C. Vincent, D. Six, and A. Rabatel (2017), Which empirical model is best suited to simulate glacier mass balances?, *Journal of Glaciology*, 63, 39–54, doi: 10.1017/jog.2016.110.
- Sakai, A., and K. Fujita (2017), Contrasting glacier responses to recent climate change in high-mountain Asia, *Scientific Reports*, 7(1), 13,717, doi: 10.1038/s41598-017-14256-5.
- Sakai, A., M. Nakawo, and K. Fujita (1998), Melt rate of ice cliffs on the Lirung Glacier, Nepal Himalayas, 1996, *Bulletin of Glacier Research*, 16, 57–66.
- Sakai, A., N. Takeuchi, K. Fujita, and M. Nakawo (2000), Role of supraglacial ponds in the ablation process of a debris-covered glacier in the Nepal Himalayas, *Debris-covered Glaciers (proceedings of a workshop held at Seattle, Washington, USA, September 2000)*, 265.
- Sakai, A., M. Nakawo, and K. Fujita (2002), Distribution characteristics and energy balance of ice cliffs on debris-covered glaciers, Nepal Himalaya, *Arctic, Antarctic and Alpine Research*, 34(1), 12–19.
- Sakai, A., T. Nuimura, K. Fujita, S. Takenaka, H. Nagai, and D. Lamsal (2015), Climate regime of Asian glaciers revealed by GAMDAM glacier inventory, *The Cryosphere*, 9(3), 865–880, doi: 10.5194/tc-9-865-2015.
- Salerno, F., N. Guyennon, S. Thakuri, G. Viviano, E. Romano, E. Vuillermoz, P. Cristofanelli, P. Stocchi, G. Agrillo, Y. Ma, and G. Tartari (2015), Weak precipitation, warm winters and springs impact

- glaciers of south slopes of Mt. Everest (central Himalaya) in the last 2 decades (1994-2013), *The Cryosphere*, 9, 1229–1247, doi: 10.5194/tc-9-1229-2015.
- Salerno, F., S. Thakuri, G. Tartari, T. Nuimura, S. Sunako, A. Sakai, and K. Fujita (2017), Debris-covered glacier anomaly? Morphological factors controlling changes in the mass balance, surface area, terminus position, and snow line altitude of Himalayan glaciers, *Earth and Planetary Science Letters*, 471, 19 – 31, doi: <https://doi.org/10.1016/j.epsl.2017.04.039>.
- Sasaki, O., O. Noguchi, Y. Zhang, Y. Hirabayashi, and S. Kanae (2016), A global high-resolution map of debris on glaciers derived from multi-temporal ASTER images, *The Cryosphere Discussions*, 2016, 1–24, doi: 10.5194/tc-2016-222.
- Savéan, M., F. Delclaux, P. Chevallier, P. Wagnon, N. Gongga-Saholiariliva, R. Sharma, L. Neppel, and Y. Arnaud (2015), Water budget on the Dudh Koshi River (Nepal): Uncertainties on precipitation, *Journal of Hydrology*, 531, 850–862, doi: 10.1016/j.jhydrol.2015.10.040.
- Schaner, N., N. Voisin, B. Nijssen, and D. P. Lettenmaier (2012), The contribution of glacier melt to streamflow, *Environmental Research Letters*, 7(3), 034,029, doi: 10.1088/1748-9326/7/3/034029.
- Schauwecker, S., M. Rohrer, C. Huggel, A. Kulkarni, A. Ramanathan, N. Salzmann, M. Stoffel, and B. Brock (2015), Remotely sensed debris thickness mapping of Bara Shigri Glacier, Indian Himalaya, *Journal of Glaciology*, 61, 675–688, doi: 10.3189/2015JoG14J102.
- Scherler, D. (2014), Climatic limits to headwall retreat in the Khumbu Himalaya, eastern Nepal, *Geology*, 42, 1019–1022, doi: 10.1130/G35975.1.
- Scherler, D., B. Bookhagen, and M. R. Strecker (2011a), Spatially variable response of Himalayan glaciers to climate change affected by debris cover, *Nature Geoscience*, 4, 156–159, doi: 10.1038/ngeo1068.
- Scherler, D., B. Bookhagen, and M. R. Strecker (2011b), Hillslope-glacier coupling: The interplay of topography and glacial dynamics in High Asia, *Journal of Geophysical Research: Earth Surface*, 116(F2), doi: 10.1029/2010JF001751.
- Schrama, E. J. O., B. Wouters, and R. Rietbroek (2014), A mascon approach to assess ice sheet and glacier mass balances and their uncertainties from GRACE data, *Journal of Geophysical Research: Solid Earth*, 119(7), 6048–6066, doi: 10.1002/2013JB010923.
- Sevestre, H., and D. I. Benn (2015), Climatic and geometric controls on the global distribution of surge-type glaciers: implications for a unifying model of surging, *Journal of Glaciology*, 61(228), 646–662, doi: 10.3189/2015JoG14J136.
- Shaw, T. E., B. W. Brock, C. L. Fyffe, F. Pellicciotti, N. Rutter, and F. Diotri (2016), Air temperature distribution and energy-balance modelling of a debris-covered glacier, *Journal of Glaciology*, 62, 185–198, doi: 10.1017/jog.2016.31.
- Shea, J. M., W. W. Immerzeel, P. Wagnon, C. Vincent, and S. Bajracharya (2015), Modelling glacier change in the Everest region, Nepal Himalaya, *The Cryosphere*, 9(3), 1105–1128, doi: 10.5194/tc-9-1105-2015.
- Shean, D. (2017), High Mountain Asia 8-meter DEMs Derived from Along-track Optical Imagery, Version 1., doi: 10.5067/GSACB044M4PK, NASA National Snow and Ice Data Center Distributed Active Archive Center. Boulder, Colorado USA.
- Shean, D. E., O. Alexandrov, Z. M. Moratto, B. E. Smith, I. R. Joughin, C. Porter, and P. Morin (2016), An automated, open-source pipeline for mass production of digital elevation models (DEMs) from very-high-resolution commercial stereo satellite imagery, *{ISPRS} Journal of Photogrammetry and Remote Sensing*, 116, 101 – 117, doi: <http://dx.doi.org/10.1016/j.isprsjprs.2016.03.012>.

- Sherpa, S. F., P. Wagnon, F. Brun, E. Berthier, C. Vincent, Y. Lejeune, Y. Arnaud, R. B. Kayastha, and A. Sinisalo (2017), Contrasted surface mass balances of debris-free glaciers observed between the southern and the inner parts of the Everest region (2007-2015), *Journal of Glaciology*, 63(240), 637–651.
- Six, D., and C. Vincent (2014), Sensitivity of mass balance and equilibrium-line altitude to climate change in the French Alps, *Journal of Glaciology*, 60, 867–878, doi: 10.3189/2014JoG14J014.
- Skamarock, W. C., and J. B. Klemp (2008), A time-split nonhydrostatic atmospheric model for weather research and forecasting applications, *Journal of Computational Physics*, 227, 3465–3485, doi: 10.1016/j.jcp.2007.01.037.
- Small, R. J., M. J. Clark, and T. J. P. Cawse (1979), The formation of medial moraines on Alpine glaciers, *Journal of Glaciology*, 22, 43–52, doi: 10.1017/S0022143000014040.
- Soncini, A., D. Bocchiola, G. Confortola, U. Minora, E. Vuillermoz, F. Salerno, G. Viviano, D. Shrestha, A. Senese, C. Smiraglia, and G. Diolaiuti (2016), Future hydrological regimes and glacier cover in the Everest region: The case study of the upper Dudh Koshi basin, *Science of the Total Environment*, 565, 1084–1101, doi: 10.1016/j.scitotenv.2016.05.138.
- Steiner, J. F., F. Pellicciotti, P. Buri, E. S. Miles, W. W. Immerzeel, and T. D. Reid (2015), Modelling ice-cliff backwasting on a debris-covered glacier in the Nepalese Himalaya, *Journal of Glaciology*, 61(229), 889–907, doi: 10.3189/2015jog14j194.
- Swithbank, C. (1950), The Origin of Dirt Cones on Glaciers, *Journal of Glaciology*, 1, 461–465, doi: 10.1017/S0022143000012880.
- Tapley, B. D., S. Bettadpur, M. Watkins, and C. Reigber (2004), The gravity recovery and climate experiment: Mission overview and early results, *Geophysical Research Letters*, 31, L09,607, doi: 10.1029/2004GL019920.
- Thakuri, S., F. Salerno, C. Smiraglia, T. Bolch, C. D'Agata, G. Viviano, and G. Tartari (2014), Tracing glacier changes since the 1960s on the south slope of Mt. Everest (central Southern Himalaya) using optical satellite imagery, *The Cryosphere*, 8(4), 1297–1315, doi: 10.5194/tc-8-1297-2014.
- Thibert, E., R. Blanc, C. Vincent, and N. Eckert (2008), Instruments and Methods Glaciological and volumetric mass-balance measurements: error analysis over 51 years for Glacier de Sarennes, French Alps, *Journal of Glaciology*, 54, 522–532, doi: 10.3189/002214308785837093.
- Thompson, S., D. I. Benn, J. Mertes, and A. Luckman (2016), Stagnation and mass loss on a Himalayan debris-covered glacier: processes, patterns and rates, *Journal of Glaciology*, 62(233), 467–485, doi: 10.1017/jog.2016.37.
- Thompson, S. S., D. I. Benn, K. Dennis, and A. Luckman (2012), A rapidly growing moraine-dammed glacial lake on Ngozumpa Glacier, Nepal, *Geomorphology*, 145, 1–11, doi: 10.1016/j.geomorph.2011.08.015.
- Treichler, D., and A. Kääb (2016), ICESat laser altimetry over small mountain glaciers, *The Cryosphere*, 10(5), 2129–2146, doi: 10.5194/tc-10-2129-2016.
- Tribe, A. (1992), Automated recognition of valley lines and drainage networks from grid digital elevation models: a review and a new method, *Journal of Hydrology*, 139(1), 263–293, doi: 10.1016/0022-1694(92)90206-B.
- Usman, M., and M. Furuya (2018), Interannual modulation of seasonal glacial velocity variations in the Eastern Karakoram detected by ALOS-1/2 data, *Journal of Glaciology*, pp. 1–12.
- Vaughan, D., J. Comiso, I. Allison, J. Carrasco, G. Kaser, R. Kwok, P. Mote, T. Murray, F. Paul, J. Ren, E. Rignot, O. Solomina, K. Steffen, and T. Zhang (2013), *Observations: Cryosphere in Climate Change 2013: The Physical Science Basis. Contribution of Working Group I to the Fifth Assessment Report of*

- the Intergovernmental Panel on Climate Change*, book section 4, p. 317–382, Cambridge University Press, Cambridge, United Kingdom and New York, NY, USA, doi: 10.1017/CBO9781107415324.012.
- Vijay, S., and M. Braun (2016), Elevation Change Rates of Glaciers in the Lahaul-Spiti (Western Himalaya, India) during 2000–2012 and 2012–2013, *Remote Sensing*, 8(12), 1038, doi: 10.3390/rs8121038.
- Vijay, S., and M. Braun (2018), Early 21st century spatially detailed elevation changes of Jammu and Kashmir glaciers (Karakoram–Himalaya), *Global and Planetary Change*, 165, 137 – 146, doi: <https://doi.org/10.1016/j.gloplacha.2018.03.014>.
- Vincent, C., A. Ramanathan, P. Wagnon, D. P. Dobhal, A. Linda, E. Berthier, P. Sharma, Y. Arnaud, M. F. Azam, P. G. Jose, and J. Gardelle (2013), Balanced conditions or slight mass gain of glaciers in the Lahaul and Spiti region (northern India, Himalaya) during the nineties preceded recent mass loss, *The Cryosphere*, 7(2), 569–582, doi: 10.5194/tc-7-569-2013.
- Vincent, C., P. Wagnon, J. M. Shea, W. W. Immerzeel, P. Kraaijenbrink, D. Shrestha, A. Soruco, Y. Arnaud, F. Brun, E. Berthier, and S. F. Sherpa (2016), Reduced melt on debris-covered glaciers: investigations from Changri Nup Glacier, Nepal, *The Cryosphere*, 10(4), 1845–1858, doi: 10.5194/tc-10-1845-2016.
- Vincent, C., A. Fischer, C. Mayer, A. Bauder, S. P. Galos, M. Funk, E. Thibert, D. Six, L. Braun, and M. Huss (2017), Common climatic signal from glaciers in the European Alps over the last 50 years, *Geophysical Research Letters*, 44, 1376–1383, doi: 10.1002/2016GL072094.
- Wagnon, P., C. Vincent, Y. Arnaud, E. Berthier, E. Vuillermoz, S. Gruber, M. Ménégoz, A. Gilbert, M. Dumont, J. M. Shea, D. Stumm, and B. K. Pokhrel (2013), Seasonal and annual mass balances of Mera and Pokalde glaciers (Nepal Himalaya) since 2007, *The Cryosphere*, 7(6), 1769–1786, doi: 10.5194/tc-7-1769-2013.
- Wang, D., and A. Kääb (2015), Modeling Glacier Elevation Change from DEM Time Series, *Remote Sensing*, 7(8), 10,117–10,142, doi: 10.3390/rs70810117.
- Wang, J., C. Song, J. T. Reager, F. Yao, J. Famiglietti, Y. Sheng, G. MacDonald, F. Brun, H. Müller Schmied, R. Marston, and Y. Wada (2018), Recent Global Decline in Endorheic Basin Water Storage and Its Impact on Sea Level Budget, *in press. Nature Geoscience*.
- Wang, Q., S. Yi, L. Chang, and W. Sun (2017), Large-Scale Seasonal Changes in Glacier Thickness Across High Mountain Asia, *Geophysical Research Letters*, 44(20), 2017GL075,300, doi: 10.1002/2017GL075300.
- Ward, D. J., and R. S. Anderson (2011), The use of ablation-dominated medial moraines as samplers for 10be-derived erosion rates of glacier valley walls, Kichatna Mountains, AK, *Earth Surface Processes and Landforms*, 36, 495–512, doi: 10.1002/esp.2068.
- Watson, C. S., D. J. Quincey, J. L. Carrivick, and M. W. Smith (2016), The dynamics of supraglacial ponds in the Everest region, central Himalaya, *Global and Planetary Change*, 142, 14 – 27, doi: <https://doi.org/10.1016/j.gloplacha.2016.04.008>.
- Watson, C. S., D. J. Quincey, M. W. Smith, J. L. Carrivick, A. V. Rowan, and M. R. James (2017a), Quantifying ice cliff evolution with multi-temporal point clouds on the debris-covered Khumbu Glacier, Nepal, *Journal of Glaciology*, 63(241), 823–837.
- Watson, C. S., D. J. Quincey, J. L. Carrivick, and M. W. Smith (2017b), Ice cliff dynamics in the Everest region of the Central Himalaya, *Geomorphology*, 278, 238 – 251, doi: <http://dx.doi.org/10.1016/j.geomorph.2016.11.017>.
- Watson, C. S., D. J. Quincey, J. L. Carrivick, M. W. Smith, A. V. Rowan, and R. Richardson (2018),

- Heterogeneous water storage and thermal regime of supraglacial ponds on debris-covered glaciers, *Earth Surface Processes and Landforms*, 43(1), 229–241, doi: 10.1002/esp.4236.
- Wagh, A. S. (1857), On Mounts Everest and Deodanga, *Proceedings of the Royal Geographical Society of London*, 2(2), 102–115, doi: 10.2307/1799335.
- Weiler, M., J. Seibert, and K. Stahl (2018), Magic components—why quantifying rain, snowmelt, and icemelt in river discharge is not easy, *Hydrological Processes*, 32(1), 160–166.
- WGMS (2017), Global Glacier Change Bulletin No. 2 (2014–2015).
- Willis, M. J., A. K. Melkonian, M. E. Pritchard, and J. M. Ramage (2012), Ice loss rates at the Northern Patagonian Icefield derived using a decade of satellite remote sensing, *Remote Sensing of Environment*, 117, 184–198, doi: <http://dx.doi.org/10.1016/j.rse.2011.09.017>.
- Wirbel, A., A. H. Jarosch, and L. Nicholson (2018), Modelling debris transport within glaciers by advection in a full-Stokes ice flow model, *The Cryosphere*, 12(1), 189–204, doi: 10.5194/tc-12-189-2018.
- Wu, K., S. Liu, Z. Jiang, J. Xu, J. Wei, and W. Guo (2018), Recent glacier mass balance and area changes in the Kangri Karpo Mountains from DEMs and glacier inventories, *The Cryosphere*, 12(1), 103–121, doi: 10.5194/tc-12-103-2018.
- Wu, Z., and S. Liu (2012), Imaging the debris internal structure and estimating the effect of debris layer on ablation of Glacier ice, *Journal of the Geological Society of India*, 80(6), 825–835.
- Xiang, Y., T. Yao, Y. Gao, G. Zhang, W. Wang, and L. Tian (2018), Retreat rates of debris-covered and debris-free glaciers in the Koshi River Basin, central Himalayas, from 1975 to 2010, *Environmental Earth Sciences*, 77(7), 285.
- Xin, W., L. Shiyin, H. Haidong, W. Jian, and L. Qiao (2012), Thermal regime of a supraglacial lake on the debris-covered Koxkar Glacier, southwest Tianshan, China, *Environmental Earth Sciences*, 67(1), 175–183.
- Yang, K., H. Lu, S. Yue, G. Zhang, Y. Lei, Z. La, and W. Wang (2018), Quantifying recent precipitation change and predicting lake expansion in the Inner Tibetan Plateau, *Climatic Change*, 147(1), 149–163, doi: 10.1007/s10584-017-2127-5.
- Yao, T., L. Thompson, W. Yang, W. Yu, Y. Gao, X. Guo, X. Yang, K. Duan, H. Zhao, B. Xu, J. Pu, A. Lu, Y. Xiang, D. B. Kattel, and D. Joswiak (2012), Different glacier status with atmospheric circulations in Tibetan Plateau and surroundings, *Nature Clim. Change*, 2(9), 663–667, doi: 10.1038/nclimate1580.
- Yatagai, A., K. Kamiguchi, O. Arakawa, A. Hamada, N. Yasutomi, and A. Kitoh (2012), APHRODITE: Constructing a Long-Term Daily Gridded Precipitation Dataset for Asia Based on a Dense Network of Rain Gauges, *Bulletin of the American Meteorological Society*, 93(9), 1401–1415, doi: 10.1175/BAMS-D-11-00122.1.
- Yi, S., and W. Sun (2014), Evaluation of glacier changes in high-mountain Asia based on 10 year GRACE RL05 models, *Journal of Geophysical Research: Solid Earth*, 119(3), 2504–2517, doi: 10.1002/2013JB010860.
- Yi, S., Q. Wang, L. Chang, and W. Sun (2016), Changes in Mountain Glaciers, Lake Levels, and Snow Coverage in the Tianshan Monitored by GRACE, ICESat, Altimetry, and MODIS, *Remote Sensing*, 8(10), 798, doi: 10.3390/rs8100798.
- Yin, Z.-Y., X. Zhang, X. Liu, M. Colella, and X. Chen (2008), An Assessment of the Biases of Satellite Rainfall Estimates over the Tibetan Plateau and Correction Methods Based on Topographic Analysis, *Journal of Hydrometeorology*, 9, 301–326, doi: 10.1175/2007JHM903.1.

- Zekollari, H., and P. Huybrechts (2018), Statistical modelling of the surface mass-balance variability of the Morteratsch glacier, Switzerland: strong control of early melting season meteorological conditions, *Journal of Glaciology*, 64(244), 275–288.
- Zemp, M., E. Thibert, M. Huss, D. Stumm, C. Rolstad Denby, C. Nuth, S. U. Nussbaumer, G. Moholdt, A. Mercer, C. Mayer, P. C. Joerg, P. Jansson, B. Hynek, A. Fischer, H. Escher-Vetter, H. Elvehøy, and L. M. Andreassen (2013), Reanalysing glacier mass balance measurement series, *The Cryosphere*, 7(4), 1227–1245, doi: 10.5194/tc-7-1227-2013.
- Zemp, M., H. Frey, I. Gärtner-Roer, S. U. Nussbaumer, M. Hoelzle, F. Paul, W. Haeberli, F. Denzinger, A. P. Ahlstrøm, B. Anderson, S. Bajracharya, C. Baroni, L. N. Braun, B. E. Cáceres, G. Casassa, G. Cobos, L. R. Dávila, H. Delgado Granados, M. N. Demuth, L. Espizua, A. Fischer, K. Fujita, B. Gadek, A. Ghazanfar, J. Ove Hagen, P. Holmlund, N. Karimi, Z. Li, M. Pelto, P. Pitte, V. V. Popovnin, C. A. Portocarrero, R. Prinz, C. V. Sangewar, I. Severskiy, O. Sigurdsson, A. Soruco, R. Usabaliyev, and C. Vincent (2015), Historically unprecedented global glacier decline in the early 21st century, *Journal of Glaciology*, 61(228), 745–762, doi: 10.3189/2015JoG15J017.
- Zhang, G., T. Yao, C. K. Shum, S. Yi, K. Yang, H. Xie, W. Feng, T. Bolch, L. Wang, A. Behrangi, H. Zhang, W. Wang, Y. Xiang, and J. Yu (2017), Lake volume and groundwater storage variations in Tibetan Plateau's endorheic basin, *Geophysical Research Letters*, 44(11), 5550–5560, doi: 10.1002/2017GL073773.
- Zhang, G., T. Bolch, W. Chen, F. Brun, E. Berthier, J. F. Crétaux, and T. Yao (in prep.), Comprehensive estimation of lake volume changes on the Tibetan Plateau during 1970s–2015 and basin-wide glacier contribution.
- Zhang, Y., K. Fujita, S. Liu, Q. Liu, and T. Nuimura (2011), Distribution of debris thickness and its effect on ice melt at Hailuoguo glacier, southeastern Tibetan Plateau, using in situ surveys and ASTER imagery, *Journal of Glaciology*, 57, 1147–1157, doi: 10.3189/002214311798843331.
- Zhang, Z., J. C. Chan, and Y. Ding (2004), Characteristics, evolution and mechanisms of the summer monsoon onset over Southeast Asia, *International Journal of Climatology*, 24(12), 1461–1482.
- Zhang, Z., S. Liu, J. Wei, J. Xu, W. Guo, W. Bao, and Z. Jiang (2016), Mass Change of Glaciers in Muztag Ata-Kongur Tagh, Eastern Pamir, China from 1971/76 to 2013/14 as Derived from Remote Sensing Data, *PLoS ONE*, 11, e0147327, doi: 10.1371/journal.pone.0147327.
- Zhou, Y., Z. Li, and J. Li (2017), Slight glacier mass loss in the Karakoram region during the 1970s to 2000 revealed by KH-9 images and SRTM DEM, *Journal of Glaciology*, 63(238), 331–342, doi: 10.1017/jog.2016.142.
- Zhou, Y., Z. Li, J. Li, R. Zhao, and X. Ding (2018), Glacier mass balance in the Qinghai–Tibet Plateau and its surroundings from the mid-1970s to 2000 based on Hexagon KH-9 and SRTM DEMs, *Remote Sensing of Environment*, 210, 96–112, doi: 10.1016/j.rse.2018.03.020.